EXPERIMENTAL AND NUMERICAL INVESTIGATIONS OF SINGLE ABRASIVE-GRAIN CUTTING

by

David James Anderson

Submitted in partial fulfilment of the requirements
for the degree of Doctor of Philosophy

at

Dalhousie University
Halifax, Nova Scotia
April 2011

DALHOUSIE UNIVERSITY

DEPARTMENT OF MECHANICAL ENGINEERING

The undersigned hereby certify that they have read and recommend to the Faculty of Graduate Studies for acceptance a thesis entitled "EXPERIMENTAL AND NUMERICAL INVESTIGATIONS OF SINGLE ABRASIVE-GRAIN CUTTING" by David James Anderson in partial fulfilment of the requirements for the degree of Doctor of Philosophy.

Dated: April 1, 2011

External Examiner: _____

Research Supervisor: _____

Examining Committee: _____

_____

Departmental Representative: _____

DALHOUSIE UNIVERSITY

DATE: April 1, 2011

AUTHOR: David James Anderson

TITLE: EXPERIMENTAL AND NUMERICAL INVESTIGATIONS OF SINGLE ABRASIVE-GRAIN CUTTING

DEPARTMENT OR SCHOOL: Department of Mechanical Engineering

DEGREE: PhD CONVOCATION: May YEAR: 2011

_____

Signature of Author

Table of Contents

List of Figures

List of Tables

Abstract

The cutting action of a single abrasive grain was investigated using a combination of high-speed scratch tests and finite element models. The high-speed scratch tests were unique in that the cutting conditions of a grinding operation were closely replicated. Two geometries were tested: a round-nosed stylus to approximate a 15-grit abrasive grain and a flat-nosed stylus to approximate a worn 46-grit abrasive grain. The three-dimensional finite element model was unique in that a hybrid Euler-Lagrange method was implemented to efficiently model the interaction between an abrasive grain and a workpiece. The finite element model was initially validated using indentation tests to remove the complexities of relative motion from the validation process. The validation was completed through comparisons to the experimental scratch tests. The results of the analysis revealed several key findings. Rubbing, plowing, and cutting do not display distinct transitions; rather, they coexist with different weightings depending on the scratching speed and the depth of cut. The normal forces increased for a given depth of cut as the scratching speed was increased due to strain-rate hardening of the workpiece. The tangential forces decreased for a given depth of cut as the scratching speed was increased due to a reduction in the coefficient of friction and a change in the cutting mechanics from plowing to cutting. The change in the cutting mechanics was investigated by analyzing the evolution of the scratch profiles as the depth of cut and scratching speed were changed. It was found that higher scratching speeds produced less material pile-up and this was attributed to a change in the cutting mechanics. Due to the change in the cutting mechanics, the specific energy decreased as the depth of cut and scratching speed were increased. A numerical case study revealed that reducing the grain size resulted in: lower forces, lower specific energies, and smaller volumes of subsurface stresses. The finite element model was adapted to work in conjunction with the flat-nosed stylus creating the first model capable of simulating the cutting of an abrasive grain in three dimensions.

List of Abbreviations and Symbols Used

Abbreviations

ACEnet	Atlantic Computational Excellence Network
ALE	Arbitrary Lagrangian-Eulerian
ANSI	American National Standards Institute
C	Cutting
CNC	Computer Numerical Control
E	Elastic
EP	Elastoplastic
G	Grinding
GDP	Gross Domestic Product
HIS	Half Index Shift
L	Lagrange
MC	Micro Cutting
MEMS	Micro-Electrical Mechanical System
MPP	Massively Parallel Processing
MUSCL	Monotone Upwind Schemes for Conservation Laws
S	Structural
SEM	Scanning Electron Microscope
SPH	Smooth Particle Hydrodynamics
TEP	Thermo-Elastoplastic
TS	Thermo-Structural
U	Eulerian

Symbols

a	Depth of Cut
a_c	Contact Radius
A	Johnson-Cook Strength Parameter
A_c	Contact Area
A_E	Element Area
A_S	Stylus Area
b	First Order Correction to Γ_0
B	Johnson-Cook Strength Parameter
c	Wave Speed
C	Johnson-Cook Strain Modifier
CN	Courant Number
C_p	Specific Heat at Constant Pressure
C_{sp}	Speed of Sound
C^*	Constraint Factor
$\vec{d}$	Depth of Penetration
d_g	Grain Diameter

d_w	Diameter of Grinding Wheel
e	Material Number
E_E	Elastic Modulus
E_{int}	Internal Energy
E_K	Bulk Modulus
E_P	Plastic Hardening Modulus
E_T	Tangent Modulus
E_{tot}	Total Energy
f	ALE Body Motion
F	Indentation Force
F_C	Cutting Force
F_f	Force on Fluid
F_F	Friction Force
F_{fs}	Fluid-Structure Coupling Force
F_H	Horizontal Force
F_{NF}	Normal to Friction Force
F_{Norm}	Normal Force
F_{NS}	Normal to Shear Force
F_s	Force on Slave Coupling Point
F_S	Shear Force
F_{Tan}	Tangential Force
F_T	Thrust Force
F_V	Vertical Force
F_Y	Force to Cause Yielding
G	Shear Modulus
h	Chip Thickness
h_m	Maximum Chip Thickness
H	History Variable
HK	Knoop Hardness
HRc	Rockwell Hardness C Scale
j	Node Number
J	Volumetric Strain
k	Element Edge
K	Thermal Conductivity
l	Element Face Number
l_c	Contact Length
l_{char}	Characteristic Length
l_s	Shear Plane Length
L	Inter-grain spacing
m	Thermal Softening Coefficient
M	Element Mass
MRR	Material Removal Rate
n	Hardening Exponent
N	Element Shape Function

NR	Nose Radius
p	Pressure
P	Power
P_b	Relative Volume of Bond Material
P_{FE}	Power from Finite Element Model
P_g	Relative Volume of Abrasive Grain
P_v	Relative Volume of Void Porosity
q_f	Fluid-Structure Coupling Scale Factor
Q	Material Constants
R	Round-Nosed Stylus Radius
R^1, R^2, R^3	Resultant Forces
s	Second Order Approximation to the Slope S
sgn	Signum Function
S	Slope of Function Φ
S_1, S_2, S_3	Slope Coefficients
SRC	Cowper-Symonds Strain Rate Parameter
SRP	Cowper-Symonds Strain Rate Parameter
t_c	Chip Thickness After Cut
t^n	Time at State n
t_o	Chip Thickness Before Cut
Δt	Time Step
T	Current Temperature
$TSSFAC$	Time Step Scale Factor
T_{amb}	Ambient Temperature
T_{melt}	Melting Temperature
ΔT	Change in Temperature
$\vec{u}$	Material Velocity
U	Specific Energy
U_c	Cutting Specific Energy
U_p	Plowing Specific Energy
U_r	Rubbing Specific Energy
U_{tot}	Total Specific Energy
v	Contact Discontinuity Velocity
$\vec{v}$	Reference Coordinate System Velocity
$\vec{v}_f$	Fluid Velocity
v_p	Particle Velocity
v_s	Shock Wave Velocity
v_w	Wheel Velocity
v_{wp}	Workpiece Speed
$\vec{v}_s$	Structure Velocity
V	Element Volume
V^f	Volume Fraction
w	Width of Cut
$\vec{w}$	Difference of Material Velocity and Reference Coordinate Velocity

$\vec{x}$	ALE Coordinate
X	Flat-Nosed Stylus Width
$\vec{X}$	Lagrangian Coordinate
Y	Grit Number
Z	Element Number

Greek Symbols

α	Thermal Expansion Coefficient
α_R	Rake Angle
α_T	Tabor Constant for True Stress
β	Friction Angle
β_T	Tabor Constant for Plastic Strain
γ	Flat-Nosed Stylus Angle
Γ_0	Grüneisen Gamma
δ	Displacement
δ_c	Cutting Displacement
δ_p	Plowing Displacement
δ_r	Rubbing Displacement
ε_p	Plastic Strain
$\dot{\varepsilon}_0$	Reference Strain Rate
$\overline{\varepsilon}_p$	Effective Plastic Strain
$\dot{\overline{\varepsilon}}_p$	Effective Plastic Strain Rate
$\left(\dot{\varepsilon}_p\right)_{ij}$	Plastic Component of Rate of Deformation Tensor
$\dot{\varepsilon}^v$	Volumetric Strain Rate
$\dot{\varepsilon}'$	Deviatoric Strain Rate
ζ	Dynamic Viscosity
θ	Round-Nosed Stylus Contact Angle
κ	Spring Stiffness
K	Hardening Modulus
λ	Flat-Nosed Stylus Angle
μ	Force Ratio
μ_a	Adhesion Friction
μ_D	Density Ratio
μ_p	Plowing Friction
ν	Poisson's Ratio
ρ	Current Density
ρ_0	Nominal Density
ς	Flat-Nosed Stylus Angle
$\varsigma(j)$	Index of Node j in the Connectivity Matrix of Element Z
$\overline{\sigma}$	Effective Stress
$\bar{\bar{\sigma}}$	Cauchy Stress
σ_0	Initial Yield Strength

σ_U	Ultimate Tensile Strength
σ_Y	Yield Tensile Strength
Σ	Stress Update Algorithm
τ	Shear Stress
φ	Shear Plane Angle
Φ	Flux
Υ	Flat-Nosed Stylus Half Cone Angle
χ	Scratch Angle
ψ	Scratch Taper Angle
Ψ	Element Centered Variable

Acknowledgements

Before proceeding, I feel it is necessary to thank those that have contributed to the success of my work. Firstly, I must thank my supervisory committee for their assistance and guidance throughout my tenure as a PhD candidate. Much praise must be directed towards my supervisor, Dr. Andrew Warkentin, for without his guidance, experience, funding, and above all, his patience this work would have been all for not. I feel I have become a better researcher, presenter, and technical communicator because of his efforts. Secondly, I must thank the Atlantic Computational Excellence Network [ACEnet], the regional high-performance computing consortium for Universities in Atlantic Canada, for providing the computational resources necessary for this work. Finally, I must thank both the Canadian Foundation for Innovation [CFI] and the Natural Sciences and Engineering Research Council of Canada [NSERC] for providing financial contributions towards this work. The grants provided by CFI and NSERC provided the necessary equipment that allowed me to pursue my research. The Alexander Graham Bell Canadian Graduate Scholarship awarded to me through NSERC was both fulfilling and unexpected as it proved my ability to perform top-level research.

Chapter 1 Introduction

The grinding operation is industrially important due to its versatility as it is employed in the manufacture of common components, such as: gears, camshafts, bearing races, and turbine blades. It is capable of shaping difficult to machine materials into complex parts with high dimensional accuracy and smooth surface finishes. The economical impact of the grinding operation is staggering. It is estimated that 14% of the United States' gross domestic product [GDP] is accounted for by the manufacturing industry [1] and 20% - 25% of all manufacturing expenditures are related to the grinding operation [2]. The World Bank reported that the United States' 2008 GDP was $14 trillion [3], which provides a conservative estimate of the economic impact of the grinding operation to be $397 billion.

The economic impact of the grinding operation lends itself to be a very desirable research topic as improvements to the process, such as: reduced cost, reduced scrap rate, improved part quality, or improved cycle times, may lead to higher profits.

1.1 Motivation

The motivation for this work stems from the need and desire to better comprehend the grinding operation. Historically, much of the research devoted to grinding has focused on experimental observations and modeling of the overall process and macroscopic effects, such as: workpiece temperatures, global forces, and power consumption; however, these effects should be considered to be the summation of the effects of individual abrasive grains. Unfortunately, due to the variability and stochastic nature of grinding wheels, it is difficult to completely characterize the grinding process for all grinding wheel compositions, workpiece materials, and process parameters. The key to the characterization of the grinding process at the macro-scale requires a better understanding of the phenomena at the micro-scale; specifically, at the interface of the abrasive grain and the workpiece. By creating a micro-scale model of the grinding process it may be possible to better understand the forces, pressures, stresses, strains, temperatures, and material removal mechanisms, eventually leading to improved grinding wheel design and process parameter selection.

This research is significant as it represents the next logical step towards the understanding of the grinding process. The results may provide insight into the design and selection of grinding wheels, the optimization of process parameters, and the calculation of fundamental grinding parameters, such as the uncut chip thickness and the contact length.

1.2 Purpose

The purpose of this work was to create a geometrically and physically accurate, experimentally-validated, single abrasive-grain cutting model based on the Eulerian finite element formulation. The finite element model was progressively developed in stages with each iteration undergoing experimental validation. These stages included comparisons to analytical and experimental indentation data and experimental scratching data. The completed finite element model was then used to thoroughly investigate the cutting mechanics of an abrasive grain engaging a steel workpiece.

1.3 Thesis Outline

The full body of this work will evolve over the following chapters. In Chapter 2 fundamental concepts in grinding theory and practice will be reviewed. In Chapter 3 a literature review of analytical and finite element modeling of metal cutting and grinding will be presented and reviewed. Additionally, Chapter 3 will discuss the key mathematics associated with the finite element modeling aspects of this work. Chapter 4 will discuss the indentation testing that was performed to test the feasibility of the chosen finite element method, to investigate the effects of several key numerical parameters, and to validate the contact mechanics of the system. Chapter 5 will present the experimental high-speed scratching apparatus that was developed for the present work as well as the data post-processing techniques. Chapter 6 will present the results from experimental high-speed scratch tests using a round-nosed stylus geometry. The experimental data will be used alongside a validated finite element model to perform an in-depth analysis of the scratching process. Chapter 7 will continue the analysis of high-speed scratching using a flat-nosed stylus geometry. Finally, Chapter 8 will provide a summary and conclusions regarding the work that was undertaken for this thesis, as well as a statement of the contributions that this work has produced.

Chapter 2 Grinding Theory

Grinding is an abrasive machining operation where small abrasive particles are formed into disk-shaped tools which are fed into a workpiece at high peripheral velocities. The combined efforts of the abrasive particles are capable of quickly removing large amounts of material. Unlike conventional metal cutting tools where the cutting geometry is well defined and constant, the cutting edges of a grinding wheel are the stochastically sized, shaped, and positioned abrasive particles that are in a constant state of flux due to wheel loading and abrasive wear, fracture, and pull-out.

Grinding operations are capable of forming parts out of traditionally difficult to machine materials, such as: ceramics and hardened steels, to high dimensional accuracy and smooth surface finishes. Two general classes of grinding exist: surface grinding and deep grinding. Surface grinding is the more traditional method where many, shallow, high-speed passes are required to form a part feature, such as a surface plate. Deep grinding is a relatively newer method where fewer, deeper, low-speed passes are required, such as in the manufacture of

the root of a turbine blade. Often, part features can be made in a single pass of the grinding wheel when using the deep grinding operation.

The grinding operation as a whole spans two length scales. At the macro-scale, overall effects are readily observable and measurable, such as the forces exerted on the workpiece, the power consumed during a grinding pass, the temperature build-up in the workpiece, and the resultant surface roughness of the workpiece. However, it is at the micro-scale where the foundation of material removal is laid. Therefore, the purpose of this chapter is to introduce key kinematic quantities that relate to the macro-scale of grinding followed by an analysis of the grinding operation at the micro-scale.

2.1 Grinding Wheels

In order to understand grinding micro-mechanics, an understanding of the construction of grinding wheels is required. A grinding wheel is a ternary system that is composed of small, hard, non-metallic, abrasive particles, a bonding material, and porosity. An SEM micrograph of a typical grinding wheel is shown in Figure 2.1, where the abrasive grains, bond material, and voids are clearly visible. The abrasive grains are responsible for material removal, the bonding material is the glue that holds the grains in place, and the voids provide chip clearance and coolant transport into the grinding zone. The marking system for conventional grinding wheels is defined by the American National Standards Institute [ANSI] by Standard B74.13 - 1977 [4]. This marking standard, illustrated in Figure 2.2, provides the user with key information regarding the construction of the grinding wheel.

The abrasive grain type must be selected based on the material to be ground and should include high hardness, wear resistance, toughness, and friability as general properties, where friability refers to the capacity of the abrasive grain to fracture when dull thus exposing fresh, sharp, cutting edges. Aluminum oxide and silicon carbide are the two most common abrasives used in production grinding. Aluminum oxide tends to be suitable for ferrous and high-strength alloys, while silicon carbide tends to be suitable for ductile metals such as aluminum and brittle materials such as cast iron. Silicon carbide is not suitable for ferrous materials due to the strong affinity between the carbon in the silicon carbide and the iron in the steel. Superabrasives such as cubic boron nitride and diamond are generally reserved for

demanding applications where the workpiece material is very hard, such as: hardened tool steels, ceramics, and carbides.

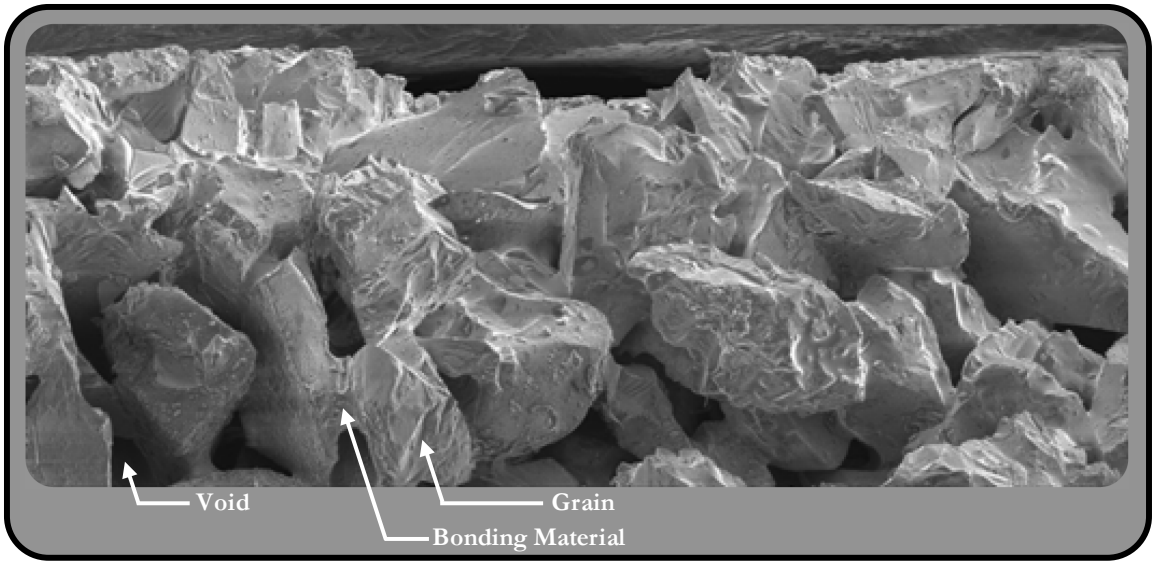

Figure 2.1 - SEM micrograph of an 80-grit grinding wheel.

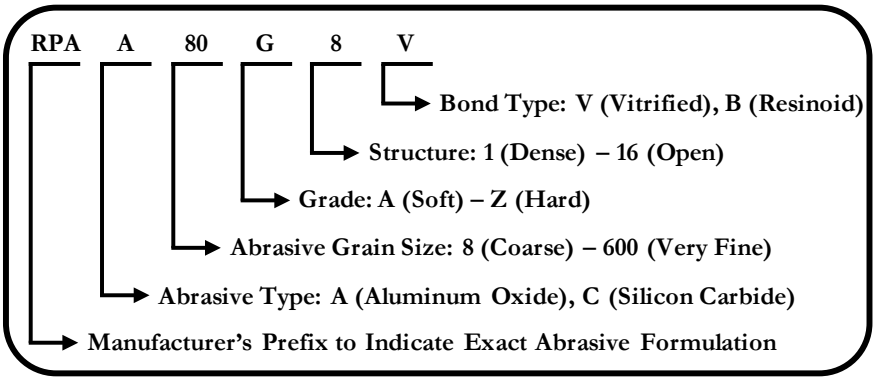

Figure 2.2 - ANSI Standard grinding wheel marking system.

The size of the abrasive grains play a pivotal role in the material removal rate and surface finish of the grinding operation. Larger abrasive grains promote higher material removal rates at the expense of surface finish while smaller abrasive grains permit a smoother surface finish at a lower material removal rate. The abrasive grains that form a grinding wheel are sorted by grit size using a standard mesh, or sieve, where a higher grit number refers to smaller grains. Malkin [2] approximated the average diameter, in mm, of a grain d_g according to:

$$d_g = 15.2Y^{-1} \tag{2.1}$$

where Y is the grit number. Grinding wheels are commonly referred to by their grit number; for instance, a grinding wheel with an abrasive grain size of 80 would be called an 80-grit grinding wheel.

The wheel grade and wheel structure are a coupled system where the relative volumes of abrasive grain P_g, bonding material P_b, and void space P_v is expressed as:

$$P_g + P_b + P_v = 1.0 \tag{2.2}$$

The grade of a grinding wheel indicates the bonding material's ability to retain the abrasive grain during cutting, while the structure of a grinding wheel indicates the porosity of the grinding wheel. Generally, harder wheels contain more bonding material and softer wheels contain less bonding material, while open wheels contain less bonding material and dense wheels contain more bonding material. Hard wheels are well suited for large material removal rates and soft workpiece materials while soft wheels are well suited to low material removal rates and hard workpiece materials. Open wheels are desirable to promote the flushing of debris during the grinding operation while dense wheels are preferred for improved surface finish and dimensional control.

The bonding material must be strong, tough, and resistant to high temperatures in order to securely hold the abrasive grains in place during cutting. Typical bond materials are vitrified and resinoid. A vitrified bond consists of baked clay and ceramic materials and tends to be strong, rigid, able to withstand elevated temperatures, and is relatively unaffected by the cooling fluids commonly used during production grinding operations. A resinoid bond is composed of thermosetting resins and possess very high strength making it suitable for rough grinding and cut-off operations.

2.2 Grinding Wheel Wear

The wear cycle of a grinding wheel is complex and affected by many factors, such as: the initial condition of the grinding wheel, the workpiece material, the process parameters, and the type and quantity of cutting fluid used. Grinding wheel wear can be categorized as either fracture wear or attritious wear [5].

Fracture wear occurs when the cutting forces of a dull abrasive grain exceed the fracture strength of the abrasive or bond material and can be beneficial as new, sharp, cutting edges become exposed resulting in improved cutting action, which is often referred to as self-sharpening. Unfortunately, fracture wear tends to create an irregular wheel surface resulting in a degradation of the workpiece surface finish. Attritious wear is a gradual process where initially sharp grains become dull creating a flat region of the abrasive grain, commonly referred to as a wear flat. As the attritious wear continues, the wear flats become larger and the cutting action becomes less efficient due to an increase in rubbing between the abrasive grain and the workpiece. As will be discussed later in this Chapter, rubbing is not desirable.

2.3 Macro-Scale Kinematics

The interaction between a grinding wheel and a workpiece is shown in Figure 2.3, where the relative dimensions are exaggerated for clarity. The figure shows that the grinding wheel, with a diameter of d_w and peripheral velocity v_w, engages the workpiece, translating at a velocity of v_{wp}, at a prescribed depth of cut a. The relative directions of the workpiece and wheel velocities determine the type of grinding being performed. Down grinding is performed when the workpiece is translating to the left and the two velocities point in the same direction, as shown in the figure, while up grinding is performed when the workpiece is translating to the left and the two velocities point in the opposite direction. The line defining the contact between the grinding wheel and the workpiece is known as the contact length l_c and is found from:

$$l_c = \sqrt{a d_w} \tag{2.3}$$

and is typically assumed to be a straight line due to the large difference between the diameter of the grinding wheel and the depth of cut $(d_w \gg a)$. The volume of workpiece material removed in time is known as the material removal rate MRR and is found from:

$$MRR = a v_{wp} w \tag{2.4}$$

where w is the width of cut. The power P consumed during grinding is a function of the wheel peripheral velocity and the tangential force F_T:

$$P = v_w F_T \tag{2.5}$$

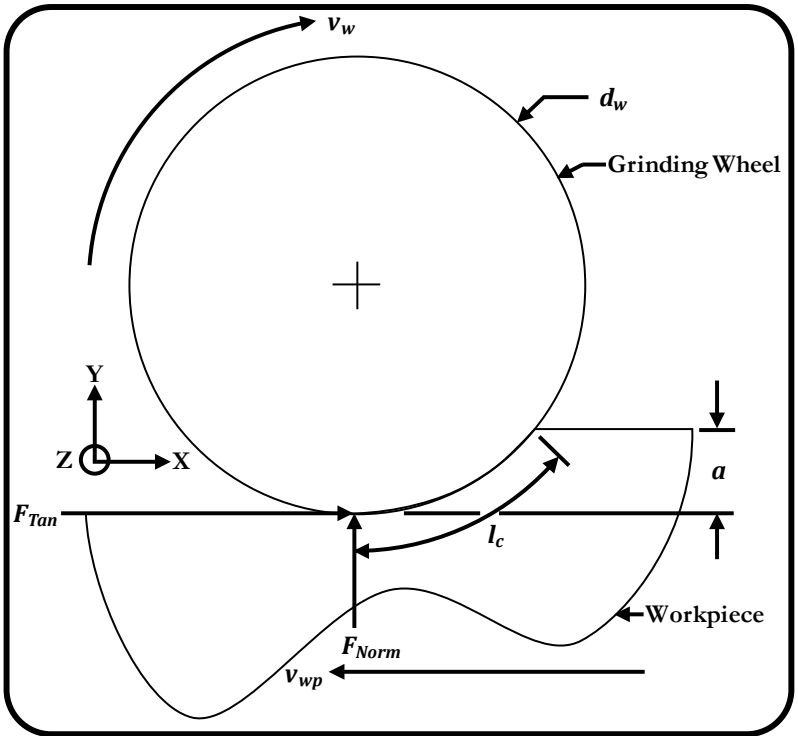

Figure 2.3 - Macro-scale kinematic parameters.

By combining Equations (2.4) and (2.5), one can calculate the amount of energy that is required to remove a unit volume of material; the specific energy U:

$$U = \frac{P}{MRR} \tag{2.6}$$

It should be noted that the power P, the normal force F_{Norm}, the tangential force F_{Tan}, and the material removal rate MRR are average values distributed along the contact length l_c. Also included in Figure 2.3 is the coordinate system chosen for this work, where the Z-axis is positive coming out of the page.

2.4 Micro-Scale Kinematics

The interaction between the grinding wheel and the workpiece is somewhat different and more complicated at the micro-scale. The path that an abrasive grain follows as it interacts with the workpiece is a complicated trochoidal motion that results from the simultaneous rotational motion of the grinding wheel and the translational motion of the workpiece. Figure 2.4 shows the result of the grain motion simplified for a single grain. A grain in imminent contact with the workpiece is shown embedded in a grinding wheel at time t^n. At

time t^{n+1} the grain has exited the workpiece and removed the shaded material. Evidently, the thickness of the removed material changes with the position of the grain and is known as the instantaneous chip thickness h. For up grinding, the maximum grain engagement occurs at the end of the cut producing the maximum chip thickness h_m, which is found from:

$$h_m = 2L\frac{v_{wp}}{v_w}\sqrt{\frac{a}{d_w}} \tag{2.7}$$

where L is the inter-grain spacing. In down grinding, the maximum grain engagement occurs at the beginning of the cut.

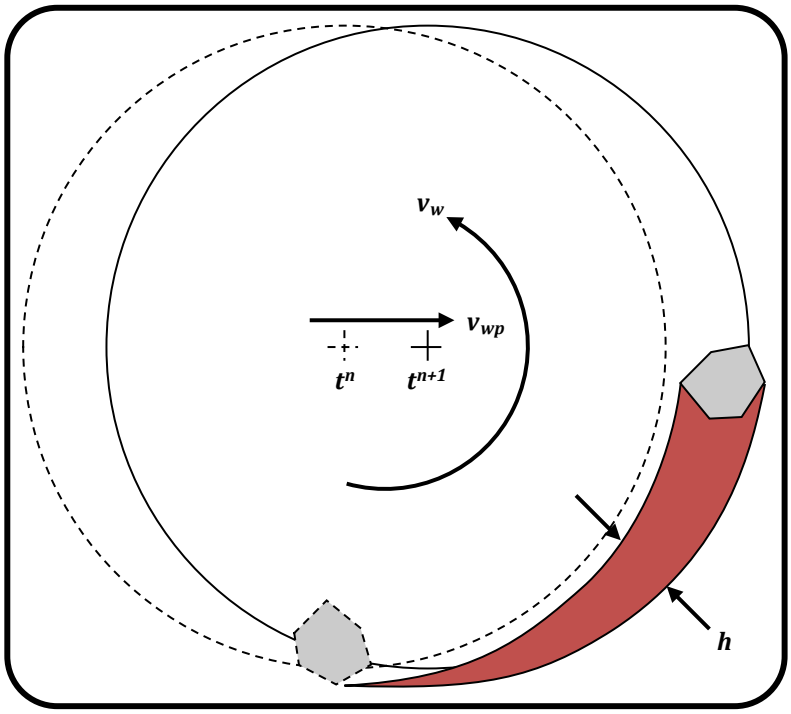

Figure 2.4 - Trochoidal grain path.

Clearly, the grain-workpiece interaction changes considerably as the uncut chip thickness increases. As reported by Marshal and Shaw [6] the chips produced in grinding are much smaller than those produced in conventional machining and, therefore, conventional cutting theory cannot be applied to grinding. Hahn [7] proposed that the increase in the specific energy during grinding was a result of the increased rubbing between the grains and the workpiece. Hahn's theories and the change in uncut chip thickness has spawned the three-phase material removal model of single abrasive-grain cutting. Several authors, including

Malkin [2] and Marinescu *et al.* [8] deduced that the three fundamental phases, namely: rubbing, plowing, and cutting, as shown in Figure 2.5, sum to create the necessary material removal. Rubbing occurs when the uncut chip thickness is in the range of $0 \leq h \leq \delta_r$ and consists of elastic deformation and heat generation through friction and can be considered wasted energy as no material removal occurs. Plowing occurs as the uncut chip thickness increases to the range of $\delta_r < h \leq \delta_p$ and consists of a combination of elastic and plastic deformation. During this phase the workpiece material tends to bulge ahead of the abrasive grain to form a plowed lip followed by side flow as the motion continues. Some elastic recovery occurs in the wake of the abrasive grain; however, a residual scratch or groove is created as a result of plastic workpiece deformation. Plowing creates some localized material removal; however, this process is inefficient as there is no material ejected from the workpiece. Cutting occurs once the uncut chip thickness increases to the range of $\delta_p < h \leq \delta_c$ and primarily consists of plastic deformation. At this phase the forces are sufficient to shear the workpiece material into a chip which is then ejected from the workpiece. This phase tends to be efficient as there is little energy wasted through elastic deformation. Subramanian *et al.* [9] succinctly summarize the rubbing, plowing, and cutting phases as surface modification processes, material displacement processes, and material removal process, respectively. Zhao *et al.* [10] performed grinding experiments at ultra-high wheel speeds of 80 m/s to 200 m/s and found that the three phase model required modification. They proposed that at these ultra high-speeds a small volume of workpiece material under the grain undergoes a phase change as a result of the high temperatures and pressures experienced due to the grain-workpiece impact. This material then flows ahead of the grain in a manner similar to high-speed extrusion where it is eventually removed by the grain. Effectively, the extrusion causes a reduction in the uncut chip thickness leading to lower forces, higher rates of wheel wear, higher contact temperatures, and higher material removal rates.

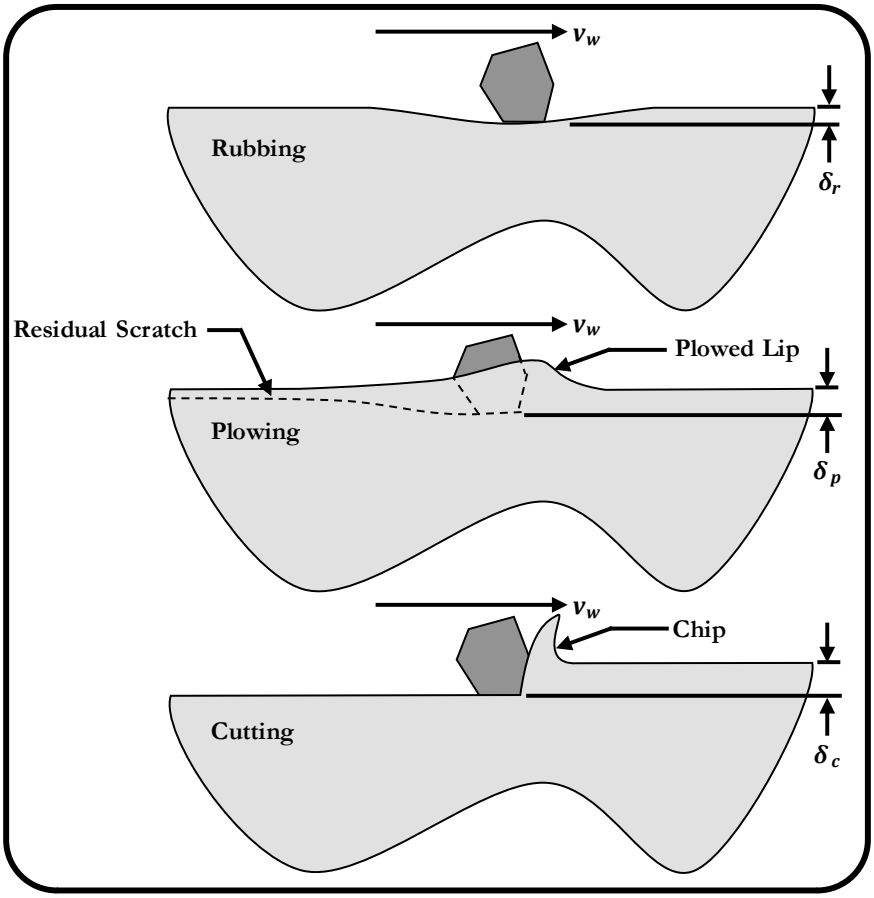

Figure 2.5 - Rubbing, plowing, and cutting phases of grain-workpiece interaction.

Ultimately, the ideal grinding operation would minimize the rubbing and plowing phases while maximizing the cutting phase; however, this is complicated by the stochastic nature of the abrasive grains and their distribution in a grinding wheel. As illustrated in Figure 2.6, the size, shape, spacing, and protrusion height of abrasive grains may not be ideal, which may lead to inconsistent uncut chip thicknesses and some grains doing more work than others. The stochastic construction of a grinding wheel is clearly evident in the SEM micrograph of Figure 2.1 which shows the variability of the grains and their packing structure.

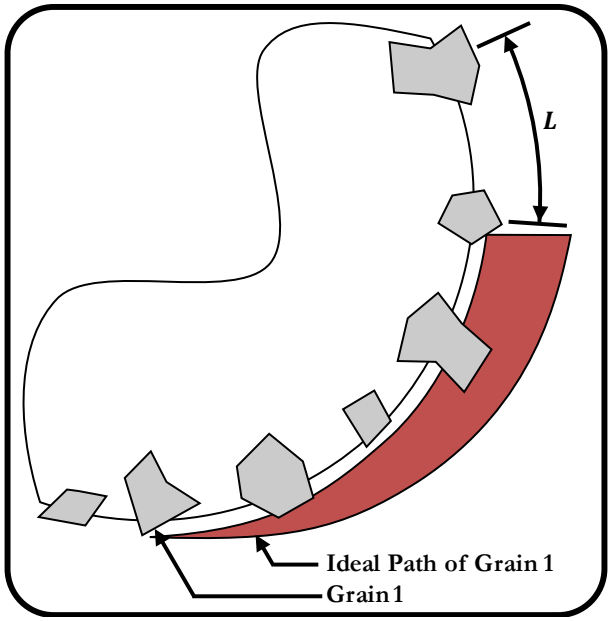

Figure 2.6 - Stochastic grain size, shape, and distribution.

2.5 Grinding Energy

As was the case with chip formation, the trochoidal grain motion influences the specific energy of the grinding operation. Studies [11,6] have shown that larger specific energies were found when the process parameters were adjusted to reduce the uncut chip thickness and that the specific energy in grinding is considerably higher than a conventional metal cutting process, usually on the order of 10 times larger [12]. There are two theories used to explain this size effect phenomenon. The first theory attempts to explain the size effect from a materials viewpoint in that as the scale becomes smaller, materials become stronger due to reduced dislocations. The second theory is based on the three phase cutting theory, discussed previously, and requires additional explanation.

Grinding and other metal cutting operations tend to be considered adiabatic due to the high cutting speeds and large strains; therefore, the heat generated from plastic deformation does not have sufficient time to conduct into the remainder of the workpiece. This adiabatic condition seems to indicate that there is an energy limit that can be supported by the workpiece and is related to the amount of energy required to raise the temperature of a unit volume of material from ambient to a molten state. Malkin [2] indicates that the melting energy per unit volume of iron is approximately 10.5 J/mm^3, which is typically representative

of most steels. However, production grinding operations tend to produce specific energies of approximately 20 - 60 J/mm^3, which is far higher than the melting energy. Incidentally, it is quite evident from observations of the grinding operation that workpiece melting does not occur; therefore, there must be additional contributions to the specific energy.

As shown by Malkin [2], the total specific energy in grinding U_{tot} is the sum of the specific energies for rubbing U_r, plowing U_p, and cutting U_c:

$$U_{tot} = U_r + U_p + U_c \tag{2.8}$$

In a set of experiments performed by Malkin, the specific energy decreased to a minimum of 13.8 J/mm^3 as the material removal rate was increased. It is generally accepted that in a metal cutting operation approximately 75% of the energy is associated with material shearing and 25% is associated with the chips rubbing against the cutting tool. These energy ratios in combination with the minimum specific energy produce a value of 10.4 J/mm^3 for shearing, which is close to the theoretical value of 10.5 J/mm^3 reported earlier. This suggests that 13.8 J/mm^3 is the specific energy contribution associated with cutting and the remainder must be a result of rubbing and plowing, which further emphasizes that rubbing and plowing are generally wasted energy. It is usually difficult to isolate the rubbing and plowing energies in grinding as they are tightly coupled; however, Doman [13] was able to separate the two components using an experimentally-verified finite element model. The model was able to separate the two energies using an element erosion algorithm that systematically deleted elements based on an effective plastic strain limit. The energy associated with the deleted elements represented the energy required to form a scratch and was tracked separately of the rubbing energy, thus permitting independent study of the rubbing and plowing energies.

2.6 Summary

This chapter has introduced the basics of the grinding operation and outlined the important macro- and micro-scale kinematic relationships that are relevant to this work. Of note was the trochoidal motion of the abrasive grains through the workpiece and the resulting increase in the uncut chip thickness and the three phases of material removal; namely, rubbing, plowing, and cutting. It was also shown that the specific energy of the grinding operation is larger when compared to traditional metal cutting as a result of the energies

associated with the rubbing and plowing phases. The specific cutting energy in grinding was shown by Malkin to be approximately 13.8 J/mm^3, which represents the potential lower limit of total specific grinding energy for ferrous materials.

Chapter 3 Metal Cutting and Chip Formation

The purpose of this section is two-fold: to review the current methods used to model chip formation in metal cutting and to review some of the mathematical principles that are implemented in the finite element modeling software that was used for this work.

A literature review revealed that there is a large body of work devoted to modeling the chip formation in conventional metal cutting and micro cutting and a lack of published work devoted solely to grinding. Therefore, this section will begin with an introduction to chip formation in conventional metal cutting and grinding and will briefly outline some of the more important analytical models. This introduction will be followed by a review of the primary finite element methods utilized to model chip formation. The pros and cons of each formulation will then be reviewed. Additionally, an overview of LS-DYNA®, the implemented hydrocode utilized for the finite element models of this thesis, will be presented along with a discussion of the material models, the equation of state, and the tool-workpiece coupling definition.

3.1 Chip Formation

Although conventional metal cutting is not the focus of this work; it is nonetheless beneficial to briefly discuss the topic as an introduction to the physics of chip formation in general. Chip formation is a complex mechanism that is dependent on the strength of the workpiece material, the cutting tool geometry, and the cutting conditions. The basic geometry of chip formation in conventional metal cutting is shown in Figure 3.1, which depicts the basic two-dimensional orthogonal cutting model. The cutting tool, with rake angle α_R, engages the workpiece at a depth of cut of t_0, which is also known as the undeformed chip thickness. Shearing of the workpiece occurs along the primary shear zone at an angle of φ and the resulting chip flows along the rake face of the cutting tool where a secondary shear zone is created by friction. The resulting chip has a thickness of t_c while the primary shear zone has a length of l_s. Rubbing of the newly created surface is prevented by the relief angle of the cutting tool.

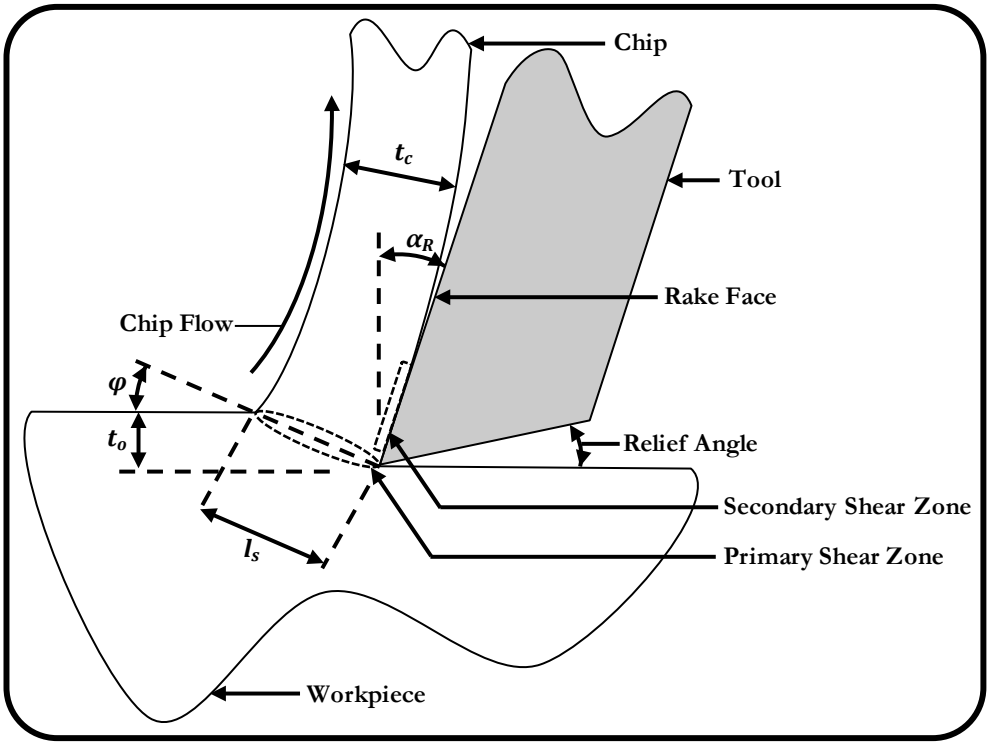

Figure 3.1 - Two-dimensional chip formation geometry in conventional metal cutting.

Chip formation in grinding is further complicated by the aggressive geometry of abrasive grains, as shown in Figure 3.2. Abrasive grains typically have negative rake angles and a non-existent relief angle due to wear flat development. The subsequent rubbing on the newly created surface tends to lead to a tertiary shear zone.

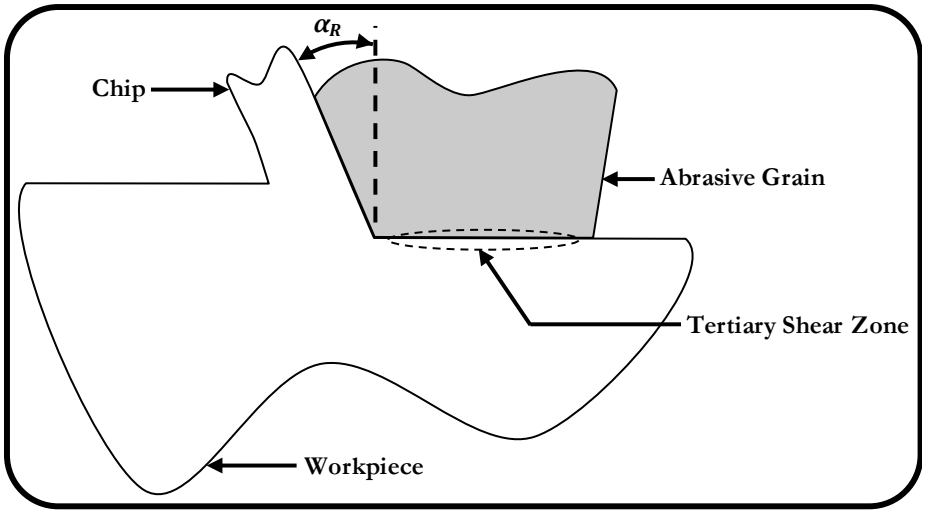

Figure 3.2 - Two-dimensional chip formation geometry in grinding.

3.2 Analytical Models

Table 3.1 summarizes some of the available analytical models for chip formation. This list is by no means exhaustive; rather, it is a sampling of the available models for grinding, conventional cutting, and micro cutting. The table identifies the dimensionality of the model as either 2 or 3, where a two-dimensional model is considered when only the cutting and thrust forces are investigated and a three-dimensional model is considered when the axial force is also considered. The model type is differentiated as either purely structural [S] or thermo-structural [TS] in which tool-workpiece heat transfer is considered. The material is designated as either elastic [E], elastoplastic [EP], or thermo-elastoplastic [TEP]. It should be noted that the material was assumed elastic if there was no discussion on the implemented material model. The process that the model simulates is designated as either cutting [C], micro cutting [MC], or grinding [G]. Finally, the inclusion of the nose-radius geometry and experimental validation are each indicated with a check mark [✓].

Table 3.1 - Analytical model overview.

Model	Reference	Dimension	Type	Material	Process	Nose Radius	Experimental Validation
Merchant	[14]	2	S	E	C		✓
Malkin	[15]	2	S	E	G		✓
Ostrovskii	[16]	2	TS	TEP	G		
Moufki *et al.*	[17]	3	TS	TEP	C		✓
Molinari and Moufki	[18]	3	TS	TEP	C	✓	✓
Strenkowski *et al.*	[19]	3	S	EP	C	✓	✓
Usui *et al.*	[20]	3	S	EP	C		✓
Bao and Tansel	[21]	2	S	E	MC		✓
Kang *et al.*	[22]	2	S	E	MC	✓	✓
Zaman *et al.*	[23]	3	S	E	MC		✓
Son *et al.*	[24]	2	S	EP	MC	✓	✓
Newby *et al.*	[25]	3	S	E	MC		✓

The metal cutting models summarized in Table 3.1 will be discussed in the subsequent paragraphs.

The forces involved in chip formation as developed by Merchant [14] are depicted in Figure 3.3. The forces caused by the interaction of the tool with the chip are the friction force F_F and the normal to the friction force F_{NF}. The forces that the workpiece imparts to the chip are the shear force F_S and the normal to the shear force F_{NS}. The aforementioned forces are not measureable because their directions vary with tool geometry and cutting conditions. The cutting force F_C and the thrust force F_T are measureable quantities and can be used to determine the other forces through trigonometric relationships, as shown in Figure 3.4 and Equations (3.1) - (3.4).

$$F_F = F_C \sin \alpha_R + F_T \cos \alpha_R \tag{3.1}$$

$$F_{NF} = F_C \cos \alpha_R - F_T \sin \alpha_R \tag{3.2}$$

$$F_S = F_C \cos \varphi - F_T \sin \varphi \tag{3.3}$$

$$F_{NS} = F_C \sin \varphi + F_T \cos \varphi \tag{3.4}$$

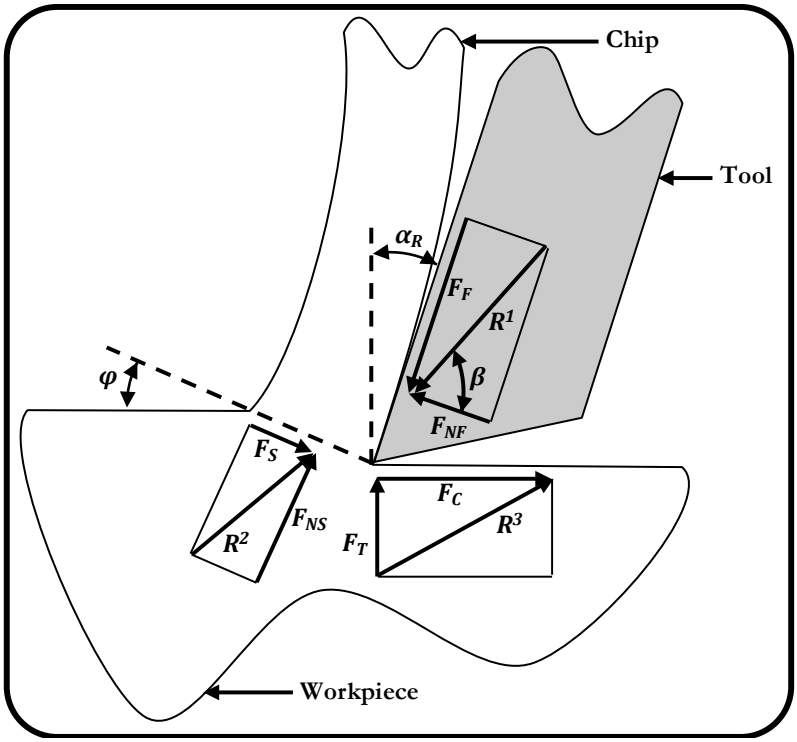

Figure 3.3 - Chip formation forces.

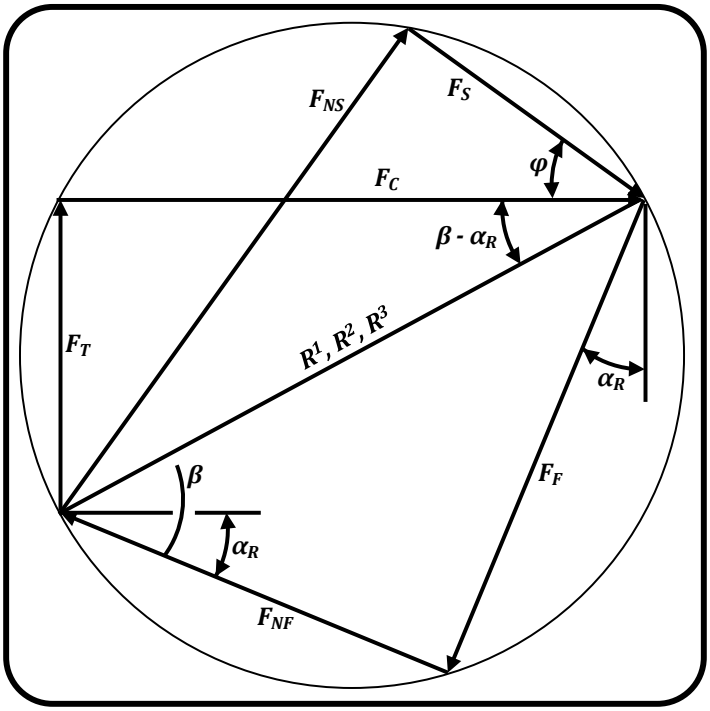

Figure 3.4 - Trigonometric representation of chip formation forces.

Merchant [14] was able to calculate the shear stress on the shear plane by assuming that the shear strength was constant along the plane according to:

$$\tau = \frac{F_C \cos\varphi - F_T \sin\varphi}{(t_o w / \sin\varphi)} \tag{3.5}$$

where w is the thickness of the cut. Merchant surmised that the shear angle φ is created such that the shear stress imposed to the workpiece is equal to the shear strength of the material. All other possible shear angles would not create sufficient stress in the workpiece to cause shearing, and subsequently, chip formation. Effectively, the workpiece chooses a shear plane angle that minimizes energy. This angle can be found by taking the derivative of the shear stress τ with respect to the shear plane angle φ and setting the derivative to zero. The well known "Merchant Equation" is then obtained by solving for φ:

$$\varphi = 45 + \frac{\alpha_R}{2} - \frac{\beta}{2} \tag{3.6}$$

where β is the friction angle. The major assumption of this model is that the shear strength of the material is constant and unaffected by strain rate and temperature, which is violated during real machining operations. Nevertheless, this model has been well accepted by the community as a basic calculation tool relating the rake angle, friction angle, and shear plane angle and can be used to determine a general understanding of metal cutting [12].

A consequence of the negative rake angle that is typical of abrasive grains is the decrease in the shear plane angle resulting in larger shear plane areas. This increase in shear plane area requires higher forces to initiate material shearing; thus increasing the energy requirements of the process, as shown by Malkin [15]. In his work, Malkin performed cutting experiments using tools with large negative rake angles to simulate the effects of chip formation in grinding and found that the shear energy required for chip formation was very close to the melting energy of the workpiece material, which is the energy limit for adiabatic deformation.

The work of Ostrovskii [16] is interesting as it is one of the first models that differentiated the mechanism of chip formation between cutting and grinding. In the presented model, the formation of a chip was considered both in relation to the motion of the abrasive grain as well as the deformation of the workpiece material ahead of the abrasive grain. The model

was solved using slip line fields, was based on plasticity theory, and took into account the friction, shear, and rake angles, the yield point of the material, the coefficient of friction on the rake face, the abrasive grain diameter, and the built-up height of the chip.

Moufki *et al.* [17] created a three-dimensional thermo-structural model of oblique metal cutting. The model was very robust in that it included a temperature dependent friction relation at the tool-chip interface, a thermo-elastoplastic material model, and was capable of predicting the chip flow angle as a function of cutting speed, undeformed chip thickness, rake angle, and the inclination angle of the cutting tool. Unfortunately, this model required substantial tuning from orthogonal cutting experiments. Molinari and Moufki [18] later refined the previous work and adapted the model for turning. The updated model included the effects of the nose radius of the tool by decomposing the cutting edges into interacting segments and summing their effects. The advantages of this model were that local temperatures along the cutting edge were obtained in addition to the global forces and chip flow direction. In the second part of the paper [26] the model was used to perform parametric studies to prove the usefulness of the model to tool designers.

Although all of these models are useful for predicting chip flow angles and the resultant tool forces, their major drawback is that they all require experimental orthogonal cutting data to be implemented. Strenkowski *et al.* [19] overcame this limitation by utilizing the results from a finite element simulation as inputs to the analytical model created by Usui *et al.* [20]. Usui's three-dimensional model used the energy approach to approximate cutting as a series of orthogonal slices and required cutting tests to determine the shear stress, shear angle, and friction angle, as shown in the second part of their work [27]. Strenkowski's finite element model was used to predict these values, thus freeing the tool designer from performing experimental tests.

The micro cutting models that follow are included as they simulate a process that is similar to grinding; namely, small depths of cut, negative rake angles caused by the tool nose radius, and a trochoidal tool path caused by the combined rotation and translation of the tool.

Bao and Tansel [21] created an experimentally-verified model for micro end milling to quickly predict the maximum cutting force, the variation of the cutting force in one tool revolution, and the surface quality. Their model calculated the chip thickness based on the trochoidal movement of the tool, while previous models only considered the tool rotation. For conventional end milling the forward movement is not as critical to the calculations due to the small feed per tooth to tool nose-radius ratio; whereas in micro end milling there is a large feed per tooth to tool nose-radius ratio.

Kang *et al.* [22] created an experimentally-verified model for micro end milling to determine cutting forces. Unlike Bao and Tansel's model [21], the Kang *et al.* model assumed that the chip thickness was only a function of the tool rotation; however, the nose radius of the tool was considered. The effect of the nose radius on cutting becomes significant at depths approaching and less than the nose radius due to the artificially high negative rake angle that is created.

Zaman *et al.* [23] created a slightly different variation of the micro end milling model by calculating the theoretical chip area of the engaged tool as opposed to the undeformed chip thickness. Since tool engagement tends to be greater in micro end milling the effect of the helix angle of the tool cannot be neglected. Zaman *et al.* use this fact to calculate an axial force acting on the tool to produce a three-dimensional model.

Son *et al.* [24] created an experimentally-verified model based on the tool-workpiece friction coefficient and the tool nose radius to study the minimum achievable depth of cut that would produce a continuous chip. Based on their results they concluded that smaller nose radii and higher coefficients of friction result in smaller achievable depths of cut. This work is interesting as a simple equation was developed to predict the minimum achievable continuous chip, which may be transferable to grinding.

An empirical model was created by Newby *et al.* [25] to aid in the determination of cutting force constants for micro end milling force prediction models. The empirical model was based on theories similar to Bao and Tansel [21] in that the chip thickness was calculated based on the trochoidal movement of the tool.

3.3 Finite Element Models

Finite element modeling involves discretization of a continuum into finite sections over which the conservation and constitutive equations are solved. The chosen frame of reference, either material or spatial, leads to different approaches to solve for the deformations of the continuum. When dealing with finite element analysis the material frame of reference is known as the Lagrangian formulation and the spatial frame of reference is known as the Eulerian formulation. Finite element modeling of chip formation has progressed steadily over the past 40 years as the necessary computational power has become increasingly affordable and the simulation codes have become more robust. Finite element modeling possesses several advantages as compared to its analytical counterparts, such as: multi-dimensional contour plots of results, contact analysis, and less experimental data is required as a model input. The following sections review the various works based on the implemented finite element formulations, which are: Lagrangian, Eulerian, Arbitrary Lagrangian-Eulerian, and Smooth Particle Hydrodynamics.

Table 3.2 summarizes some of the available finite element models for chip formation. This list is by no means exhaustive; rather, it is a sampling of the available models for grinding, conventional cutting, and micro cutting. For a thorough bibliography the reader is referred to the work of Mackerle [28,29]. The table identifies the dimensionality of the model as either 2 or 3. The formulation of the model is designated as either Lagrangian [L], Eulerian [U], Arbitrary Lagrangian-Eulerian [ALE], or Smooth Particle Hydrodynamics [SPH]. The model type is differentiated as either purely structural [S] or thermo-structural [TS] in which tool-workpiece heat transfer is considered. The material is designated as either elastic [E], elastoplastic [EP], or thermo-elastoplastic. It should be noted that the material was assumed elastic if a discussion on the implemented material model was lacking. The process that the model simulates is designated as either cutting [C], micro cutting [MC], or grinding [G]. Finally, experimental validation is indicated with a check mark [✓].

Table 3.2 - Finite element model overview.

Model	Reference	Dimensionality	Formulation	Type	Material	Process	Experimental Validation
Vaz Jr *et al.*	[30]	3	L	TS	TEP	C	✓
Kalhori	[31]	2	L	TS	TEP	C	
Borouchaki *et al.*	[32]	2	L	S	EP	C	
Marusich and Ortiz	[33]	2	L	TS	TEP	C	
Klocke *et al.*	[34]	2	L	TS	TEP	C	✓
Mamalis *et al.*	[35]	2	L	TS	TEP	C	✓
Grzesik *et al.*	[36]	2	L	TS	TEP	C	✓
Shet and Deng	[37]	2	L	TS	TEP	C	
Shi *et al.*	[38]	2	L	TS	TEP	C	✓
Liu and Guo	[39]	2	L	TS	TEP	C	
Baker *et al.*	[40]	2	L	TS	TEP	C	✓
Guo and Yen	[41]	2	L	S	TEP	C	
Lai *et al.*	[42]	2	L	S	TEP	MC	✓
Subbiah and Melkote	[43]	2	L	S	TEP	MC	✓
Liu and Melkote	[44]	2	L	S	TEP	MC	✓
Ohbuchi and Obikawa	[45]	2	L	TS	TEP	G	✓
Doman *et al.*	[46]	3	L	S	EP	G	✓
Benson and Okazawa	[47]	2	U	S	TEP	C	✓
Raczy *et al.*	[48]	2	U	S	TEP	C	✓
Joyot *et al.*	[49]	2	ALE	S	TEP	C	✓
Miguelez *et al.*	[50]	2	ALE	S	TEP	C	
Ozel and Zeren	[51]	2	ALE	TS	TEP	C	
Barge *et al.*	[52]	2	ALE	S	TEP	C	
Movahhedy *et al.*	[53]	2	ALE	TS	TEP	C	✓
Pantale *et al.*	[54]	3	ALE	TS	TEP	C	✓
Olovsson *et al.*	[55]	2	ALE	S	EP	C	
Limido *et al.*	[56]	2	SPH	S	TEP	C	✓
Espinosa *et al.*	[57]	3	SPH	S	TEP	C	✓
Akarca *et al.*	[58]	2	SPH	S	TEP	C	✓

3.3.1 Lagrangian

The Lagrangian finite element formulation has been popular in the solid mechanics community and is characterized by the fact that the numerical grid, or mesh, is tied to the material; therefore, the material and mesh move together, as seen in Figure 3.5. This implementation is popular in solid mechanics because: it can accurately and efficiently track material interfaces, it can incorporate complex constitutive material models, it can handle

unconstrained flow over free boundaries, and it is a mature technology. There are several difficulties with the Lagrangian formulation, including: the contact definition, excessive mesh deformation, and the fracture criteria.

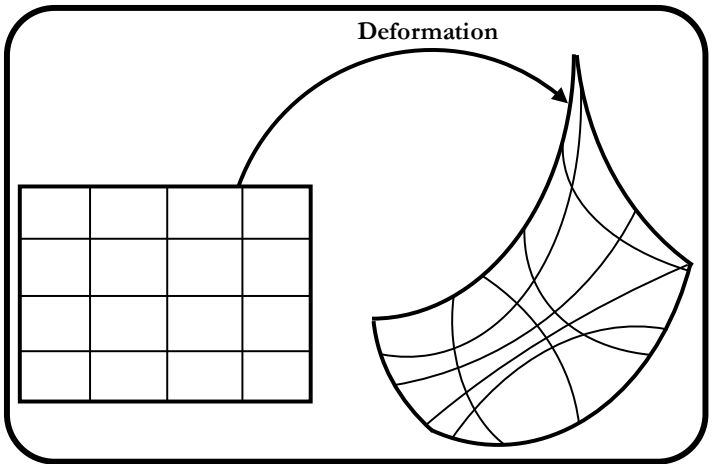

Figure 3.5 - Lagrangian deformation.

The general solution procedure for the Lagrangian formulation requires several steps and is summarized as follows [59]:

1. The nodal forces are calculated based on the stress, pressure, and other forces at time t^n for each element.
2. The nodal accelerations are obtained by dividing the nodal forces by the nodal masses.
3. The nodal acceleration is integrated to give the nodal velocity at time $t^{n+1/2}$.
4. The nodal velocity is integrated to give the nodal displacement at time t^{n+1}.
5. The constitutive material model is integrated from time t^n to t^{n+1} based on the nodal displacements.
6. The internal energy is updated based on the work done from time $t^n$to t^{n+1}.
7. The pressure from the equation of state is calculated from the density and energy at time t^{n+1}.
8. A new time step is calculated based on the speed of sound through each element.
9. Advance the time and return to step 1.

In order for Lagrangian bodies to interact a contact definition is required because two Lagrangian bodies will pass through each other without one. The contact definition is important because it controls the forces of the two interacting bodies. If it is defined improperly there may be excessive leakage across the contact boundary or excessive system stiffness resulting in model instabilities.

Excessive mesh deformations occur when there are large workpiece deformations, such as during a forging process, as shown in Figure 3.6. These mesh deformations may lead to mesh tangling or negative volumes as well as poor element properties, as shown in Figure 3.7. Mesh smoothing or adaptive remeshing schemes are frequently used to alleviate severe mesh distortions; however, these processes tend to be computationally expensive and difficult to implement in three-dimensions. The three main types of remeshing schemes are h-adaptivity, p-adaptivity, and r-adaptivity [30]. In h-adaptivity, the size of the elements is changed, which results in a different number of elements and new node connectivity, as shown in Figure 3.6. In p-adaptivity, the degree of the interpolating shape function of the elements is increased to improve the solution accuracy. In r-adaptivity, the nodes of the elements are relocated, which in effect is a smoothing routine [31], as shown in Figure 3.7. The areas of highest mesh distortion tend to be immediately ahead of the cutting tool where the material is separating to form a chip. Borouchaki *et al.* [32] produced a thorough mathematical derivation of h-adaptivity and applied it to several elastoplastic problems; one of which was orthogonal cutting. The initially very course model successfully adapted to the cutting and created a discontinuous chip. Kalhori [31] created a continuously remeshed cutting model to study continuous and saw-toothed chip formation as well as the residual stresses imparted to a workpiece by the cutting action. Vaz Jr. *et al.* [30] expanded the work of Kalhori to create a three-dimensional model. Their numerical results were verified using extensive experimental observations, including: tool forces, chip morphology obtained from a quick-stop device, subsurface hardness measurements to estimate the depth of the machine-affected zone, and X-ray diffraction measurements to determine residual stresses. The verified model was then utilized to study tool design in two dimensions as well as chip formation in three dimensions. Marusich and Ortiz [33] created a two-dimensional thermo-structural model with continuous remeshing to simulate the various chip morphologies at varying cutting speeds. At a high speed of 30 m/s continuous chips were formed, at a low

speed of 10 m/s saw-toothed chips were formed, and at a moderate speed of 20 m/s discontinuous chips were formed, all of which were in agreement with experimental observations. Klocke *et al.* [34] used continuous remeshing to create a two-dimensional model of high-speed cutting that compared well with experimental observations. Mamalis *et al.* [35] created a two-dimensional continuously remeshed model to study the effects of the tool nose radius and cutting speed on the cutting forces, temperatures, and stresses. Grzesik *et al.* [36] also successfully used adaptive remeshing to study the thermal characteristics of the cutting process and the heat transfer between coated tools and the workpiece in two dimensions.

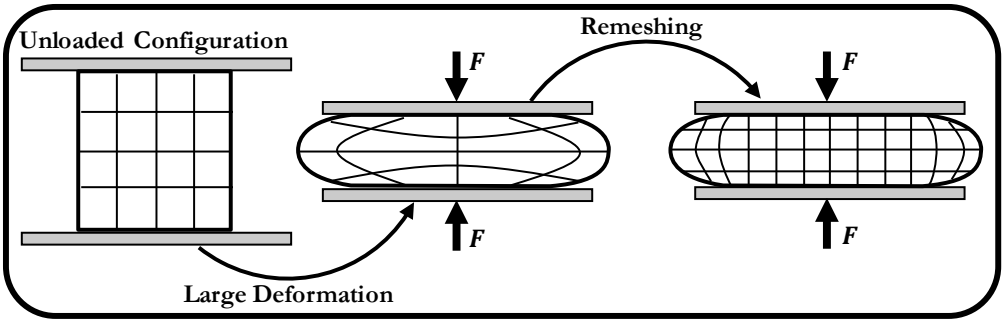

Figure 3.6 - Lagrangian h-adaptivity.

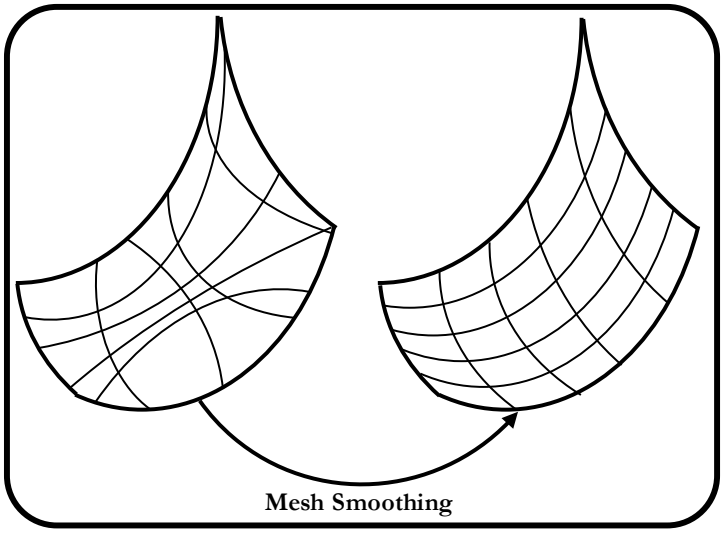

Figure 3.7 - Lagrangian r-adaptivity.

One method that has been utilized to bypass the need for remeshing is to artificially skew the elements in the material to be removed. This skewing is designed so that as the material

deforms into a chip the skew is removed and the elements become more regular in shape, as shown in Figure 3.8. Shet and Deng [37] used this procedure to perform a general analysis of the cutting operation in two dimensions with respect to forces, stresses, strains, strain rates, and temperatures. Shi *et al.* [38] used the model of Shet and Deng [37] to study the effect of friction on cutting and found that higher coefficients of friction produced less rounded chips, a decrease in the shear angle, and increases in the contact length, the cutting force, and the maximum temperature.

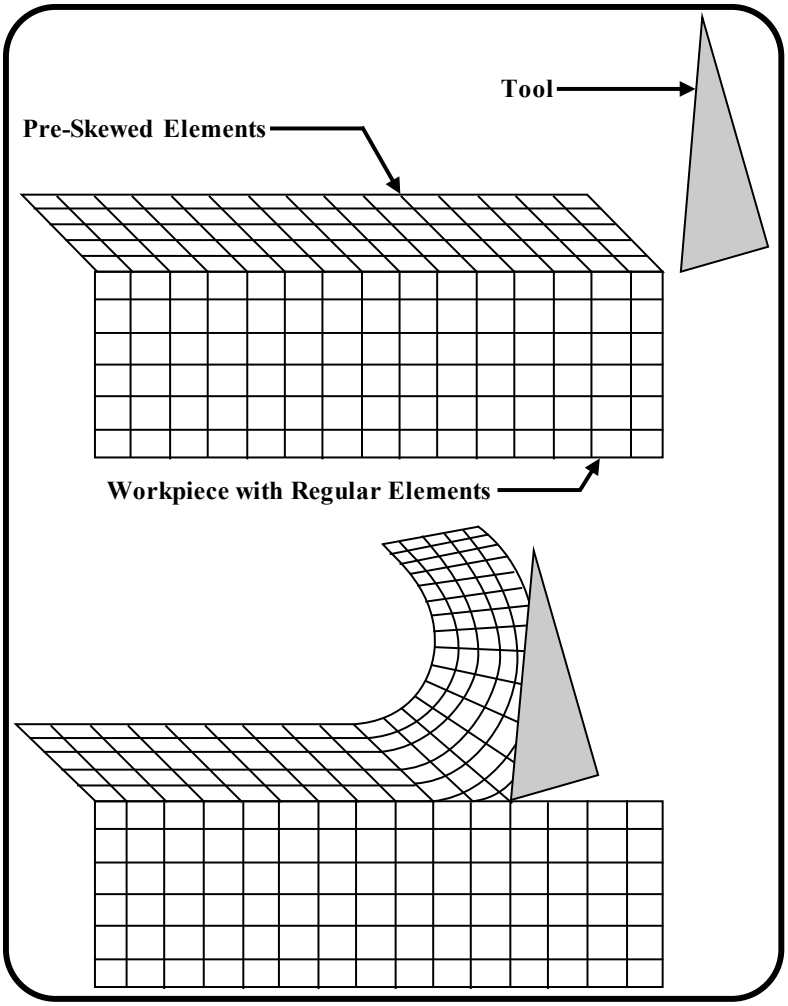

Figure 3.8 - Pre-skewed Lagrangian elements.

In order to properly simulate a metal cutting operation fracture criteria need to be specified to allow the tool to split the workpiece. There are two common forms of fracture criteria; pre-defined parting lines [35,36,40], also known as geometrical criteria, and element failure

[33,41], also known as physical criteria. The pre-defined parting line, shown in Figure 3.9, consists of a line of two sets of nodes at a location in the workpiece that is equivalent to the depth of cut. As the tool moves through the workpiece along the parting line the two sets of nodes are allowed to separate; one set staying in the workpiece, the other set traveling with the chip as it forms. This process can be viewed as the tool unzipping a zipper. Although this method is efficient it does not create an accurate portrayal of the finished surface and it does not allow for the formation of discontinuous chips. Additionally, unrealistically wavy finished surfaces may occur if the nodes of the parting line undergo substantial displacements ahead of the tool. The work by Baker *et al.* [40] utilized the parting line method in a unique manner to study the two-dimensional formation of saw-toothed chips. Rather than defining a complicated thermo-elastoplastic material damage model to initiate cracking along the shear band an additional parting line was introduced to open a crack along the shear band after a chip had partially formed. The major drawback to this work was that the artificial cracking method could not answer whether cracking was responsible for saw-toothed chip formation; however, it was useful to study plastic deformation in the vicinity of a formed crack. Liu and Guo [39] uniquely utilized the parting line method to study the effects of sequential cuts in two dimensions. Essentially, two parting lines were defined in the workpiece at two depths of cut and the mechanical state after the first cut was used as the initial condition for the second cut. Their work found that tensile residual stresses after the first cut may be changed to more favorable compressive residual stresses by optimizing the second cut. They also found that sequential cuts have little effect on the cutting forces, chip geometry, and temperatures.

The element failure criteria consists of systematically deleting elements that either exceed a user defined value, which can be based on elemental stresses or strains, or exceed a damage tolerance value defined by a material damage model. This type of fracture tends to yield more realistic finished surface profiles; however, the computational costs are high and prone to numerical instabilities. The added benefit of this type of failure criteria is that it is possible to simulate discontinuous chips, as shown by Guo and Yen [41].

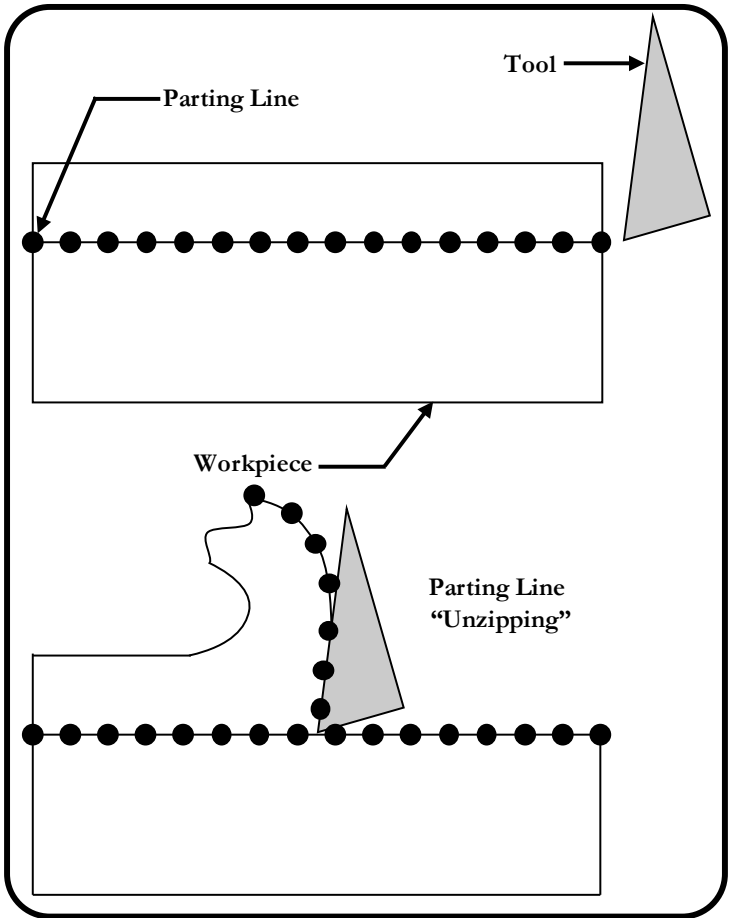

Figure 3.9 - Pre-defined parting line.

Conventional cutting transitions to micro cutting as the depth of cut decreases. At sufficiently small depths of cut, usually in the range of $t_0 \approx NR$ [42,60], where NR is the nose radius of the cutting tool, plowing becomes dominant and cutting ceases due to the ratio of the tool nose radius NR to the depth of cut, as shown in Figure 3.10. Lai *et al.* [42] created a two-dimensional micro cutting model that demonstrated the plowing effect at small depths of cut. An interesting contribution from their work was the modification of the Johnson-Cook plasticity model to include a scale variable to properly model the size effect. Conventional finite element analysis is non-dimensional; therefore, the flow stress is independent of the scale of the problem. To correct for this Lai *et al.* [42] introduced a variable to establish a relationship between the scale and the flow stress. Their results showed a measurable improvement in the workpiece stresses at the micro-scale without affecting the results at the macro-scale. Li *et al.* [61] later used the model to create an

accurate analytical surface roughness model that compared well to experimental measurements.

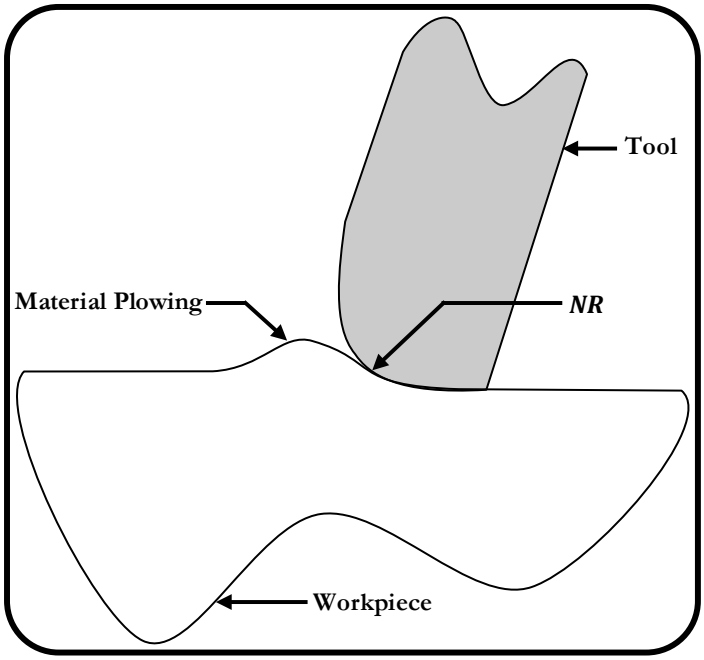

Figure 3.10 - Material plowing due to tool nose radius.

Subbiah and Melkote [43] used evidence of ductile tearing at the chip root as the reasoning to implement a parting line separation criteria in their experimentally-validated two-dimensional micro cutting model. The model was then used to study the energy consumed during chip formation. The results showed an increase in the specific energy associated with the material separation as the depth of cut was decreased; thus showing evidence of the size effect.

Liu and Melkote [44] created an adaptively remeshed two-dimensional model to study how material strengthening mechanisms contribute to the size effect in micro cutting. Their results showed that strain gradient strengthening has a significant contribution to the size effect at low cutting speeds and small depths of cut, while temperature has a significant contribution at high cutting speeds and large depths of cut. A later study by Liu and Melkote [60] used the same model to investigate the effect the tool nose radius has on the size effect. They concluded that the tool nose radius partially contributes to the size effect

by altering the material flow pattern, which increased the plastic shear zone, and by increasing the tool-chip contact length at small depths of cut.

The aforementioned models have only dealt with conventional and micro cutting with little emphasis on grinding. It can be argued that micro cutting is applicable to grinding due to the small depths of cut and comparatively large nose radii, which effectively create a negative rake angle similar to that of an abrasive grain.

The work of Ohbuchi and Obikawa [45] is also based on the ideas of orthogonal metal cutting; however, by specifying a tool with a large negative rake angle they created a two-dimensional model that attempted to more closely resemble grinding. By implementing the skewed element approach and a thermo-elastoplastic material model they were able to successfully simulate continuous and saw-toothed chip formations, where the simulated chip thicknesses showed good agreement with that found from experimental observations. A later study [62] used the model to investigate the effects that depth of cut and rake angle have on the grinding process. An extension of this work [63] was used to create a surface generation model that considered the upheaval and material removal caused by various grain shapes, cutting speeds, and elastic deformation.

Doman *et al.* [46] created a unique three-dimensional model of grinding where the abrasive grain was approximated by a sphere. The experimentally-validated model utilized an element erosion technique to successfully isolate the transition from rubbing to plowing. The validated model was used to investigate the effect that grain size and depth of cut had on material deformation. The results indicated that larger grains reduced the energy consumed by friction and increased the workpiece deformation energy. It was also found that an energy peak occurred at the onset of plowing as the depth of cut was increased due to the drop in workpiece deformation energy associated with plowing.

As the preceding discussion has shown there is an extensive collection of works utilizing the Lagrangian formulation to simulate metal cutting in two dimensions. There are comparatively few works dedicated to grinding, which necessitates a three-dimensional

model due to the complex geometry of abrasive grains. Therefore, a state-of-the-art model for grinding must be created in three dimensions and must also be experimentally-validated.

3.3.2 Eulerian

The Eulerian finite element formulation has been popular in the fluid mechanics community and is characterized by the fact that the mesh is fixed in space with the material flowing through it and that new free material surfaces are naturally created without the need for element separation or erosion criteria. This implementation is popular in fluid mechanics as the mesh forms the control volume of the simulation. The prerequisite of knowing the final shape of the material makes the Eulerian formulation well suited to forging operations and poorly suited to ballistic impacts where it may be difficult to predict the path of the debris. The spatially fixed mesh allows large material deformations to occur without the need for smoothing or adaptive remeshing strategies. New free surfaces can be generated due to the ability of the Eulerian formulation to have more than one material present per element; however, a void volume is required to capture the expanding free surfaces. Other difficulties associated with the Eulerian formulation include the fluid-structure coupling definition and the difficulty to include a damage or fracture criteria to simulate discontinuous chips. Additionally, this formulation tends to perform optimally if a regular, orthogonal mesh is implemented as it allows the advection algorithms to operate along straight lines, thus making it difficult to perform local mesh refinements. Advection algorithms perform the necessary calculations to transport the solution variables as the material deforms through the mesh.

The solution for the Eulerian formulation is generally more complicated than the Lagrangian formulation and is typically treated in two steps; a Lagrangian step and an advection step. This procedure is typically known as the operator split method and is shown schematically in Figure 3.11. The general solution of the Eulerian formulation is summarized as follows [59]:

1. Perform a Lagrangian step as outlined in Section 3.3.1.
2. Remap the solution from the Lagrangian step back onto the Eulerian mesh using advection algorithms.

a. Remap the element-centered solution variables, for example: pressure, density, and internal energy.
b. Remap the node-centered solution variables, for example: momentum.

3. Advance the time step and return to step 1.

The additional computational costs of a Eulerian solution results from the need to track the volume, stress tensor, and the history of each material present in each element and because the Lagrangian source terms must also be accounted for. Additional costs are also incurred due to the need for a sufficiently large void volume to capture any new free surfaces of interest; otherwise, material expanding outside the computational mesh will be lost.

The fluid-structure coupling definition utilized in a Eulerian formulation is conceptually very similar to that of a Lagrangian contact definition; however, in a Eulerian simulation the coupling definition is preventing the Eulerian fluid from penetrating the Lagrangian body.

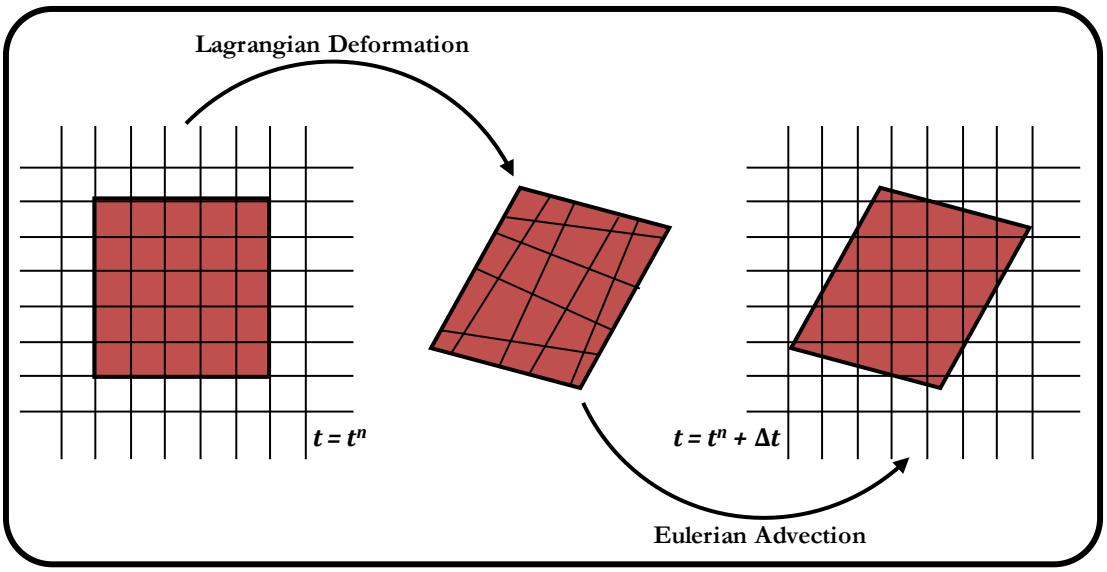

Figure 3.11 - Eulerian deformation.

It becomes difficult to define material fracture criteria for a Eulerian simulation as the mesh is stationary and, therefore, nodes and elements cannot be deleted to produce a crack or to create a segmented chip as in the Lagrangian formulation. Cracks can only be created by the

natural flow of the material around an obstruction. Consequently, the Eulerian formulation is more well suited to studying continuous chip formation.

There seem to be relatively few works published that utilize the Eulerian formulation to simulate metal cutting; however, there are many uses to simulate blast loading [64], ballistic impacts [65], and bird strikes [66], for instance.

Raczy *et al.* [48] created an experimentally-verified two-dimensional cutting model using the Eulerian formulation. The model was mainly a proof of concept; however, it was used to test two different material models, namely an elastic plastic hydrodynamic model and the Johnson-Cook plasticity model. Their results indicated that the hydrodynamic material model was more accurate at predicting the stress distribution and cutting force while the Johnson-Cook material model was more accurate at predicting the strain distribution.

Benson and Okazawa [47] performed tests comparing the Eulerian formulation to experimental turning results and found that the chip formation and shape were agreeable. This work also showed that it is possible to implement a damage or fracture model using the Eulerian formulation to simulate discontinuous chips; however, doing so required the creation of a custom research code.

3.3.3 Arbitrary Lagrangian-Eulerian

As has been shown, the Lagrangian and Eulerian formulations both have advantages and disadvantages as it pertains to the simulation of metal cutting. However, it can be argued that the strong points of one formulation are the weak points of the other [53]. The Arbitrary Lagrangian-Eulerian [ALE] formulation capitalizes on the strengths of both formulations. The ALE formulation is unique in that its mesh is neither tied directly to the workpiece, as in the Lagrangian formulation, nor is it fixed in space, as in the Eulerian formulation. Rather, the mesh can move independently of the material along an arbitrary path, as well as rotate, expand, and contract as needed by the simulation. The full mathematical derivations used to solve the ALE formulation are complex and will not be reproduced here for brevity; however, the reader is directed to [67,68,69,70] for thorough derivations. A general outline of the ALE equations will be given in Section 3.4.3.

The two solution methods available for the ALE formulation are the decoupled and the coupled solution. In the decoupled solution the Lagrangian and Eulerian solutions are obtained sequentially and proceed as follows [54,71]:

1. Perform Lagrangian step as outlined in Section 3.3.1.
2. A new mesh is created based on the desired mesh motion and smoothing to reduce distorted elements.
3. Remap the solution from the Lagrangian step back onto the newly created mesh using Eulerian advection algorithms.
    a. Remap the element-centered solution variables.
    b. Remap the node-centered solution variables.
4. Advance the time step and return to step 1.

Step 2 is synonymous with an r-adaptivity remeshing scheme, which does not need to be performed with every Lagrangian step; instead, it is typically performed every 5 – 10 steps, depending on the model to be solved. By limiting the number of smoothing steps it is possible to realize considerable savings in computational time [55].

In the coupled solution both the Lagrangian and Eulerian solutions are obtained simultaneously. Although this method can be more accurate than the decoupled solution as there is no need for an advection step, the computational costs are typically higher.

It would seem that the ALE formulation is gaining favor amongst researchers; however, many of the works in the literature tend to be related to initial model development with investigations to follow at a later time. Olovsson [55] created an early two-dimensional model to study and develop appropriate algorithms for metal cutting using the ALE method. Miguelez *et al.* [50] created a simple two-dimensional model to study the effect of the rake angle on the shear plane angle and cutting forces. Their results showed the well-known effect that a more negative rake angle results in higher cutting forces and smaller shear plane angles. This work also compared the cutting force as a function of cutting speed results of the finite element model to an analytical model and found that the finite element model had the same trends as the analytical model. Ozel and Zeren [51] created a finite element model

to study the subsurface stresses that result from high-speed machining. Their results indicated that there was a general pattern of tensile stresses near the machined surface and compressive stresses below the surface followed by a gradual taper to un-stressed material. Joyot *et al.* [49] used their two-dimensional model to determine temperatures, chip geometry, and cutting forces. They found that the highest temperatures occurred in the secondary shear zone and that the highest temperature gradient occurred near the tool tip. Their experimental validation showed acceptable agreement in the cutting forces and the chip thicknesses.

Barge *et al.* [52] created a two-dimensional model to investigate the effects that mesh density and hourglass control had on solution results. Their results indicated that the mesh density and hourglass control had a larger effect on the chip morphology than on the force result.

Movahhedy *et al.* [72] created a thermo-structural ALE model that was later used to study the effect of tool geometry on the continuous chip formation process [73]. Their results showed that different chamfer angles did not significantly affect the chip removal process due to a material dead zone that formed under the chamfer, which acted as the primary cutting edge at low to medium cutting speeds; however, cutting forces increased with the size of the chamfer.

Pantalé *et al.* [54] created a three-dimensional model of metal cutting and compared the predicted temperature profiles on the tool to the wear marks of the tool used for the experimental validation. It was found that there was correlation between the simulated temperatures and the wear patterns. This work was later extended to include material damage effects to allow the study of unsteady-state metal cutting, specifically milling, with results that compared well to experimental data.

3.3.4 Smooth Particle Hydrodynamics

Smooth Particle Hydrodynamics [SPH] is a Lagrangian technique that was initially developed in the 1970's as a means to simulate astrophysical phenomena [74]. SPH is an interesting numerical approach as compared to the previously mentioned formulations because it is a meshless method, which means that is it does not require a computational grid to perform

simulations. Rather, SPH operates by representing the material as a group of Lagrangian particles. These particles interact with one another based on a smoothing length and a statistical kernel function [56], as shown in Figure 3.12. Essentially, the smoothing length provides an individual particle's search radius to find neighbouring particles, while the kernel function is used to provide how strongly or weakly the particles interact. Without the need for a grid the user no longer needs to be wary of mesh tangling, mesh smoothing, adaptive remeshing, or fracture definitions. Despite its obvious advantages, SPH is still immature when compared to the more heavily-used Lagrangian and Eulerian grid-based methods and tends to be more computationally intensive as a large node density is required and statistical functions are required to define the interaction of the particles.

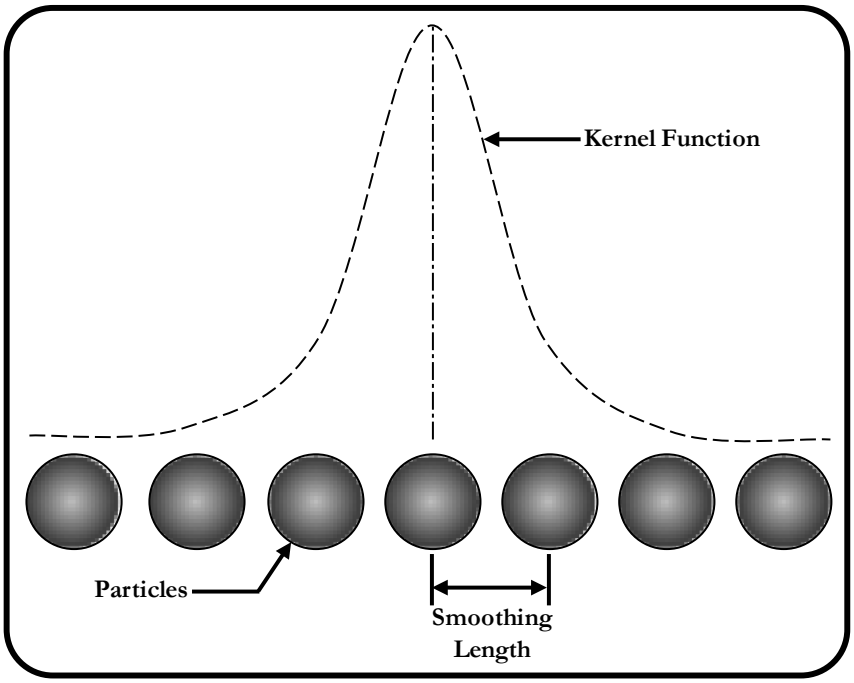

Figure 3.12 - SPH smoothing length and kernel function.

There has been relatively little work published that utilizes the SPH method to simulate metal cutting; however, it has been used to simulate other metal forming processes [75] as well as impact events [76].

Limido *et al.* [56] used SPH to simulate high-speed cutting and compared the results to both experimental and finite element results. The study showed that the SPH method compared

well to both the experimental and numerical data without the need to adjust parameters, such as: coefficients of friction or fracture criteria. Espinosa *et al.* [57] later expanded the work of Limido *et al.* [56] to create a three-dimensional model and successfully predicted milling forces. Akarca *et al.* [58] compared the results from a validated two-dimensional Eulerian cutting model to those of an SPH cutting model; however, their SPH node density was kept the same as their Eulerian node density, which tends to contradict the works of Huertas-Ortecho [66] and Schwer [77,78] whom indicate that a higher SPH node density is required for accurate result.

3.3.5 Hybrid Euler-Lagrange

Evidently, choosing a suitable finite element formulation to simulate metal cutting in three dimensions can be difficult as each posses its own pros and cons, as summarized in Table 3.3.

Table 3.3 - Finite element formulation comparison for three-dimensional metal cutting.

Parameter	Lagrangian	Eulerian	ALE	SPH
Mesh Deformation	Very High	None	High	None
Discontinuous Chips	Difficult	Very Difficult	Difficult	Not Difficult
Node Density	Low	High	Moderate	Very High
Computational Cost	Low	Moderate	Moderate to High	Very High

For the present work, a unique finite element implementation was chosen that combined the Eulerian and Lagrangian formulations. In the high deformation zone, where chip formation and large plastic strains occurred, the Eulerian formulation was implemented. This choice simplified the modeling in two ways. Firstly, a fracture definition was not required to initiate chip formation as the workpiece material will naturally flow around the cutting tool; however, the downside was that discontinuous chips could not be simulated. Secondly, adaptive remeshing was avoided, which is well established in two dimensions but very difficult to implement in three dimensions. In the regions where the deformations were small the Lagrangian formulation was implemented. This choice was beneficial as it reduced the computational time by reducing the node density and the number of elements that required a costly advection step as compared to a purely Eulerian approach. This hybrid formulation may seem to be the ALE formulation; however, there was no arbitrary mesh motion, nor was there any mesh smoothing. Therefore, this implementation can be

considered a hybrid Euler-Lagrange implementation; the benefits of which are large deformations without the need for adaptive remeshing and reduced computational time as only a small volume of material required an advection step to remap the solution variables. The nodes at the boundary of the Euler and Lagrange elements are treated as Lagrange. These boundary nodes move during the Lagrangian step of the Eulerian calculations but they do not return to their original location; therefore, they are not included in the advection calculations. Schwer [78] utilized a similar hybrid method to assess different, non-Lagrangian, formulations to simulate ballistic penetration into concrete, which was the only work known to the present author that utilized this hybrid method. Based on a literature review this hybrid method has not been used to simulate chip formation in grinding or conventional metal cutting.

3.4 LS-DYNA® Overview

The finite element code that was used for this work is the commercially available LS-DYNA® hydrocode created by Livermore Software Technology Corporation. This finite element code is a general purpose finite element code that is widely used for research and commercial work. The program contains a complete set of tools to simulate non-linear structural mechanics, heat transfer, and fluid-structure interaction problems using both implicit and explicit time step integration. LS-DYNA® natively supports Lagrangian, Eulerian, ALE, and SPH formulations and contains a variety of contact and coupling algorithms, adaptive remeshing algorithms, element failure definitions, and a vast material model library. LS-DYNA® version 971 release 4.2.1 was used for the entirety of this work. The models were solved using massively parallel processing [MPP] algorithms on dedicated computational clusters to reduce run times. Important control cards that were used for this work will be included for reference purposes and will be represented by: (*CONTROL_CARD_EXAMPLE). Detailed explanations of the control cards can be found in the latest user manual [79].

The following sections will discuss the LS-DYNA® time step integration scheme, material models, ALE equations, advection algorithms, mixture theories, and fluid-structure coupling as it pertains to this work.

3.4.1 Explicit Time Step Integration

There are two forms of time step integration available in LS-DYNA®; namely, implicit and explicit. Implicit time step integration is generally used for low velocity events happening over long time scales. This method is un-conditionally stable and involves fewer time steps of longer duration. The solution is obtained by using matrix algebra to invert the system of equations, which is inefficient as large numerical efforts are required to form, store, and invert the equations. Explicit time step integration is generally used for high velocity events occurring over short time scales. This method is conditionally stable and involves many time steps of short duration. The solution is obtained by solving the explicit algebraic equations for each node to determine the nodal displacements, which is numerically efficient.

Explicit time step integration (*CONTROL_TIMESTEP) was used for this work as the Eulerian formulation in LS-DYNA® does not currently support implicit time step integration. Given the choice, explicit time step integration would be chosen due to the high velocities and short time duration of the simulations. The new time step Δt^{n+1} is a function of the speed of sound C_{sp} in the material and the characteristic length l_{char} of the smallest element according to [79]:

$$\Delta t^{n+1} = TSSFAC \cdot \min\left(\frac{l_{char}}{C_{sp}}\right) \tag{3.7}$$

where $TSSFAC$ is a scale factor used to adjust the time step to improve the numerical stability, C_{sp} is found in three dimensions from:

$$C_{sp} = \sqrt{\frac{E_E(1-\nu)}{\rho(1+\nu)(1-2\nu)}} \tag{3.8}$$

and where E_E is the elastic modulus, ρ is the current density, and υ is Poisson's ratio. The time step must be less than the time required for a wave to propagate through the smallest dimension of an element, which is known as the Courant condition; therefore, $TSSFAC < 1$.

3.4.2 Material Models

Several constitutive material models were employed throughout this work. The diamond tool was modeled using both a perfectly rigid material (*MAT_RIGID) as well as a Hookean elastic material (*MAT_ELASTIC), with mechanical and thermal properties listed in Table 3.4. The results from each formulation were compared to assess the viability of assuming a rigid tool, as will be further discussed in Section 4.3.3.1.

Table 3.4 - Natural diamond mechanical and thermal properties [80].

Property	Value
ρ_0 (kg/mm^3)	3.51x10^{-6}
HK	8000
ν	0.1
E_E (GPa)	1200
α (μm/m°C @ 20°C)	1.18
C_p (J/kgK)	0.472
K (W/mK)	2000
T_{melt} (K)	4300

The AISI 4340 steel workpiece, whose chemical composition is shown in Table 3.5, was modeled using a combination of Hookean elastic and Johnson-Cook plasticity materials (*MAT_JOHNSON_COOK). The elastic material definition was utilized during the initial model development to reduce computational times and to allow model validation with known analytical models, as will be shown in Section 4.5. An elastic material definition was also utilized in the far-field workpiece material, where stresses were below the elastic limit, to reduce computational requirements. The Johnson-Cook plasticity model was utilized in all regions where plastic deformation occurred. This empirically-fitted viscoplasticity model is strain, strain rate, and temperature dependent and is widely used from quasi-static to ballistic regimes. This plasticity model was chosen as its effectiveness has been independently verified and the strength constants are readily available from multiple sources, such as: [47,81,82,83,84,85]. The general form of the Johnson-Cook model is [81,82]:

$$\bar{\sigma} = \left[A + B\bar{\varepsilon}_p^n\right]\left[1 + C\ln\frac{\dot{\bar{\varepsilon}}_p}{\dot{\varepsilon}_0}\right]\left[1 - \left(\frac{T - T_{amb}}{T_{melt} - T_{amb}}\right)^m\right] \tag{3.9}$$

where $\bar{\sigma}$ is the effective stress, $\bar{\varepsilon}_p$ is the effective plastic strain, $\dot{\bar{\varepsilon}}_p$ and $\dot{\varepsilon}_0$ are the effective plastic and reference strain rates, and T, T_{amb}, and T_{melt} are the current, ambient, and

melting temperatures. The effective stress is a quantity that determines whether further plastic deformation takes place by defining the size of the yield surface while the effective plastic strain is a monotonically increasing scalar value that grows whenever the material is yielding and is calculated according to:

$$\bar{\varepsilon}_p = \int_0^t \sqrt{\frac{2}{3}\left(\dot{\varepsilon}_p\right)_{ij}\left(\dot{\varepsilon}_p\right)_{ij}}\, dt \tag{3.10}$$

where $\left(\dot{\varepsilon}_p\right)_{ij}$ is the plastic component of the rate of deformation tensor. The change in temperature ΔT is associated with the plastic work induced in the material by:

$$\Delta T = \frac{1}{\rho C_p}\int \bar{\sigma} d\bar{\varepsilon}_p \tag{3.11}$$

where ρ is the density and C_p is the specific heat. Essentially, the first bracket of Equation (3.9) models the strain hardening of the yield stress, the second bracket models the effect of strain-rate hardening on the yield stress, and the third bracket models the effect of thermal softening on the yield stress. The strength constants, A, B, n, C, m, and $\dot{\varepsilon}_0$ are empirically-derived values and are shown in Table 3.6, while the mechanical and thermal properties are shown in Table 3.7. The strain n and strain rate C dependence is small when compared to the temperature dependence m; therefore, the values of n and C can be assumed to be constant for all workpiece tempers, as mentioned by Banerjee [86]. The reference strain rate $\dot{\varepsilon}_0$ is used in LS-DYNA® as the quasi-static cutoff and must be chosen according to the test conditions used to determine A and B. An incorrect value may produce incorrect flow stresses. Figure 3.13 compares the response of Equation (3.9), assuming a quasi-static strain rate of 1.0 s^{-1}, against the results from a unit cell tension test in LS-DYNA® for various constant strain rates. The figure shows good agreement in the stresses and also shows that the quasi-static cutoff is effectively limiting strain-rate effects to 1.0 s^{-1} or greater. One consequence of the quasi-static cutoff is that the yield strength of the material will be artificially high at low strain rates [87]. The Johnson-Cook material model implemented in the Eulerian formulation is a hydrodynamic model and, therefore, only computes the deviatoric stress. The full state of stress is the summation of the deviatoric and hydrostatic stresses; therefore, an equation of state is required to calculate the hydrostatic stress.

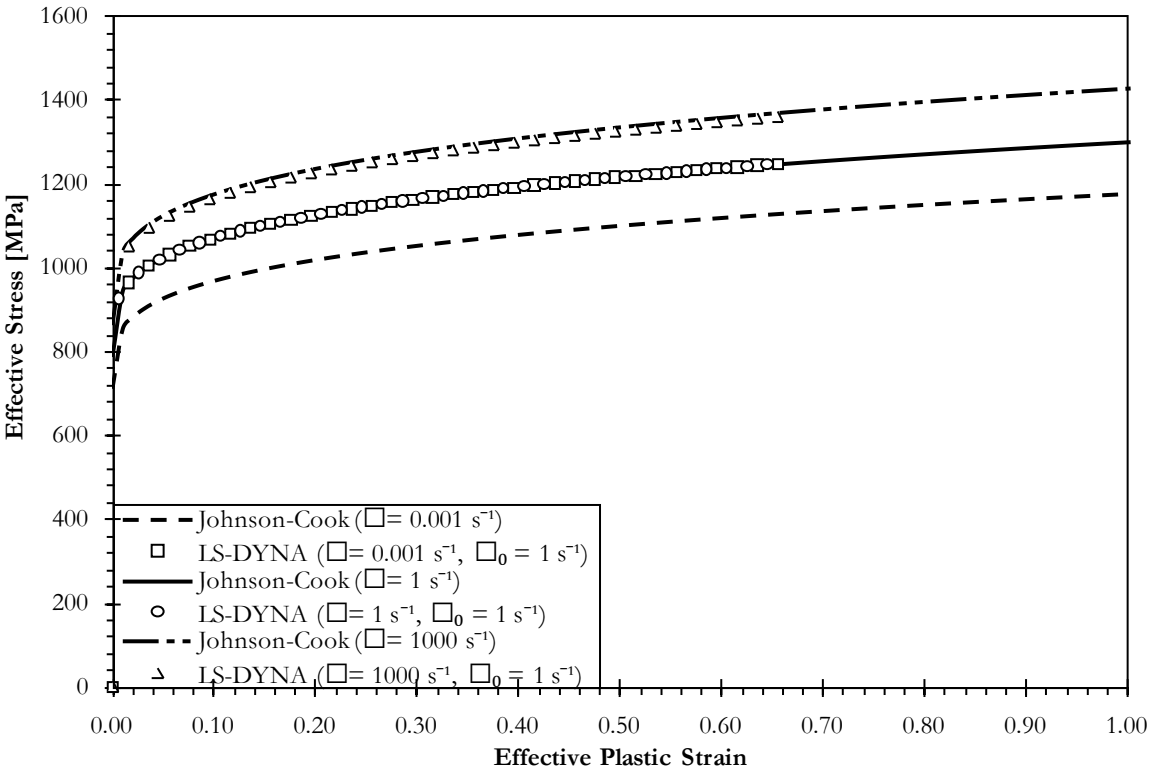

Figure 3.13 - Effective stress at constant strain rate for Johnson-Cook parameters and $\dot{\varepsilon}_0$ = 1.0 s^{-1}.

Table 3.5 - AISI 4340 chemical composition [80].

Element	C	Mn	P	S	Si	Cr	Ni	Mo	Al	Cu
Weight%	0.420	0.750	0.006	0.030	0.270	0.790	1.750	0.250	0.030	0.210

Table 3.6 - Johnson-Cook strength constants for AISI 4340 [83].

Property	Value
A (GPa)	0.792
B (GPa)	0.510
n	0.26
C	0.014
m	1.03
$\dot{\varepsilon}_0$ (s^{-1})	1.0
T_{amb} (K)	293

Table 3.7 - AISI 4340 mechanical and thermal properties [80].

Property	Value
ρ_0 (kg/mm^3)	7.85x10^{-6}
HRc	25
σ_U (GPa)	0.958
σ_Y (GPa)	0.883
ν	0.29
E_E (GPa)	205
G (GPa)	80
α (µm/m°C)	12.4
C_p (J/kgK)	477
K (W/mK)	44.5
T_{melt} (K)	1793

The Mie-Grüneisen equation of state (*EOS_GRUNEISEN) was used in conjunction with the Johnson-Cook material model. This equation of state defines the pressure-volume relationship for materials undergoing both compression and expansion. For materials subjected to compression the equation of state has the form [88]:

$$p = \frac{\rho_0 C_{sp}^2 \mu_D \left[1 + \left(1 - \frac{\Gamma_0}{2}\right)\mu_D - \frac{b}{2}{\mu_D}^2\right]}{\left[1 - (S_1 - 1)\mu_D - S_2 \frac{{\mu_D}^2}{\mu_D + 1} - S_3 \frac{{\mu_D}^3}{(\mu_D + 1)^2}\right]} + (\Gamma_0 + b\mu_D)E_{int} \tag{3.12}$$

and for expanded materials:

$$p = \rho_0 C_{sp}^2 \mu_D + (\Gamma_0 + b\mu_D)E_{int} \tag{3.13}$$

where p is the pressure, ρ_0 is the nominal density, E_{int} is the internal energy per initial volume, C_{sp} is the intercept of the $v_s - v_p$ curve and is more commonly known as the speed of sound in the material, S_1, S_2, and S_3 are the coefficients of the slope of the $v_s - v_p$ curve, Γ_0 is the Grüneisen gamma, and b is the first order correction to Γ_0, and the density ratio μ_D is defined as:

$$\mu_D = \frac{\rho}{\rho_0} - 1 \tag{3.14}$$

and where v_s is the shock wave velocity and v_p is the particle velocity. Table 3.8 lists the user defined constants (S_1, S_2, S_3, Γ_0, b).

Table 3.8 - Mie-Grüneisen constants for AISI 4340 [83].

Property	Value
C_{sp}(m/s)	5850
S_1	164
S_2	294
S_3	500
Γ_0	1.16
b	1.0

The Johnson-Cook material model can be very demanding to solve and may lead to convergence issues resulting in premature solution termination. This situation was encountered when the three-dimensional workpiece deformations became complex as will be shown in Chapter 7. The remedy was to chose a less complex material model at the expense of numerical accuracy as compared to the experimental data. The simplified plasticity model chosen obeyed the well-known isotropic hardening rule (*MAT_PLASTIC_KINEMATIC) and accounted for both strain and strain-rate hardening. Thermal softening was neglected with this material model. The general form of the model is:

$$\sigma_Y = \sigma_0 + E_P \bar{\varepsilon}_p \tag{3.15}$$

where σ_Y is the current yield strength of the material, σ_0 is the initial yield strength of the material, $\bar{\varepsilon}_p$ is the effective plastic strain as defined above, and E_P is the plastic hardening modulus calculated from:

$$E_P = \frac{E_T E_E}{E_E - E_T} \tag{3.16}$$

where E_T is the tangent modulus of the material. The tangent modulus can be found by calculating the slope of the plastic portion of the true-stress true-strain curve. Strain rate effects are accounted for using the Cowper and Symonds model [89] which scales the yield stress according to the factor:

$$1 + \left(\frac{\dot{\varepsilon}}{SRC}\right)^{\frac{1}{SRP}} \tag{3.17}$$

where SRC and SRP are strain-rate parameters. The additional terms for use with this plasticity model can be seen in Table 3.9

Table 3.9 - Additional terms for plastic kinematic material model.

Property	Value
E_T (GPa)	0.168
SRC (s^{-1})	40
SRP	5

3.4.3 ALE Equations

In this section the general description of the Lagrangian and Eulerian equations for mass, momentum, and energy will be presented. For simplicity the ALE equations will be presented as they contain both the Lagrangian and Eulerian formulations.

The motion of an ALE body f with respect to the total time derivative from a reference coordinate system is expressed as [90]:

$$\frac{\mathrm{d}f(\vec{X},t)}{\mathrm{d}t} = \frac{\partial f(\vec{x},t)}{\partial t} + \vec{w}\cdot\overrightarrow{grad}f(\vec{x},t) \tag{3.18}$$

where $\vec{w} = \vec{u} - \vec{v}$, $\vec{X}$ is the Lagrangian coordinate, $\vec{x}$ is the ALE coordinate, $\vec{u}$ is the material velocity, and $\vec{v}$ is the velocity of the reference coordinate system, which is represented by the mesh. Therefore, to obtain a purely Lagrangian solution $\vec{v}$ is set to $\vec{u}$. Similarly, to obtain the Eulerian solution $\vec{v}$ is set to zero.

The equations for the conservation of mass, momentum, and energy in the ALE formulation are given by:

$$\frac{\partial\rho}{\partial t} + \rho\mathrm{div}(\vec{u}) + \vec{w}\cdot\mathrm{grad}(\rho) = 0 \tag{3.19}$$

$$\rho\frac{\partial\vec{u}}{\partial t} + \rho\vec{w}\cdot\overrightarrow{\overline{grad}}(\vec{u}) = \overrightarrow{\mathrm{div}}(\bar{\bar{\sigma}}) + \vec{f} \tag{3.20}$$

$$\rho\frac{\partial E_{tot}}{\partial t} + \rho\vec{w}\cdot\overrightarrow{\mathrm{grad}}(E_{tot}) = \bar{\bar{\sigma}}:\overrightarrow{\overline{\mathrm{grad}}}(u) + \vec{f}\cdot\vec{u} \tag{3.21}$$

where E_{tot} is the total energy and $\bar{\bar{\sigma}}$ is the total Cauchy stress given by:

$$\bar{\bar{\sigma}} = -p\cdot\bar{\bar{I}}\delta + \zeta\left(\overline{\overline{\mathrm{grad}}}(\vec{u}) + \overline{\overline{\mathrm{grad}}}(\vec{u})^T\right) \tag{3.22}$$

and where p is the pressure, δ is the displacenemt, and ζ is the dynamic viscosity. The non-linear term $\vec{w}$ is one of the major difficulties in the time-integration of Equations (3.19) -

(3.21); thus, an operator split method is typically employed, which divides the complicated ALE problem into a less complicated Lagrangian problem followed by a Eulerian advection. The steps of the Lagrangian problem are outlined in Section 3.3.1 and the equilibrium equations are:

$$\rho \frac{\mathrm{d}\vec{u}}{\mathrm{d}t} = \overrightarrow{div}(\bar{\bar{\sigma}}) + \vec{f} \tag{3.23}$$

$$\rho \frac{\mathrm{d}E_{tot}}{\mathrm{d}t} = \bar{\bar{\sigma}} : \overline{\overline{grad}}(\vec{u}) + \vec{f} \cdot \vec{u} \tag{3.24}$$

The current density ρ is calculated from the integrated form as opposed to the conservative form for improved accuracy and simplicity:

$$\rho J = \rho_0 \tag{3.25}$$

where ρ_0 is the initial density and J is the volumetric strain provided by the Jacobian:

$$J = \det\left(\frac{\partial x_i}{\partial X_i}\right) \tag{3.26}$$

The Eulerian advection step transports the mass, momentum, and energy across each element from the displaced Lagrangian mesh back to the initial mesh position according to:

$$\begin{aligned} &\frac{\partial \Phi}{\partial t} + \vec{w} \cdot \mathrm{grad}(\Phi) = 0, \\ &\Phi(\vec{x}, 0) = \Phi_0(x) \end{aligned} \tag{3.27}$$

where the initial condition $\Phi_0(x)$ is the solution to the Lagrangian calculations of Equations (3.23) and (3.24). The solution to Equation (3.27) is obtained using a finite volume advection algorithm.

3.4.4 Advection Algorithms

Although there are several first- and second-order accurate advection schemes available as, shown by Benson [59], only those utilized for this work will be discussed. Two advection algorithms (*CONTROL_ALE) are required; one for the element-centered variables, such as: density, internal energy, the stress tensor, and the history variables, and one for the momentum as it is centered at the nodes. The Van Leer MUSCL algorithm was used for the element-centered variables, while the Half Index Shift algorithm was used for the momentum. The internal energy is advected instead of the total energy because the internal energy is used in the evaluation of the equation of state. Kinetic energy is not conserved

during the momentum advection; therefore, the total energy of the system may decrease with time. The loss of kinetic energy is a result of the diffusion of the velocity through the mesh.

It is desirable that the advection algorithm be accurate, stable, conservative, and monotonic. Monoticity is achieved if the range of the solution variables does not increase during the remap step [88]. There are two assumptions present during the remap step [59]:

1. The topology of the mesh is fixed.
2. The mesh motion during a step is less than the characteristic lengths of the surrounding elements.

The second assumption is simply a restatement that the Courant Number CN must be less than one:

$$CN = \frac{u\Delta t}{\Delta x} < 1 \tag{3.28}$$

where $u\Delta t$ is the transport volume and is purely geometrical; therefore, it is not associated with any of the underlying physics of the problem.

3.4.4.1 Van Leer MUSCL Algorithm

The monotone upwind schemes for conservation laws [MUSCL] algorithm is a second order extension of the Donor Cell algorithm, which is defined in one dimension as [59]:

$$\Phi_{j+1/2}^{n+1} = \Phi_{j+1/2}^{n} + \frac{\Delta t}{\Delta x}\left(f_j^{\Phi} - f_{j+1}^{\Phi}\right) \tag{3.29}$$

$$f_j^{\Phi} = \frac{1}{2} v_j \left(\Phi_{j-1/2}^{n} + \Phi_{j+1/2}^{n}\right) + \frac{1}{2}\left|v_j\right| \left(\Phi_{j-1/2}^{n} - \Phi_{j+1/2}^{n}\right) \tag{3.30}$$

The value of Equation (3.30) is dependent on the sign of v at node j, which defines the upwind direction. $\Phi_{j-1/2}^{n}$, $\Phi_{j+1/2}^{n}$, and v_j are the initial values of Φ to the left and right of node j and the velocity of the contact discontinuity at node j, respectively. The MUSCL algorithm replaces the constant distribution of Φ over an element with a higher order interpolation function, $\Phi_{j+1/2}^{n}(x)$. The value of Φ at the element centroid is assumed to be the average value of Φ over the element as opposed to the value at $x_{j+1/2}$ [59]:

$$\Phi^n_{j+1/_2}\Delta x_{j+1/_2} = \int_{x_j}^{x_{j+1}} \Phi^n_{j+1/_2}(x)\mathrm{d}x \tag{3.31}$$

The maximum and minimum values of $\Phi^n_{j-1/2}$, $\Phi^n_{j+1/2}$, and $\Phi^n_{j+3/2}$ are used to impose the monoticity constraint in the range of Φ, $\left[\Phi^{min}_{j+1/2}, \Phi^{max}_{j+1/2}\right]$. Monoticity is imposed by requiring that the maximum and minimum values of $\Phi^n_{j+1/2}(x)$ fall within the range determined by three elements or by restricting the average value of Φ in the transport volumes associated with element $j + 1/2$. The second definition allows a larger magnitude of Φ to be transported to adjacent elements as compared to the first definition [59].

The piecewise linear function of ϕ expanded about the element centroid is:

$$\Phi^n_{j+1/_2}(x) = S^n_{j+1/_2}\left(x - x^n_{j+1/_2}\right) + \Phi^n_{j+1/_2} \tag{3.32}$$

where x is now the volume coordinate, which is simply the volume swept along the path between the element centroid and the point.

By letting $s^n_{j+1/2}$ be a second order approximation of the slope, the limited value of the slope $S^n_{j+1/2}$ according to the first limiting approach is determined by assuming the maximum permissible values occur at the element boundaries [59].

$$S^n_{j+1/_2} = \frac{1}{2}\{\mathrm{sgn}(s^L) + \mathrm{sgn}(s^R)\} * \min\left(|s^L|, \left|s^n_{j+1/_2}\right|, |s^R|\right) \tag{3.33}$$

$$s^L = \frac{\Phi^n_{j+1/_2} - \Phi^n_{j-1/_2}}{2\Delta x_{j+1/_2}} \tag{3.34}$$

$$s^R = \frac{\Phi^n_{j+3/_2} - \Phi^n_{j+1/_2}}{2\Delta x_{j+1/_2}} \tag{3.35}$$

The slope $S^n_{j+1/2}$ according to the second limiting approach is determined by assuming the maximum permissible values occur at the centroid of the transport volumes.

$$s^L = \frac{\Phi^n_{j+1/_2} - \Phi^n_{j-1/_2}}{x_{j+1/_2} - \left(x_j + \frac{1}{2}\max(0, v_j)\Delta t\right)} \tag{3.36}$$

$$s^R = \frac{\Phi^n_{j+3/2} - \Phi^n_{j+1/2}}{\left(x_{j+1} - \frac{1}{2}\min(0, v_{j+1})\Delta t\right) - x_{j+1/2}} \tag{3.37}$$

Evidently, Equations (3.36) and (3.37) will limit the slope at the element boundary even if the element is the downstream element at the boundary. For example, if v is negative, only s^R would limit the value of S^n. If the element is the downstream element at both boundaries, then the slope in the element has no effect of the solution [59].

The upstream approximation of Φ is evaluated to find the flux at node j.

$$f_j^{\phi} = \frac{v_j}{2}\left(\Phi_j^- + \phi_j^+\right) + \frac{|v_j|}{2}\left(\Phi_j^- - \Phi_j^+\right) \tag{3.38}$$

$$\Phi_j^+ = S^n_{j+1/2}\left(x^C - x^n_{j+1/2}\right) + \Phi^n_{j+1/2} \tag{3.39}$$

$$\Phi_j^- = S^n_{j-1/2}\left(x^C - x^n_{j-1/2}\right) + \Phi^n_{j-1/2} \tag{3.40}$$

$$x^C = x_j^n + \frac{1}{2}\Delta t v_j \tag{3.41}$$

The higher order approximation of the slope $S^n_{j+1/2}$ is not unique and the simplest approach is to fit a parabola through the centroids of the three adjacent elements and evaluate its slope at $x^n_{j+1/2}$. If the value of Φ at the element centroids is assumed to be equal to the element average this algorithm defines a projection [59]:

$$s^n_{j+1/2} = \frac{\left(\Phi^n_{j+3/2} - \Phi^n_{j+1/2}\right)\Delta x_j^2 + \left(\Phi^n_{j+1/2} - \Phi^n_{j1/2}\right)\Delta x_{j+1}^2}{\Delta x_j \Delta x_{j+1}\left(\Delta x_j + \Delta x_{j+1}\right)} \tag{3.42}$$

$$\Delta x_j = x^n_{j+1/2} - x^n_{j-1/2} \tag{3.43}$$

The advection in three dimensions is performed isotropically in LS-DYNA® by:

$$\Phi_Z^{n+1} = \frac{1}{V_Z^{n+1}}\left(V_Z^n \Phi_Z^n + \sum_{l=1}^{6} f_l^{\phi}\right) \tag{3.44}$$

where the fluxes through each face l of element Z are calculated simultaneously and the fluxes Φ are calculated using the one dimensional expressions [88]. One caveat of advecting material through the element faces is the potential loss of material at the corners of an expanding body, as shown in Figure 3.14. The isotropic solution scheme in three

dimensions permits round surfaces to be employed; however, it is advisable to maintain a regular, orthogonal mesh pattern in high deformation zones to reduce the likelihood of advection errors. Moreover, the direction of the mesh should be aligned with the predominant direction of material flow.

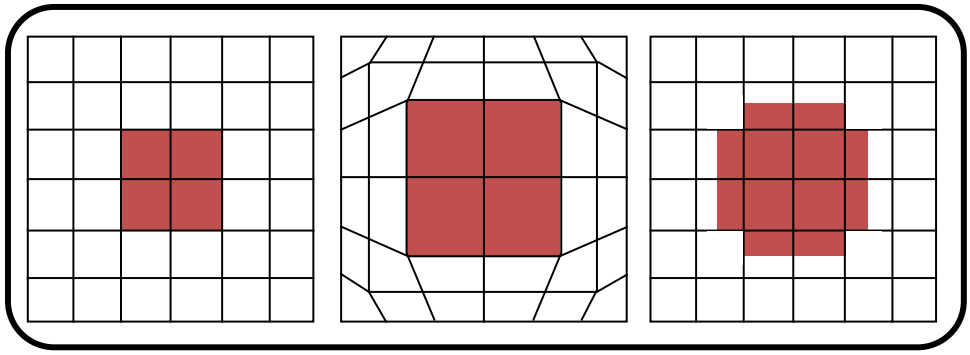

Figure 3.14 - Loss of material due to advection.

3.4.4.2 The Half Index Shift Algorithm

The Half Index Shift [HIS] algorithm is used to advect the node-centered momentum instead of the nodal velocity to guarantee the conservation of momentum. This method operates by defining new solution variables, transporting them, and subsequently rebuilding the new velocities. The average element momentum is derived from the average nodal velocities. The change in the average element momentum as a result of the advection is then used to incrementally update the velocities of the nodes defining the element. The mass M transported across the edge k of an element is found directly from the transported density ρ [91]:

$$\Delta M_k = \rho_k \Delta V_k \tag{3.45}$$

where V is the volume. Two new element-centered variables are defined as [91]:

$$\Psi^1_{j+1/2} = v_j \tag{3.46}$$

$$\Psi^2_{j+1/2} = v_{j+1} \tag{3.47}$$

which are transported using the MUSCL algorithm along with the masses. The new nodal velocity is then calculated directly from the updated values from [91]:

$$v_{j+1/2} = \frac{1}{2}\frac{\left(M_j\Psi_j^2 + M_{j+1}\Psi_{j+1}^1\right)}{M_{j+1/2} + \Delta M_j - \Delta M_{j+1}} \tag{3.48}$$

In three dimensions there are eight new element-centered variables created for each of the three velocities:

$$\Psi_Z^i = v_j, \qquad j = 1,8 \tag{3.49}$$

with each variable corresponding to a velocity at one of the eight nodes. The element-centered variables are transported, and the new velocities for each node are found from:

$$v_j = \frac{1}{8}\sum_{Z=1}^{\text{nel}} \frac{M_Z\Psi_Z^{\varsigma(j)}}{M_j} \tag{3.50}$$

where the function $\varsigma(j)$ is the index of node j in the connectivity matrix defining element Z [91].

3.4.5 Element Mixture Theory

Multiple materials may occupy the same element in the Eulerian formulation as a result of the spatially fixed mesh. In this work only two materials are considered, the workpiece and the void. The mixture theories define how the element mean strain rate is partitioned amongst the various materials and calculates the mean stress from the stresses in the different materials. There are two mixture theories implemented in LS-DYNA®. The simplest mixture theory is known as the mean strain-rate mixture theory and gives each material within an element the same strain rate. A slightly more complex method is a single iteration to create a pressure equilibrium in the element. Regardless of the chosen mixture theory, the elemental mean stress is the volume weighted average of the material stresses:

$$\sigma^{n+1} = \sum_{m=1}^{M} \sigma_m^{n+1} V_m^f \tag{3.51}$$

where V_m^f is the volume fraction of material m to the total element volume [47].

3.4.5.1 The Mean Strain-Rate Mixture Theory

This mixture theory is simple, robust, energy conservative, and sufficiently accurate for problems involving high pressures and strain rates. Each material in an element is assigned

the mean strain rate of the element, $\dot{\varepsilon}^{n+1/2}$. The stresses σ and history variables H are updated independently for each material m through the stress update algorithm Σ:

$$[\sigma_m^{n+1}, H_m^{n+1}] = \Sigma\left(\sigma_m^n, h_m^n, \dot{\varepsilon}^{n+1/2}, \Delta t, Q_m\right) \tag{3.52}$$

where Q are the material constants.

3.4.5.2 Pressure Equilibrium Mixture Theory

This mixture theory is typically more appropriate when mixing materials with very different compressibility [79] and is most effective when a small amount of solid material occupies an otherwise empty cell. This situation may lead to the solid material experiencing large volumetric strain rates and unphysically high pressures; therefore, a single iteration of the pressure equilibrium mixture theory allows the materials to relax towards a pressure equilibrium.

The pressure p for each material m is linearized in terms of the volumetric strain rate $\dot{\varepsilon}_m^v$ and the wave speed c:

$$p_m^{n+1} = p_m^n - \rho c_m^2 \Delta t \dot{\varepsilon}_m^v \tag{3.53}$$

and solved subject to the strain-rate constant:

$$\sum_{m=1}^{M} \dot{\varepsilon}_m^v V_m^f = \dot{\varepsilon}^v \tag{3.54}$$

The strain rate for each material is now the sum of the element deviatoric strain rate $\dot{\varepsilon}'$ and the material volumetric strain rate:

$$\dot{\varepsilon}_m = \dot{\varepsilon}' + \dot{\varepsilon}_m^v \boldsymbol{I} \tag{3.55}$$

3.4.6 Fluid-Structure Coupling

The role of the fluid-structure coupling is to prevent the master (Eulerian) body from penetrating the slave (Lagrangian) body, thus allowing the slave body to exert forces on the master body (*CONSTRAINED_LAGRANGE_IN_SOLILD). An incorrect coupling definition may allow the master body to penetrate the slave body, which is known as fluid leakage. As will be discussed later in this section, some fluid leakage is acceptable as

attempting to completely eliminate it may lead to system instability. For this work the slave body is the tool and the master body is the workpiece.

The reference configuration at a time of t^n is shown to the left in Figure 3.15. From the figure it can be seen that the Lagrangian structure has coupling points applied while the Eulerian fluid has fluid particles inserted near the coupling points. The number of coupling points is a user controlled function in LS-DYNA® and their density must be chosen based on the relative resolutions of the interacting structure and fluid mesh. Too many coupling points may lead to numerical instabilities while too few may allow the fluid to excessively leak past the structure. The fluid particles are automatically inserted and removed as necessary while their mass and velocity are interpolated based on the finite element shape functions. If a perfect coupling condition were created the fluid particles would lie in the same spatial location as the coupling points.

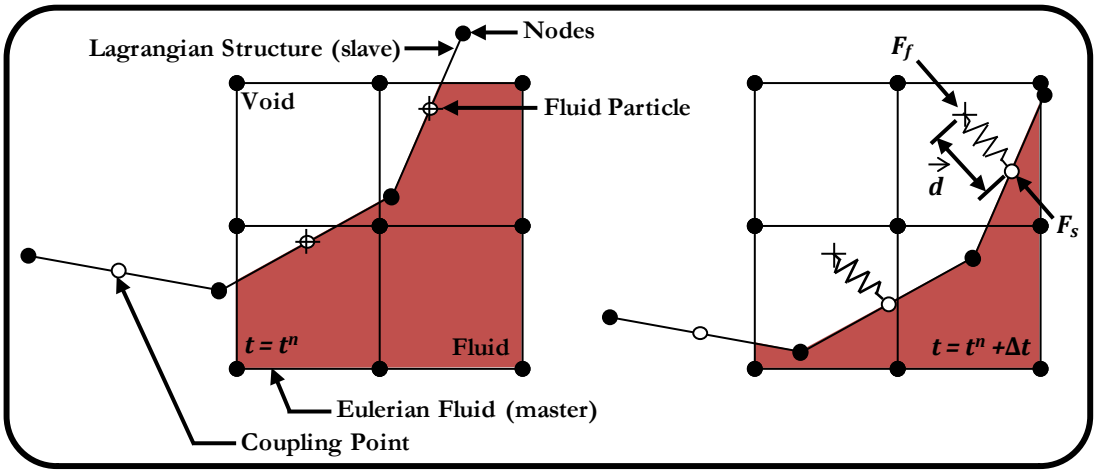

Figure 3.15 - Conceptual sketch of fluid-structure coupling.

As the model advances to the next time step the depth of penetration $\vec{d}$ is incrementally updated using the relative velocity of the structure and fluid mesh $\left(\vec{v}_s - \vec{v}_f\right)$ according to [90]:

$$\vec{d}^{n+1} = \vec{d}^{n} + \left(\vec{v}_s^{\,n+1/2} - \vec{v}_f^{\,n+1/2}\right) \cdot \Delta t \tag{3.56}$$

The fluid-structure coupling is essentially a spring system, whereby the coupling forces are calculated based on the penetration depth and the spring stiffness according to:

$$F_{fs} = \kappa \cdot \vec{d} \tag{3.57}$$

where κ is the spring stiffness. The force F_{fs} is applied to both the master and slave bodies in opposing directions to satisfy equilibrium at the coupling interface. The force on the slave coupling points is simply:

$$F_s = -F_{fs} \tag{3.58}$$

whereas the force on the fluid is distributed amongst the fluid element nodes based on the shape functions at each node j $(j = 1,8)$. Therefore, the force must be scaled by the shape function N_j:

$$F_{f,j} = N_j \cdot F_{fs} \tag{3.59}$$

These coupling forces tend to allow a small amount of fluid leakage. It may be tempting to specify a very high coupling stiffness to completely eliminate fluid leakage; however, the coupling interface adds stiffness to the overall system which affects the eigenfrequency spectra. As the system stiffness increases the time step decreases, eventually leading to an unstable model.

The spring stiffness κ is calculated from [90]:

$$\kappa = q_f \frac{K A_E^2}{V} \tag{3.60}$$

where K is the bulk modulus of the fluid, A_E is the area of the structure element in contact with the fluid element and q_f is a scale factor that is used to tune the stiffness of the fluid-structure coupling. In this work q_f is used to tune the model to minimize leakage and to improve the correlation with the experimental data as will be shown in Section 4.3.3.2.

3.5 Summary

This chapter has introduced the basic physics of chip formation in metal cutting and reviewed some of the more recent works. The commercial finite element hydrocode LS-DYNA® was introduced with a review of the available finite element formulations. A hybrid Eulerian-Lagrangian formulation was chosen based on its modeling flexibility and a review of the underlying mathematics was presented. A literature review, summarized in Table 3.1 and Table 3.2, spanning both analytical and finite element models revealed little work in the

area of modeling chip formation in grinding at the abrasive grain level with the exception of the work performed by Ohbuchi and Obikawa [45] and Doman *et al.* [46]. The work of Ohbuchi and Obikawa was thorough but it lacked more intensive experimental validation. The work of Doman *et al.* was unique; however, the cutting speeds were too low and a thermo-elastoplastic model was not used. Therefore, in an effort to extend the current knowledge of chip formation in grinding a comprehensive finite element model with experimental validation was required. The model will be formulated in three dimensions, will incorporate a thermo-elastoplastic material model, and will be quantitatively verified by direct force comparisons.

Chapter 4 Indentation Testing

Indentation testing is an ideal method to tune and verify a finite element model of single abrasive-grain cutting as it removes the complexities of relative motion from the equation; thereby, allowing more controlled mesh convergence studies. In this work indentation tests were used to verify the functionality of a finite element model by comparison to classical analytical methods. Once the finite element model was proven to function properly, it was compared to experimental indentation data to verify its accuracy. The control card settings and converged element size were then utilized as the basis of the scratching model, which will be discussed in Chapter 5.

4.1 General Considerations

Spherical indentation testing is often utilized to identify surface mechanical properties of materials, such as: hardness and the elastic modulus, and is industrially important as the tests are non-destructive and can be performed on in-service parts. Indentation tests are performed by slowly advancing a hard tool into a softer workpiece. The state of stress in the

workpiece, when loaded with a blunt tool, is a function of the applied pressure and can be subdivided into three regimes: fully elastic, elastoplastic, and fully plastic [92], as shown in Figure 4.1. Tabor [93] recommends the following general relationship between the mean contact pressure p, the yield strength σ_Y, and a constraint factor C^*:

$$p \propto C^* \sigma_Y \tag{4.1}$$

where the constraint factor typically has a value slightly higher than unity ($C^* \approx 1.1$) at first yield, depending on Poisson's ratio. Therefore, the fully elastic regime occurs when the mean pressure is less than $1.1\sigma_Y$. The elastoplastic regime is attained as the mean pressure is increased beyond $1.1\sigma_Y$ producing a zone of plastically deformed material below the surface. The surface stresses remain elastic during the elastoplastic regime due to the confining pressures created by the surrounding material. The volume of plastically deformed material continues to increase with increasing pressure and eventually reaches the surface at which point the fully plastic regime is created. Once the fully plastic regime is attained the mean contact pressure will have a constant value of approximately $C^* \sigma_Y$ where the constraint factor C^* is approximately 3 for metals [94].

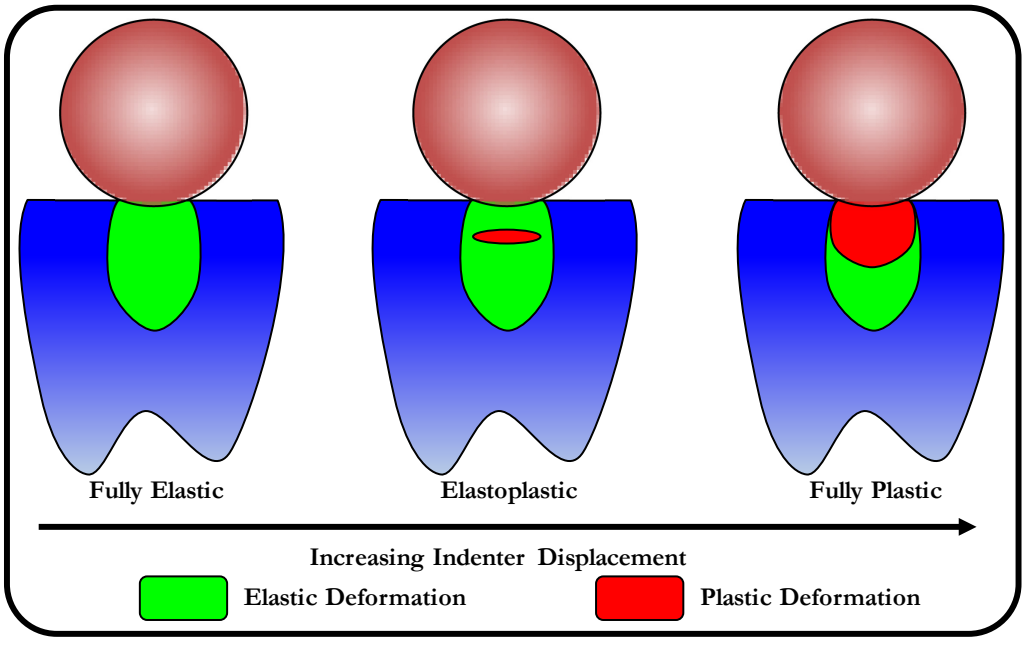

Figure 4.1 - Deformation stages with increasing indenter displacement.

The bulk of the recently published works tend to be related to modern methods of material characterization and numerically modeling the response of materials. A thorough review of

indentation subject matter was not relevant to this work; therefore, only a brief discussion of some works will be presented. An excellent resource is the bibliography created by Mackerle [95] on the finite element method used to simulate indentation testing. Material characterization techniques have become efficient at determining hardening parameters of metals.

Kucharski and Mroz [96,97] used a spherical indentation method involving the measurement of the indentation depth during loading and unloading to create plastic loading curves and negate the effects of elastic recovery. A finite element model was created using the identified plastic hardening parameters. The results of the finite element model compared well to tensile test data for brass, steel, and aluminum. Kucharski and Mroz [98] later expanded their technique to determine the yield stress of metals.

Nayebi *et al.* [99] proposed a new method to determine the mechanical parameters of steel using a minimization of error scheme between the equation $\delta = J(\sigma_Y, n)F^{K(\sigma_Y,n)}$ and the load-displacement curve from a spherical indentation test, where the functions J and K depended on the indenter displacement δ, the yield stress σ_Y, the applied load F, and the hardening exponent n. The results agreed with the data obtained from tensile test experiments.

Hyungyil *et al.* [100] used a numerical approach based on incremental plasticity theory to study the effects of material properties and the coefficient of friction on the load-displacement curve. Their results showed that the load-displacement curve successfully converted to a stress-strain curve and that a point at $0.8R$ away from the indentation center showed negligible friction and strain-gradient effects, where R was the diameter of the spherical indenter.

Finite element modeling of the material response to indentation has become more widespread and is an essential tool to emerging fields, such as: thin film coatings. The performance of thin film coatings has become an important subject lately due to the desire

to prolong the wear life and reduce the friction of highly stressed components, such as: gear trains, engine components, and high performance bushings and bearings.

Chudoba *et al.* [101] used a finite element model to verify the accuracy of an analytical elastic model of a coated surface. The analytical model was then compared to experimental results with complete agreement. Once the validity of the analytical model was verified it was used to predict the onset of plastic deformation within a coated surface. Their results showed that plastic deformation occurred sooner in thin, as opposed to thick, coatings despite both coatings having the same plastic hardness.

Vanimisetti *et al.* [102] created a finite element model to study the response of thin films on hard substrates subjected to spherical indentation. Their work revealed that bending deformation in the film occurred when the contact radius was approximately 0.2 - 0.3 times the film thickness.

During indentation the workpiece material may sink-in or pile-up around the indenter, as shown in Figure 4.2, thus altering the contact radius a. The instantaneous contact radius is difficult to measure, yet is a primary variable in analytical models. One of the main advantages finite element modeling has over analytical methods is the ability to determine the true contact radius and, thereby, provide a more accurate description of the state of stress in the workpiece. Rodriguez and Maneiro [103] provide a procedure involving the elastic unloading of the workpiece material and the residual indentation radius to prevent pile-up effects from affecting analytical results. Taljat and Pharr [104] performed numerical experiments to determine the effects that material properties have on the formation of pile-up. They concluded that sink-in tends to occur in the elastic regime in accordance with Hertzian contact mechanics, pile-up develops in the elastoplastic regime depending on the strain hardening exponent and the coefficient of friction, and pile-up becomes fully developed well into the fully plastic regime.

4.2 Theoretical Considerations

This section will provide a brief derivation of the force-displacement relationships for fully elastic, elastoplastic, and fully plastic spherical indentation.

4.2.1 Fully Elastic Response

The elastic interaction between two spherical objects in contact was described by Hertz [105] and is readily applicable to a spherical tool and a flat workpiece. The mean pressure p as a function of the contact radius a_c and indenter radius R is given by:

$$p = \frac{4E^*}{3\pi}\left(\frac{a_c}{R}\right) \tag{4.2}$$

where E_E^* is the equivalent elastic modulus between the specimen E_E and the indenter E_{Ei} and is found from:

$$\frac{1}{E_E^*} = \frac{1-\nu^2}{E_E} + \frac{1-\nu_i^2}{E_{Ei}} \tag{4.3}$$

and where ν is Poisson's ratio.

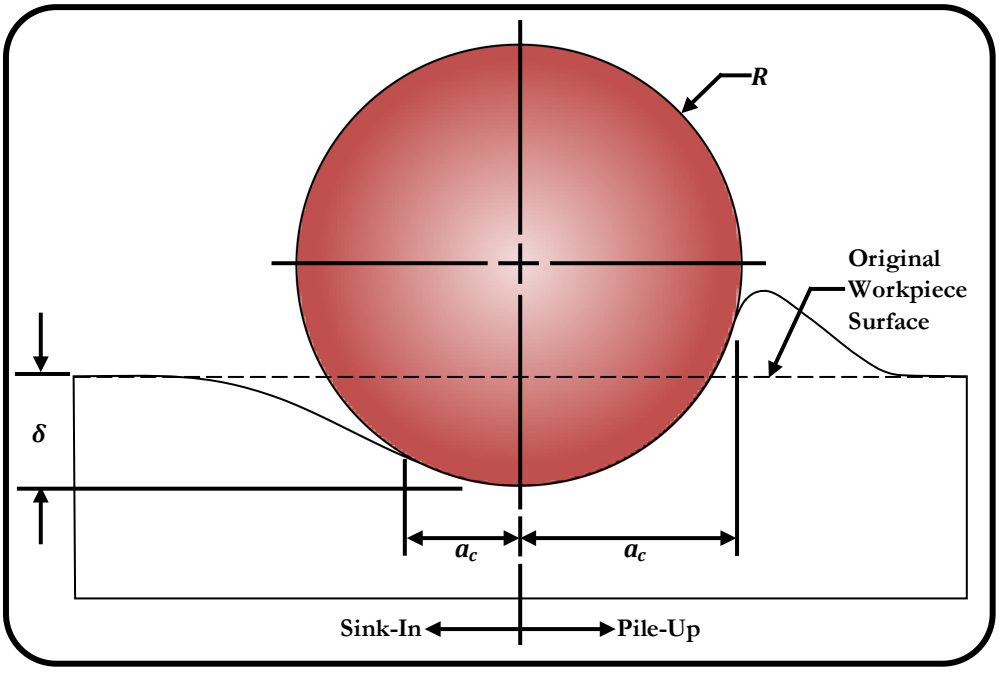

Figure 4.2 - Sink-in and pile-up geometry.

For this work the applied force F and the displacement δ were the measured quantities of interest. The applied force can be found from the force-pressure relationship:

$$p = \frac{F}{\pi {a_c}^2} \tag{4.4}$$

and the displacement is found from:

$$\delta = \frac{{a_c}^2}{R} \tag{4.5}$$

By substituting Equations (4.4) and (4.5) into Equation (4.2) the following force-displacement relationship is found:

$$F = \frac{4}{3} E_E^* R^{1/2} \delta^{3/2} \tag{4.6}$$

4.2.2 Elastoplastic Response

Currently there is no closed-form analytical solution for elastoplastic indentation; however, Tabor [93] empirically related the pressure-contact radius curve $(p \sim a_c/R)$ to the true-stress plastic-strain curve $(\sigma_T \sim \varepsilon_p)$ using the following relationships:

$$\varepsilon_p = \beta_T \left(\frac{a_c}{2R}\right) \tag{4.7}$$

$$\sigma_T = \frac{p}{\alpha_T} \tag{4.8}$$

where σ_T is the true stress, ε_p is the plastic strain, and α_T and β_T were found to have values of 2.8 and 0.4, respectively. Biwa and Storakers [106] expressed the material plasticity using the power law flow rule:

$$\bar{\sigma} = K \varepsilon_p^n \tag{4.9}$$

where $\bar{\sigma}$ is the flow stress, K is the hardening modulus, and n is the hardening exponent. The mean pressure is then obtained by combining Equations (4.7), (4.8) and (4.9):

$$p = \alpha_T K \beta_T^n \left(\frac{a_c}{2R}\right)^n \tag{4.10}$$

Moreover, the ratio:

$$\frac{{a_c}^2}{\delta(2R)} = c^2 \tag{4.11}$$

is constant and depends only on the hardening exponent n according to:

$$c^2 = 1.41e^{-0.97n} \tag{4.12}$$

By combining Equations (4.10), (4.11), and (4.12) and substituting into Equation (4.4) yields the following force-displacement relationship for elastoplastic materials:

$$F = \pi \alpha_T K \beta_T^n c^{n+2} (2R)^{1-n/2} \delta^{n/2+1} \tag{4.13}$$

It should be noted that Equation (4.13) is only valid for indentation depths up to approximately 10% of the indenter radius as the power law flow rule is not valid for deep indentation, as shown by Lu *et al.* [107].

4.2.3 Fully Plastic Response

As previously mentioned, fully plastic indentation occurs once the yield surface expands to the surface of the workpiece and tends to occur when $E^* a/R\sigma_Y \approx 40$. Provided that neither pile-up, nor sink-in occur at the edges of the impression then the displacement can be approximated by [92]:

$$\delta = \frac{{a_c}^2}{2R} \tag{4.14}$$

Assuming a constant fully plastic contact pressure $3.0\sigma_Y$ provides the following force-displacement relationship [92]:

$$F = 0.81 \left(\frac{\delta {E_E^*}^2}{R\sigma_Y^2} \right) F_Y \tag{4.15}$$

where the force required to cause yielding F_Y is found from [92]:

$$F_Y = 21.2 \left(\frac{R^2 \sigma_Y^2}{{E_E^*}^2} \right) \tag{4.16}$$

Substituting Equation (4.16) into Equation (4.15) yields the following fully plastic force-displacement relationship:

$$F = 17.172 \delta R \tag{4.17}$$

Obviously, pile-up does occur in metals at suitably large indentation depths, nevertheless; Equation (4.17) provides a reasonable indication of the fully plastic response. Since the contact radius a increases due the presence of pile-up, one would expect the equation to under predict the forces for a given indentation depth.

4.3 Finite Element Model

The finite element model was created using the elements, material models, and fluid-structure coupling definition as discussed in Section 3.4. The indentation direction was chosen to be along the Y-axis and the loading was created by slowly advancing the indenter into the workpiece material. A representation of the indentation model is shown in Figure 4.3, which shows the general mesh topology employed for this model as well as the Eulerian and void material zones. Note that the element sizes in the figure have been enlarged to improve the clarity of the mesh.

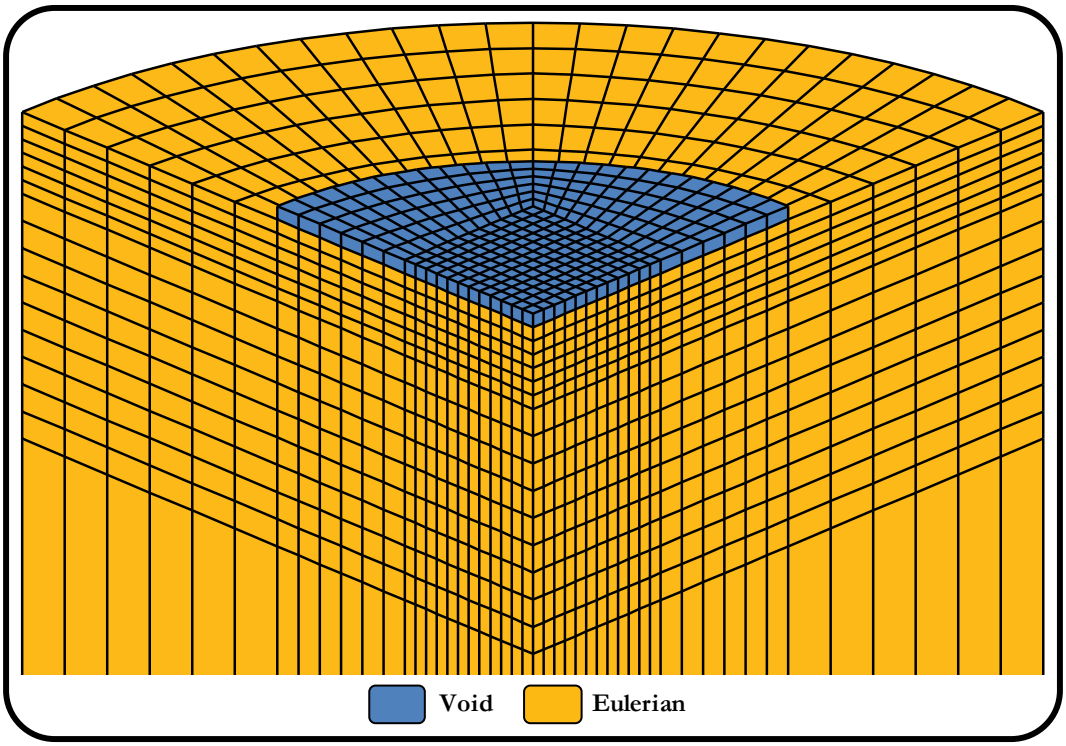

Figure 4.3 - Representative indentation model.

4.3.1 Boundary Conditions

Symmetry of the indentation process was exploited, and as such only a quarter model was created. Appropriate boundary conditions were required to account for the material removed by the symmetry definition. Nodes on the XY-face were constrained from translating along the Z-axis and rotating around the X- and Y-axes. Nodes on the YZ-face were constrained from translating along the X-axis and rotating around the Y- and Z-axes.

The nodes on the bottom surface of the workpiece were constrained from translating along the Y-axis.

4.3.2 Mesh Setup

The computational mesh was designed such that all of the elements within the contact region were perfect cubes with an aspect ratio of 1. The elements outside the contact region were gradually increased in size to reduce the number of required elements, thus decreasing the computational time. A mesh convergence study was conducted to determine the element size required for an accurate solution. Element sizes were reduced from 32 μm to 2 μm, for both the indenter and the workpiece, by continuously dividing the element size in half, which preserved the overall topology of the mesh within the contact region, as shown in Figure 4.4. A rigid indenter and an elastic workpiece material were chosen to allow a direct comparison to the Hertz solution. The results of the convergence study are shown in Figure 4.5, which shows an increase in the finite element model accuracy as compared to the Hertz solution as the element size was reduced. Element sizes of 2 μm and 4 μm produced normal forces of 77.43 kN and 72.60 kN, which was within 0.1% and 6.4% of the Hertz solution of 77.54 kN, respectively. A consequence of the reduced element size was a 7.3 fold increase in the solution time from 1277 seconds to 9334 seconds for the 4 μm and the 2 μm elements, respectively. An element size of 4 μm was chosen for the remainder of the indentation tests based on the results of the convergence study and considering both the solution accuracy and solution time.

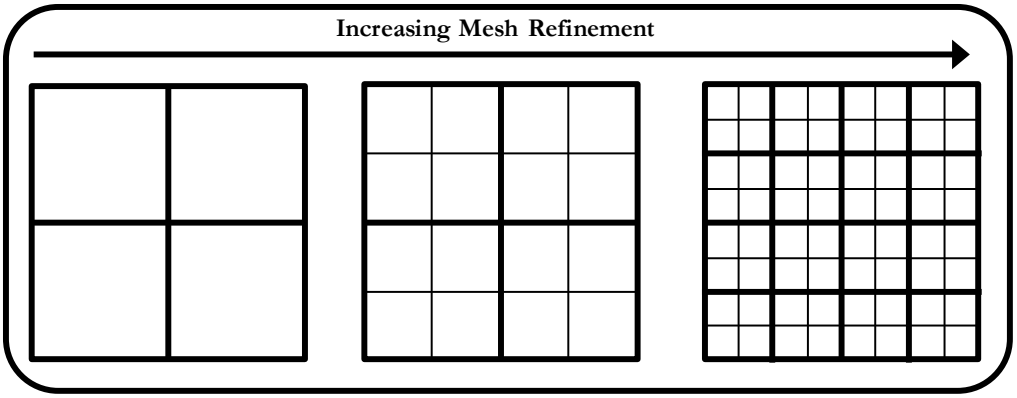

Figure 4.4 - Mesh refinement topology.

4.3.3 Finite Element Model Refinements

Several refinements were made to the indentation model to improve the solution accuracy and reduce the solution time. These refinements included: changing the indenter material definition, adjusting the fluid-structure coupling penalty factor, testing the asphericity of the indenter, reducing the number of contact coupling points, and implementing a hybrid Euler-Lagrange numerical formulation. Moreover, the solution time reduction by using a cluster based computing environment was investigated.

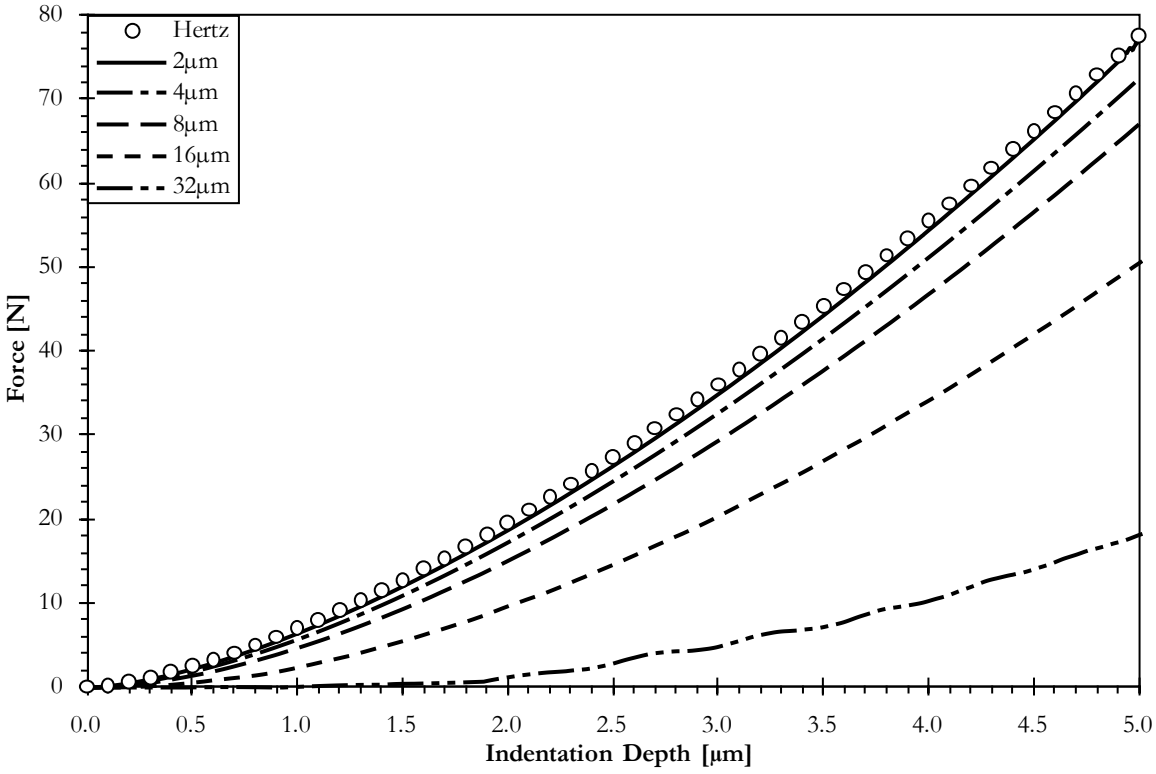

Figure 4.5 - Indentation mesh convergence study results.

4.3.3.1 Indenter Material Definition

As shown in Section 3.4.2 there was a large discrepancy between the stiffness of the diamond indenter (1200 GPa) and the steel workpiece (205 GPa), suggesting that it was safe to assume the indenter as rigid. A rigid assumption was ideal as it reduced the quantity of elements required to define the indenter, thus reducing the solution time. Figure 4.6 shows the comparison between the normal force produced by an elastic indenter and a rigid indenter and indicates that the deviation continually decreased from a maximum of 18.9% to

a minimum of 1.0% at an indentation depth of 5 μm, thus proving that the rigid assumption was reasonable.

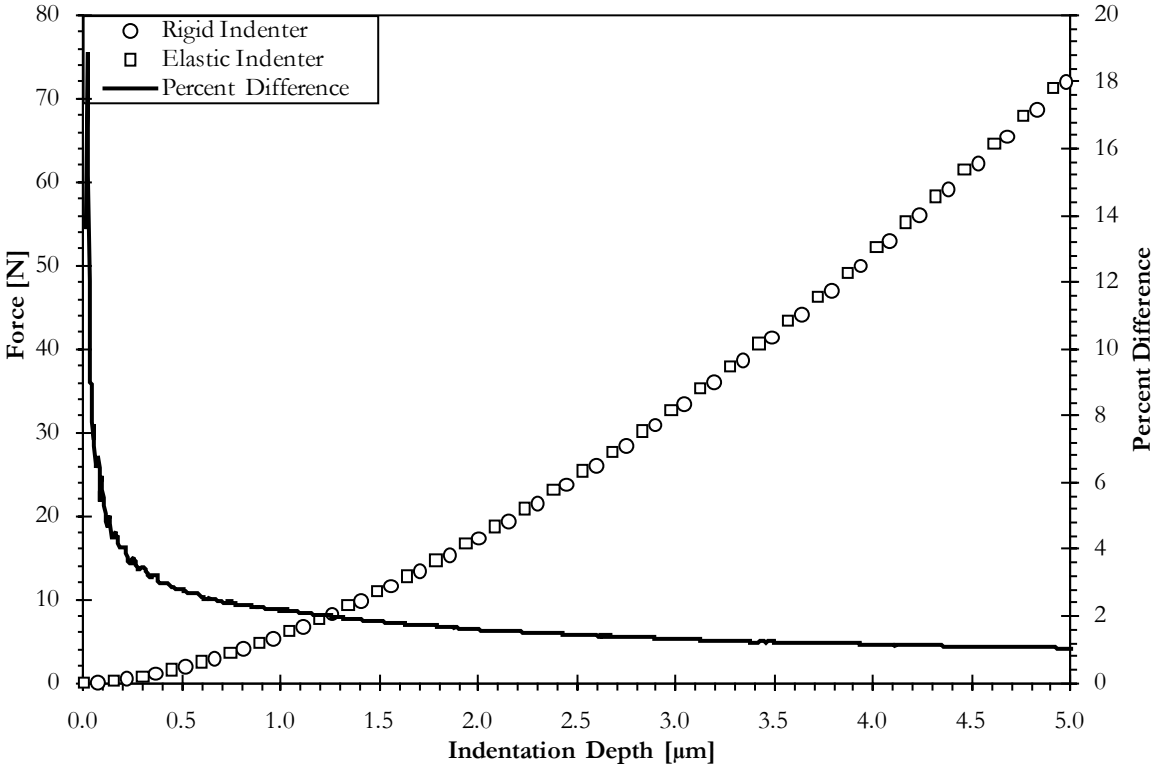

Figure 4.6 - Rigid and elastic indenter material comparison.

4.3.3.2 Fluid-Structure Coupling Penalty Factor

As shown in Equation (3.60) in Section 3.4.6 there was a variable q_f that was used to tune the coupling stiffness of the fluid-structure interaction. Correctly setting this variable was crucial as it could drastically affect the simulation results. If it was set too high then excessively high pressures may have resulted; if it was set too low then excessively large leakage may have occurred. Both situations result in poor solution accuracy and may lead to numerical instability. The default value was an adequate starting point; however, the variable can be defined as a load curve to gain improved control over the coupling pressure versus the penetration depth. The load curve was defined by specifying an estimated coupling pressure for a given maximum allowable penetration and can be scaled to alter the contact stiffness. The coupling pressure was estimated based on a previous simulation at the default settings and the maximum allowable penetration was chosen based on the element size. The

effect of choosing different pressures and penetrations had a marked effect on the simulation results as shown in Figure 4.7 - Figure 4.10. The coupling pressures were kept the same in all of the figures and ranged from 0.025 GPa to 0.225 GPa while the maximum allowable penetration was altered from $1x10^{-3}$ mm to $1x10^{-6}$ mm. It can be seen that the forces for $1x10^{-3}$ mm and $1x10^{-4}$ mm of allowable penetration were well below the Hertz solution while the forces for the $1x10^{-5}$ mm and $1x10^{-6}$ mm of allowable penetration were approaching and nearly identical to the Hertz solution. It is evident from the figures that the coupling pressure had less effect on the forces as the allowable penetration was reduced. Table 4.1 shows the solution times for the various coupling pressures and allowable penetrations and indicates that, on average, the solution time increased as the allowable penetration was decreased. Based on the force results and the solution times it was decided that an allowable penetration of $1x10^{-5}$ mm should be utilized with a higher coupling pressure. Figure 4.11 shows that a coupling pressure of 0.5 GPa and an allowable penetration of $1x10^{-5}$ mm produced accurate results when compared to the Hertz solution.

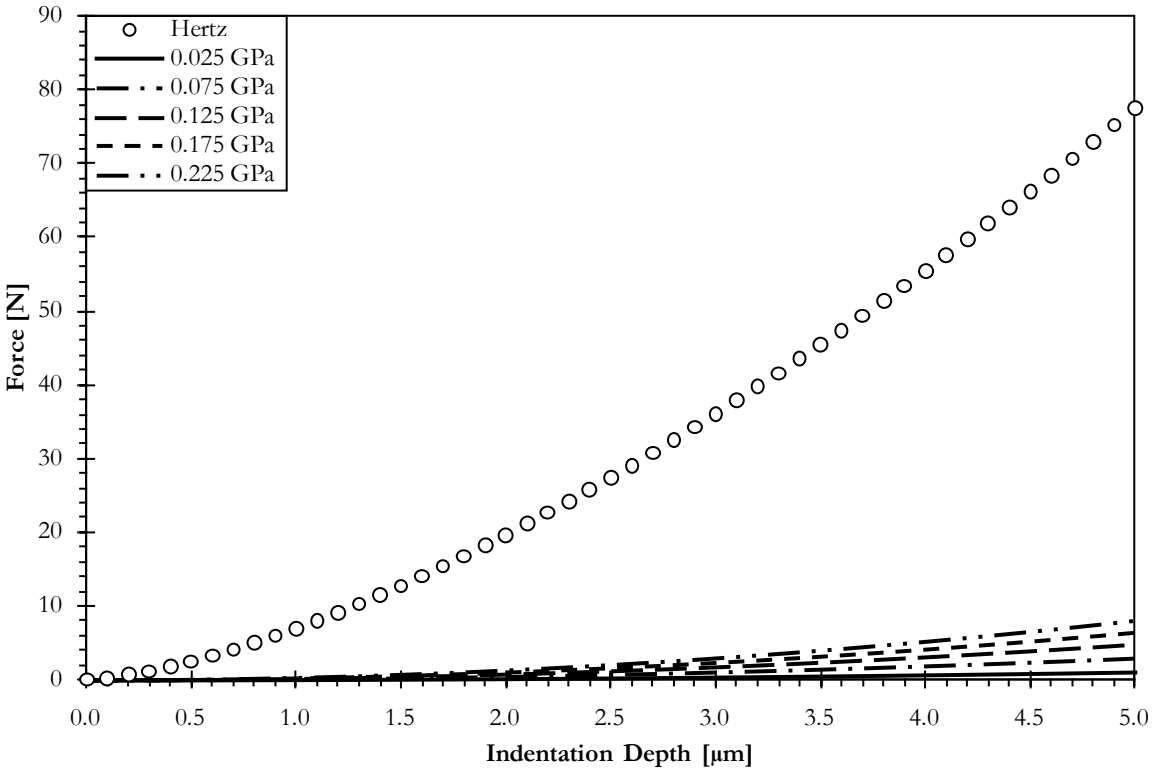

Figure 4.7 - Indentation forces for an allowable penetration of $1x10^{-3}$ mm.

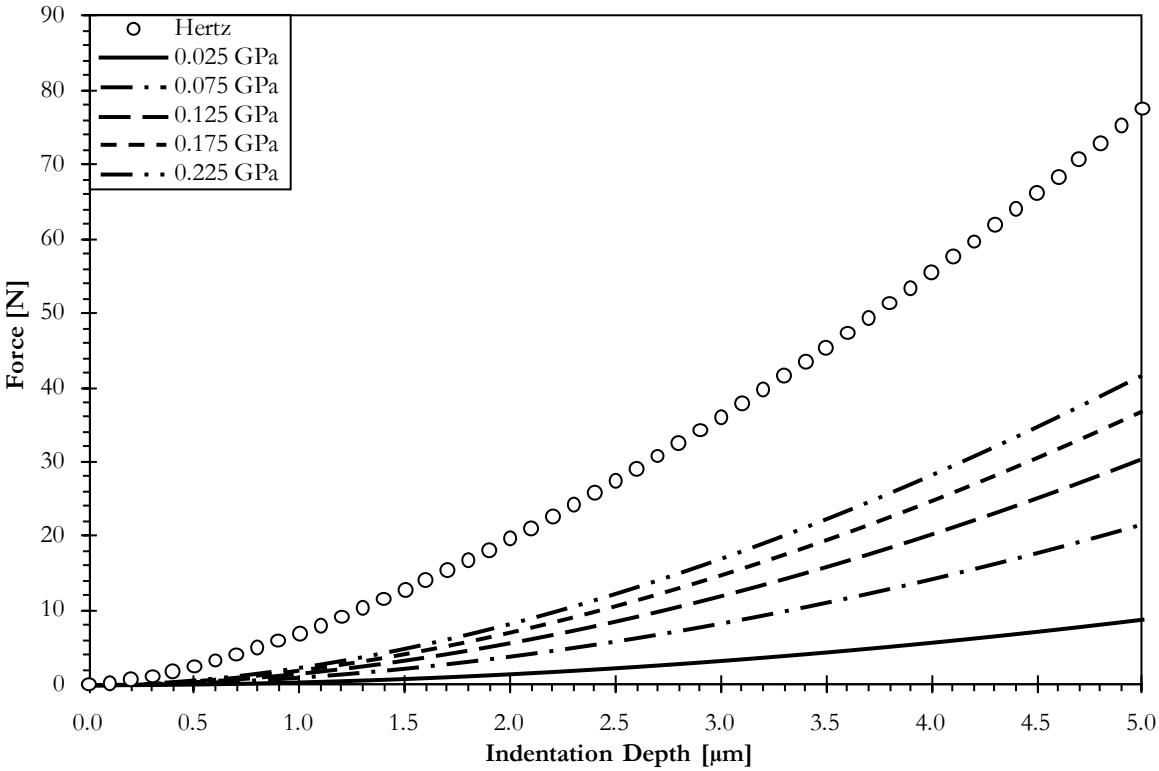

Figure 4.8 - Indentation forces for an allowable penetration of $1x10^{-4}$ mm.

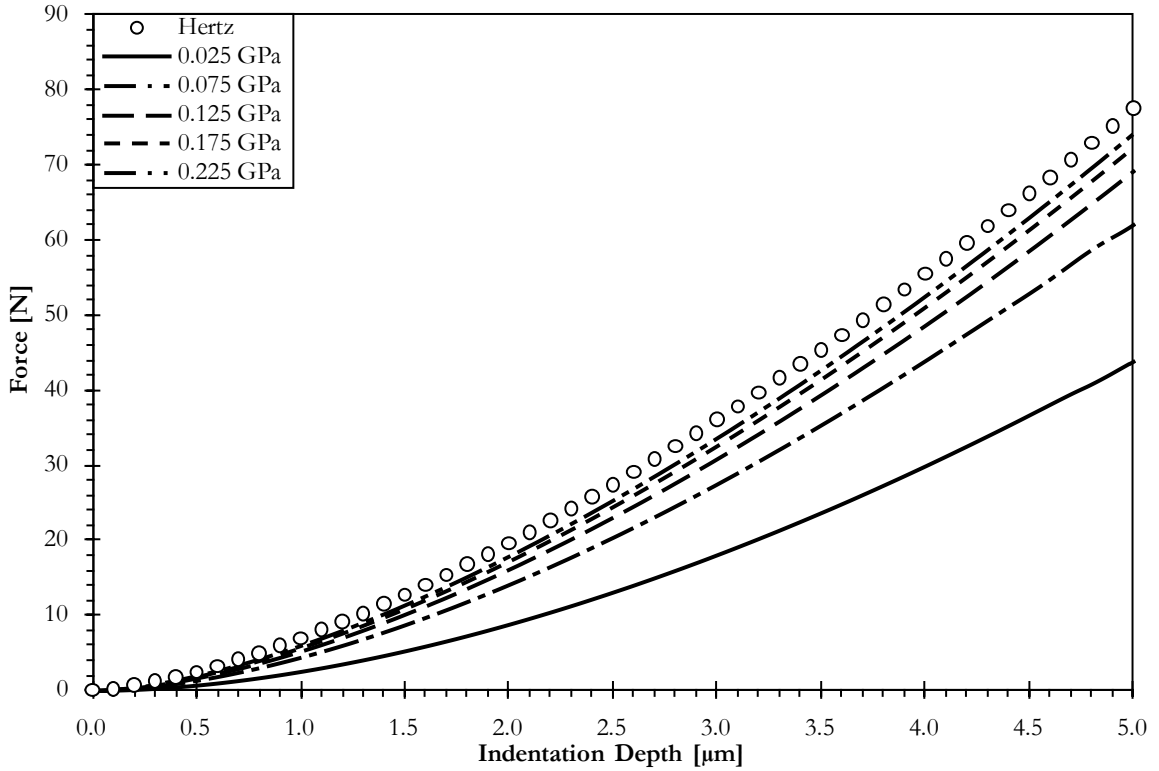

Figure 4.9 - Indentation forces for an allowable penetration of $1x10^{-5}$ mm.

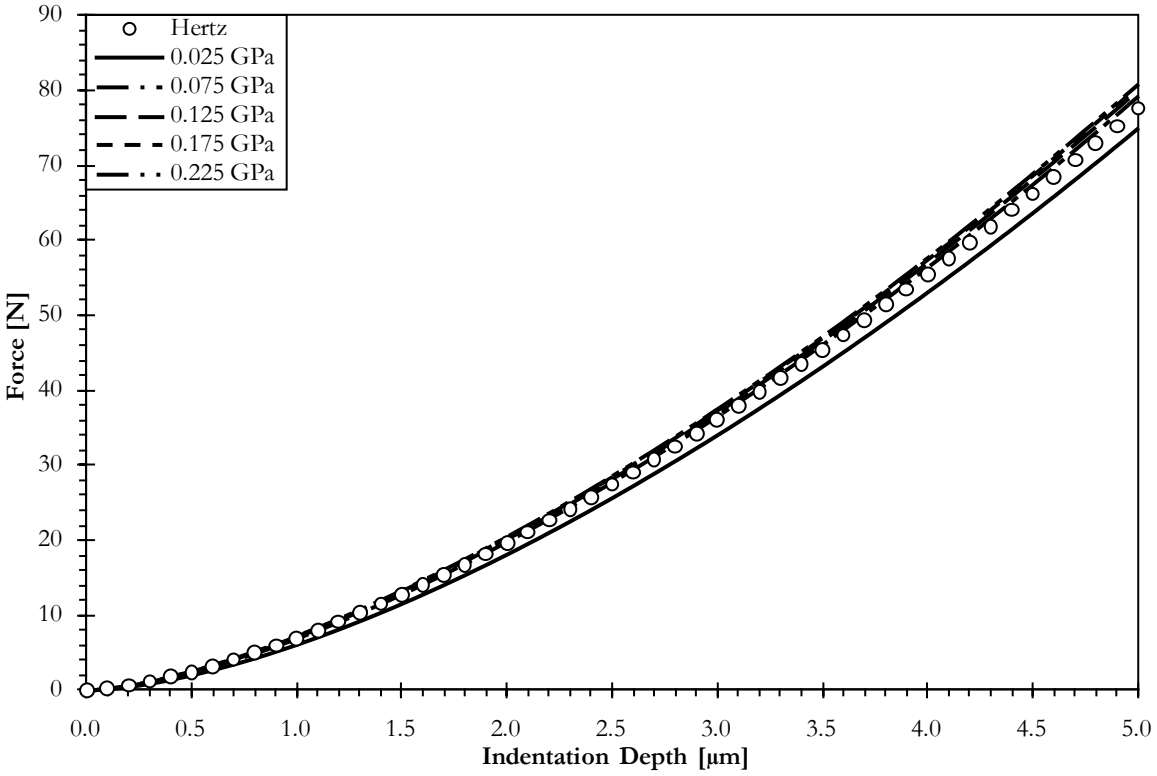

Figure 4.10 - Indentation forces for an allowable penetration of $1x10^{-6}$ mm.

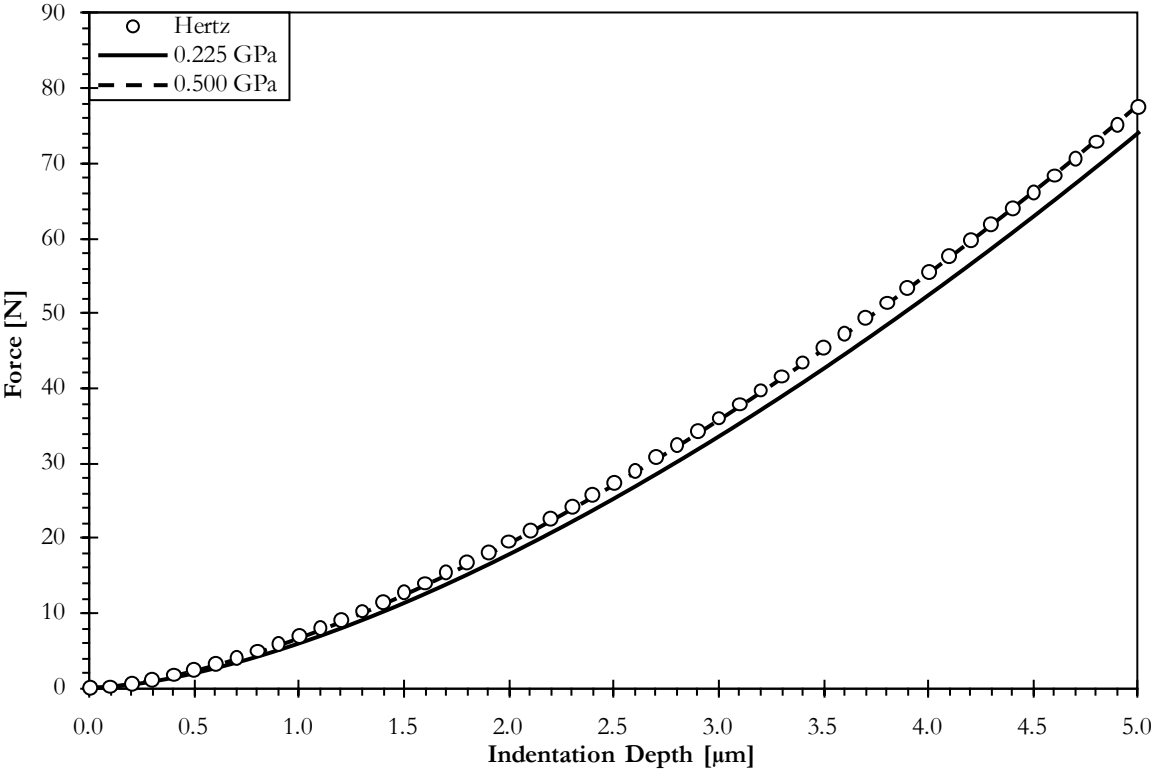

Figure 4.11 - Refined indentation forces for an allowable penetration of $1x10^{-5}$ mm.

Table 4.1 - Solution time [s] for a given contact pressure and maximum allowed penetration.

	Maximum Allowed Penetration [mm]			
Pressure [GPa]	**$1x10^{-6}$**	**$1x10^{-5}$**	**$1x10^{-4}$**	**$1x10^{-3}$**
0.025	1033	1577	932	912
0.075	1574	955	902	943
0.125	2556	954	1253	1237
0.175	3504	941	910	928
0.225	4019	972	914	906
Average [s]	2537	1080	982	985

4.3.3.3 Indenter Roundness and Asphericity

A consequence of the discretized nature of the finite element method was the difficulty associated with accurately representing the round surface of the indenter. The nodes of the finite element mesh were readily placed on the outer surface of the indenter; however, the nodes were connected by straight line segments resulting in slight asphericity when comparing the finite element mesh to the true surface, as depicted in Figure 4.12. This asphericity was exacerbated by the fact that the contact definition is based on the segments of the indenter as opposed to the nodes. The effect of the asphericity was tested by progressively refining the mesh of the indenter from 8 μm to 1 μm and observing the forces, as shown in Figure 4.13. As the figure shows there was no difference in the forces as the indenter mesh was refined. Additionally, Table 4.2 shows that the 4 μm element produced the fastest solution time; therefore, that element size was used for the remainder of this work. Furthermore, it is a well known practice to match the element sizes at the interface of two contacting bodies. The solution times may be longer with the 1 μm and 2 μm element sizes due to the larger number of elements required; however, the rigid material definition of the indenter should minimize this effect. The solution time may be longer with the 8 μm element size due to the difference in size as compared to the 4 μm workpiece elements. Effectively, the larger indenter elements provide a larger area for the workpiece to penetrate; therefore, the coupling definition must work harder to prevent leakage.

Table 4.2 - Solution time for given indenter element size.

Element Size [μm]	Solution Time [s]
1	2938
2	1263
4	903
8	1175

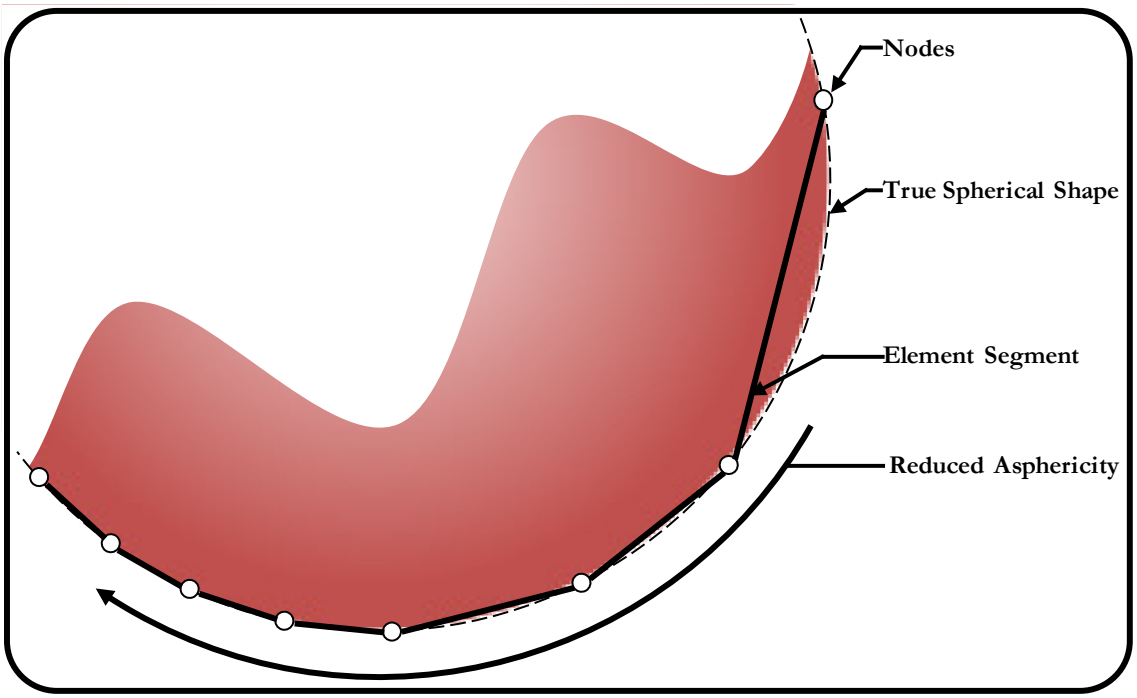

Figure 4.12 - Pictorial representation of asphericity.

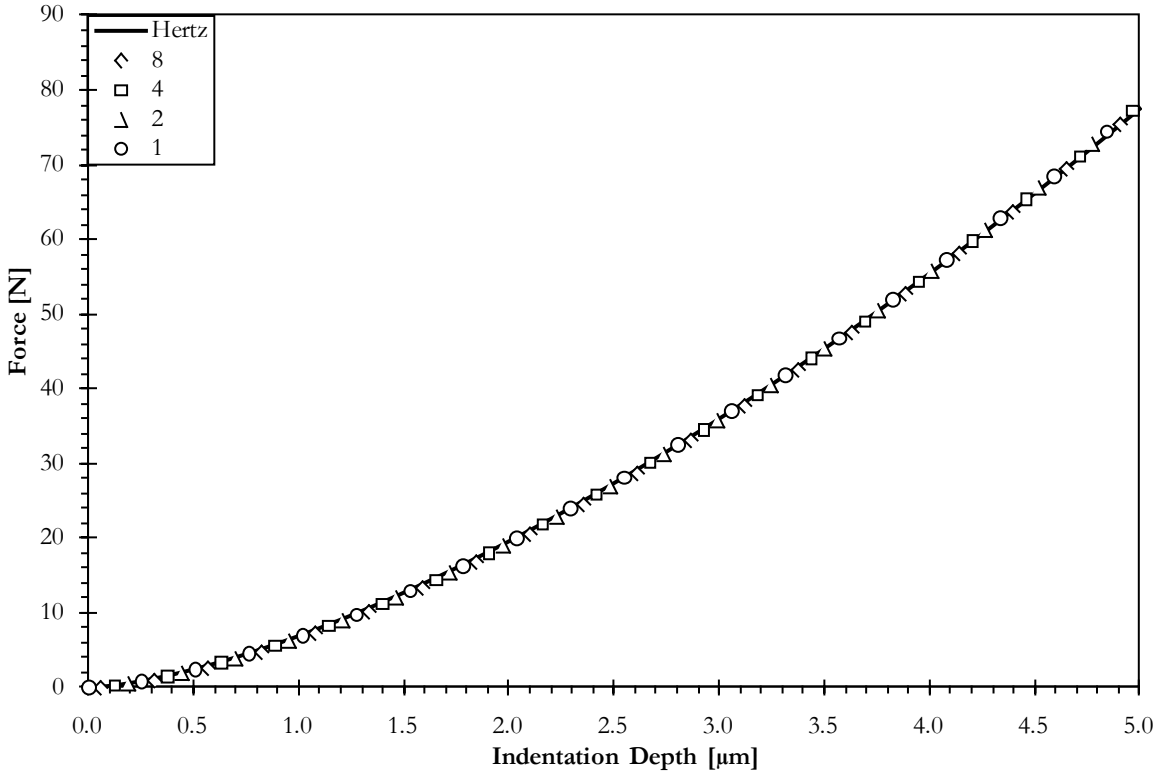

Figure 4.13 - Effect of asphericity on indentation forces.

4.3.3.4 Contact Coupling Points

As discussed in Section 3.4.6 the user can control the density of the contact coupling points that were inserted into the slave structure. It was desirable to choose a sufficient number of these contact coupling points to minimize leakage; however, it was also desirable to use as few as possible to reduce computational time. Figure 4.14 shows the results found from progressively increasing the grid density of the contact coupling points from 1 x 1 to 6 x 6 and, clearly, there was no effect on the indentation forces. A visual inspection of the numerical results indicated that there was no discernable change in the amount of fluid leakage. Table 4.3 shows the increasing solution times as the grid density of the contact coupling points was increased from 1 x 1 to 6 x 6; therefore, only one coupling point was utilized.

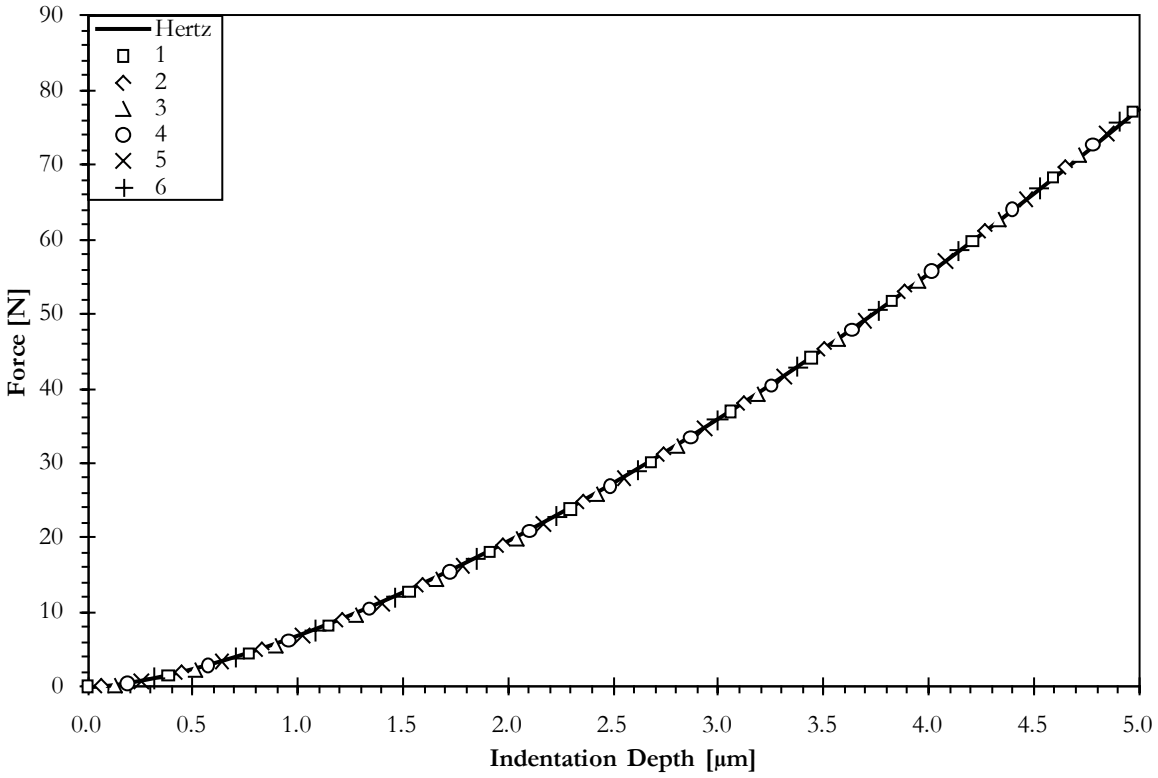

Figure 4.14 - Effect of the number of coupling points on indentation forces.

Table 4.3 - Solution time for given number of coupling points.

Coupling Points	Solution Time [s]
1x1	818
2x2	866
3x3	903
4x4	1032
5x5	1073
6x6	1208

4.3.3.5 Hybrid Euler-Lagrange

The final model refinement that was implemented was to replace the Eulerian elements experiencing low strain with Lagrangian elements to create a hybrid Euler-Lagrange model as discussed in Section 3.3.5. Three models were created for comparison purposes: a purely Eulerian model, a hybrid Euler-Lagrange model with an identical mesh topology to the purely Eulerian model, and a refined hybrid Euler-Lagrange model that utilized Lagrangian transition elements and an elastic material model near the outer periphery of the model. Figure 4.15 shows the purely hybrid Eulerian-Lagrangian mesh, while Figure 4.16 shows the refined hybrid Eulerian-Lagrangian mesh. As can be seen in Figure 4.16, the hybrid mesh allowed Lagrangian transition elements to be used; thus reducing the number of elements required at the periphery of the model. Transition elements are not suitable for purely Eulerian models due to the difficulties associated with the advection algorithms. Figure 4.17 shows that the indentation forces obtained from the three models were identical. Table 4.4 shows the number of elements and solution times for all three models as well as the percent reduction in the number of elements and solution times as compared to the purely Eulerian scenario. As the table shows a large time savings of 48.4% resulted simply by converting elements experiencing low strain to the Lagrangian formulation. It does appear worthwhile to utilize the refined hybrid mesh as it resulted in a 52.8% time savings as a result of the reduction in the number of elements and the implementation of an elastic material model at the outer regions.

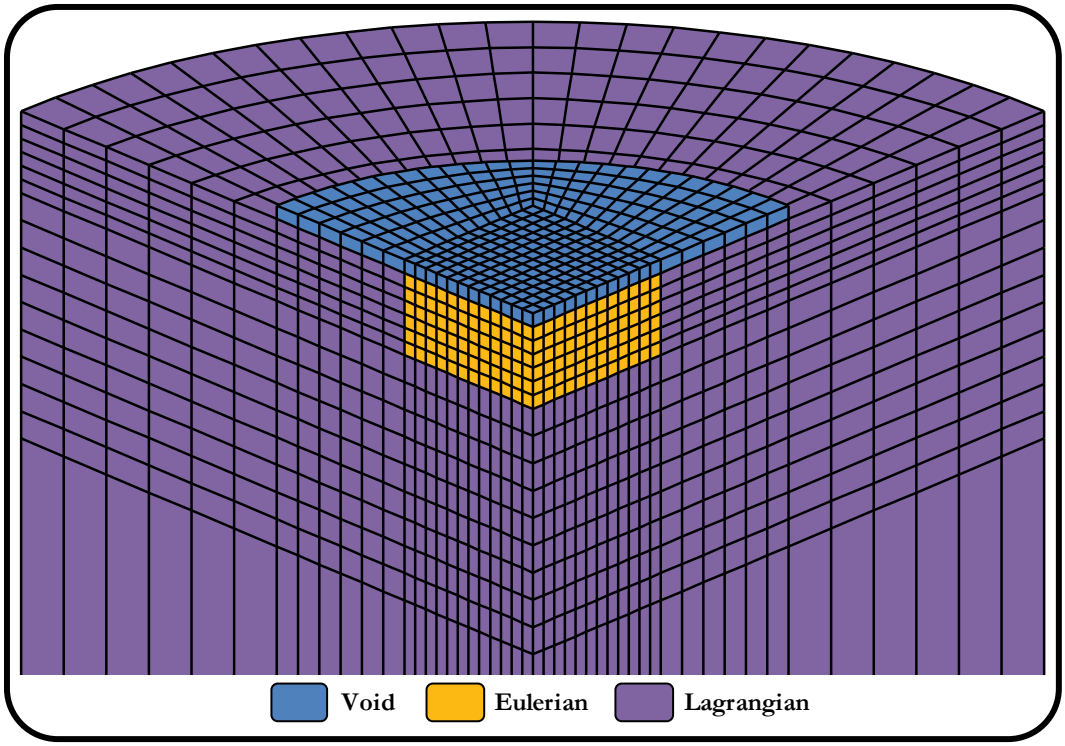

Figure 4.15 - Hybrid Euler-Lagrange mesh topology.

Table 4.4 - Numerical formulation solution time comparison.

Numerical Formulation	# Elements	% Reduction	Solution Time [s]	% Reduction
Euler	215136	0.0	42244	0.0
Hybrid Euler-Lagrange	215136	0.0	21788	48.4
Refined Euler-Lagrange	166752	22.4	19910	52.8

4.3.3.6 High-Performance Computing Cluster

Simulations were performed on a high-performance computational cluster provided by the Atlantic Computational Excellence Network [ACEnet]. This cluster provided the necessary environment to run many models concurrently as well as to distribute each model over several computing cores. Distributing a model over multiple computing cores in a cluster environment is known as Massively Parallel Processing [MPP] and is capable of considerable improvements in solution times. Theoretically, the solution time is halved by doubling the number of computing cores; unfortunately, the actual speed-up tends to be less than theory suggests and depends on: the type of model to be solved, the efficiency of the solver, and the cluster hardware. This solution speed-up is known as the scale factor of the model. For example, if a model solves in 1000 seconds on a single computing core and 125 seconds on

eight computing cores then the scale factor would be eight. Perfect scaling is achieved so long as the solution time is halved as the computing cores are doubled.

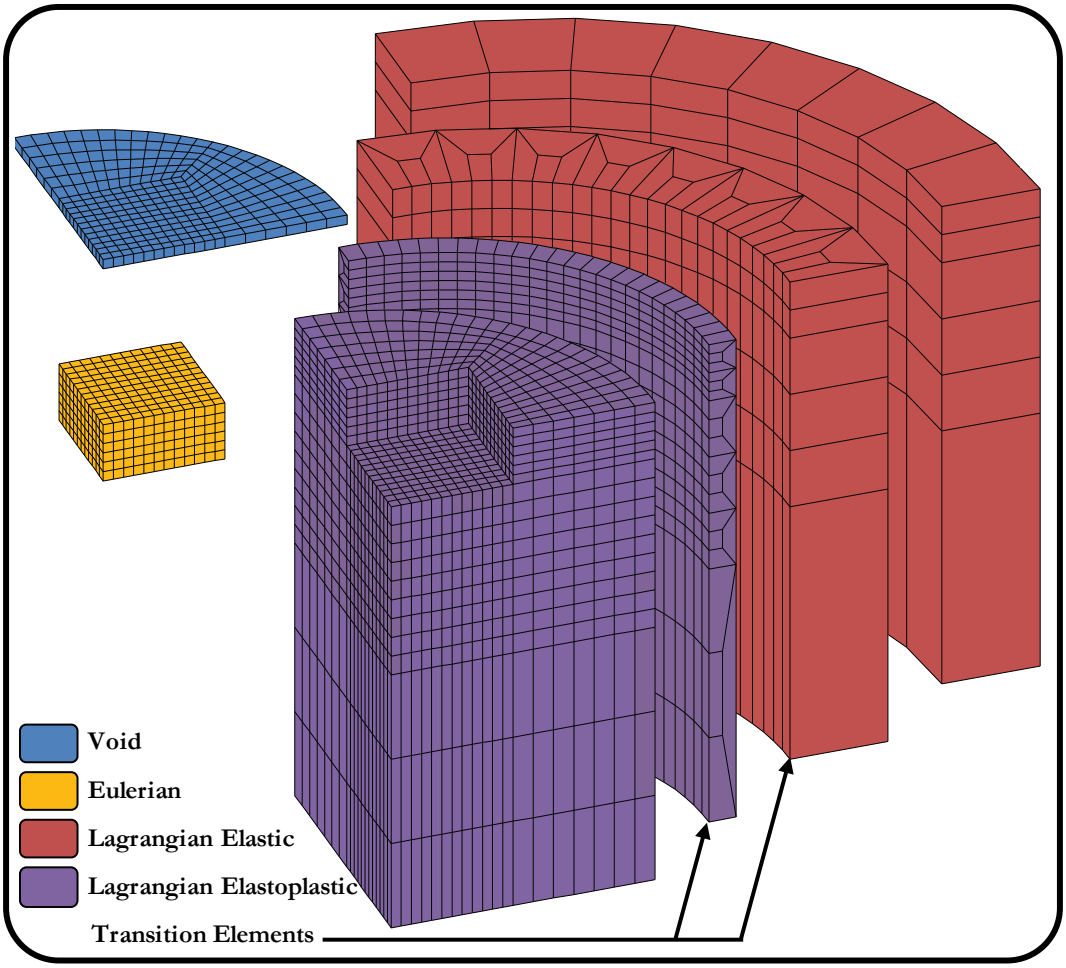

Figure 4.16 - Refined hybrid Euler-Lagrange mesh showing transition elements.

The indentation model was used to determine the optimal number of computing cores for the present work. The model was solved using a progressively increasing number of computing cores from 1 - 16 in even increments while the time required for the solution was recorded. Figure 4.18 shows the decrease in the solution time as more computing cores were employed for the solution and, clearly, there was a rapid decrease in solution time as the number of computing cores was increased until a plateau occurred at 6 computing cores. Also shown in the figure are the theoretical and actual scale factors. In a perfect computing environment the actual scale factor would follow the theoretical scale factor very closely. Again, a plateau of the scale factor occurred when 6 computational cores were employed.

These plateaus indicate two things: either the software is not optimized for MPP and/or the computing hardware is not sufficient. It is well known that LS-DYNA® is highly optimized for MPP environments and is capable of efficiently scaling with many hundreds of computing cores [108,109]; therefore, the likely reason for the plateaus is the computing hardware, specifically the gigabit Ethernet interconnects. It has been shown, for example by Shainer and Kher [108], that using interconnects with higher speeds and lower latencies are required to achieve the full scalability of LS-DYNA®. Based on these results, it was decided that 6 computational cores was ideal, which decreased solution times by a factor of approximately 4.

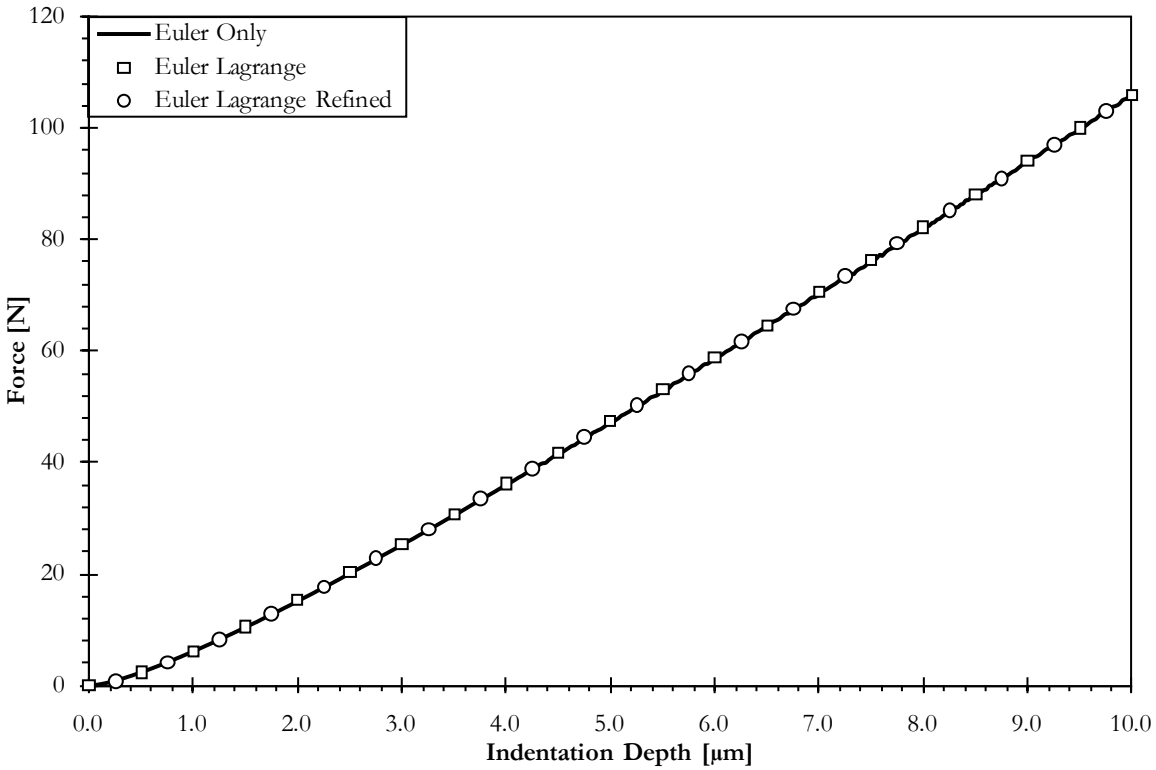

Figure 4.17 - Force comparison of hybrid formulation.

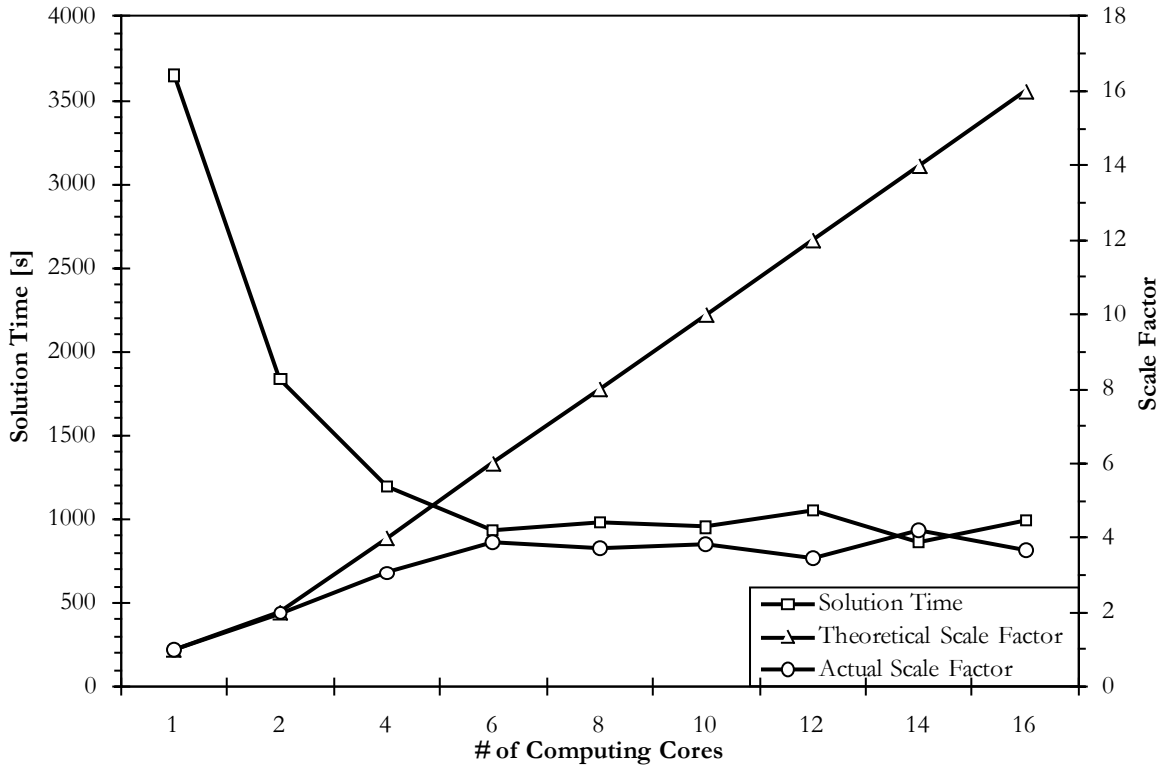

Figure 4.18 - Solution time and scale factor for increasing computing cores.

4.4 Experimental Apparatus

Indentation tests were performed using a precision ground diamond set in a 9.525 mm diameter steel shank. The diamond was ground to a 60° included angle with a 0.508 mm nose radius. The indenter was inserted into a steel fixture and secured with a compression nut, as shown in Figure 4.19. The compression nut was used to lightly compress the indenter into the housing to prevent any unwanted tool motion. The fixture assembly was mounted to the wheel housing of a Blohm Planomat® 408 CNC grinding machine, providing a rigid testbed with sub-micrometer vertical positioning accuracy. 4340 steel specimens were mounted directly to a Kistler® 9257B quartz three-component force dynamometer. The base of the steel specimens were ground prior to mounting ensuring uniform contact between the specimen and the dynamometer. The top surface of the specimens were ground flat and polished prior to the indentation tests creating a flat and smooth test surface.

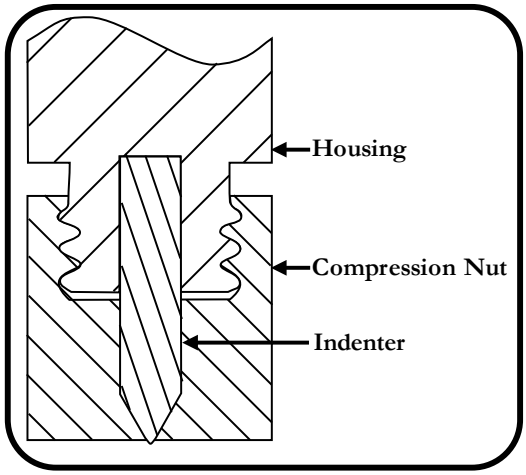

Figure 4.19 - Indentation tool mounting assembly.

The true indentation depth was measured using an optical microscopy system, similar to that used by Doman *et al.* [110], consisting of a QImaging® QICAM 10-bit digital camera with a microscope attachment, pictured in Figure 4.20. The camera was focused on a micro-electrical mechanical system [MEMS] chip mounted on the fixture assembly. The optical system resulted in a pixel size of approximately 0.4 μm. The MEMS chip was chosen as the target due to its small size and accurate dimensions. The feature of interest on the chip was a round device with a smooth outer diameter of 280 μm and its center position was tracked using a sophisticated edge detection algorithm available in National Instruments' LabVIEW® software package [111]. The edge detection algorithm operated by detecting a sharp change in grey scale value along a search ray, as shown in Figure 4.21. A circle, and its center position, was then fitted to the pixels corresponding to the outer periphery of the MEMS feature. Sub-pixel accuracies were achievable as the algorithm interpolates between pixels to determine the center position of the circle.

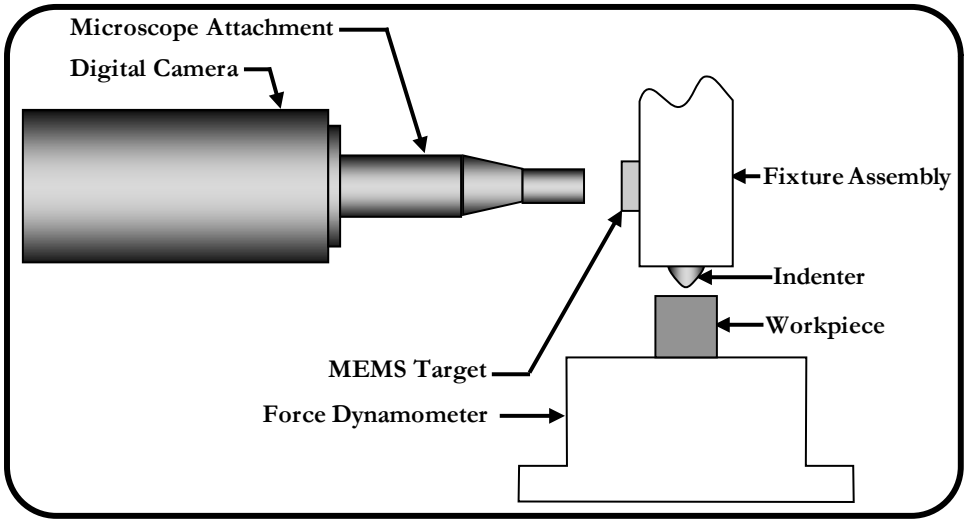

Figure 4.20 - Indentation experimental apparatus.

The system accuracy was determined using a no load displacement test in which the commanded depth was compared to the measured depth. Figure 4.22 shows this comparison as well as the best linear fit to the data and the 95% error envelope of 0.848 μm. This error accounted for the entire system including the positioning accuracy and the interpolation algorithm.

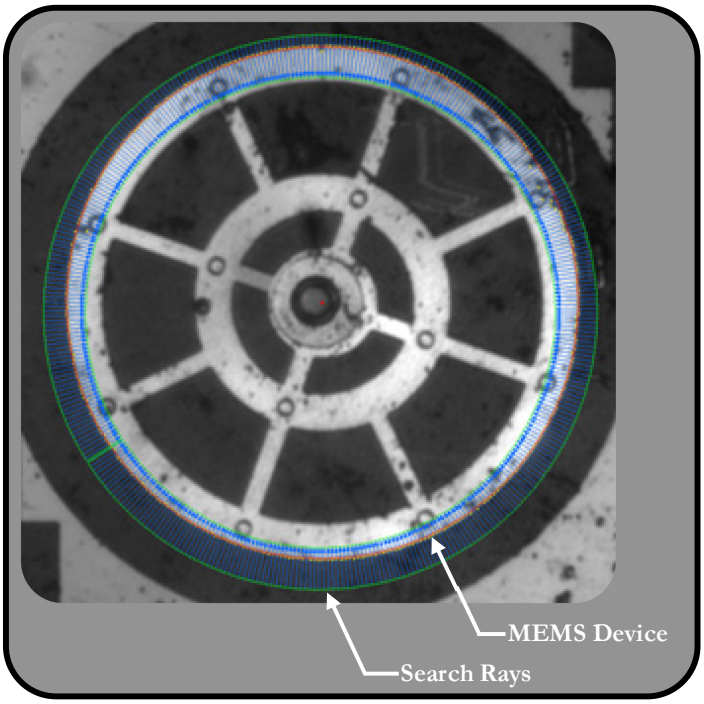

Figure 4.21 - MEMS device and search rays.

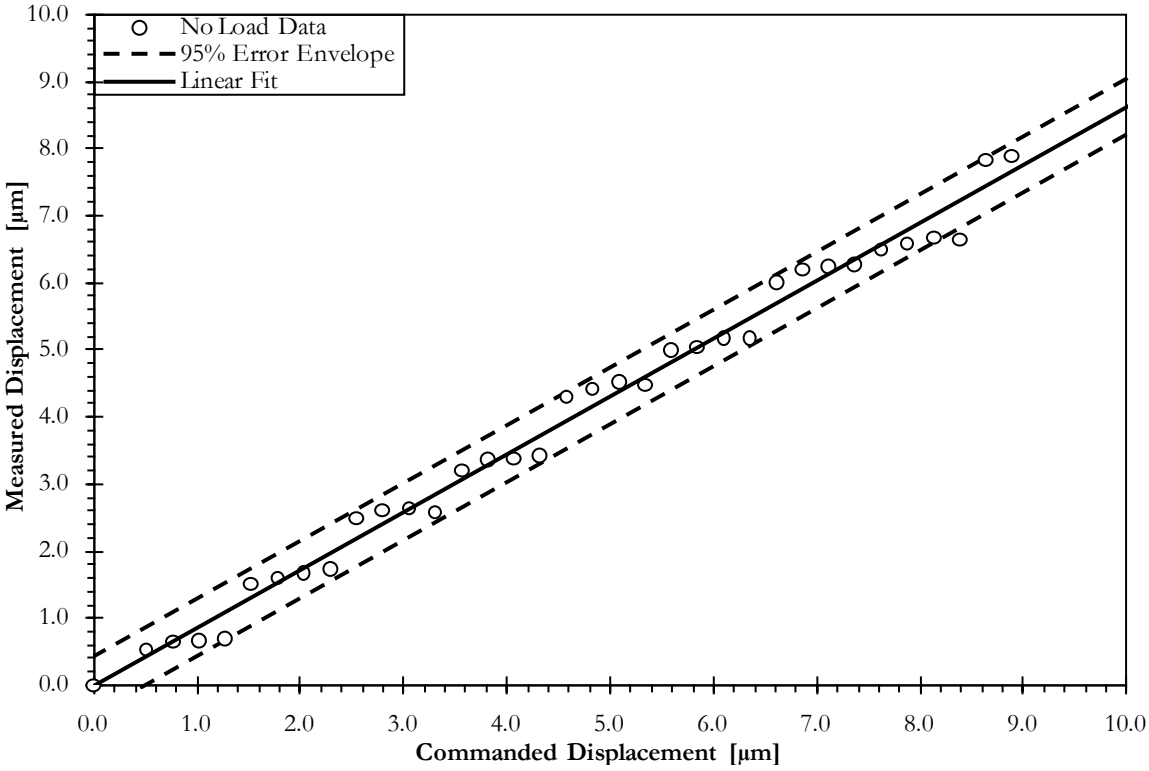

Figure 4.22 - No load indentation position accuracy.

4.5 Indentation Results

Figure 4.23 shows the comparison between the experimentally, analytically, and numerically determined indentation forces. From the figure it can be seen that the calibrated finite element model was highly accurate, with an average error of 7.2%, when compared to the experimental data; thus indicating that the chosen numerical parameters were correctly optimized. The figure also shows the overestimation of the indentation forces when using the elastic, Hertzian, model especially as larger indentation depths. The analytical elastoplastic model underestimated the indentation forces at larger indentation depths. The fully plastic analytical model overestimated the forces at low indentation depths; however, it behaved well at larger indentation depths. By comparing the responses of the three analytical models it became clear that this system was dominated by fully plastic material behavior with small amounts of elastic and elastoplastic behavior at small indentation depths.

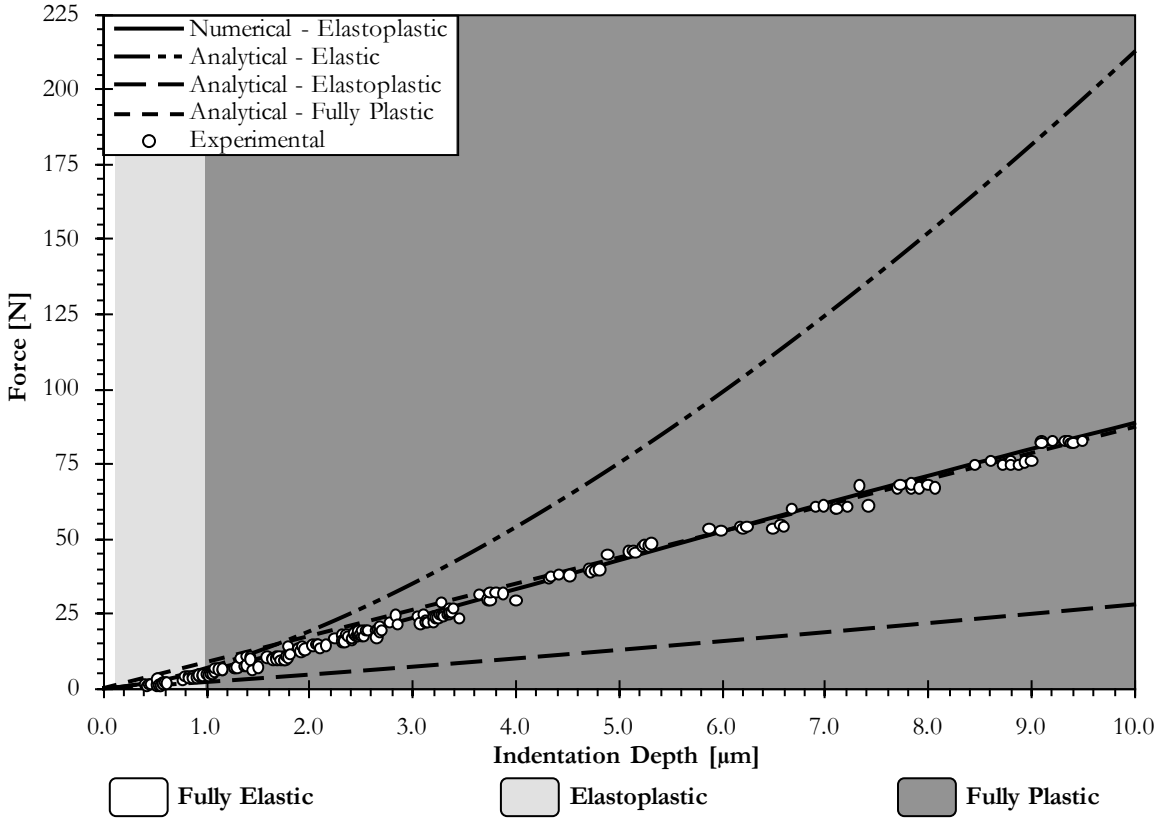

Figure 4.23 - Comparison of experimental, analytical, and numerical model predicted forces.

Figure 4.24 shows the progression of the yield surface as the indentation depth increased. From the figure it can be seen that the elastic regime occurred over small indentation depths of approximately 0.1 μm - 0.15 μm, the elastoplastic regime occurred from approximately 0.15 μm - 1.0 μm, and the fully plastic regime occurred from 1.0 μm onwards. These results correspond well with the those illustrated in Figure 4.23 and also aid in explaining the individual behavior of the analytical models.

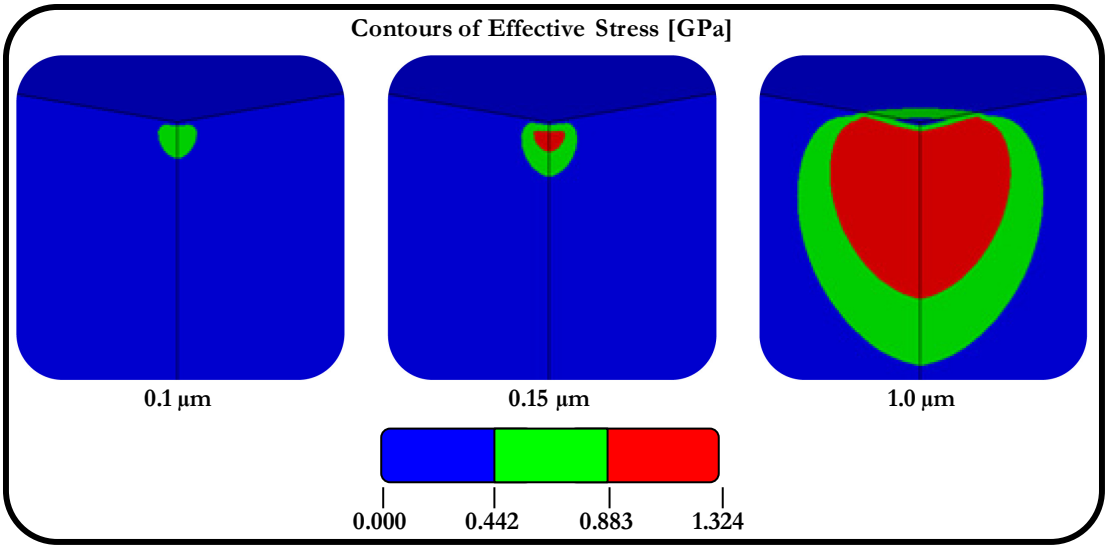

Figure 4.24 - Progression of yield surface.

It is not readily apparent from Figure 4.24 that the yielded material erupted to the surface of the workpiece and was a consequence of the mixture theory as discussed previously in Section 3.4.5. Stress averaging occurred at the boundary of the workpiece material and the void material since the two materials had vastly different material strengths; otherwise, the yielded region, shown as red in the figure, would be visible on the top surface of the workpiece as opposed to the green region. Knowing that the void material had a negligible strength when compared to the steel workpiece it was simply a matter of determining when the average stress level reached the surface, and was found to be 0.662 GPa for this scenario. Figure 4.25 shows the indenter, in grey, penetrating into the workpiece material, outlined in white. The stresses in the workpiece are represented by the line contours. The figure shows that the required average stress has reached the top surface of the workpiece at a depth of 1 µm, where the top surface of the workpiece is in contact with the outer surface of the indenter.

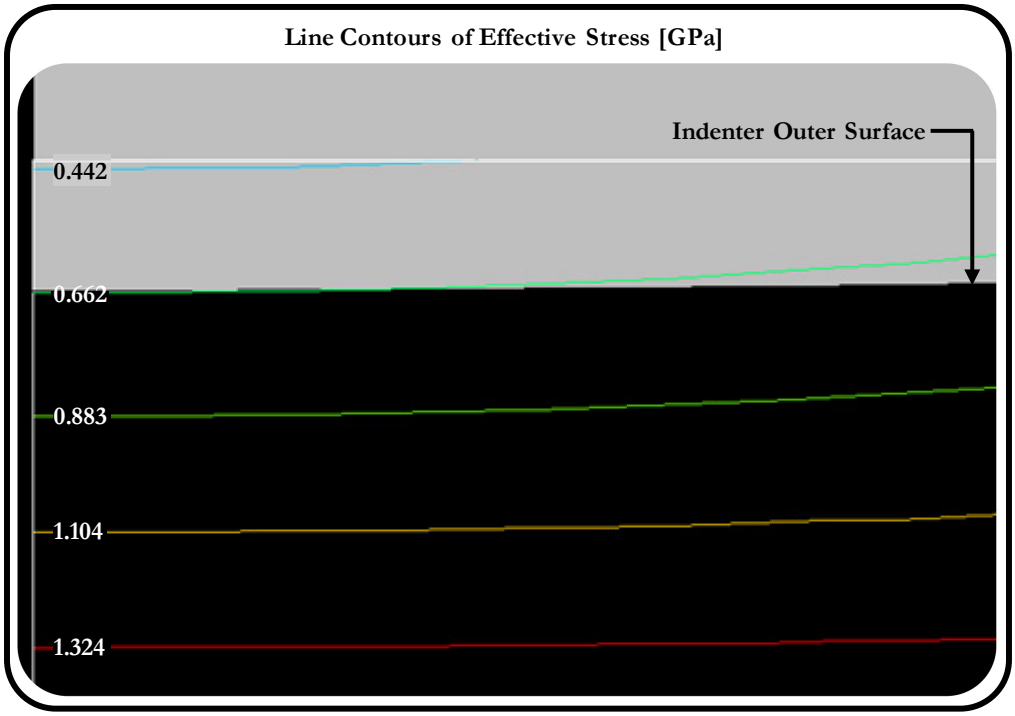

Figure 4.25 - Average yield stress occurring at indenter-workpiece boundary.

4.6 Summary

This chapter briefly outlined the theory of indentation testing and introduced an experimentally-verified finite element indentation model. Indentation testing was an ideal method to study the effects of several key numerical parameters because the complexities associated with friction and relative motion were removed. The testing revealed the correct parameters required to produce an accurate model. The parameters found from this study will be carried over to the scratching model to be discussed in a later chapter. Three key time saving strategies were also verified; namely, the use of a rigid tool material, the use of a refined hybrid Euler-Lagrange finite element formulation, and the use of a cluster computing environment. The finite element indentation model also revealed that, with the current indenter geometry, purely elastic deformation occurred at small indentation depths up to approximately 0.1 μm - 0.15 μm, elastoplastic deformation occurred from indentation depths of approximately 0.15 μm - 1.0 μm, and fully plastic deformation occurred from indentation depths of approximately 1.0 μm onwards.

Chapter 5 High-Speed Scratch Testing Method

Scratch testing can be used to study the mechanics of individual cutting edges on a grinding wheel. The present chapter will provide a brief background and review of current scratch testing methodologies and will introduce the experimental apparatus and data analysis post-processing techniques that were developed for this work. The scratch testing results will be presented in Chapter 6 and Chapter 7.

5.1 Background

Scratch testing is a common material characterization test where a stylus is dragged across a test surface under a known load at constant speed. These tests are used to determine: coefficients of friction between two materials, the toughness of materials and coated surfaces, and the load required to separate a coating from its base material. The test speeds are typically low, on the order of 0.1 m/s, and occur over relatively short distances of approximately 5 mm - 10 mm. Scratch testing can typically be grouped into two categories based on the stylus: sharp and blunt. A sharp stylus is commonly used for thin coatings and

microindentation depths, whereas a blunt stylus is more commonly used for sliding studies. A full review of scratch testing literature was beyond the scope of this work; therefore, only a few select publications will be discussed in this chapter. An excellent bibliographic resource of scratch testing as it relates to coated surfaces was created by Mackerle [112], while Li and Beres [113] created a thorough theoretical review of scratch testing for coated surfaces.

Scratch testing was used in the present work to provide a quantitative validation by directly comparing the experimental and numerical scratch forces and depths. It was felt that this was a superior validation method when compared to the more qualitative method of deformed chip shape comparison. Additionally, scratch testing was an effective method to simulate single abrasive-grain cutting provided that the cutting speeds were sufficiently high. The combination of extensive experimental testing and a validated finite element model will provide key insights into the scratching process that neither method could provide on its own.

5.2 Experimental Apparatus

For this work it was desirable to achieve high scratching speeds v_w to replicate the conditions that a grain would be subjected to during grinding, typically on the order of 10 m/s to 50 m/s. Wang *et al.* [114] used a system where a stylus was mounted to the end of a pendulum to achieve speeds in the vicinity of 1 m/s - 4 m/s. The difficulty with this system was that the scratch depth varied greatly as a function of the pendulum motion and created relatively short scratches on the order of 3 mm, depending on the depth of cut. Cai *et al.* [115] used a system where small workpiece samples were attached to the outer periphery of a spinning disk. A stylus was fed laterally into the samples to create the scratches. This system was able to achieve speeds up to 120 m/s; however, the test speeds were 0.028 m/s, 67 m/s, 90 m/s, and 120 m/s, all of which fall outside what can be considered normal grinding conditions. The major difficulty with both systems was that force dynamometers with natural frequencies ranging from 30 kHz - 200 kHz were required to capture the high-speed events over the short scratching distances. Scratches would need to occur over longer distances to bypass the need for high natural frequency force dynamometers; thus, a system

combining the rotary speeds from the work of Cai *et al.* [115] with the stationary workpiece from the work of Wang *et al.* [114] was created.

The developed system was based on a Blohm Planomat® CNC grinding machine, which provided a rigid test bed with sub-micrometer positioning resolution. Forces were measured using a Kistler® 9275B three-component quartz force dynamometer and a 5019B charge amplifier. The sensitivities and measurement ranges of the force dynamometer are shown in Table 5.1 according to the coordinate axes adopted for this work. The forces that were measured by the dynamometer were those in the global horizontal F_H and global vertical F_V directions. To convert these forces to the desired tangential F_{Tan} and normal F_{Norm} forces required the following transformation [116]:

$$F_{Tan} = F_V \sin\chi + F_H \cos\chi \tag{5.1}$$

$$F_{Norm} = F_V \cos\chi - F_H \sin\chi \tag{5.2}$$

where χ is the angle formed between the arc's centerline and the point of interest, as shown in Figure 5.1.

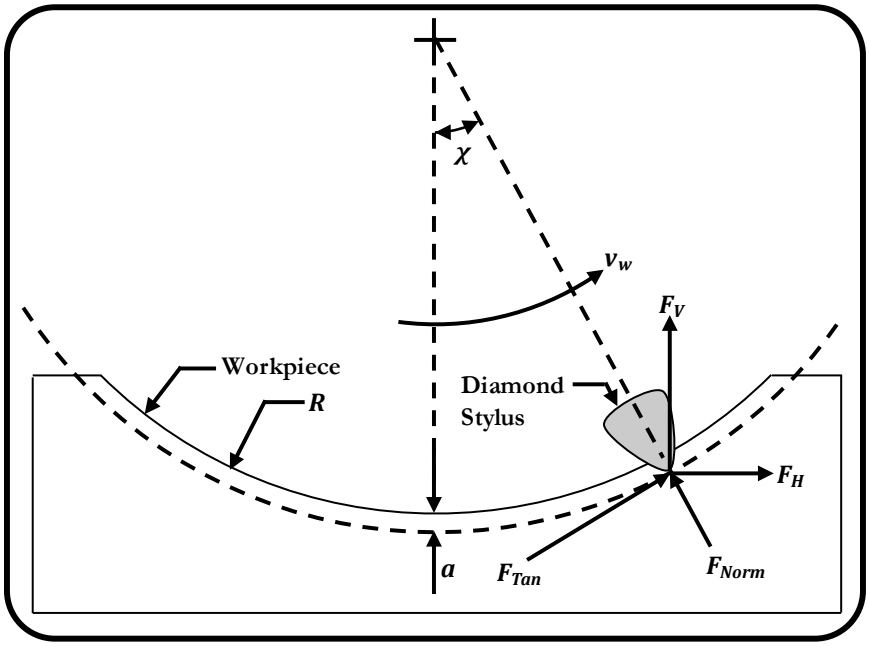

Figure 5.1 - Schematic of scratching process.

Table 5.1 - Force dynamometer specifications.

	F_X	F_Y	F_Z
Sensitivity [pC/N]	-7.5	3.7	-7.5
Measurement Range [kN]	±5	±5	±5

5.2.1 Scratching Stylus

Two custom diamond scratching styli were used for the experimental validation portion of this work: a round-nosed stylus to approximate an abrasive grain, and a flat-nosed stylus to approximate an abrasive grain with a wear flat as shown in Figure 5.2. The round-nosed stylus consisted of a cone shaped tool with a 60° included angle and a nose radius of 0.508 mm. The flat-nosed stylus consisted of a cone shaped tool with a 30° included angle with a flat spot ground on the end with a radius of 0.162 mm. Based on Equation (2.1) the round-nosed stylus is approximately equivalent to a 15-grit abrasive grain, which is considered to be a large grain but is still within the realm of common abrasive grain sizes. A stylus with a smaller nose radius would have required prohibitively expensive manufacturing methods. The geometry of the flat-nosed stylus corresponds to a minimum of a 46-grit abrasive grain, assuming that the area is calculated at the central plane of a spherical representation of the grain. The area of the flat nose is roughly equivalent to the wear flat areas found by Lachance [5] for 46-grit grains. The results for the round-nosed stylus will be presented in Chapter 6 while the results for the flat-nosed stylus will be presented in Chapter 7.

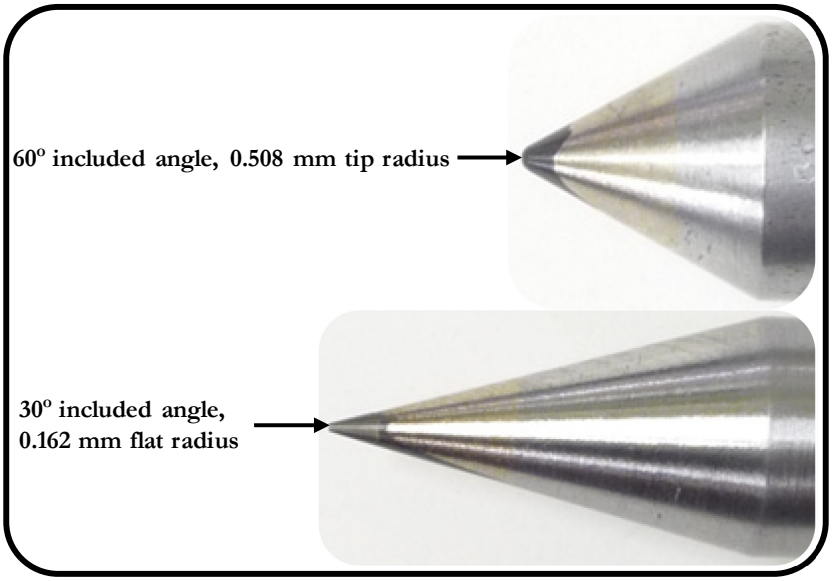

Figure 5.2 - Custom diamond styli.

5.2.2 Wheel Housing

The custom diamond styli were mounted in a statically-balanced steel wheel as shown in Figure 5.3. This wheel was mounted in-place of a standard grinding wheel. The diamond styli were mounted at the periphery of the wheel creating an effective diameter of 364 mm. The spindle rotating speed was adjusted to provide scratching speeds v_w from 5 m/s - 30 m/s in 5 m/s increments. The wheel-stylus assembly was fed transversely in the Z direction to create 29 individual scratches. The transverse feed was chosen such that the distance between scratches was sufficiently large to prevent the effects of one scratch affecting the other.

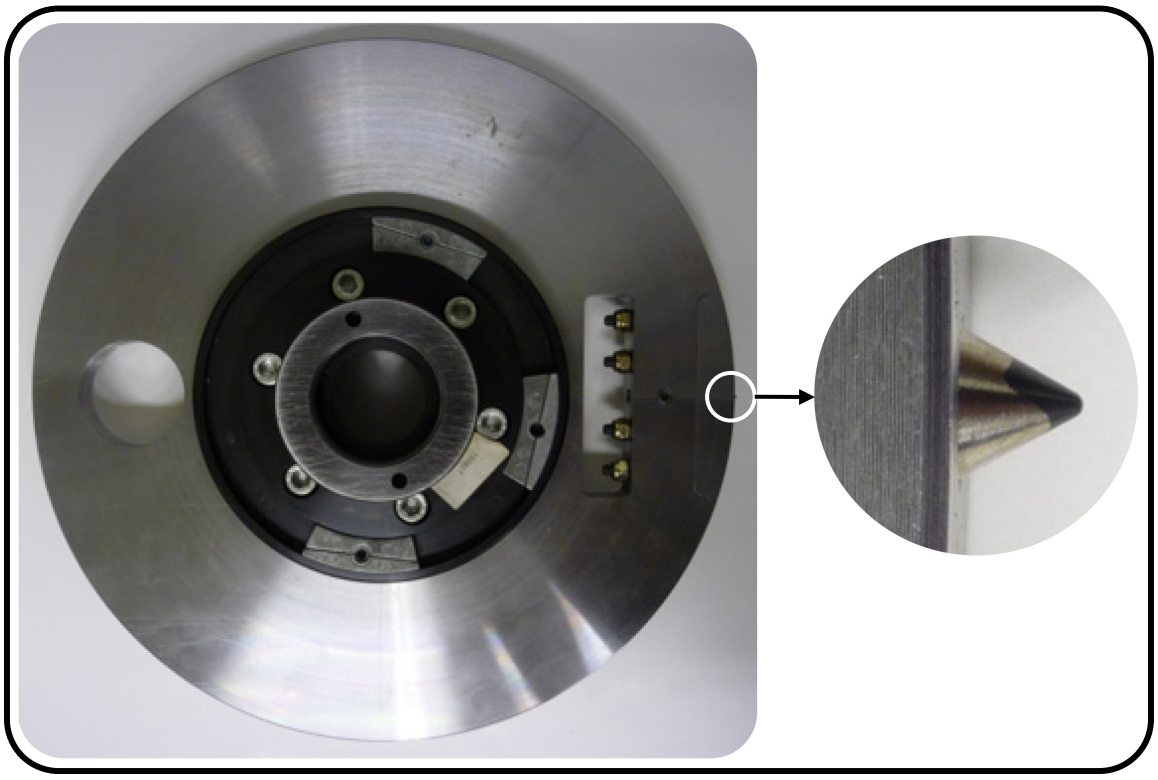

Figure 5.3 - Manufactured wheel used for scratch tests.

5.2.3 Workpieces

Custom ground AISI 4340 steel workpieces, depicted in Figure 5.4, were created in order to achieve long scratches and circumvent the need for a high natural frequency force dynamometer. The workpieces were CNC ground with a 182 mm radius R circular arc, matching that of the wheel-stylus assembly. The circular arc allowed for long scratches on

the order of 100 mm to be created. Additionally, the workpieces were tapered by approximately 0.28° in the transverse, Z, direction to create an increasing depth of cut a, as shown in Figure 5.5. In this manner scratch depths in the range of 0.3 μm to 7.5 μm could be created on a single workpiece. The base of the workpieces were ground flat to ensure full contact with the force dynamometer and the test surface was polished prior to scratching to remove any residual marks due to the grinding operation. Despite the efforts taken to smooth the test surface of the workpiece it was not possible to create a perfect surface. The measured surface roughness was found to be 0.20 μm on average with an average peak-to-valley height of 2 μm. This unavoidable surface roughness and peak-to-valley height resulted in some uncertainty at shallow depths of cut. The workpieces were removed after each scratching experiment to allow for direct measurement of the scratch profiles using an optical profilometer.

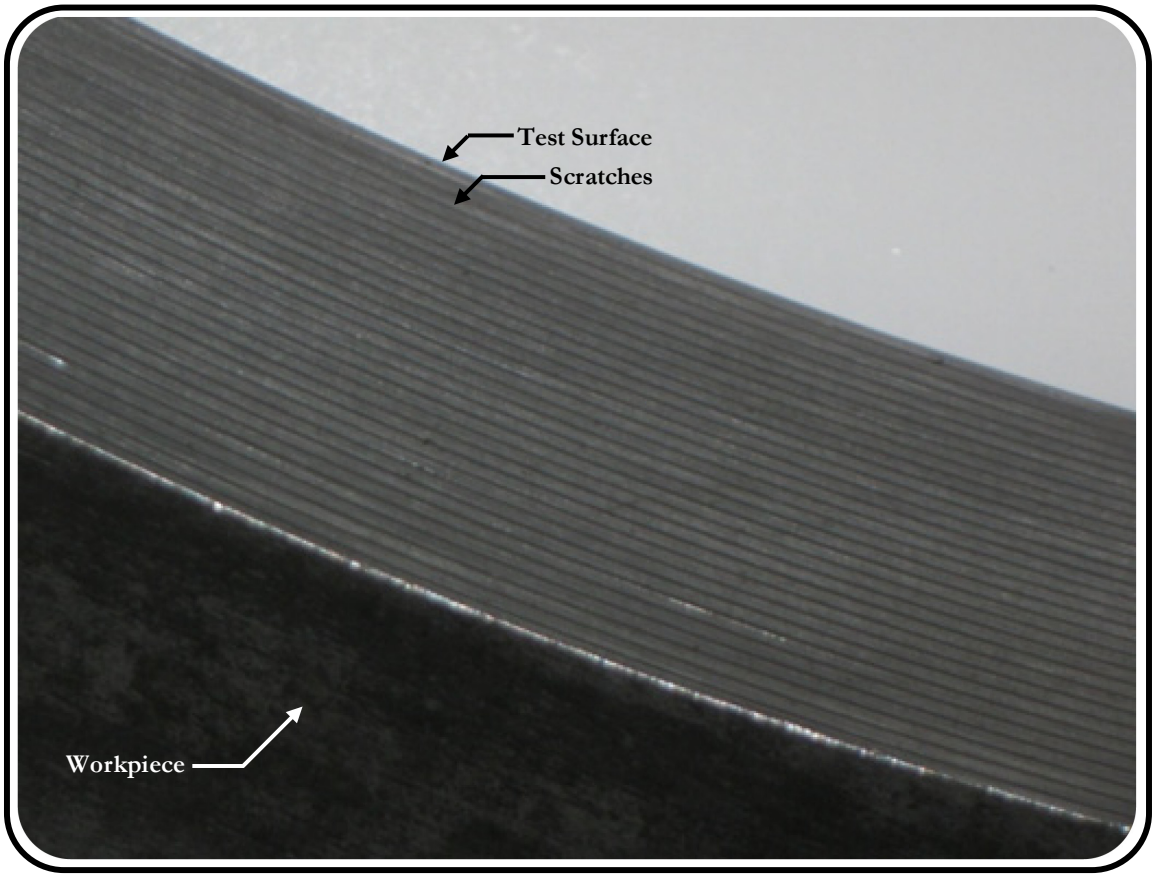

Figure 5.4 - Section of workpiece with scratches.

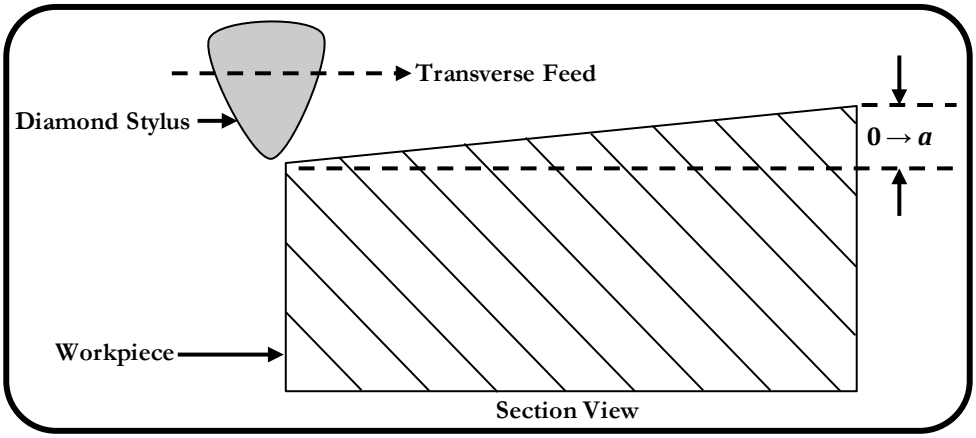

Figure 5.5 - Cross section of arced workpiece.

5.3 Scratch Profile Measurements

The scratch profiles were measured with a Micro Photonics Incorporated Nanovea® PS50 optical profilometer with a resolution of 5 nm. This profilometer operates using axial chromatism of white light. The white light source passes through an objective lens with a high degree of chromatic aberration effectively splitting the white light into its various wavelengths. These wavelengths focus at different distances from the lens and, therefore, different heights on a surface. By employing a spatial filter to the reflected light only the wavelength that is in focus is detected, thus providing a single height point on the surface. This process is repeated over a measurement area to re-create the surface. Scratch depths and pile-up heights were obtained by extracting profiles at regular intervals. This measurement system provided the unique ability to track scratch development as the depth of cut increased. An example of a scanned surface is shown in Figure 5.6 and clearly shows the resultant scratches, the piled-up material at the edges of the scratches, and the undisturbed surface, where the heights have been scaled five times their actual height for improved visibility. The surface roughness as a result of the grinding operation is also visible in the undisturbed surface as slight colour variations and ridges that run parallel to the scratches. The undisturbed surface indicates that there was not any interaction between the scratches. Scratch depths were obtained by extracting profiles from the surface at regular intervals; a portion of such a profile is displayed in Figure 5.7. As can be seen in the figure, the scratch depth a was obtained from the bottom of the scratch to the median location of

the noise envelope, where the noise envelope was the surface roughness of the workpiece following the arc grinding operation.

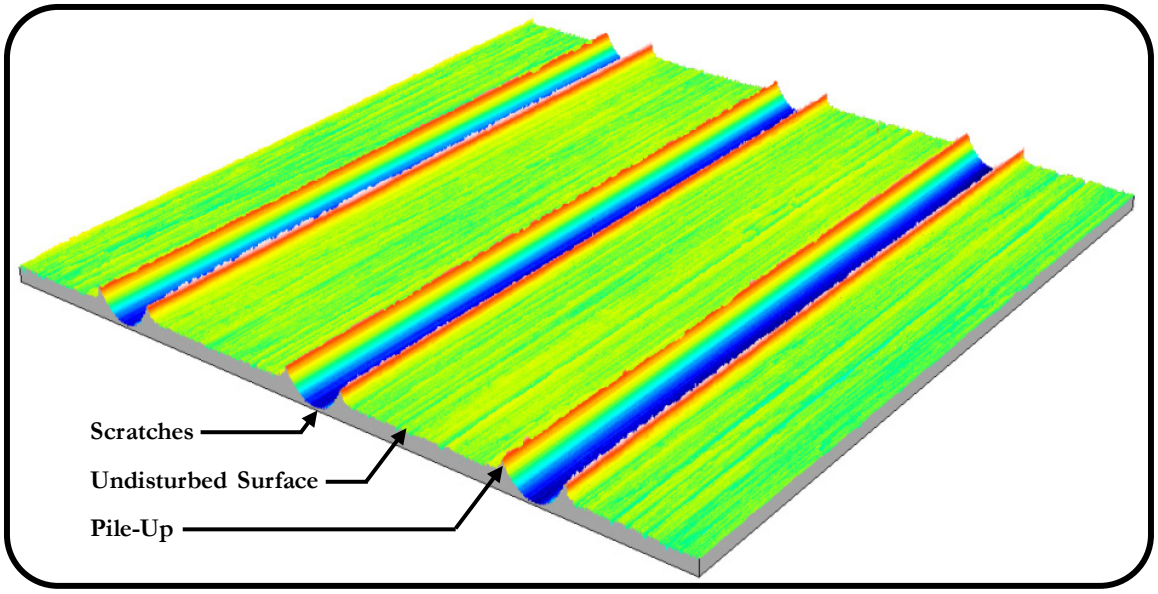

Figure 5.6 - Representative three-dimensional scan workpiece surface.

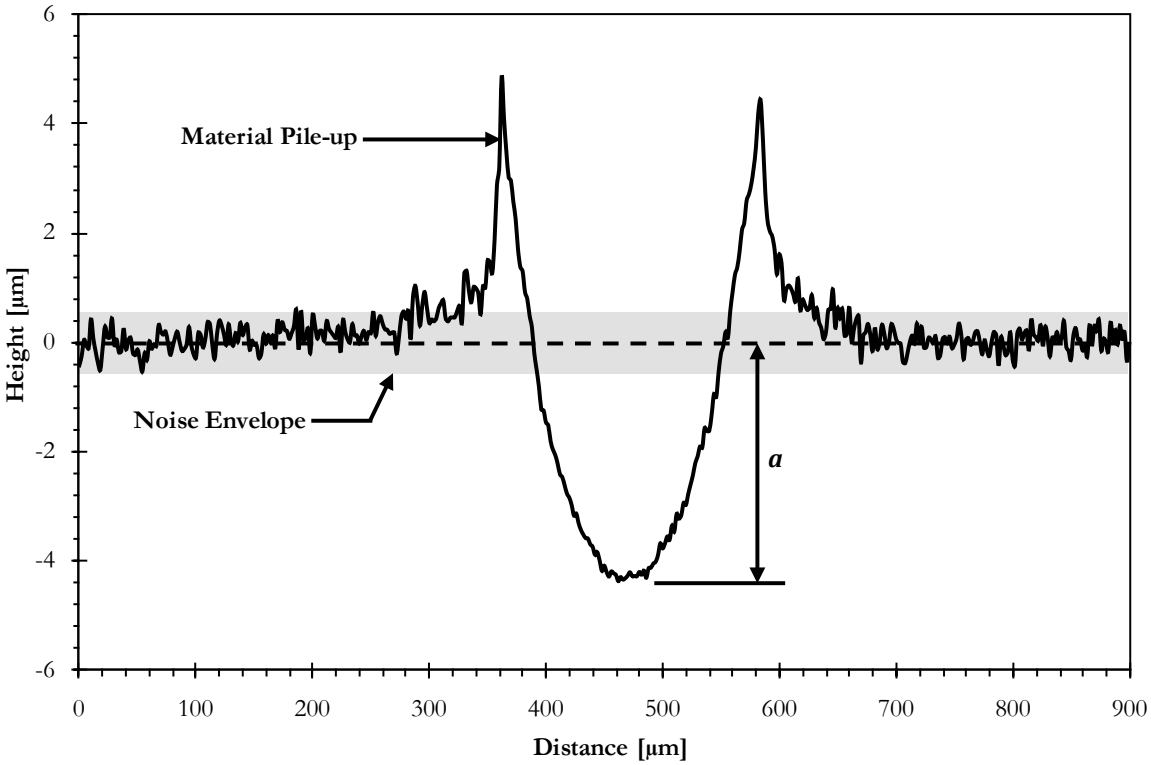

Figure 5.7 - Representative extracted profile for scratch depth measurement.

5.4 Force Data Post-Processing

One of the issues associated with high-speed scratching is the noise introduced into the force data, as shown in Figure 5.8 for a 30 m/s scratching speed, which was the worst case scenario. As can be seen in the figure there are substantial variations in the recorded forces and there are two primary regions of interest in the signal designated as "Scratching" and "Free Vibration". The scratching section occurred when the tool was engaged with the workpiece while the free vibration section occurred once the tool disengaged from the workpiece. It should be noted that the remainder of the free vibration in Figure 5.8 has been truncated to preserve the clarity of the figure.

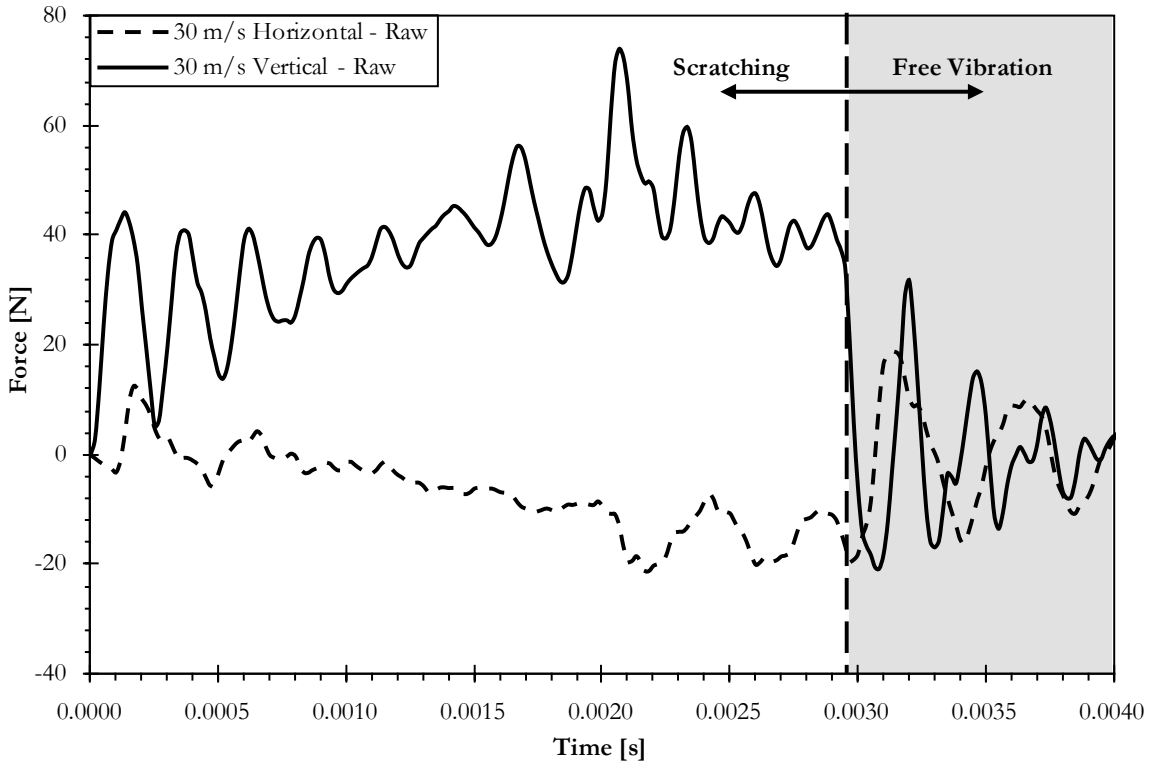

Figure 5.8 - Representative raw force curves for 30 m/s scratching speed.

By analyzing the magnitude of the power spectrum density of the various frequencies in the force signal it was possible to determine the frequencies that were being excited as well as the relative magnitudes of the excitement. Figure 5.9 shows the response in the horizontal direction for scratching speeds of 5 m/s and 30 m/s during the scratching process. As can be seen in the figure, the magnitude of the vibration increased as the scratching speed

increased and that a resonant peak was occurring at approximately 2.2 kHz. Figure 5.10 shows the response in the vertical direction for scratching speeds of 5 m/s and 30 m/s during the scratching process. As can be seen in the figure, the magnitude of the vibration increased as the scratching speed increased and that a resonant peak was occurring at approximately 4.0 kHz. Comparing Figure 5.9 and Figure 5.10 shows that the magnitude of the vibration was approximately 8.5 times stronger in the vertical direction as compared to the horizontal direction which was likely due to the larger vertical force as compared to the horizontal force.

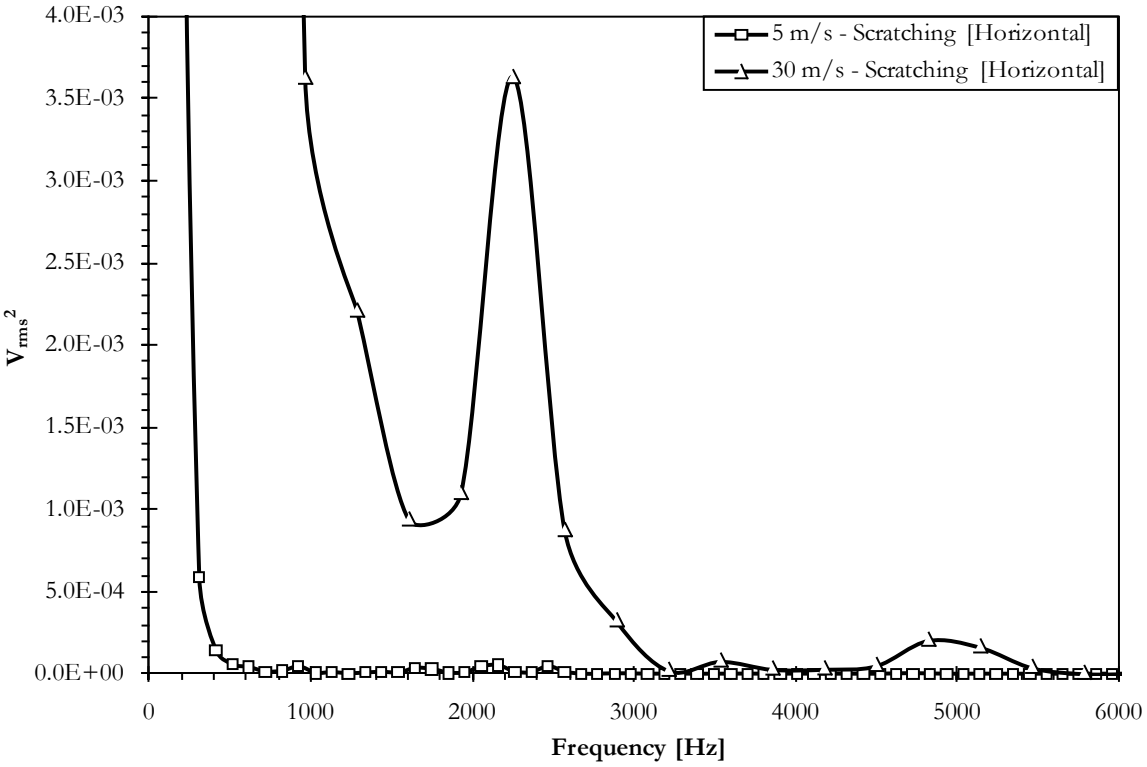

Figure 5.9 - Magnitude power spectrum density in the horizontal direction for scratching speeds of 5 and 30 m/s during scratching.

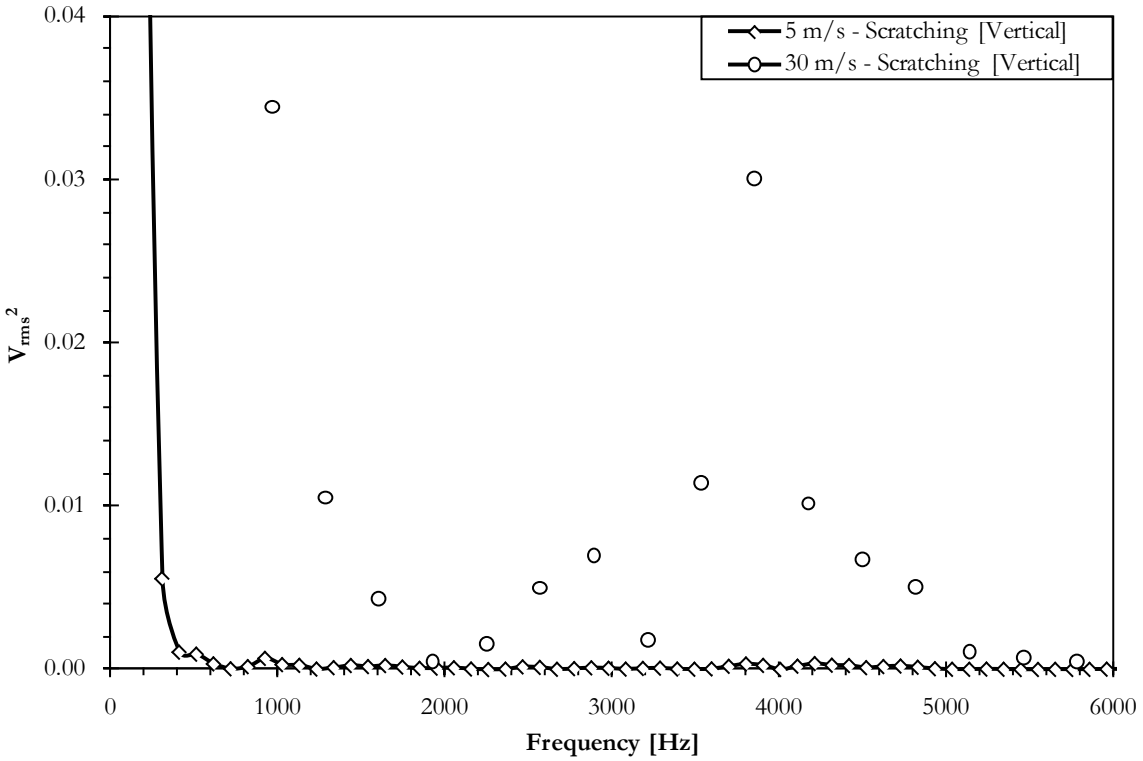

Figure 5.10 - Magnitude power spectrum density in the vertical direction for scratching speeds of 5 and 30 m/s during scratching.

A classical damped oscillation occurred in the system once the tool disengaged from the workpiece as shown by the "Free Vibration" section of Figure 5.8. The magnitude power spectrum density for scratching speeds of 5 m/s and 30 m/s after a scratch had been produced can be seen in Figure 5.11, which shows that the dynamometer was freely oscillating in the horizontal direction at approximately 2.2 kHz. Similarly, Figure 5.12 shows the magnitude power spectrum density in the vertical direction for scratching speeds of 5 m/s and 30 m/s after a scratch had been produced a peak at approximately 4 kHz. As was the case for the scratching signal, the magnitude of the vibration increased as the scratching speed increased. Although the events that occurred after the tool disengaged from the workpiece were not of interest to this work, it was essential that the free vibrations be damped out before the next scratch occurred. Careful inspection revealed this to be the case.

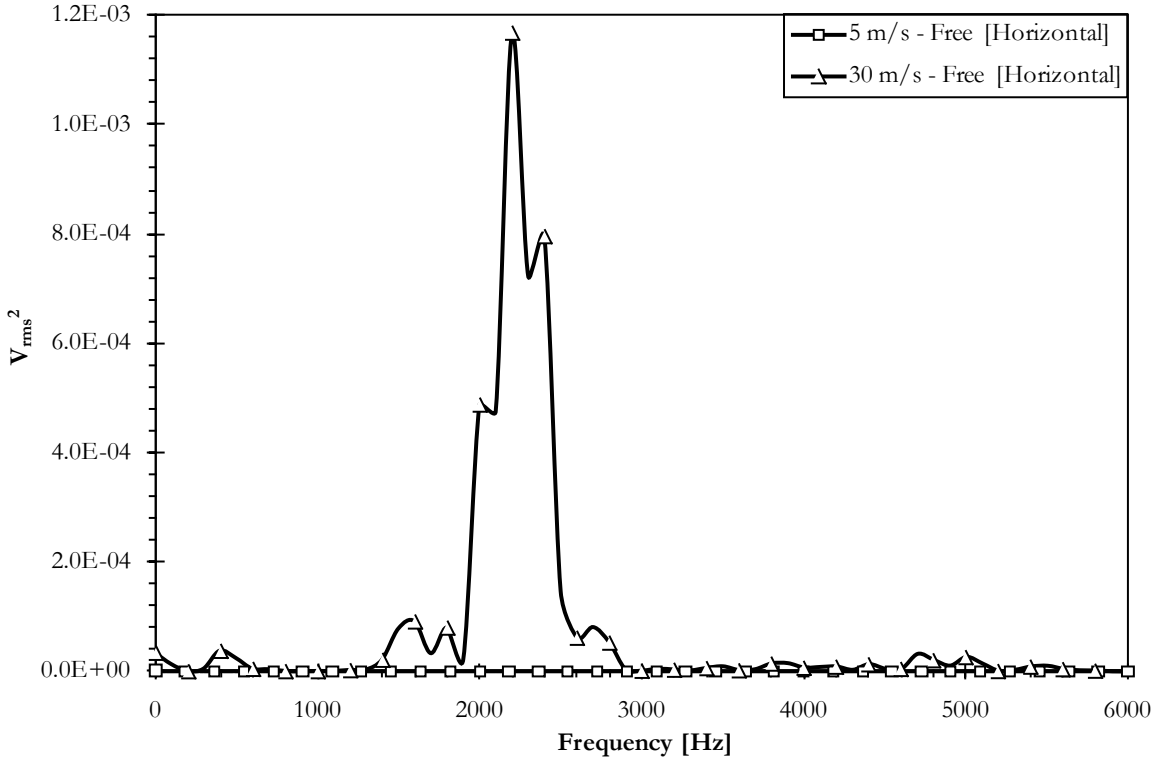

Figure 5.11 - Magnitude power spectrum density of free vibration in the horizontal direction for scratching speeds of 5 and 30 m/s.

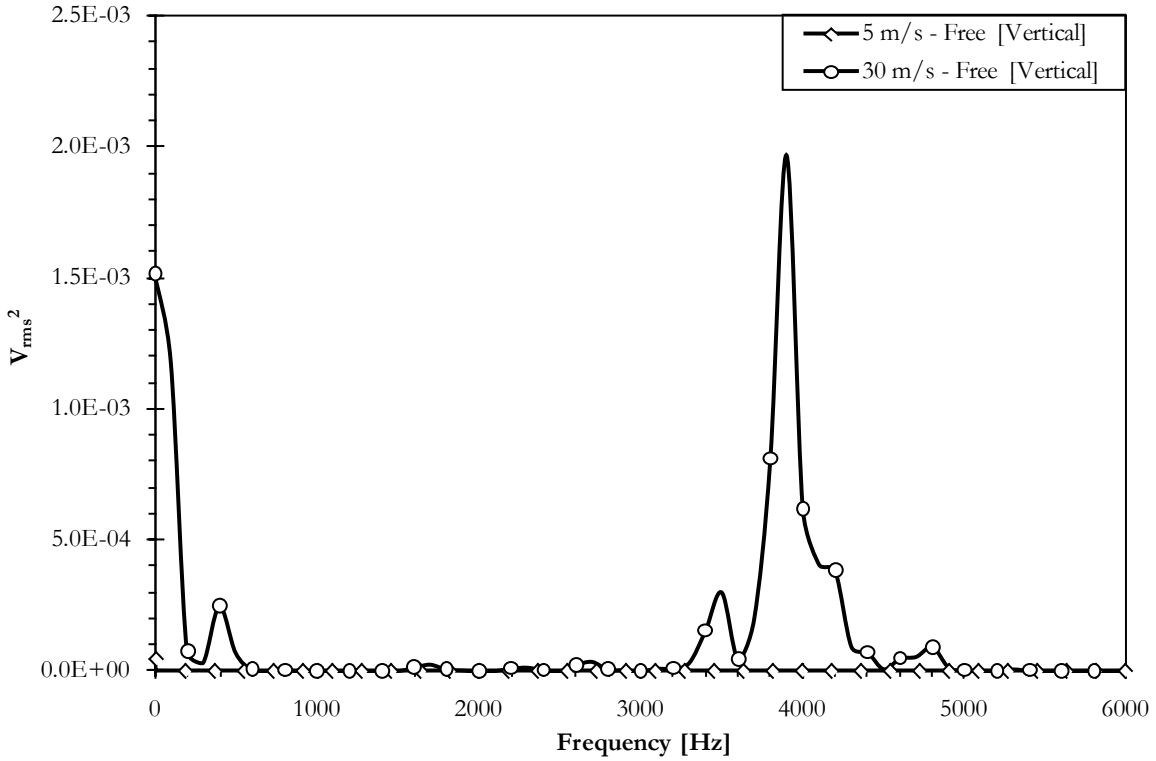

Figure 5.12 - Magnitude power spectrum density of free vibration in the vertical direction for scratching speeds of 5 and 30 m/s.

Figure 5.13 shows the magnitude of the average power spectrum density in the vertical direction obtained from an accelerometer mounted to the base plate of the grinding machine. The dynamometer was bolted directly to the base plate. The tests were performed with the grinding machine and all required accessories turned on; however, the spindle was not rotating for safety reasons. Only the vertical direction was tested as it produced the largest frequency magnitudes according to the analysis of the force data discussed above. From the figure it can be seen that the largest peak occurred at approximately 3.8 kHz; thus, it would seem that the grinding machine itself has a tendency to excite the vertical frequency of approximately 4 kHz observed in the force data.

Table 5.2 - Force dynamometer natural frequencies.

	F_X	F_Y	F_Z
Natural Frequency [kHz]	2.3	3.5	2.3

It is evident that during the scratching process two natural frequencies were being excited; 2.2 kHz in the horizontal direction and 4 kHz in the vertical direction. Both of these values were in the vicinity of the stated natural frequencies of the dynamometer as shown in Table 5.2.

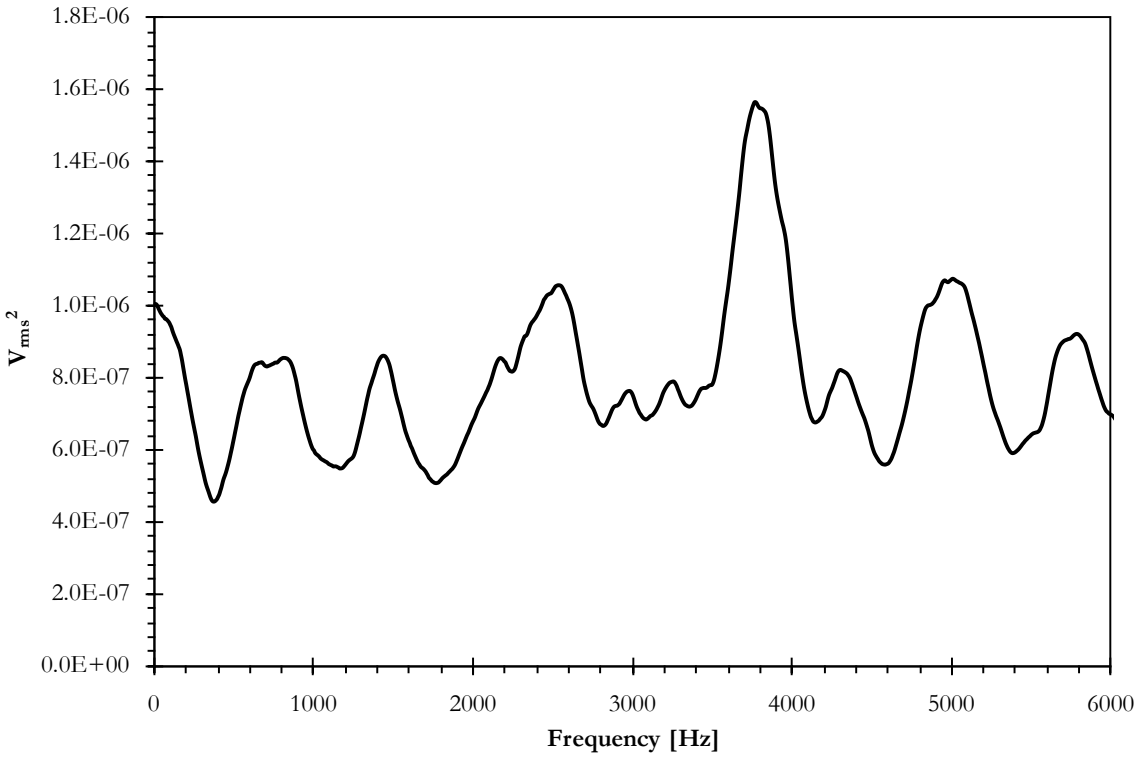

Figure 5.13 - Average magnitude power spectrum through grinding machine base plate.

Based on the preceding discussion it becomes clear that the natural frequency of the dynamometer was excited during the scratching experiments and that the magnitude of the vibrations increased as the scratching speed increased. The use of the long scratch length effectively reduced the signal loss as the frequency of vibration was much higher than the scratching event which occurred at a maximum of 275 Hz and, therefore, the desired force trends were discernable. A low-pass filter was applied to the force data to remove the unwanted oscillations in the signal, as shown in Figure 5.14, which shows that the scratching process produced smooth force signals in both the horizontal and vertical directions once filtered. A comparison between the resultant force and the scratch depths along a scratch is shown in Figure 5.15 and demonstrates excellent correlation between the two sets of experimental data. This correlation proves that the oscillations in the force data were indeed a result of vibrations and, therefore, filtering of the data was justified.

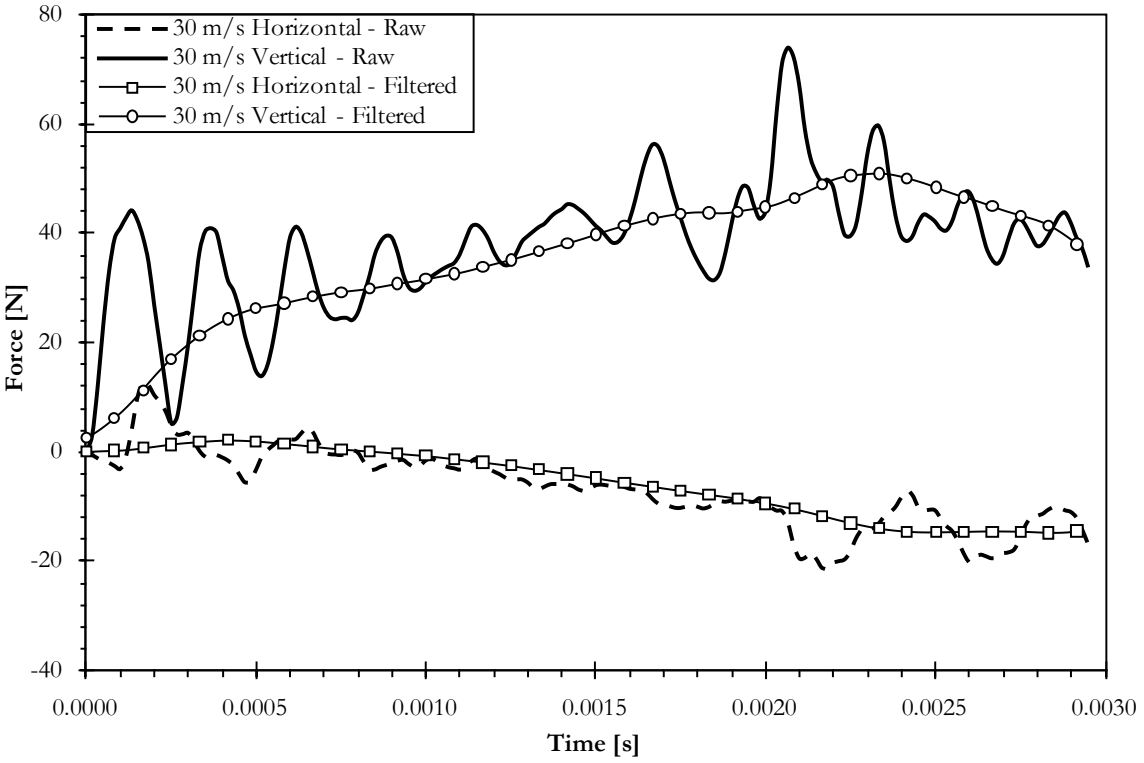

Figure 5.14 - Representative raw and filtered force curves for 30 m/s scratching speed.

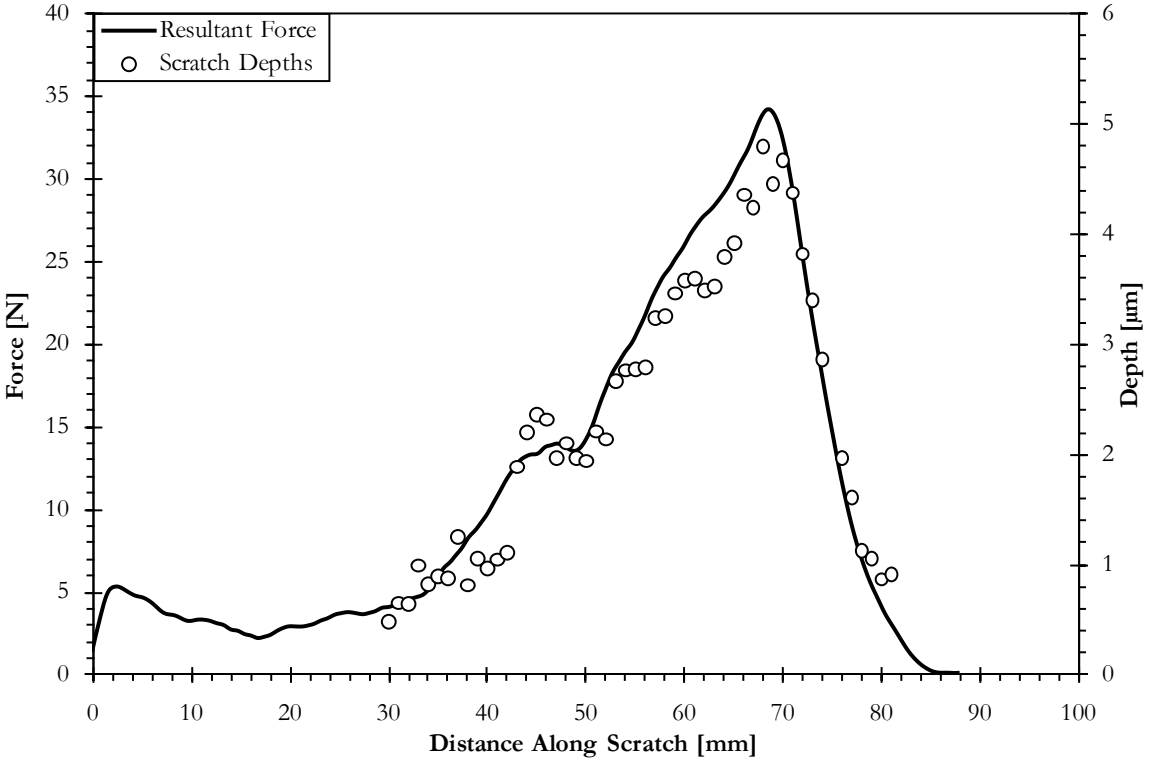

Figure 5.15 - Correlation between resultant forces and scratch depths along a scratch.

5.5 Summary

This chapter presented the experimental apparatus and data analysis techniques that were used for this work. The experimental apparatus was designed to produce scratches using two custom diamond stylus geometries. The round-nosed stylus was used at scratching speeds of 5 m/s to 30 m/s in 5 m/s increments and depths of cut from 0.3 μm to 7.5 μm. The flat-nosed stylus was used at a scratching speed of 20 m/s and depths of cut from 0.3 – 5.0 μm. The residual scratches were measured with a three-dimensional optical profilometer. The data analysis techniques successfully removed the high frequency noise from the experimental force data and transformed the horizontal and vertical recorded forces to normal and tangential forces. The next chapter will discuss the experimental and numerical scratching results for the round-nosed stylus.

Chapter 6 Round-Nosed Scratch Testing

The present chapter begins by introducing the finite element models that were developed for the round-nosed stylus geometry used in this work. The accuracy of the finite element model will be validated based on comparisons to experimental data. The finite element model will then be used in conjunction with the experimental data to thoroughly investigate the scratching process. The finite element model and scratching results for the flat-nosed stylus geometry will be presented in the next chapter. The scratching speed range was 5 m/s to 30 m/s in 5 m/s increments and the depth of cut range was 0.3 μm to 7.5 μm.

6.1 Round-Nosed Stylus Scratching Model

The finite element models employed for the round-nosed scratching simulations were conceptually similar to that used for the indentation tests; however, some modifications were required. In a similar manner that was done with the initial indentation model, the initial scratching model consisted entirely of Eulerian elements with an elastoplastic material definition. The initial model was purposely made larger than required to ensure that the

stresses did not interfere with the boundaries of the model and to ensure that the forces and stresses had achieved steady-state. Once a simulation had been completed with the conditions that would create the largest stress field, namely a scratching speed of 30 m/s and a depth of cut of 9 μm, the model was pared down to reduce the number of elements, the material model definitions were adjusted, and the hybrid Eulerian-Lagrangian structure was implemented. Areas of the model that did not experience stresses above the yield strength of the workpiece material were assigned an elastic material definition and a Lagrangian element definition. Areas of the model that did not experience large mesh deformations but did experience stresses above the yield strength of the workpiece material were assigned an elastoplastic material definition and a Lagrangian element definition. Transition elements were utilized to increase the size of the Lagrangian elements. These transition elements and larger elements were placed in areas of sufficiently low stress such that they did not reduce the accuracy of the model. Furthermore, three differently sized models were created to account for the smaller depths of cut, which produce smaller stress fields. The largest model was used for depths of cut ranging from 7 μm to 9 μm, a medium sized model was used for depths of cut ranging from 4 μm to 6 μm, and a small model was used for depths of cut ranging from 1 μm to 3 μm. A representation of the final numerical mesh for the workpiece used with the round-nosed stylus can be seen in Figure 6.1, which shows the hybrid structure of the model, the elastic and elastoplastic regions, and the transition elements, while Table 6.1 shows the number of elements and nodes for the three model sizes. Symmetry along the X-axis was exploited to reduce the size of the workpiece model by one half and appropriate boundary conditions were placed on the XY-face to account for the symmetry. The outer periphery of the model was constrained in all directions to prevent unwanted motion of the workpiece, which was valid as the stresses and strains at this location were sufficiently low. The motion of the tool was prescribed to move along the negative Y-axis to the desired depth of cut followed by translation along the negative X-axis at the desired scratching speed. The length of cut was designed to be sufficiently long to ensure that the forces obtained steady-state. Frictional heating between the stylus and the workpiece was not considered; although, the effect of temperature rise due to plastic strain was accounted for in the material model.

Table 6.1 - Number of elements and nodes for round-nosed workpiece models.

Model Size	# of Elements	# of Nodes	Depth of Cut Range [µm]
Small	34,238	45,960	1 – 3
Medium	69,002	88,836	4 – 6
Large	158,484	194,013	7 – 9

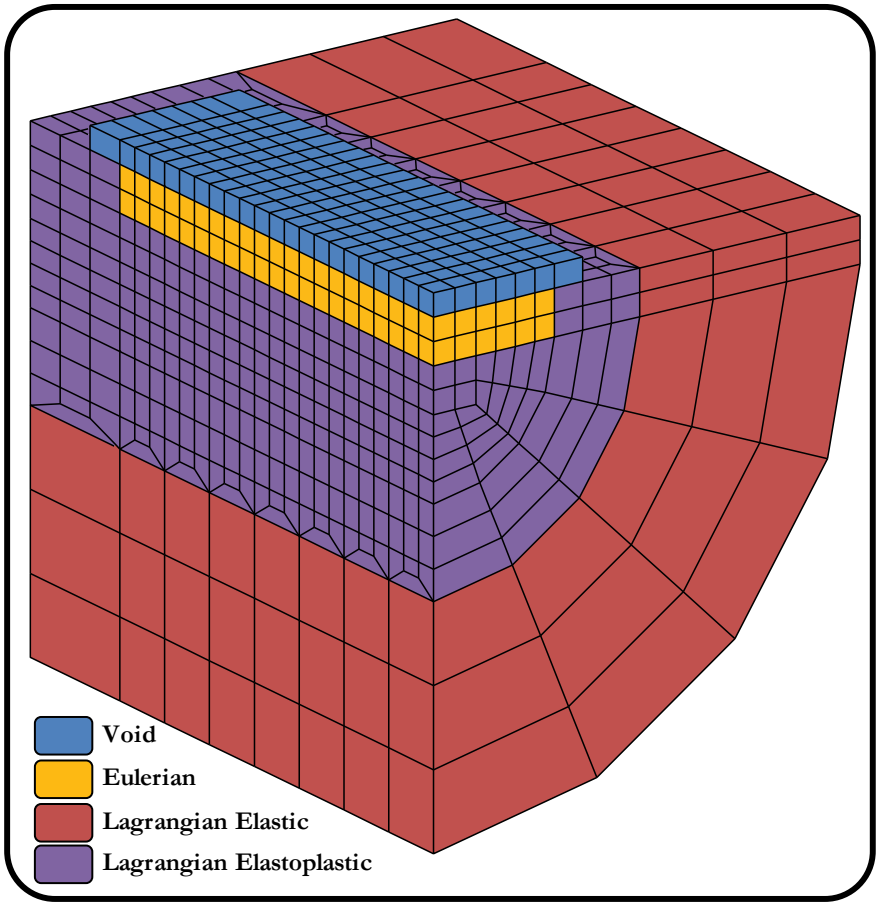

Figure 6.1 - Representative finite element workpiece mesh for the round-nosed stylus.

Figure 6.2 shows a representative image of the finite element mesh of the round-nosed diamond stylus. Since the stylus was assumed rigid, only one layer of elements was required.

The scratching simulations were solved using the ACEnet cluster. Based on the test results from the indentation simulations of Section 4.3.3.6, each model required 6 computational cores to solve in the least amount of time. The solution times ranged from approximately 3 hours for the fastest scratching speed and the smallest depth of cut to approximately 300 hours for the slowest scratching speed and the largest depth of cut. Due to the size of the ACEnet cluster it was possible to submit all of the models simultaneously, which required a

total of 324 computational cores. This cluster significantly reduced the wait times between model iterations.

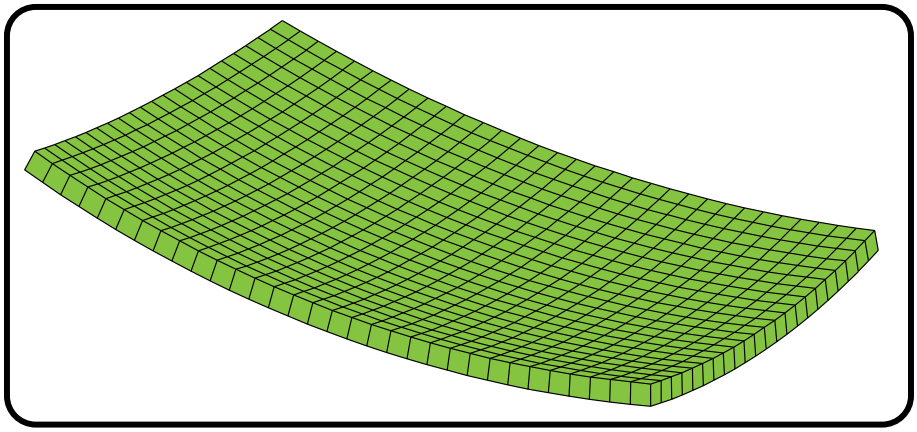

Figure 6.2 - Representative numerical mesh of the round-nosed diamond stylus.

6.2 Results

The sections to follow will present the experimental and numerical findings of the high-speed scratch tests for the round-nosed diamond stylus. An in-depth analysis will be performed on the results to provide a comprehensive understanding of the scratching process related to: the friction between the stylus and the workpiece, the material mechanics of the workpiece, and the cutting mechanics of the operation. The sections to follow will commence with a presentation of the experimental results followed by the validation of the finite element model. Next, the scratching process will be analyzed based on the observations made from the experimental data in tandem with the data from the finite element model.

6.2.1 Experimental Results

Figure 6.3 plots the raw normal forces as a function of the scratch depth as well as the lines of best fit for the six scratching speeds tested. It can be seen from the figure that the normal forces were linearly dependent on the depth of cut with R^2 values ranging from 0.95 to 0.98. The slopes of each data set were nearly identical but had an increasing offset as the scratching speed was increased. This increase in force as a function of scratching speed is an important observation because it implies that workpiece and machine tool deflections will

increase with scratching speed due to higher cutting forces, which will decrease the overall process accuracy.

Figure 6.4 plots the tangential forces as a function of the depth of cut for the six scratching speeds tested. Of note are the parabolic and linear trends visible in the data and the decrease in forces as the scratching speed was increased. The parabolic trend occurred from approximately 0.3 μm to 2.0 μm on average and the linear trend occurred from approximately 2.0 μm onwards. The trends from 0 μm to 0.3 μm were unknown because scratch depths of less than 0.3 μm were impossible to measure because they were obscured by the surface texture of the workpiece. The general shape of the trends agreed well with the results of other researchers, such as Doman [13], who associated the change in shape of the trends with the rubbing to plowing transition. Several fitting functions were investigated to describe the non-linear shape of the experimental data, yet no single function was able to adequately describe the data within an acceptable level of error. Therefore, a piecewise approach was used to create the best fit starting with a parabolic curve passing through the origin and encompassing the shallow depths of cut followed by a linear region for the higher depths of cut. A transition point was selected on the parabolic curve where the slope and offset were calculated to create the fit for the straight portion of the data. The coefficients of the parabolic curve as well as the transition point were optimized until acceptable R^2 values ranging from 0.94 to 0.98 were achieved.

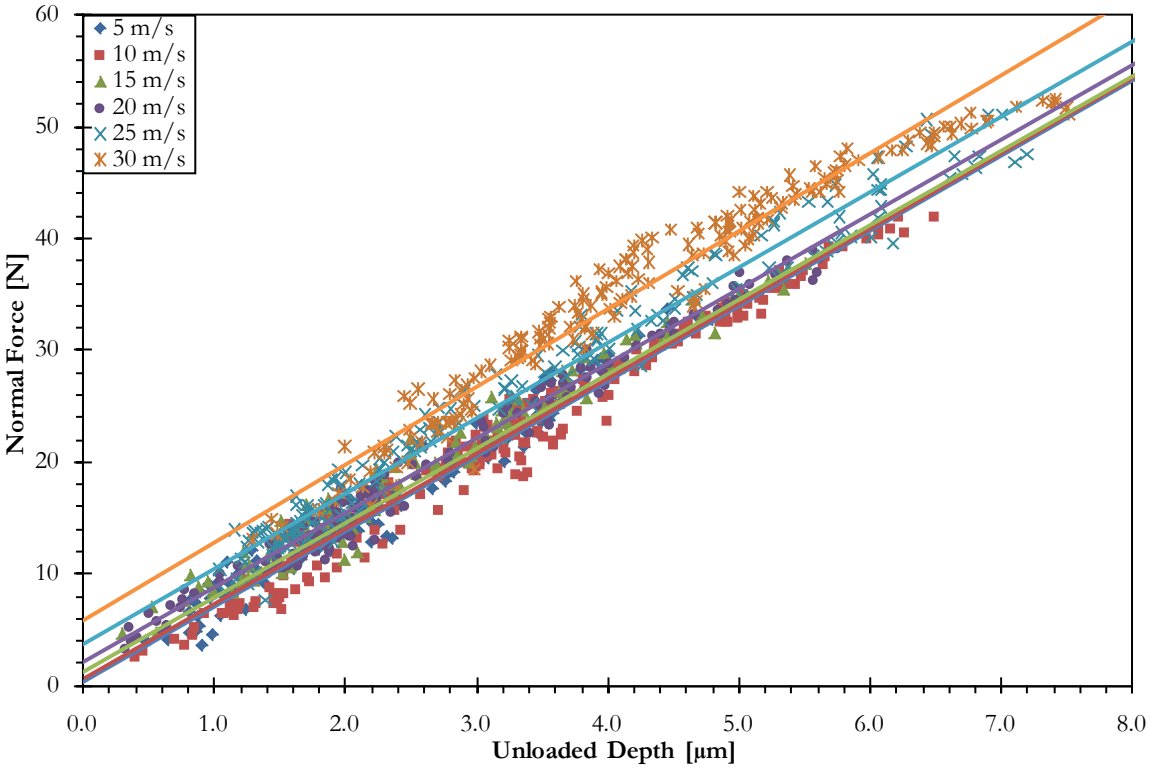

Figure 6.3 - Experimental normal force as a function of unloaded depth.

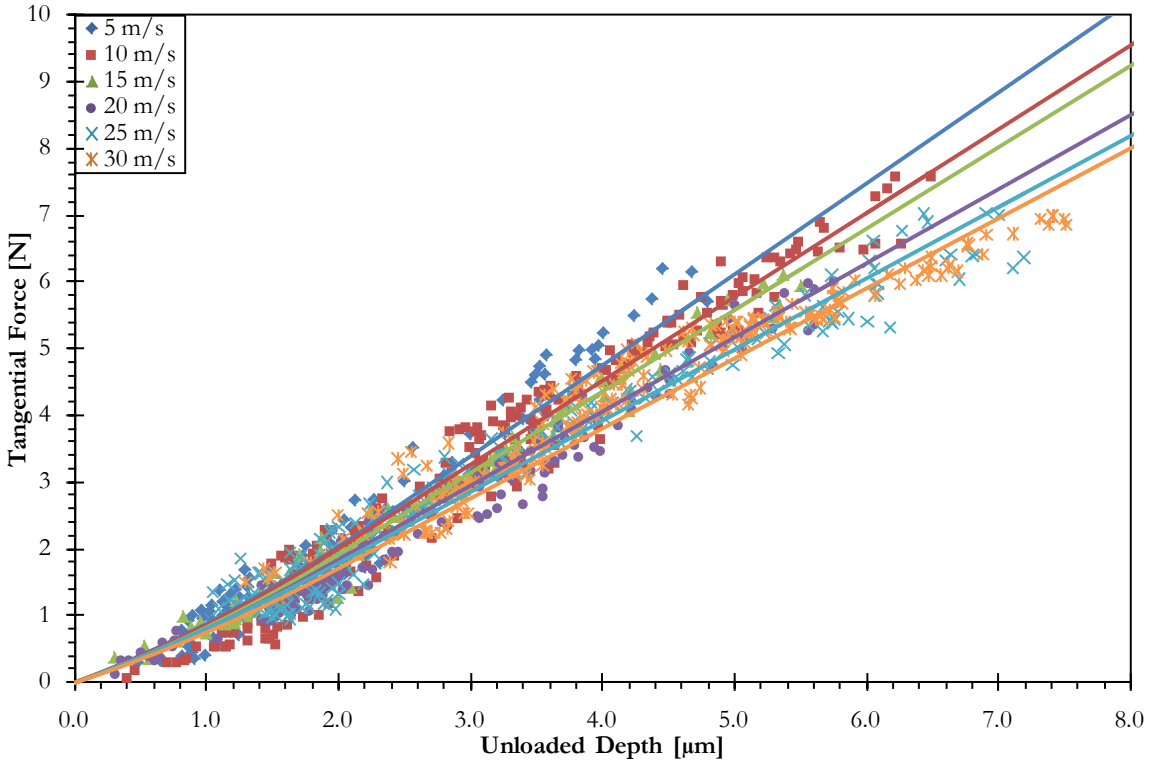

Figure 6.4 - Experimental tangential force as a function of unloaded depth.

6.2.2 Finite Element Model Validation

In the experiments, the scratch depths were measured offline after the load had been removed and will be referred to as the *unloaded* depths. Due to the geometry of the scratches and the large subsurface pressures there existed the possibility for significant amounts of elastic recovery. The purpose of this work was to compare the numerically derived forces obtained at a given depth to those from the experiments. Ideally, the finite element model would be allowed to relax after the scratches were formed, often referred to as a springback analysis. This type of analysis requires a material model that has been verified for springback as well as an element formulation that could utilize implicit time step integration, neither of which were available for the material model and element formulation chosen for this work. Therefore, it was decided to convert the *unloaded* scratch depths to the equivalent depths found in the finite element model. These converted depths will be referred to as *loaded* depths and enabled direct comparisons to the finite element models. Alternatively, the *loaded* depths from the finite element model could have been converted to the equivalent *unloaded* depths; however, this would introduce errors in the resulting stresses and strains. The forces were recorded during the loaded state and, therefore, did not require conversion.

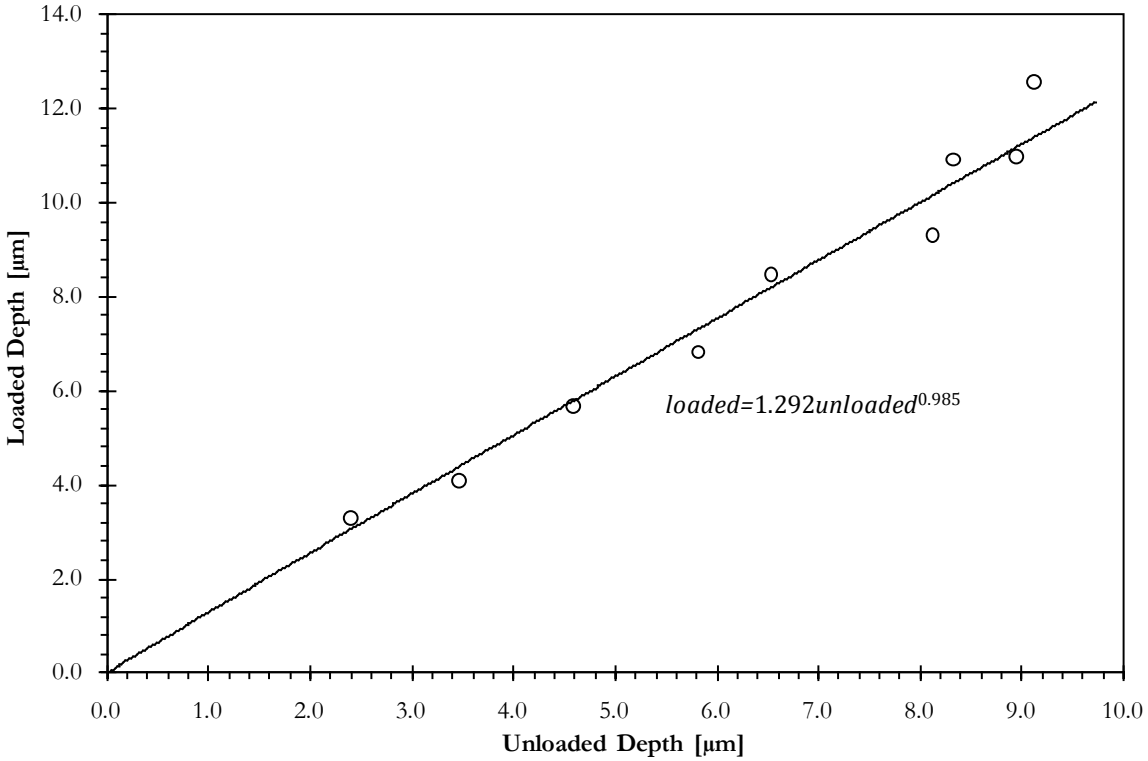

Figure 6.5 - Static springback correction curve.

The *unloaded* to *loaded* depth conversion required two independent steps to account for both the strain and strain-rate sensitivity of the workpiece material. The strain sensitivity was accounted for by a series of low-speed indentation tests that were performed in the same manner as described in Chapter 4. The residual impressions in the workpiece were measured with the optical profilometer and compared to the maximum depths recorded from the digital images. A plot, shown in Figure 6.5 was then created. A trendline fitted to the data showed a nearly linear relationship between the *loaded* depths and *unloaded* depths according to the power series:

$$loaded = 1.292 unloaded^{0.985} \tag{6.1}$$

with an R^2 value of 0.98. This conversion was equivalent to stretching the data along the X-axis of Figure 6.3 and can be considered the static springback due to strain.

However, this conversion did not eliminate the non-zero Y-intercept. As was noted earlier, the slopes of the normal forces were nearly identical but had an increasing offset as the scratching speed was increased which prevented the forces from reaching 0 N at a depth of cut of 0 μm. Further analysis showed that the offsets were a result of the strain-rate effects present during the unloading cycle of the workpiece. If one were to examine the effective stress versus effective plastic strain curve predicted by the previously discussed Johnson-Cook [81] plasticity model shown in Figure 6.6 it becomes clear that the amount of springback increases as the strain rate increases for a given amount of plastic strain, which can be considered the dynamic springback. The figure shows that if a material were loaded to a given effective plastic strain at low, quasi-static, strain rates the material would unload elastically along the slope related to the elastic modulus of the material, which would be equivalent to the static springback. As the strain rate increases the amount of unloading increases due to the increase in the strength of the material, which would be equivalent to the dynamic springback. The slope E_E of the unloading curves shown in Figure 6.6 is exaggerated for clarity as it should be equivalent to the elastic modulus. The amount of dynamic springback can be visualized by extending the trendlines of the normal forces in Figure 6.3 until they intersects with the X-axis, as illustrated in Figure 6.7. To account for the strain-rate effects the *unloaded* depths were shifted for each scratching speed until a linear trendline fitted to the data passed through the origin of the graph. Intuitively, this

adjustment is sound as there should not be a load present at a depth of cut of zero. Therefore, all of the normal forces coincided with a single trendline passing through the origin after the final correction was applied to the depths, as shown in Figure 6.8. This final correction effectively removed the strain rate dependence from the springback of the workpiece material.

In summary, the static springback caused a stretching of the data while the dynamic springback caused a shifting of the data. These two adjustments were independent of each other because the shape of the effective stress versus effective plastic strain curve does not change as the strain rate is increased; rather, the curve is shifted up as the strain rate is increased. Therefore, the effect of the strain on springback is always the same. Theoretically, if the scratches had been performed at speeds that would mimic quasi-static conditions then there would be no need for the dynamic springback. A final check was made to ensure that the static and dynamic springback were independent of each other. This check was performed by calculating the amount of springback from Figure 6.6 for each strain rate and comparing the delta between two successive strain rates. It was found that the difference between the springback of the two highest strain rates was identical to those of the two lowest strain rates for a given plastic strain, as shown in Figure 6.9. Therefore, the static and dynamic springback are independent of each other.

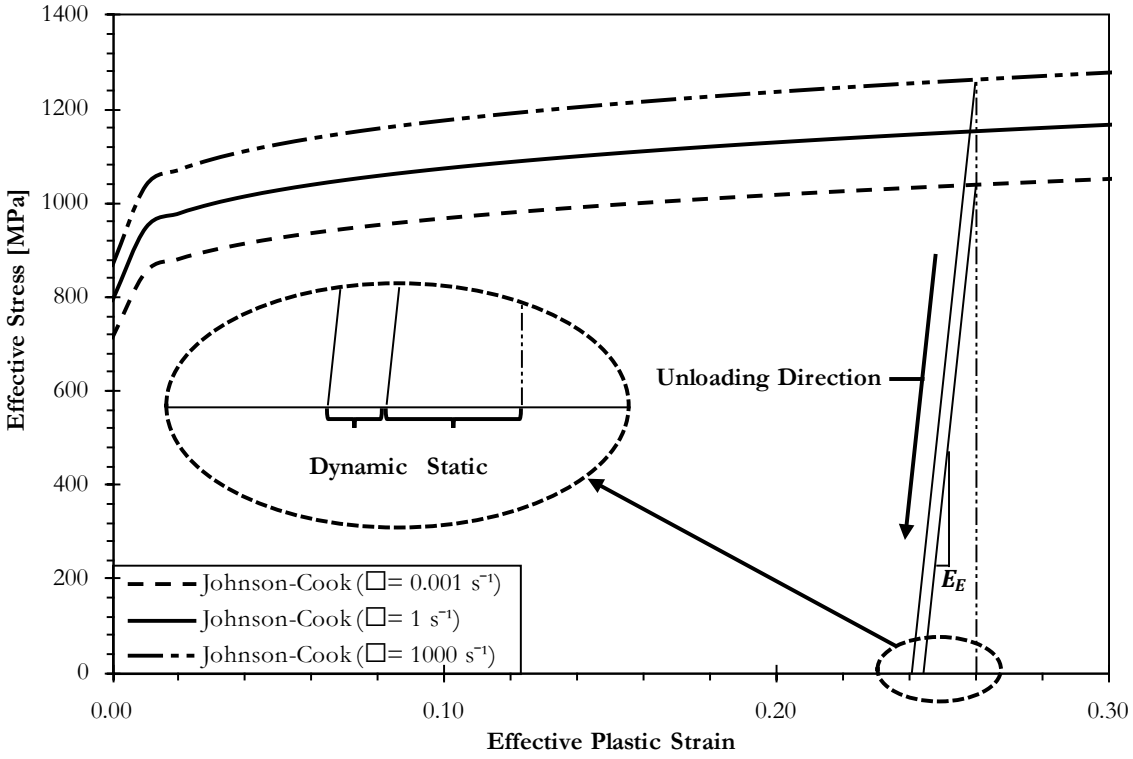

Figure 6.6 - Effect of strain rate on material springback.

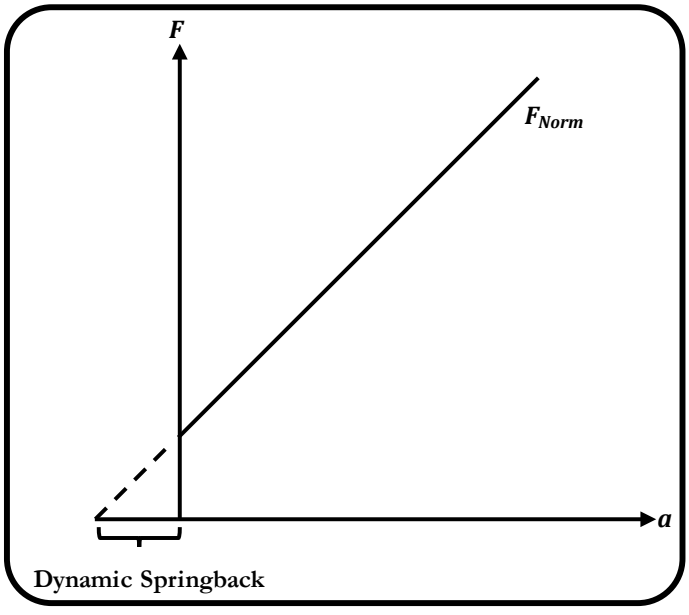

Figure 6.7 - Extension of trendline to calculate dynamic springback.

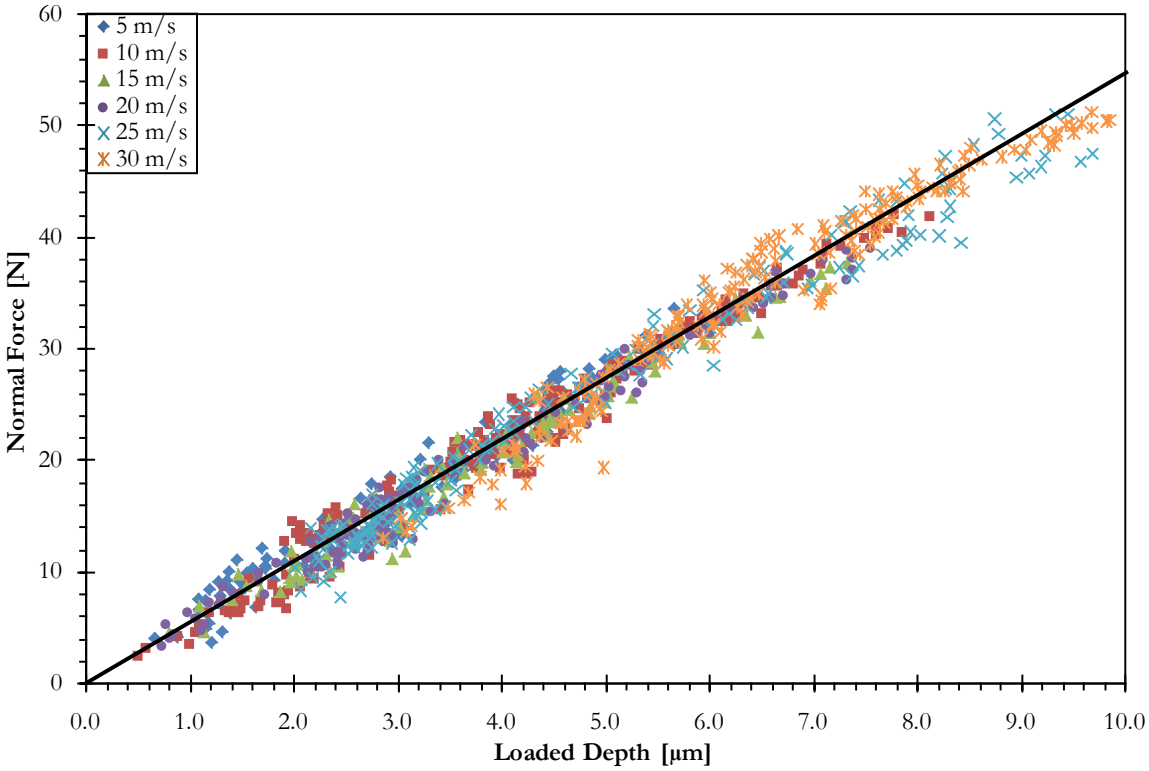

Figure 6.8 - Experimental normal force as a function of loaded depth.

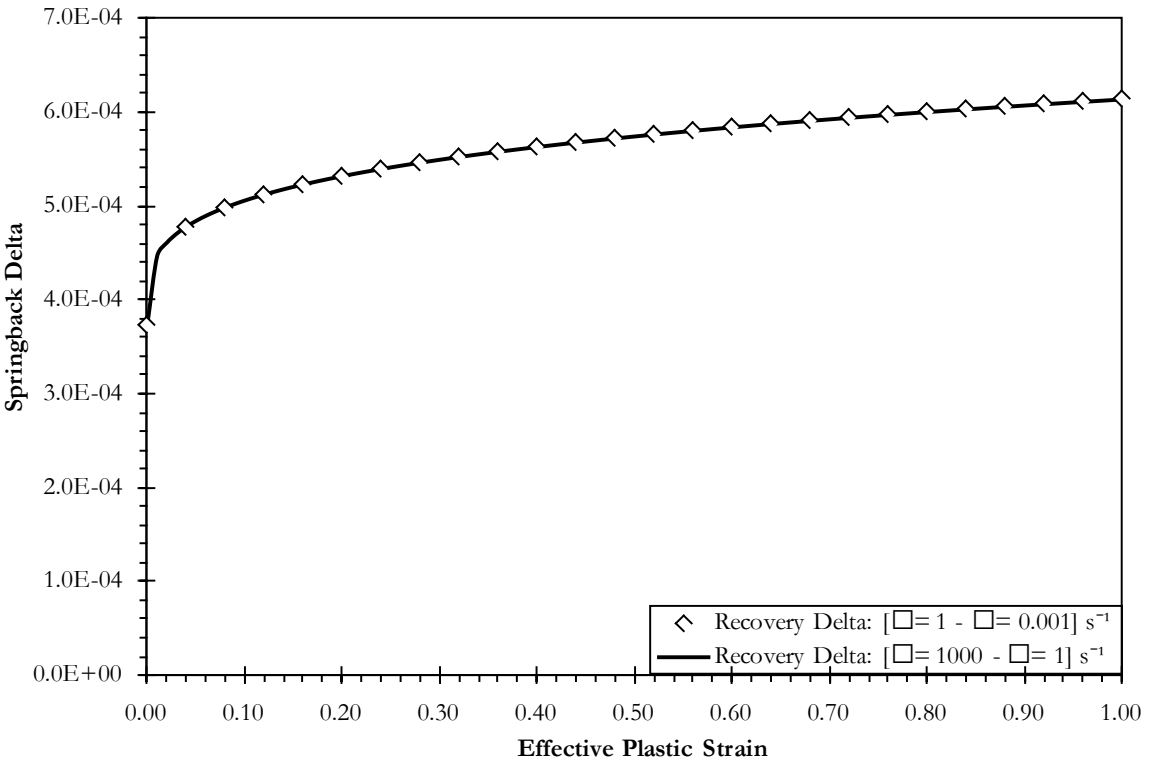

Figure 6.9 - Comparison between the springback from two sets of strain rates.

Figure 6.10 shows the comparison between the *loaded* experimental normal force data and the numerical normal force data. The experimental data lies on a single trendline passing through the origin, as previously discussed. The numerical data spreads out in a fan-like manner starting at the origin with the slowest scratching speed located on the bottom of the fan shape and the highest scratching speed located on the top of the fan shape. The slopes of the mid-range scratching speeds most closely resemble the slope of the experimental data. The error between the numerical and experimental normal force data varied from 8.4% to 12.6%, where the numerical data created a bracket around the experimental data. It was difficult to pinpoint the reason for the behaviour of the numerical normal forces as the experimental data did not display the same fan-like trend. This behaviour may be a limitation of the implemented finite element model, specifically the limited friction model available for the Eulerian formulation in LS-DYNA®, where only a single coefficient of friction may be input without any velocity or shear stress compensation. Perhaps a more robust friction model, such as the shear friction law proposed by Zorev [117], may reduce the error; however, this shear friction law has not been implemented in the software. The trends and errors are within acceptable margins of error for this work despite the fan-like behaviour of the numerical normal forces.

Figure 6.11 shows the comparison between the *loaded* experimental tangential data and the numerical tangential data. The figure shows that there was excellent agreement between the two sets of data. The numerical tangential data was fit to the experimental tangential data by adjusting the coefficient of friction of the finite element model until the minimum error between the experimental and numerical data was obtained for each scratching speed, which ranged from 7.6% to 13.7% and was within acceptable limits for this work. Figure 6.12 shows the coefficients of friction that were obtained as a result of this fitting process, and as the figure shows the values decreased in a nearly linear fashion as the scratching speed was increased, which is a well documented property of Coulomb friction [118,119]. The coefficients of friction reported in the figure are within the published values as reported by Yurkov *et al.* [120]. These comparisons between the experimental and numerical data prove that the finite element model was behaving correctly.

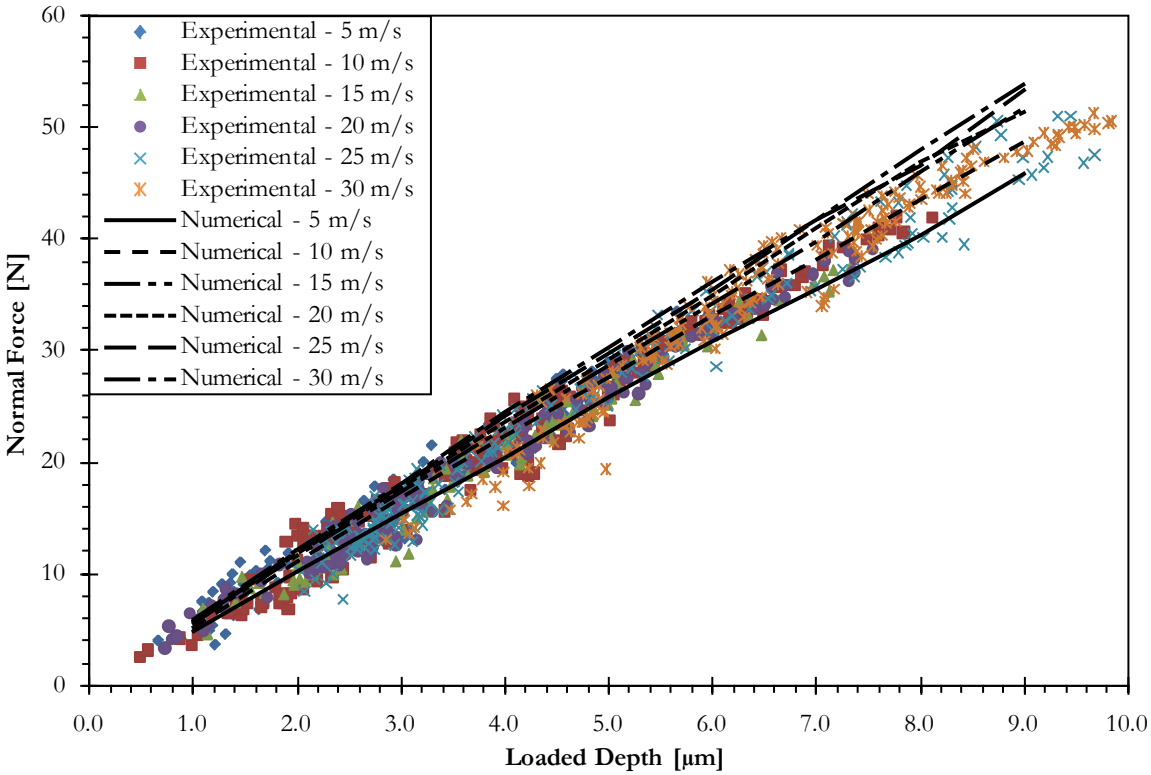

Figure 6.10 - Comparison between experimental and numerical normal forces.

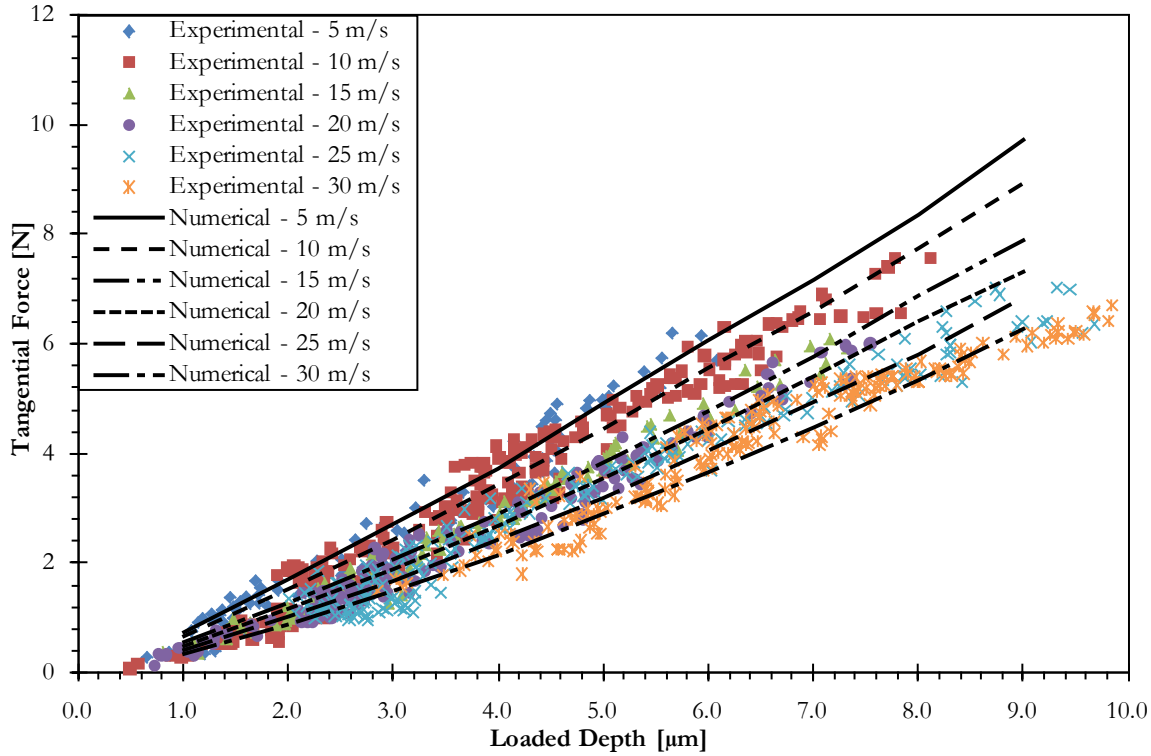

Figure 6.11 - Comparison between experimental and numerical tangential forces.

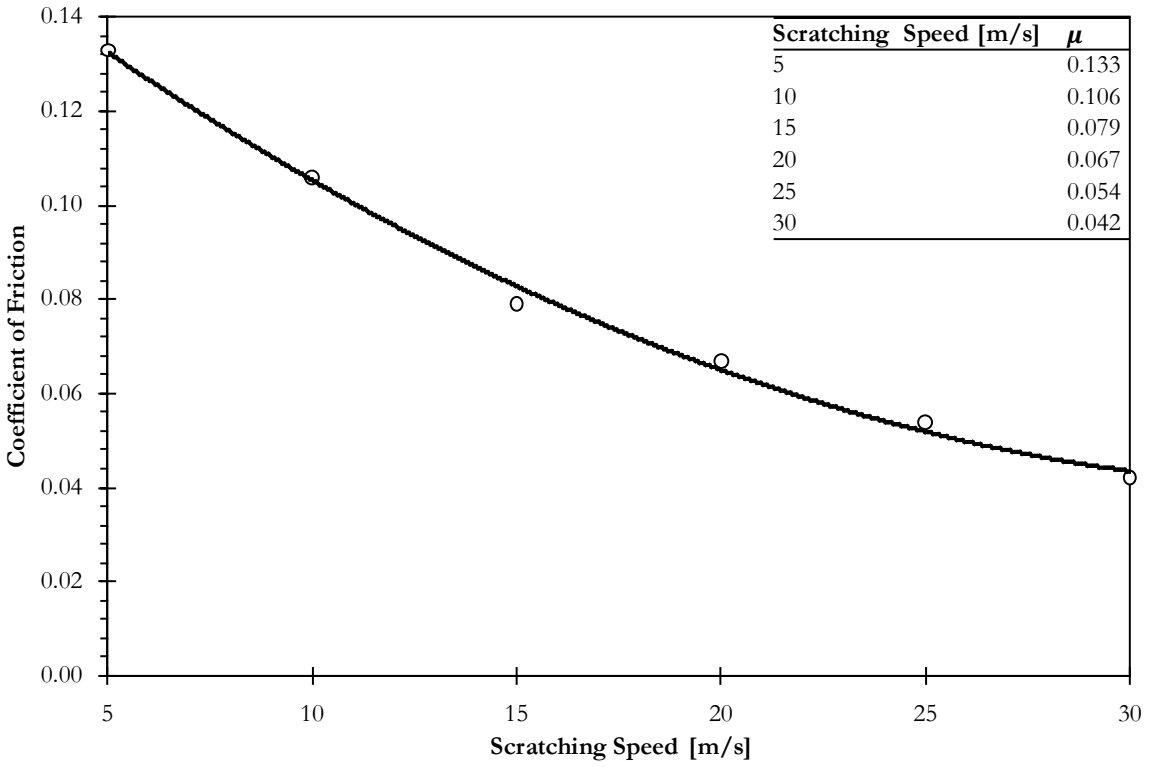

Figure 6.12 - Numerically determined coefficients of friction.

6.2.3 Analysis

The scratching process was influenced by many factors. These factors included: the stylus-workpiece friction, the cutting mechanics, and the material mechanics. The cutting mechanics were associated with the rubbing, plowing, and cutting stages of material removal, while the material mechanics were associated with the strengthening and softening effects related to the strain, strain rate, and temperature to which the workpiece was loaded. Analysis of the experimental data alone was not sufficient to produce a clear picture of the factors affecting the scratching process; therefore, the finite element model was utilized to supplement the experimental data. The finite element model was well suited to studying the material response since features of interest could be selectively deactivated, such as: friction, strain-rate hardening, and thermal softening, and direct observation of the forces and stress profiles was readily possible. The sections to follow will be divided into three main focal points that affect the scratching process: the effect of friction, the effect of the material mechanics, and the effect of the cutting mechanics.

6.2.4 Friction Effects

Figure 6.13 shows the normal forces obtained from the finite element model with and without friction and, clearly, the normal forces were not significantly affected by the presence of friction when the limitations of the finite element model are considered. As expected, friction may be safely neglected as a cause for the increasing normal forces in the *unloaded* state as frictional forces act perpendicular to the normal force.

Figure 6.14 shows the tangential forces obtained from the finite element model with and without friction. As expected, friction had a dramatic effect on the tangential forces based on the large decrease in the forces. The figure also shows that the tangential forces do not go to zero in the absence of friction; instead, all of the forces group together regardless of the scratching speed. This seems to indicate that there is an additional geometric factor that contributes to the tangential forces and prevents them from becoming zero in the absence of friction. This makes sense because the stylus is doing more plowing or cutting as the depth of cut increases.

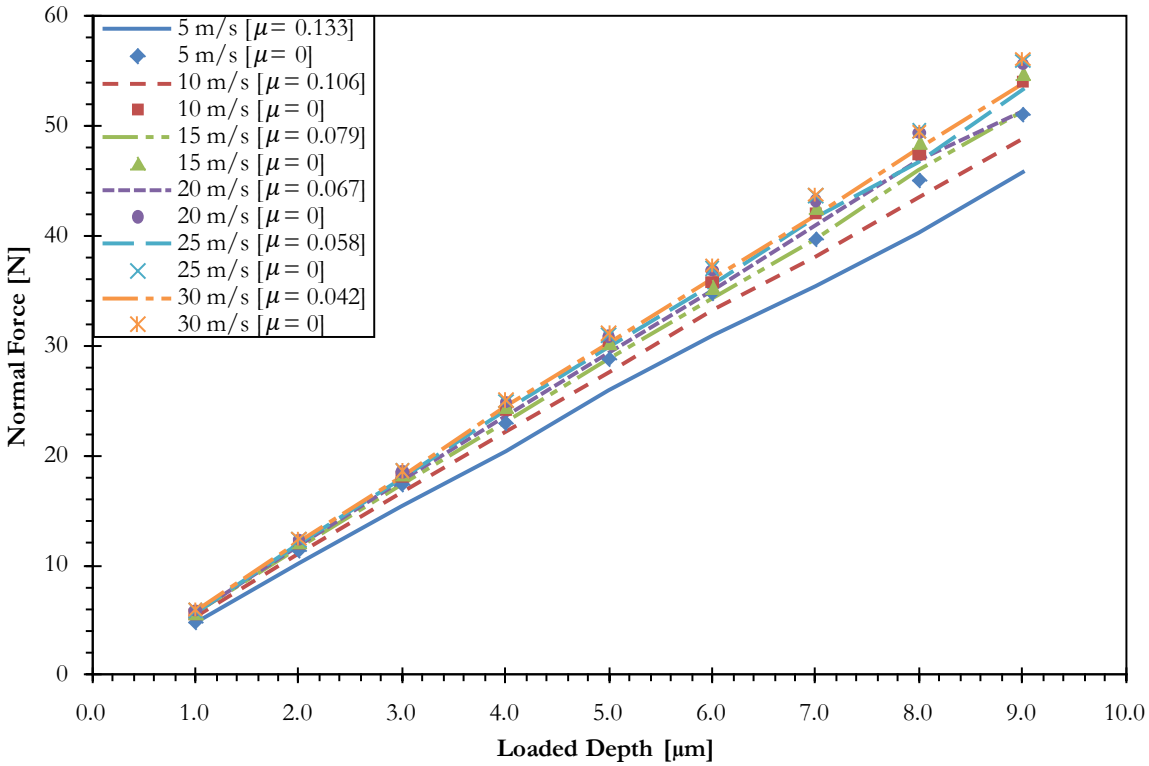

Figure 6.13 - Effect of friction of normal forces.

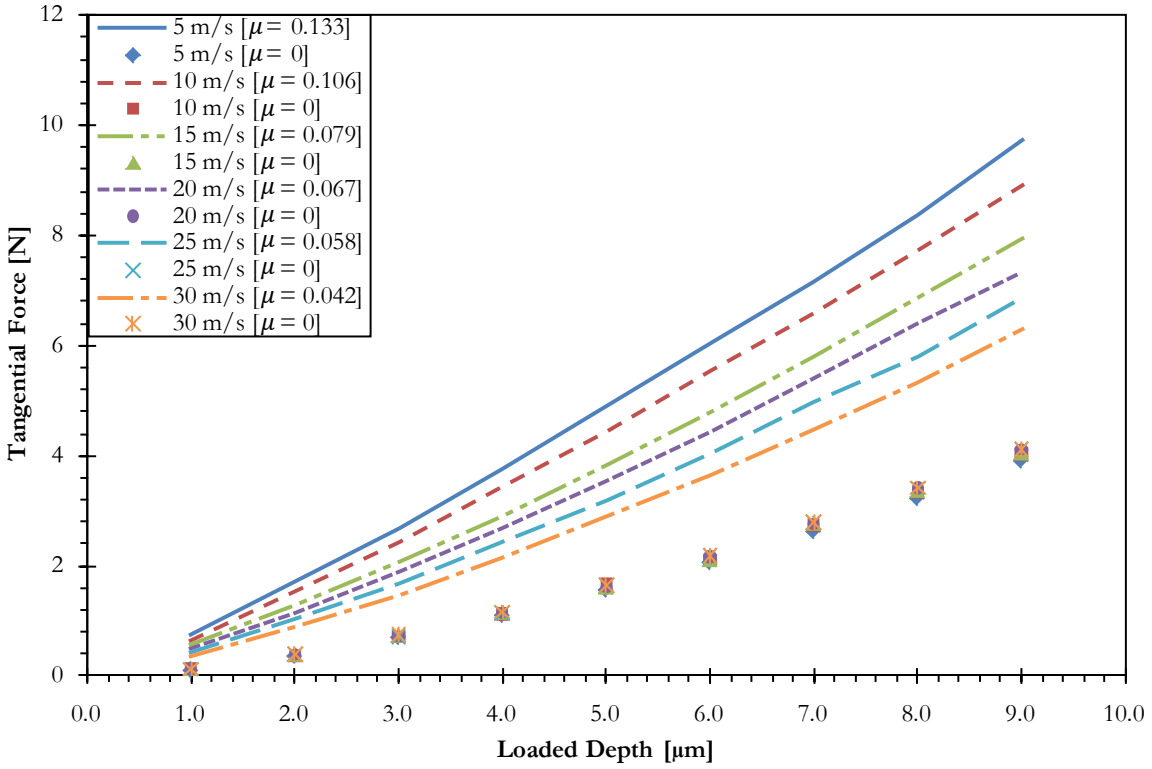

Figure 6.14 - Effect of friction of tangential forces.

The experimental force ratios $\mu = F_{Tan}/F_{Norm}$ are plotted in Figure 6.15 as a function of the *loaded* depth of cut for each scratching speed where the experimental data is represented by symbols and the fitted data is represented by lines. The fitted force ratio data was obtained from the fitted normal and fitted tangential data. It is clear from the figure that the force ratio decreased as the scratching speed was increased, which was also reported by Cai *et al.* [115]. The decrease in the coefficient of friction with an increase in the scratching speed was also supported by the results of the finite element model as it was necessary to decrease the coefficient of friction as the scratching speed was increased to create the best fit to the experimental tangential data, as shown previously in Figure 6.12. The correlation between the experimental and numerical force ratios is shown in Figure 6.16. The figure shows good agreement between the numerical force ratio data and the experimental force ratio data; however, a perfect match was not achieved due to the variance in the numerical normal force data as compared to the experimental normal force data.

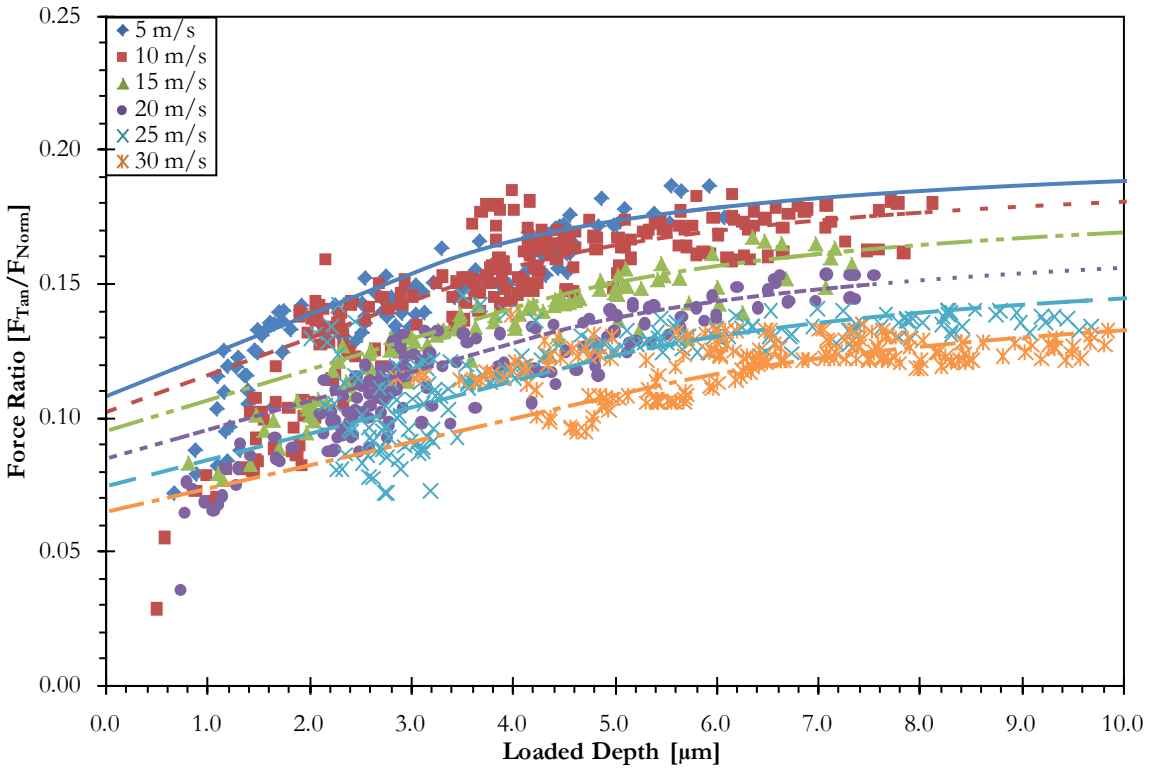

Figure 6.15 - Experimental force ratios as a function of loaded depth of cut.

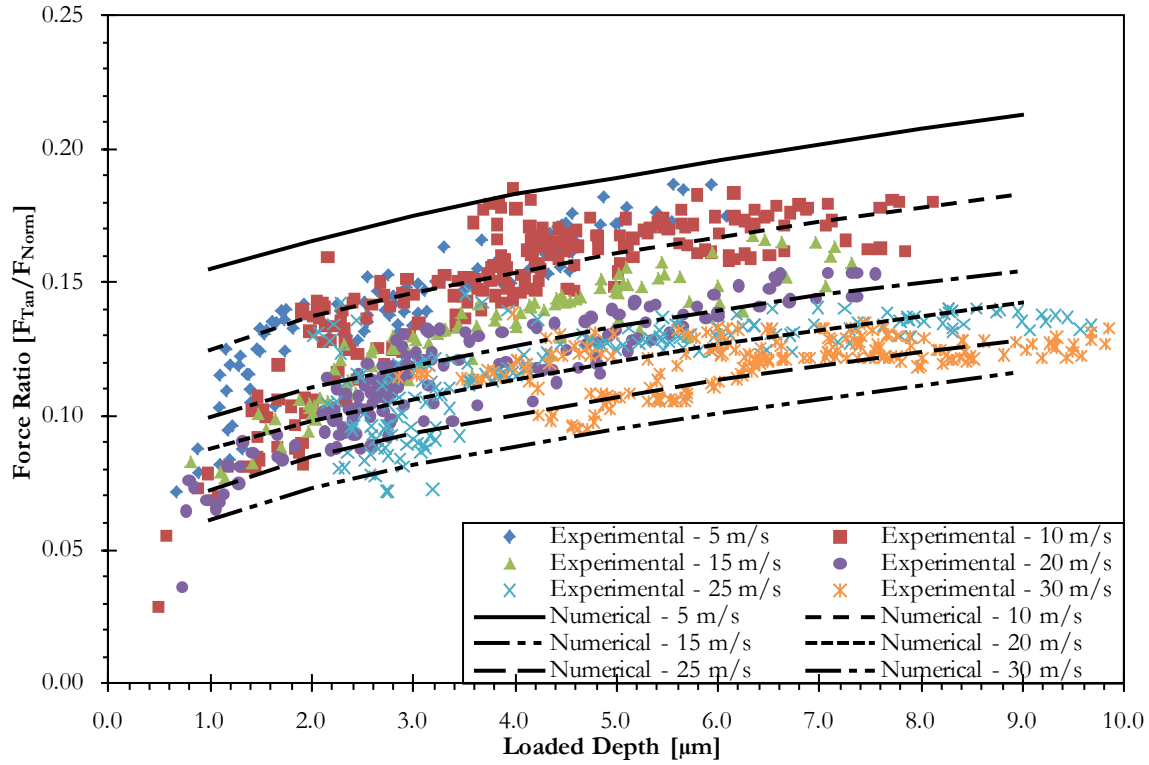

Figure 6.16 - Comparison of experimental and numerical force ratios.

Based on the preceding figures it is evident that the overall force ratios are the sum of the effects caused by the coefficient of friction and the plowed material. Subhash and Zang [121] proposed that the force ratios in scratch tests are the sum of the adhesion friction μ_a and the plowing friction μ_p. Adhesion friction is a result of the stylus sticking to the workpiece and is commonly referred to as Coulomb friction, whereas plowing friction is the result of the workpiece material ahead of the stylus providing resistance to the stylus motion. It is difficult and tedious to separate these two frictional forces experimentally; however, it is simple using the finite element model as the coefficient of friction utilized to fit the numerical tangential data to the experimental tangential data was the adhesion friction. By re-running the finite element model with a coefficient of friction of zero it was possible to determine the contribution of plowing to the force ratio, as shown in Figure 6.17. This figure shows that the adhesion friction, represented by solid lines, decreased with scratching speed as previously discussed and the plowing friction, represented by symbols on top of solid lines, remained constant for all scratching speeds.

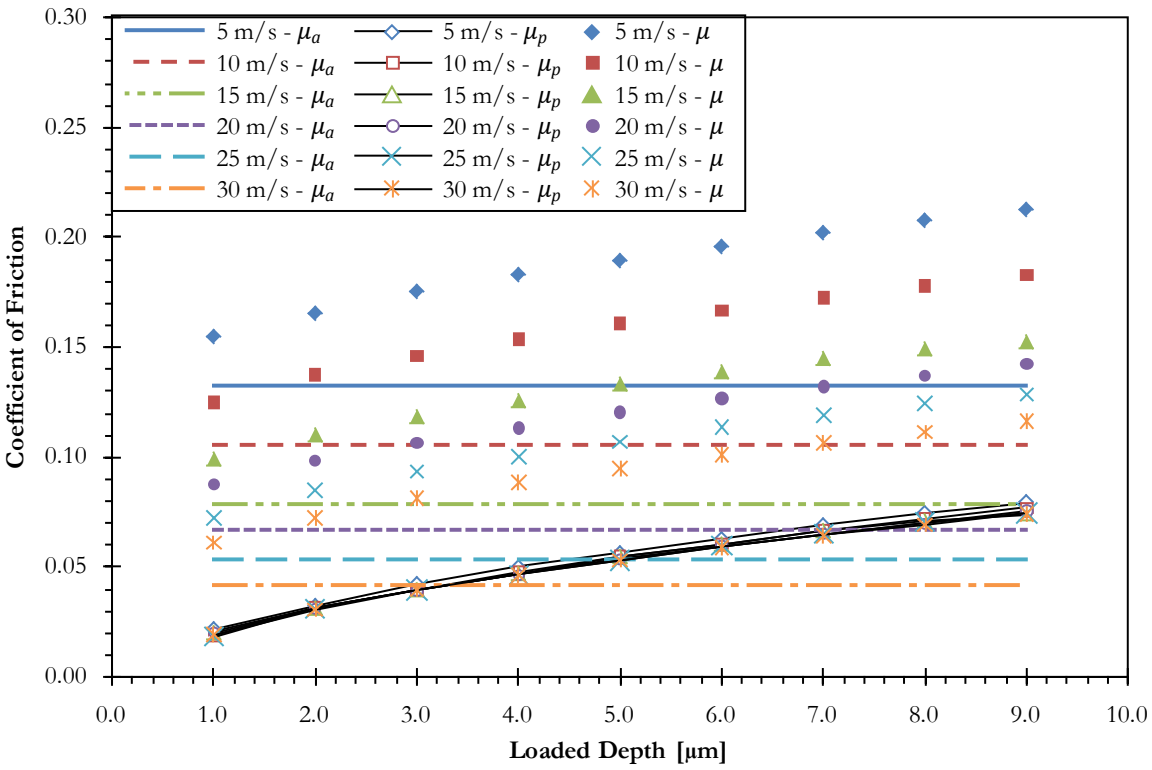

Figure 6.17 - Contributions of adhesion and plowing friction to overall coefficient of friction.

This result was important as it confirmed that adhesion friction was solely affected by the rubbing between the stylus and the workpiece while plowing friction was a result of the stylus geometry interacting with the workpiece; therefore, the coefficients of friction utilized in the finite element model for the round-nosed stylus can be confidently used for other stylus geometries provided that they are fabricated from the same material. Summing the adhesion friction and plowing friction resulted in the numerically determined force ratios, represented by symbols in Figure 6.17, which confirmed the accuracy of this procedure. For example, at a scratching speed of 15 m/s and a depth of cut of 4 μm , μ_a was 0.079, μ_p was 0.047, and μ was 0.126. Overall, a decrease in the force ratio for a given depth of cut suggests that less power was required to remove the material; hence, a more efficient process.

6.2.5 Material Mechanics Effects

The material mechanics effects can be attributed to the change in the workpiece material response due to strain-rate hardening and thermal softening.

6.2.5.1 Strain-Rate Hardening Effects

The maximum strain rates in the finite element model were found to be moderately high, ranging from approximately 50 s^{-1} at a scratching speed of 5 m/s and a depth of cut of 1 μm and approximately 1000 s^{-1} at a scratching speed of 30 m/s and a depth of cut of 9 μm, which are well within the usable range afforded by the Johnson-Cook material model. Figure 6.18 shows the subsurface strain rates for 5 m/s and 30 m/s scratching speeds at a depth of cut of 6 μm. As the figure shows, higher scratching speeds produced higher strain rates as well as a larger volume of affected material. The strain rates for the 30 m/s scratching speed were approximately 900 s^{-1}; however, the scale was chosen to illustrate the difference between the two scratching speeds. The strain rates are also shown to be localized in the region of the plowed material and directly under the stylus, which was to be expected as these were the locations of maximum deformation.

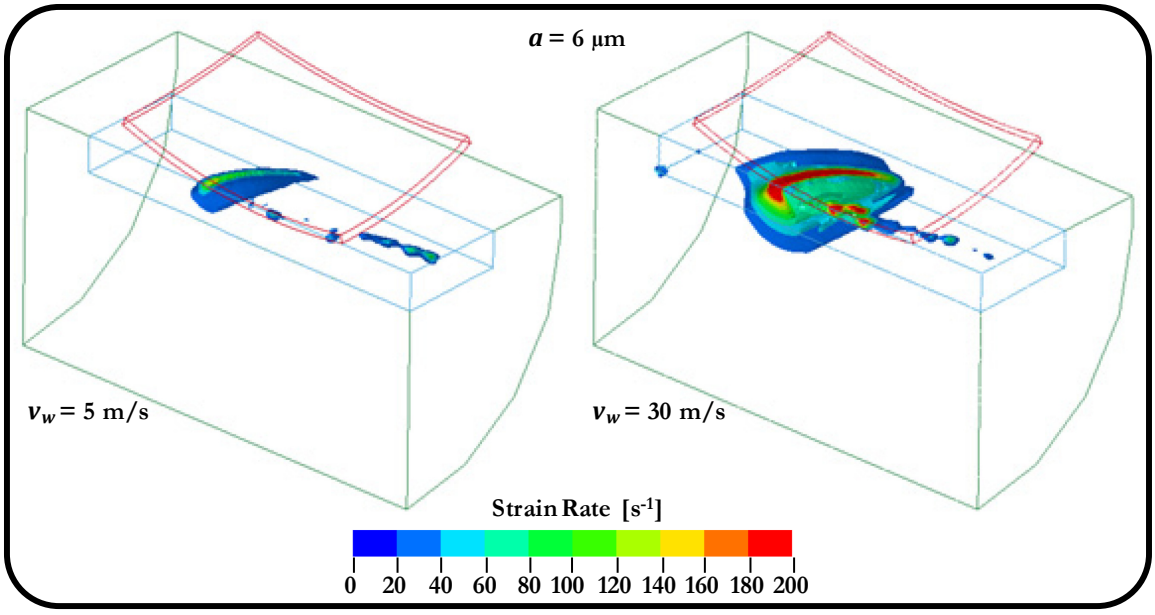

Figure 6.18 - Subsurface strain rates for 5 m/s and 30 m/s scratching speeds.

As was illustrated in Figure 6.6 there was an increase in the workpiece material strength as the strain rate was increased. Based on this figure one would expect larger stresses for an increase in the scratching speed since strain rate is a function of speed. By setting the strain-rate modifier C to zero in the previously mentioned Equation (3.9) and re-running the numerical model, the effect of the strain-rate hardening of the workpiece can be identified as shown in Figure 6.19. This figure shows that the normal forces decreased when strain-rate hardening was deactivated; therefore, strain-rate hardening results in an increase in the normal forces and is the most likely explanation for the speed dependency of the *unloaded* normal force data.

As Figure 6.4 showed the tangential forces formed a fan-like pattern, where the highest scratching speed produced the lowest tangential forces; therefore, there must be a speed dependent effect to cause the decrease in tangential forces. Figure 6.20 shows that the tangential forces decreased with strain-rate hardening deactivated; therefore, strain-rate hardening would result in an increase in tangential forces. Consequently, strain-rate hardening is not responsible for the observed decrease in the tangential forces with an increase in scratching speed.

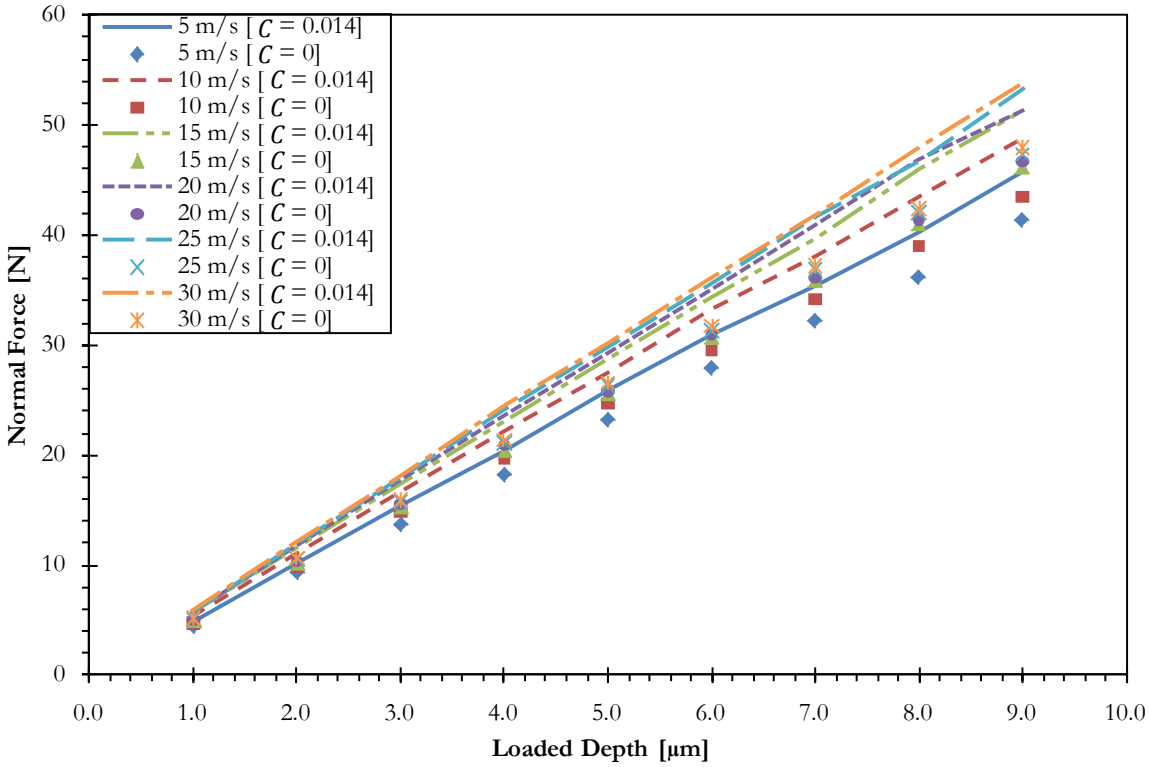

Figure 6.19 - Effect of strain-rate hardening on normal forces.

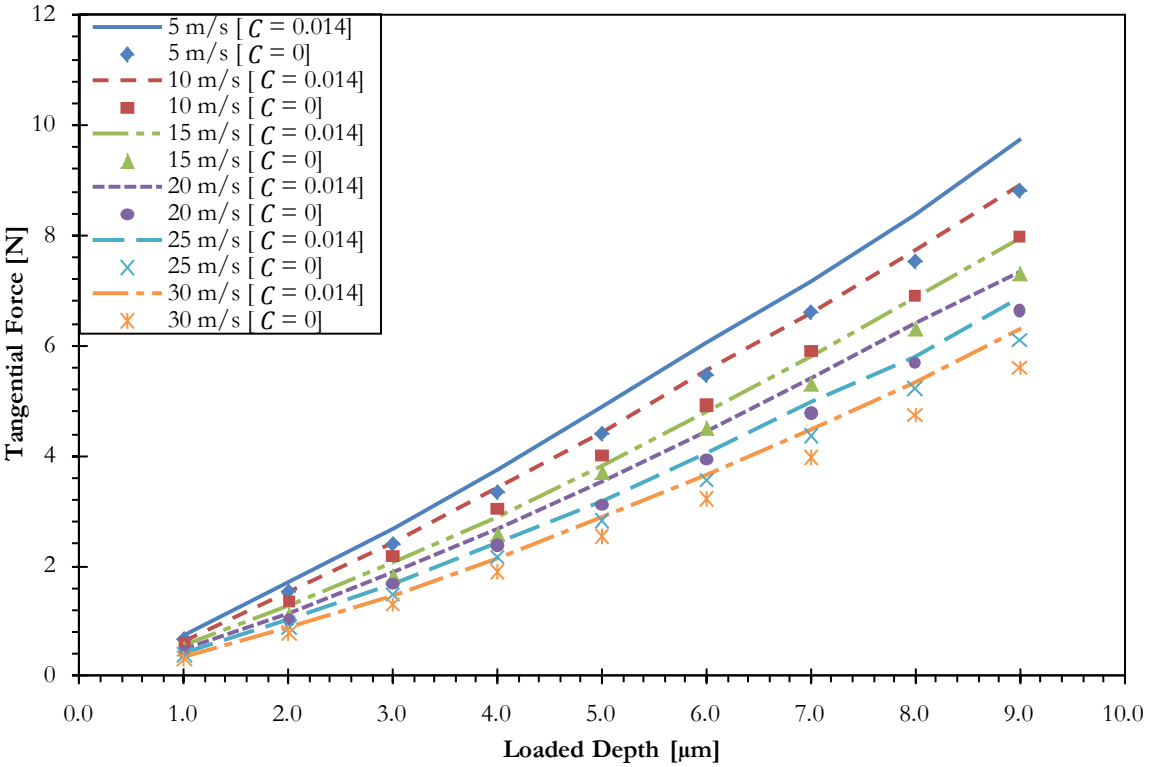

Figure 6.20 - Effect of strain-rate hardening on tangential forces.

6.2.5.2 Thermal Softening Effects

The effect of thermal softening can be investigated using the finite element model by setting the thermal softening modifier m to zero in the previously discussed Equation (3.9) and re-running the models. Figure 6.21 shows that the normal forces increased when thermal softening was deactivated; therefore, thermal softening would result in a decrease in the normal forces in the *unloaded* state. Moreover, thermal softening is only dependent on the state of effective plastic strain in the workpiece, as shown previously in Equation (3.11), and would therefore affect all of the scratching speeds equally as opposed to the observed increase in the normal forces as the scratching speed was increased. Accordingly, thermal softening is not responsible for the observed increase in the normal forces with an increase in scratching speed.

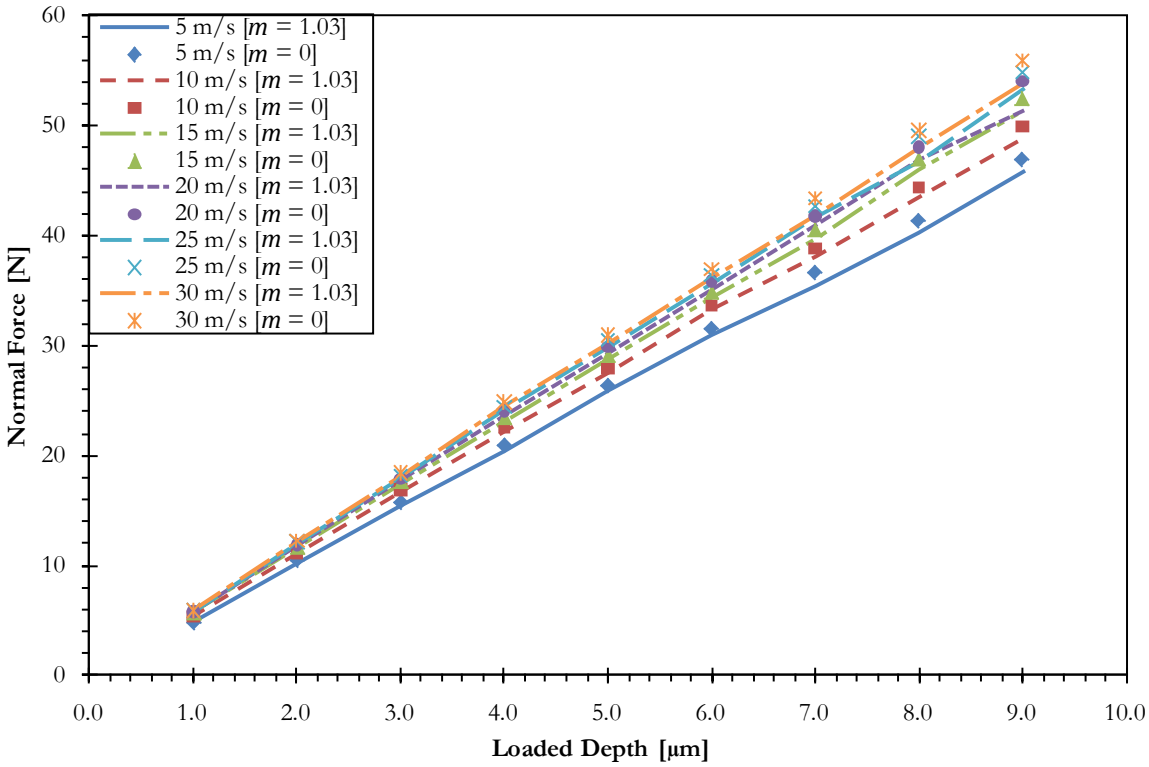

Figure 6.21 - Effect of thermal softening on normal forces.

The effect of thermal softening on the tangential forces can be seen in Figure 6.22 which shows the tangential forces with and without the thermal softening modifier set to zero. As the figure shows the tangential forces increased when thermal softening was deactivated;

therefore, thermal softening results in a decrease in tangential forces. However, as discussed above the effect of thermal softening is only dependent on the state of strain in the workpiece; hence, the forces should decrease uniformly irrespective of the scratching speed instead of the observed fan-like shape exhibited by the tangential forces. Therefore, it is unlikely that thermal softening was the main contributor to the decrease in the tangential forces that was observed in the experimental data as the scratching speed was increased.

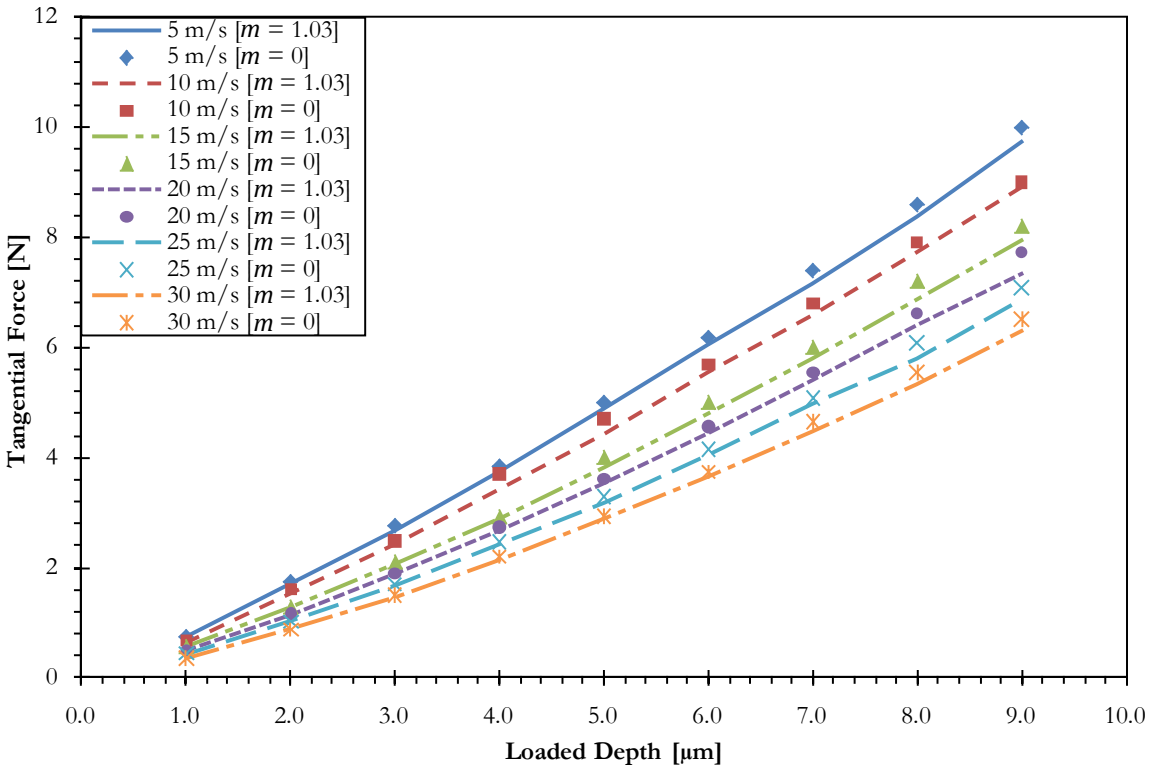

Figure 6.22 - Effect of thermal softening on tangential forces.

6.2.5.3 Material Mechanics Effects Summary

Evidently, thermal softening and strain-rate hardening compete to determine the final state of stress in the workpiece. Based on the *unloaded* normal force data it is clear that strain-rate hardening has a larger effect than thermal softening to account for the increase in normal force as a function of scratching speed. By plotting the percent change in the normal forces as compared to the benchmark values from Figure 6.19 and Figure 6.21 it was possible to determine the relative effect of strain-rate hardening and thermal softening, as shown in Figure 6.23. The figure shows the percent change in the normal force for each scratching speed as compared to the benchmark values when thermal softening was deactivated and

when strain-rate hardening was deactivated. The solid lines indicate the average change for each depth of cut while the dashed lines represent the 95% error envelopes. This figure shows that, on average, thermal softening resulted in an approximately 2% decrease in the normal forces while strain-rate hardening resulted in an approximately 11% increase in the normal forces. The figure also confirms that thermal softening was dependent only on the plastic strain as represented by the positive slope of the average line and the narrow error envelope. Had thermal softening been affected by strain rate there would have been a larger change in the forces as the scratching speed was increased. Therefore, strain-rate hardening was the likely cause for the increase in normal force as the scratching speed was increased.

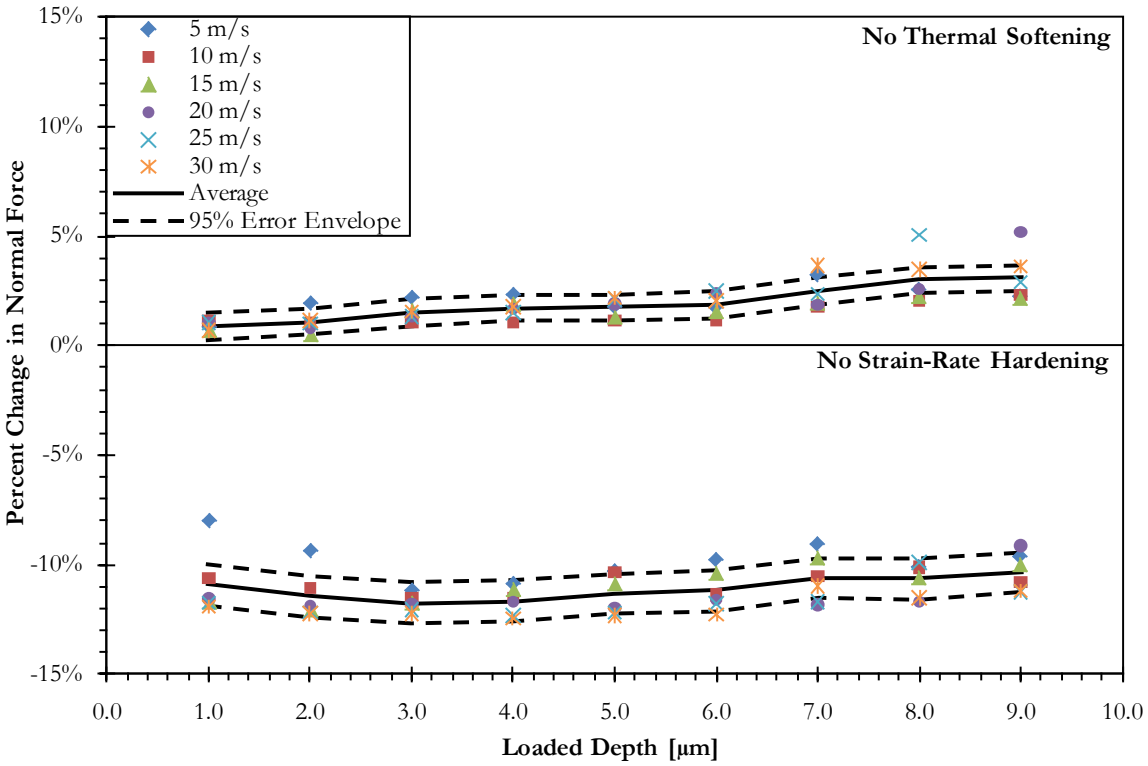

Figure 6.23 - Percent change in normal forces from benchmark values.

Figure 6.24 shows the percent change in the tangential force for each scratching speed as compared to the benchmark values when thermal softening was deactivated and when strain-rate hardening was deactivated. The solid lines indicate the average change for each depth of cut while the dashed lines represent the 95% error envelopes. This figure shows that, on average, thermal softening resulted in an approximately 2% decrease in the tangential forces while strain-rate hardening resulted in an approximately 11% increase in the

tangential forces. By comparing the changes caused by thermal softening to those caused by strain-rate hardening, one can observe that the tangential forces should increase with scratching speed; therefore, there must be additional factors contributing to the decrease in the tangential forces which will be discussed next.

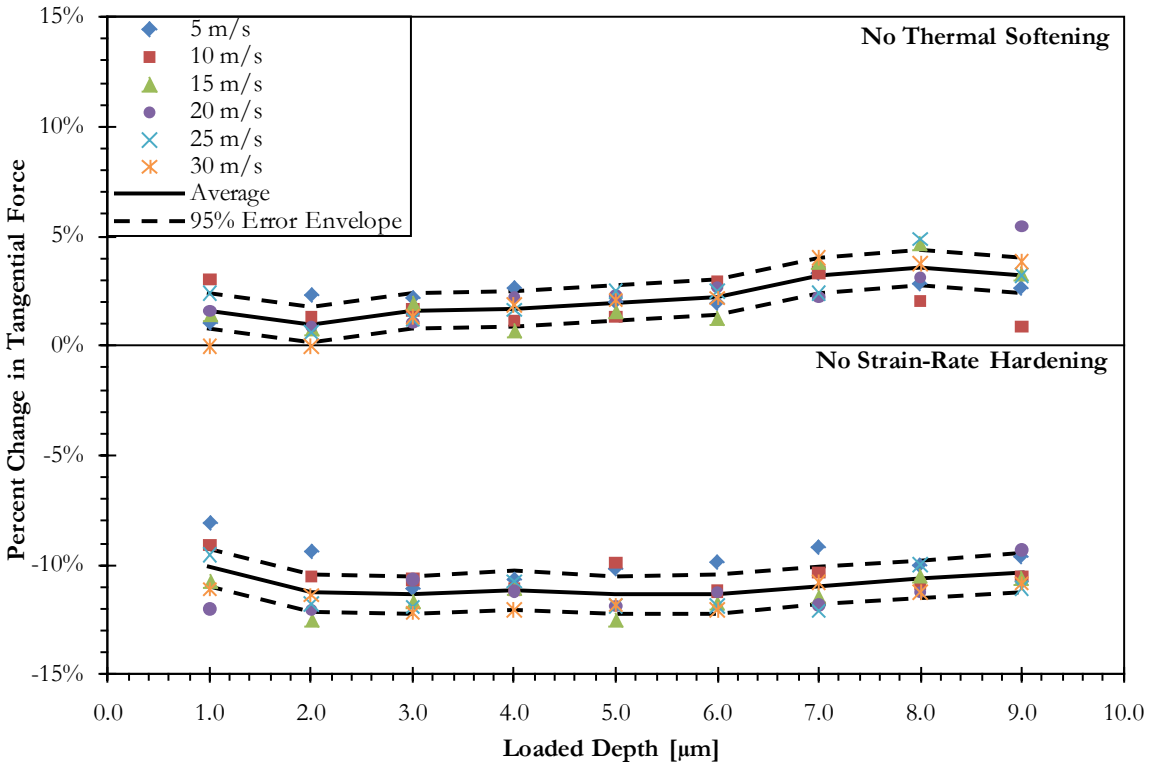

Figure 6.24 - Percent change in tangential forces from benchmark values.

6.2.6 Cutting Mechanics Effects

The process by which the cutting mechanics affects the scratching process can be divided into two general categories: cutting efficiency and depth of cut. These effects can be examined by combining the scratch profile results with the experimental and numerical force results.

6.2.6.1 Cutting Efficiency

There were several noteworthy advantages to the methods used to analyze the scratching data. The *unloaded* relationships provided insight into the final workpiece surface while the *loaded* relationships and the finite element models provided information about the process as

it was occurring. Additionally, the depth conversion process provided the ability to pinpoint the depth of cut required to transition from purely elastic rubbing to elastoplastic plowing. Pure rubbing is considered to be a fully elastic process; therefore, it is not possible to measure the depths associated with rubbing directly due to material springback. However, it was possible to infer when pure rubbing transitioned to elastoplastic rubbing and plowing based on the Y-intercepts of Figure 6.3. In the *unloaded* state there appeared to be normal forces associated with a depth of cut of zero. Using these forces it was possible to back out the equivalent *loaded* depths, which can be considered the depths required to transition from the elastic state to the elastoplastic state. These values are listed in Table 6.2 as "Elastic Transition [μm]". The elastic transition occurred at larger depths of cut as the scratching speed was increased and was likely a result of the strain-rate sensitivity of the workpiece. These values are important as they suggest that commanded depths of cut below the elastic limit will not produce any material removal. An elastoplastic state likely occurred once the commanded depths of cut became greater than the elastic limit and this may be represented by the parabolic region of the tangential forces. A fully plastic state may have been produced at the transition point from parabolic to linear trends of the tangential data. At this transition point the yield surface of the shear stress caused by the tangential force may have reached the surface producing a fully plastic state, which is similar to the progression discussed for indentation in Chapter 4. The approximate values of the elastoplastic to fully plastic transition point are listed in Table 6.2 as "Plastic Transition [μm]". As was the case with the elastic limit, the plastic transition point increased as the scratching speed was increased. The behaviour of the tangential data was similar to the indentation data in that a parabolic region represented an elastoplastic material response and a linear region represented a plastic material response, as suggested by Johnson [92].

Table 6.2 - Elastic and plastic transition depths for round-nosed stylus.

Scratching Speed [m/s]	Elastic Transition [μm]	Plastic Transition [μm]
5	0.06	3.21
10	0.10	3.50
15	0.25	4.14
20	0.40	4.19
25	0.69	4.64
30	1.09	5.31

The scratch profiles shown in Figure 6.25 are an example of the detail that can be extracted using the optical profilometer. The figure compares the profiles at five distinct depths of cut for each scratching speed and clearly demonstrates the evolution of the scratches. At the lowest depth of cut there was very little pile-up present and the profiles for all scratching speeds were very similar. At larger depths of cut the profiles exhibited larger amounts of pile-up. It is also clear from the profiles that it becomes difficult to discern between a residual groove and the surface texture of the workpiece as the depth of cut was reduced. The scratch profile for a 30 m/s scratching speed and a 2.14 μm depth of cut confirms the elastic transition results of Table 6.2 because it is apparent that the residual groove is barely discernable when compared to the surface texture at this depth of cut and scratching speed. As the table indicated the elastic transition was approximately 1.09 μm for a 30 m/s scratching speed which is roughly half the depth as shown in the scratch profile; therefore, it is not hard to visualize that the residual groove would be non-existent at approximately 1 μm depth of cut.

At first glance it would appear that the scratching speed did not affect the pile-up height; however, as shown in Figure 6.26, the average pile-up height demonstrated a decreasing trend as the scratching speed was increased. It should be noted that it was increasingly difficult to discern between piled-up material and the background surface texture of the workpiece as the depth of cut was decreased, hence the lack of data for the two shallowest depths of cut. Lower levels of pile-up material with increasing scratching speeds may be attributable to the decrease in the coefficient of friction or a change in the cutting mechanics.

As was noted in the experimental results the normal forces increased with scratching speed in the *unloaded* state. A change in the cutting mechanics may be safely neglected as a cause for the increasing normal forces in the *unloaded* state since changes from plowing to cutting typically reduce forces as cutting is a more efficient process.

As shown in Figure 6.26 the average pile-up height decreased with an increase in scratching speed, which implies that more material was removed rather than simply pushed aside and

suggests that the process efficiency has increased due to a transition from plowing to cutting. Cutting is a more efficient process than plowing; hence, a reduction in the tangential forces.

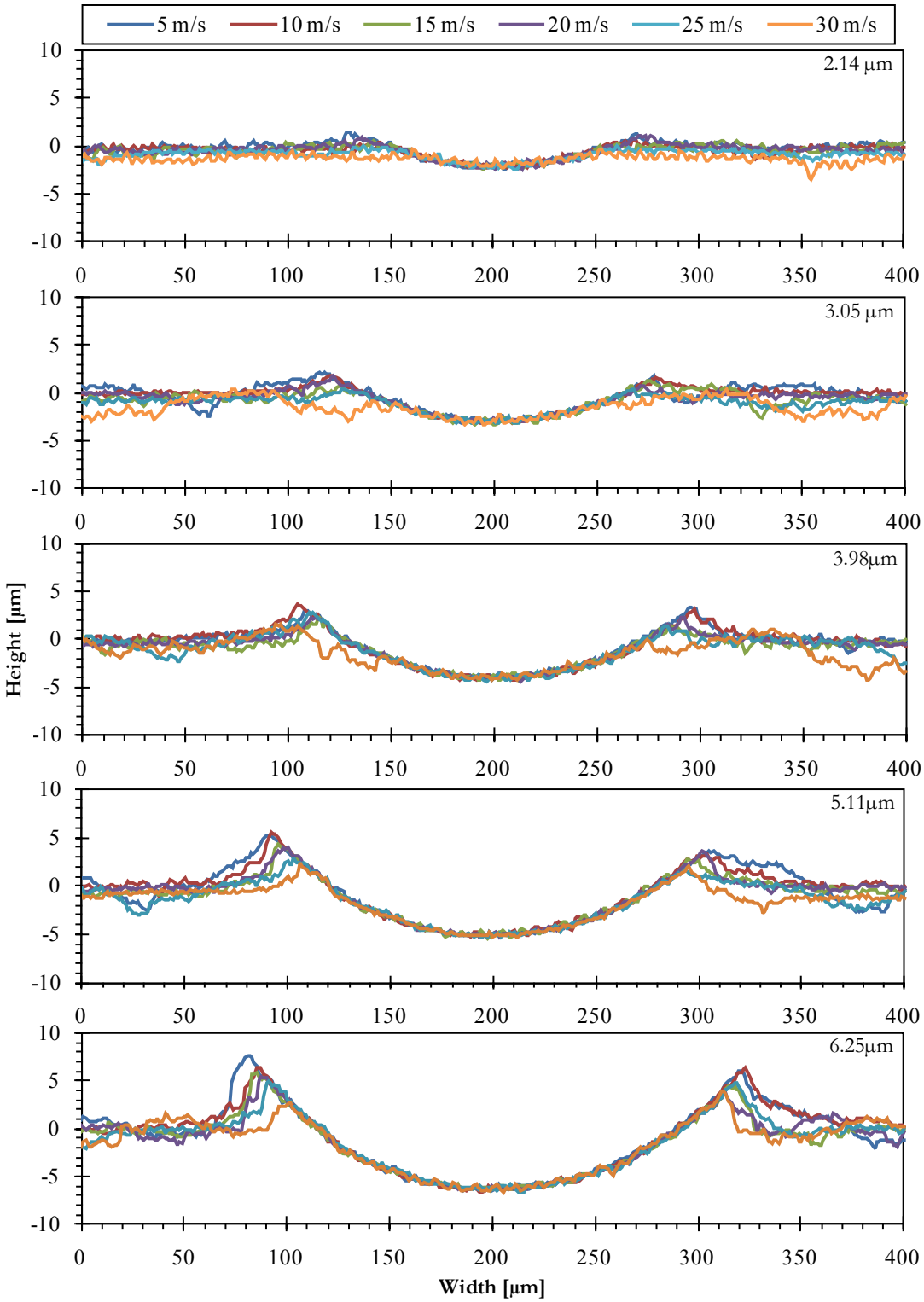

Figure 6.25 - Scratch profiles for round-nosed stylus.

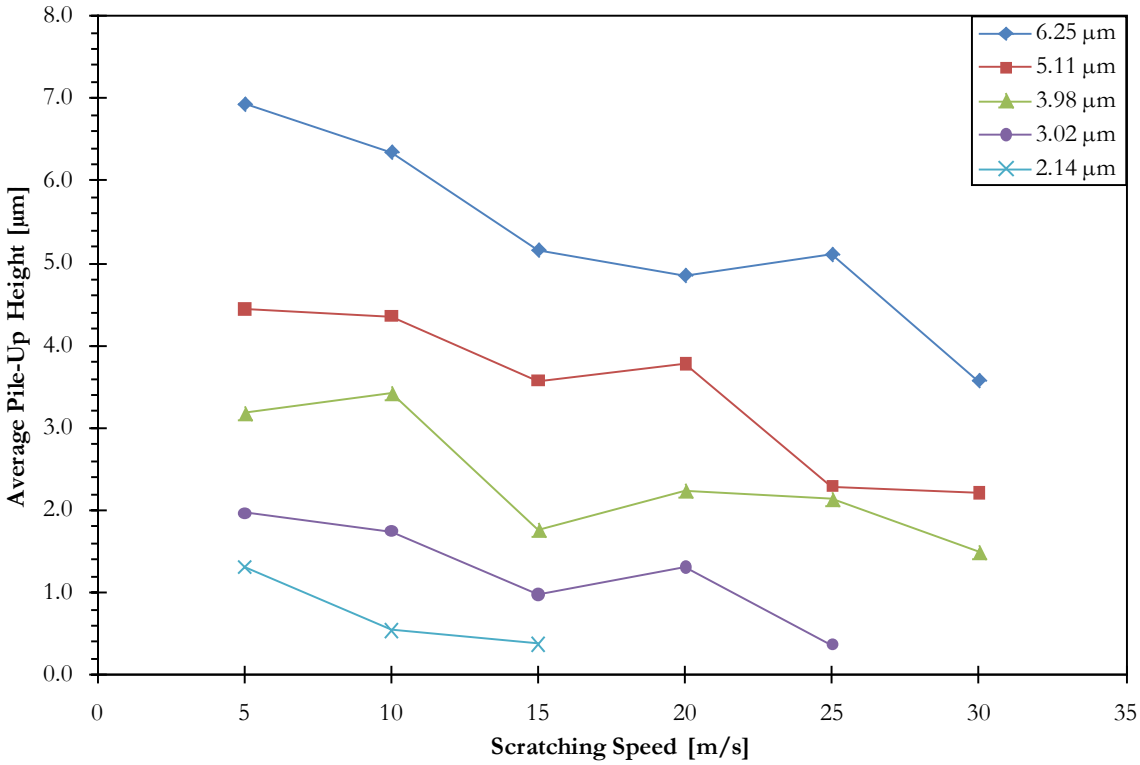

Figure 6.26 - Average pile-up height as a function of speed for round-nosed stylus.

A common quantity used to describe the process efficiency of a cutting operation is the specific energy, as discussed in Chapter 2. Since the workpiece did not move during the experiments, Equation (2.4) must be altered to:

$$MRR = A_S v_w \tag{6.2}$$

where A_S is the cross sectional area of the stylus that is engaged in the workpiece and v_w is the scratching speed. The area A_S for the round-nosed stylus is represented by Figure 6.27 and is calculated from:

$$A_S = \frac{R^2}{2}(\theta - \sin\theta) \tag{6.3}$$

where R is the radius of the round-nosed stylus and the contact angle θ is found from:

$$\theta = 2\left(\sin^{-1}\frac{w/2}{R}\right) \tag{6.4}$$

where w is the contact width found from:

$$w = 2\sqrt{(2aR) - a^2} \tag{6.5}$$

where a is the depth of cut.

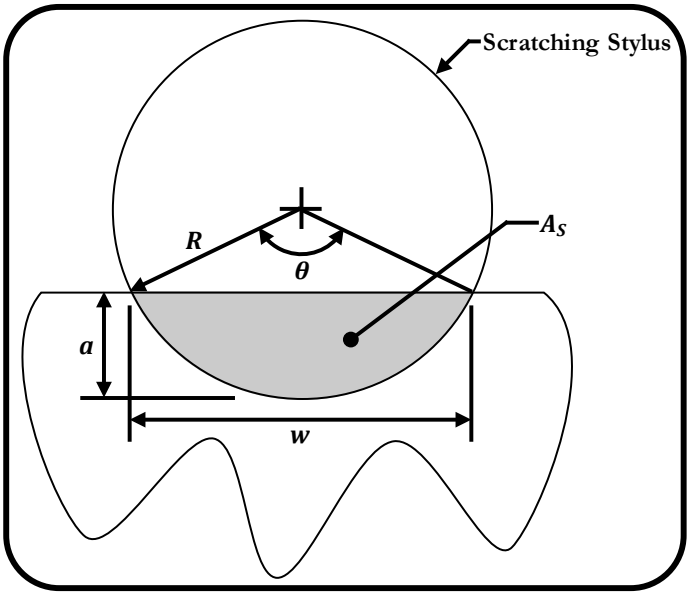

Figure 6.27 - Round-nosed stylus-workpiece interaction area representation.

As was shown in Equation (2.6) the power consumed during the scratching process is required to calculate the specific energy which is readily accomplished using the experimental data as shown in Equation (2.5); however, the finite element models compute and store the total system energy E_{tot}, which allows direct calculation of the numerical power P_{FE} by taking the time derivative:

$$P_{FE} = \frac{d}{dx}[E_{tot}(t)] \tag{6.6}$$

The calculated experimental and numerical specific energy for each scratching speed is shown in Figure 6.28. The experimental data is based on the fitted data to better illustrate the trends in the data. As can be seen in the figure, the specific energies decreased as the scratching speed was increased, which shows that higher scratching speeds produced a more efficient process. The validity of the finite element models is further enhanced by the excellent match to the experimental specific energies with an average error of 4.7%. Similar specific energy values and trends for steel were reported by Malkin [2] which helps to validate the proposed experimental approach.

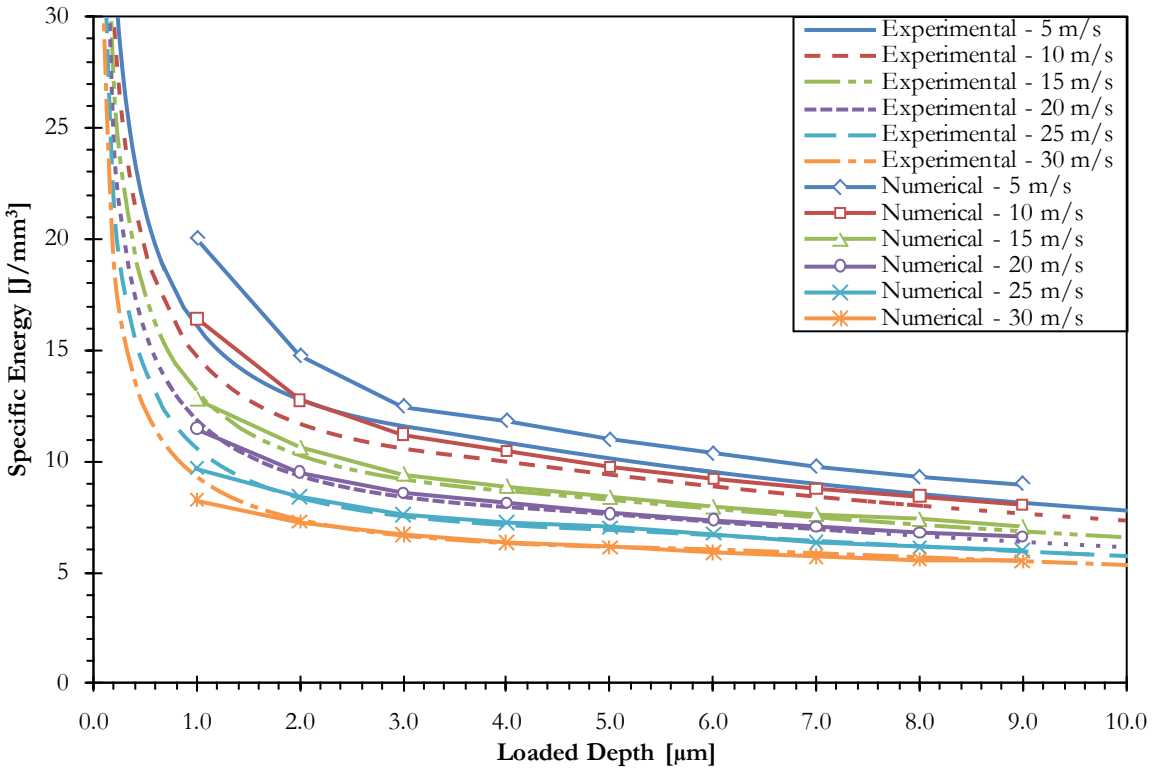

Figure 6.28 - Specific energy as a function of loaded depth for round-nosed stylus.

6.2.6.2 Depth of Cut Effects

The depth dependence of the results is clearly evident at low depths of cut based on the changes in the experimental force ratio data and the specific energy data as the depth of cut was increased. Both sets of experimental data show that the slope was initially high at low depths of cut and gradually decreased as the depth of cut was increased. Interestingly, the depth dependence seemed to occur at *unloaded* depths of cut of less than 2 µm, which was also the average location of the parabolic to linear transition point of the tangential force data. These results may be attributable to an increase in rubbing due to the surface roughness of the workpieces, which had a measured peak-to-valley height of approximately 2 µm. This phenomenon can be explained with the help of Figure 6.29 which shows the ideal round-nosed stylus superimposed on the measured surface of the workpiece at a depth of cut of 1 µm. It can be seen in the illustration that for shallow depths of cut the stylus was entering and exiting the workpiece material as it translated across the surface. It is proposed that this intermittent stylus-workpiece contact reduced the volume of constraining material ahead of the tool, which permitted the peaks to flow into the valleys and increased the

proportion of rubbing as a result. As the depth of cut was increased the tool-workpiece interaction became more continuous and, as a result, more efficient. This surface texture may help to explain the higher numerically predicted specific energies as compared to the experimental data at low depths of cut and low cutting speed as the intermittent contact would require less energy per unit volume of material removed. The finite element model represents the workpiece as a perfectly flat surface whereas in reality a surface texture exists. Additionally, the cutting tool was considered perfectly smooth whereas it may also have a pronounced surface texture. Hence, it would seem that the experimental data represents the interaction between real surfaces while the numerical data represents the interaction between ideal surfaces. Consequently, commanded depths of cut must be greater than 2 μm to achieve full contact between the stylus and the workpiece to mitigate the effects of the surface roughness. An additional contribution to the depth dependence may be related to the preparation of the workpiece. It has been shown, for example by Marinescu *et al.* [122], that the grinding operation produces a thin band of hardened material at the surface of the workpiece due to thermal and mechanical loading, which may lead to increased energy requirements to penetrate; hence, the high specific energy at low depths of cut.

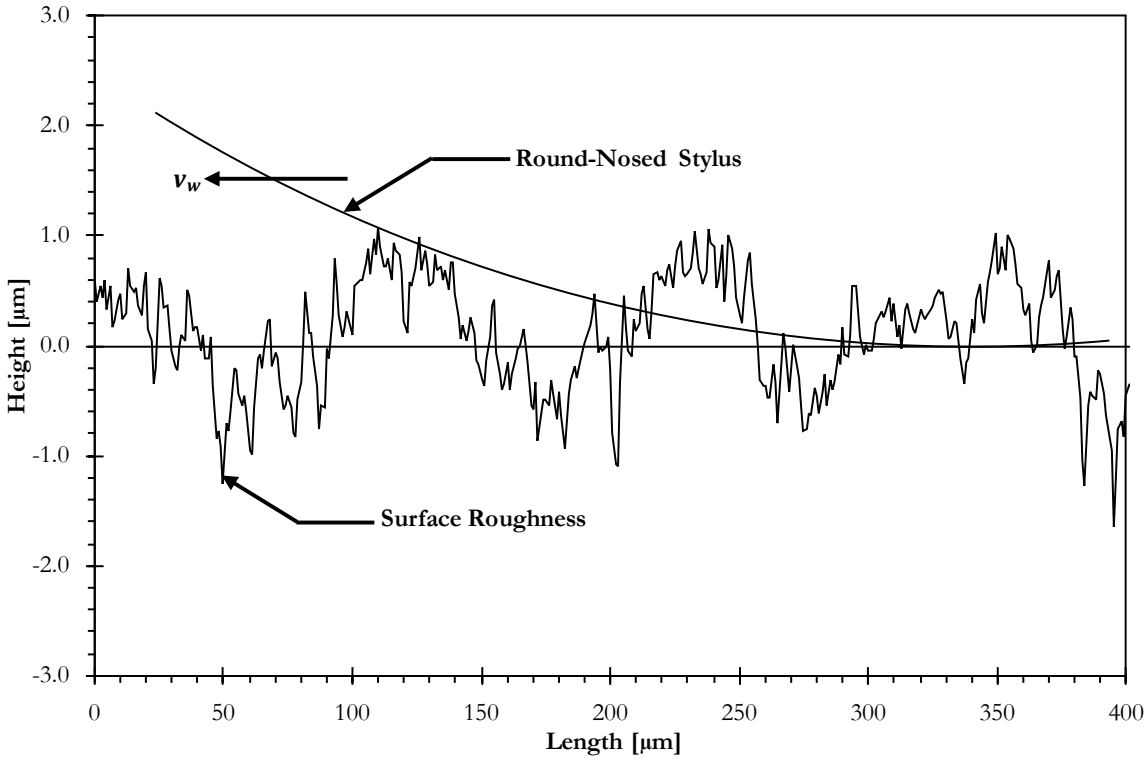

Figure 6.29 - Ideal round-nosed stylus superimposed of real workpiece surface.

6.2.7 Subsurface Stresses

It has already been shown that the finite element model is a robust tool for analyzing the scratching process alongside the experimental data. It can also be used to analyze the subsurface stresses, which is not possible with the experimental data alone.

The result that an increase in the depth of cut has on the scratching process can be seen by analyzing the subsurface stresses as shown in Figure 6.30, where the X-, Y-, and XY-stresses on the XY-symmetry plane are shown top to bottom for the same scratching speed at two different depths of cut where the images on the left are for a depth of cut of 2 μm and the images on the right are for a depth of cut of 8 μm. The dashed lines in the figure represent the approximate yield surface of the workpiece material. As expected, the stresses increased as the depth of cut was increased. Despite the increase in the depth of cut, the general trends of the stress distributions remained the same. In the X-direction, the stresses were compressive under and in front of the stylus then switched to tensile behind the stylus. This switch to tensile stresses behind the stylus can be responsible for cracking in the residual groove [123,124]. The stresses were completely compressive in the Y-direction and the largest stresses occurred directly under the stylus at the contact area. The shear stresses were compressive ahead of the stylus and tensile behind the stylus due to the shearing action of the stylus as it travelled through the workpiece.

Analysis of the stress distributions also revealed that the stresses increased as the scratching speed was increased as shown in Figure 6.31. This figure shows the X-, Y-, and XY-stresses on the XY-symmetry plane for scratching speeds of 5 m/s and 30 m/s at the same depth of cut of 3 μm and, clearly, the stresses increased with a higher scratching speed. These larger subsurface stresses at higher scratching speeds resulted in larger amounts of springback, which created the offsets in the *unloaded* normal force data.

The effect that strain-rate hardening had on the scratching process can be seen by analyzing the subsurface stresses as shown in Figure 6.32, where the X-, Y-, and XY-stresses on the XY-symmetry plane are shown top to bottom for the same scratching speed of 20 m/s and at the same depth of cut of 6 μm where the images on the left have strain-rate hardening activated and the images on the right have strain-rate hardening deactivated. The dashed

lines in the figure represent the approximate location of the yield surface of the workpiece material. As the figure shows, the size of the stress fields decreased and the approximate location of the yield surface shrank when strain-rate hardening was deactivated. Interestingly, the X-stresses became more tensile behind the stylus when strain-rate hardening was activated due to the increased material strength. Since the workpiece strengthened when strain-rate hardening was active the normal forces in the *unloaded* state would tend to increase as a larger force would be required for a given depth of cut.

The effect that thermal softening has on the scratching process can be seen by analyzing the subsurface stresses shown in Figure 6.33 which shows, from top to bottom, the X-, Y-, and XY-stresses on the XY-symmetry plane of the workpiece for the same depth of cut of 9 μm and cutting speed of 30 m/s, where the images on the left have thermal softening activated, the images on the right have thermal softening deactivated, and the approximate location of the yield surface is represented by the dashed lines. The difference in the figures is subtle as was to be expected based on the small changes in the forces as reported earlier; however, the size of the stress fields did increase and the approximate location of the yield surface grew when thermal softening was deactivated. An interesting result was that the tensile X-stresses were noticeably lower in the wake of the stylus when thermal softening was activated. This result likely occurred because thermal softening permitted the material to stretch more readily due to a reduction in material strength; thus, the tension in the workpiece was reduced.

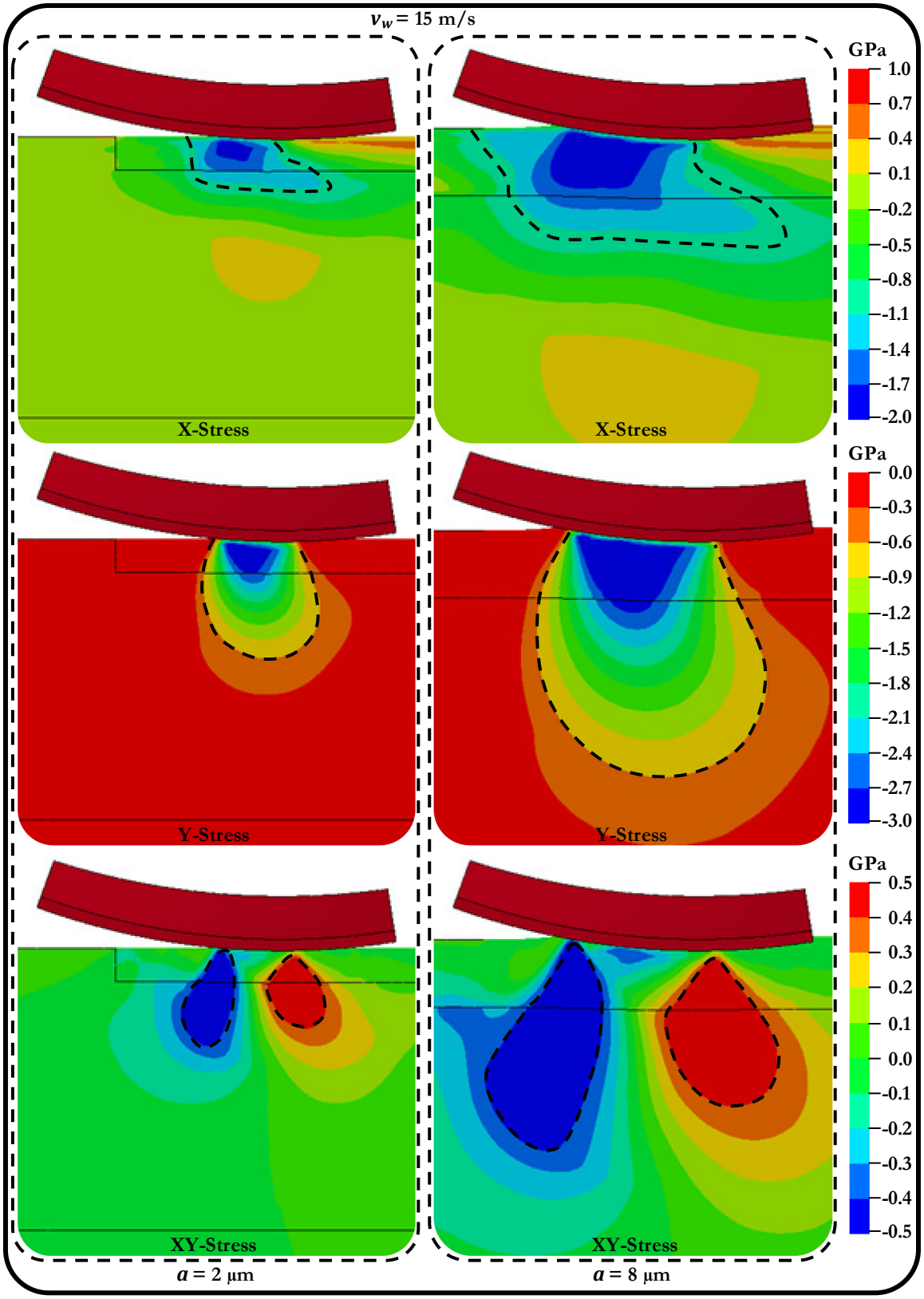

Figure 6.30 - Effect of depth of cut on subsurface stresses.

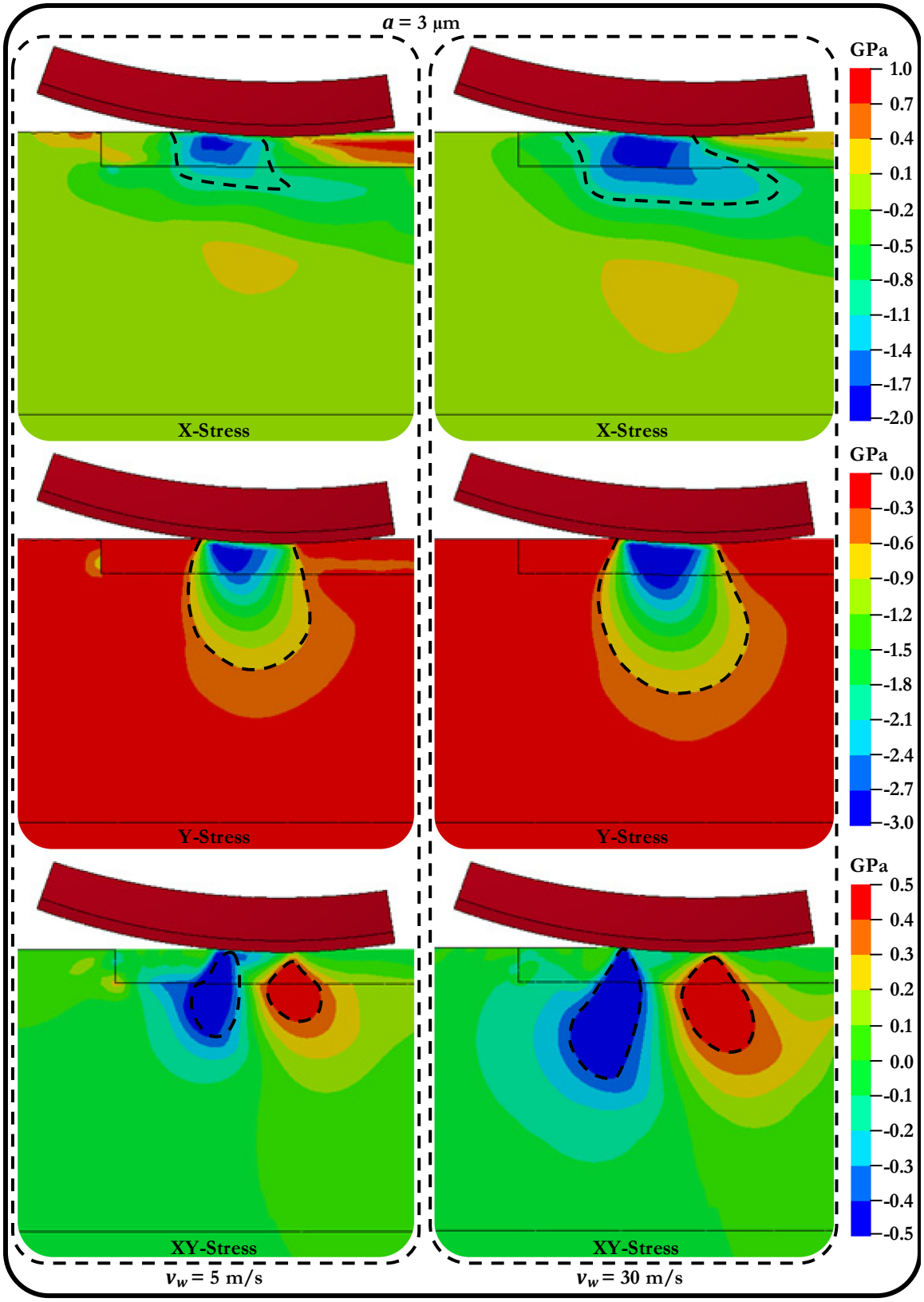

Figure 6.31 - Effect of scratching speed on subsurface stresses.

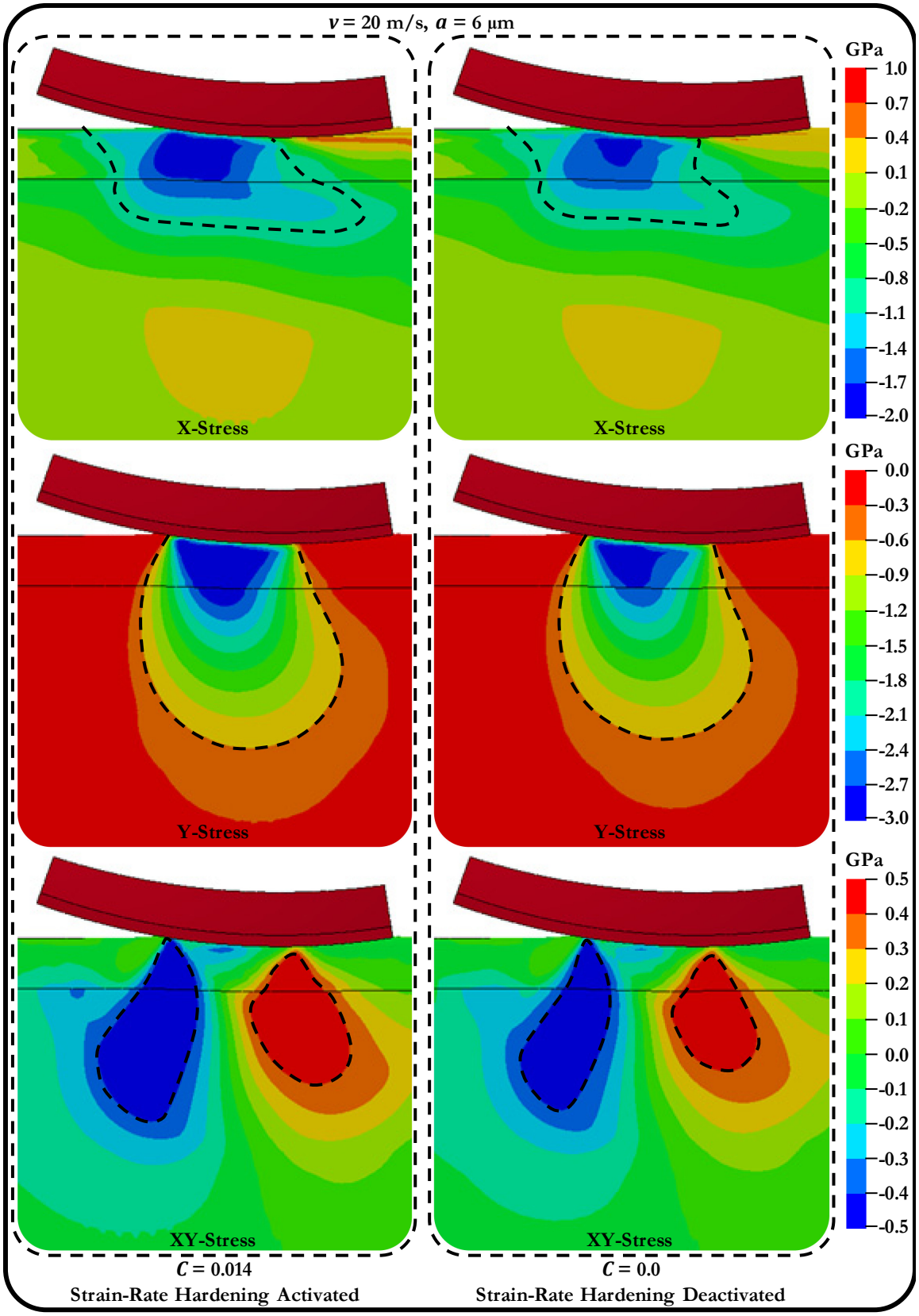

Figure 6.32 - Effect of strain-rate hardening on subsurface stresses.

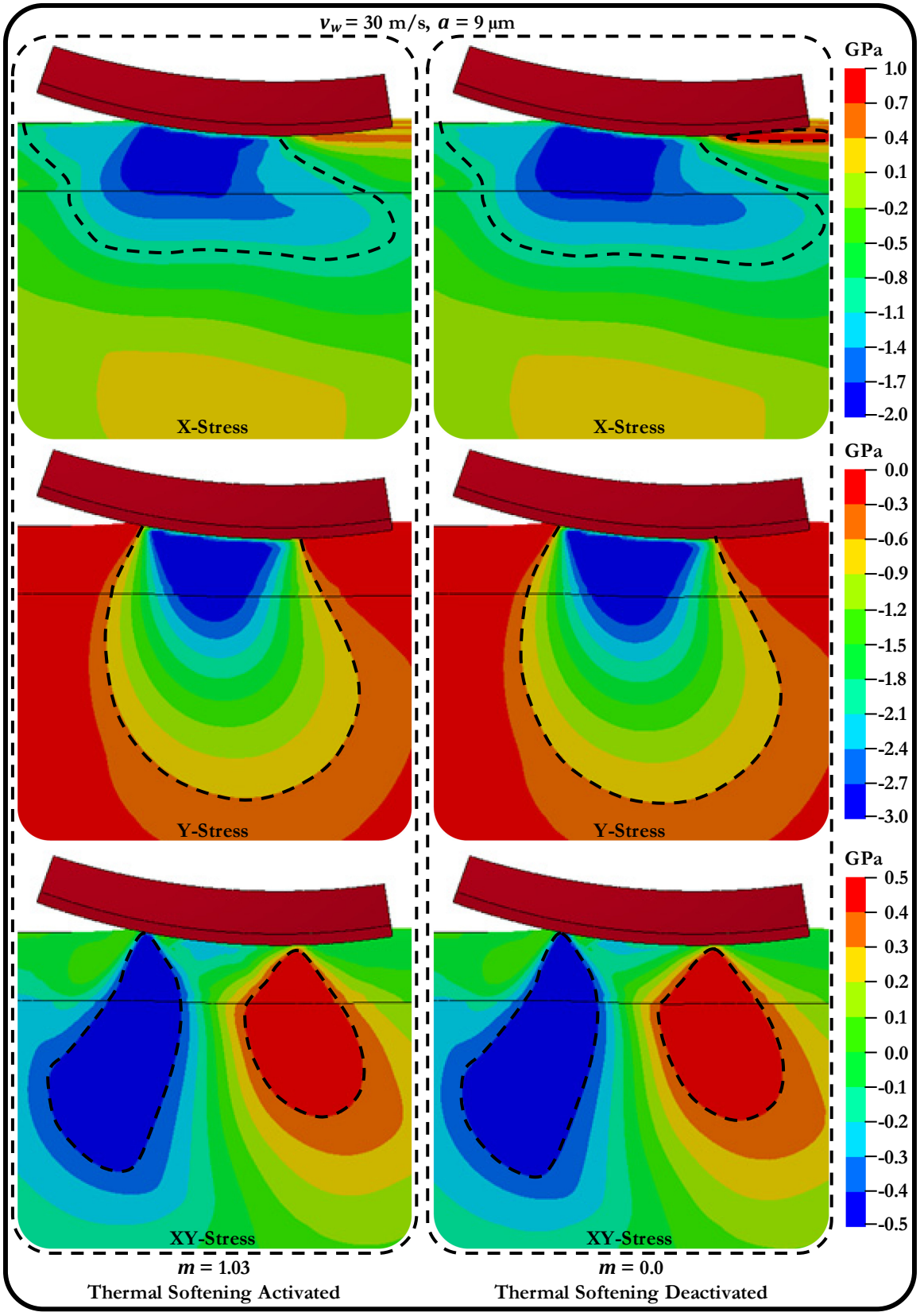

Figure 6.33 - Effect of thermal softening on subsurface stresses.

6.2.8 Discussion

As the preceding results and analysis have demonstrated, choosing the optimal process parameters to maximize the cutting effectiveness of an abrasive grain is not straightforward as there are several factors that must be taken into account. Larger depths of cut were more efficient due to the reduced specific energies; however, it was also shown that larger depths of cut produced larger scratches and larger amounts of pile-up which may result in poor surface finish qualities. Therefore, a balance must be obtained between the efficiency of the operation and the desired surface finish of the workpiece. As the scratching speed was increased the tangential forces, the force ratios, the specific energies, and the average pile-up height all decreased, which suggested that the cutting action became more efficient with an increase in scratching speed. Based on these findings it would seem that higher scratching speeds are ideal; however, this result may change when tool wear is taken into account as cutting tools tend to wear more quickly at higher cutting speeds. Additionally, it was shown that higher scratching speeds produced more springback which reduces the accuracy of the process. It is clear from all of the results that there was no clear transition from rubbing to plowing to cutting. At low depths of cut, especially below the elastic limit of the workpiece, pure rubbing occurred. As the depth of cut was increased the proportion of rubbing decreased while plowing increased. As the depth of cut was further increased cutting began and rubbing and plowing were reduced. It is likely that all three phases were occurring simultaneously with different weightings depending on the depth of cut and scratching speed. Since cutting is the desired outcome of the grinding operation it would be wise to choose the process parameters such that the uncut chip thickness encourages cutting. As was shown, this is achieved with larger depths of cut and higher cutting speeds. From a grinding perspective, the results indicate that down grinding at higher cutting speeds is ideal. In this manner, the depth of cut is highest at the beginning of the cut which will increase the cutting action and minimize the rubbing and plowing actions leading to a more efficient process. Additionally, the degradation in the surface finish due to the larger depth of cut and pile-up would be occurring near the top of the material to be removed by subsequent abrasive grains; therefore, the degradation of the finished surface will be minimized.

6.3 Case Study: Reducing the Stylus Radius

The radius of the round-nosed stylus in the previous section was 0.508 mm and approximately corresponded to a 15-grit abrasive grain. Although this grain size was within the realm of common abrasive sizes, it was large compared to the more common abrasive sizes used in industry. The purpose of this section is to numerically investigate the effect that reducing the radius of the stylus has on the scratching process. The three common abrasive grain sizes and their approximate radius chosen for the comparison are shown in Table 6.3. The original size of the round-nosed stylus is also included in the table for comparison purposes. The scratching speed was limited to 30 m/s for all of the test cases to limit the computational time required.

Table 6.3 - Grit number and corresponding grain radius.

Grit #	Radius [mm]
15	0.508
46	0.165
80	0.095
120	0.063

Figure 6.34 shows the effect of the grain size on the normal forces and shows that the normal forces decreased as the grain size was decreased. This result is not surprising as it should require a lower force to push a smaller object into a workpiece.

The change in the tangential forces as the grain size was reduced is shown in Figure 6.35 and shows that the tangential forces also decreased as the grain size was reduced. Again, this result is not surprising as a lower force should be required to push a smaller object through a material.

The effect that decreasing the grain size has on the force ratios is shown in Figure 6.36. This figure shows that the force ratios increased as the grain size was decreased. This result is interesting as it suggests that the tangential force did not decrease as quickly as the normal force. Since it is known that the adhesion friction is constant for a given scratching speed this increase in the force ratio suggests that the plowing friction has increased. An increase in the plowing friction may result in an improved process efficiency as this indicates that

there was a larger plowed lip ahead of the grain. Larger amounts of piled-up material ahead of the grain would likely form a chip more easily.

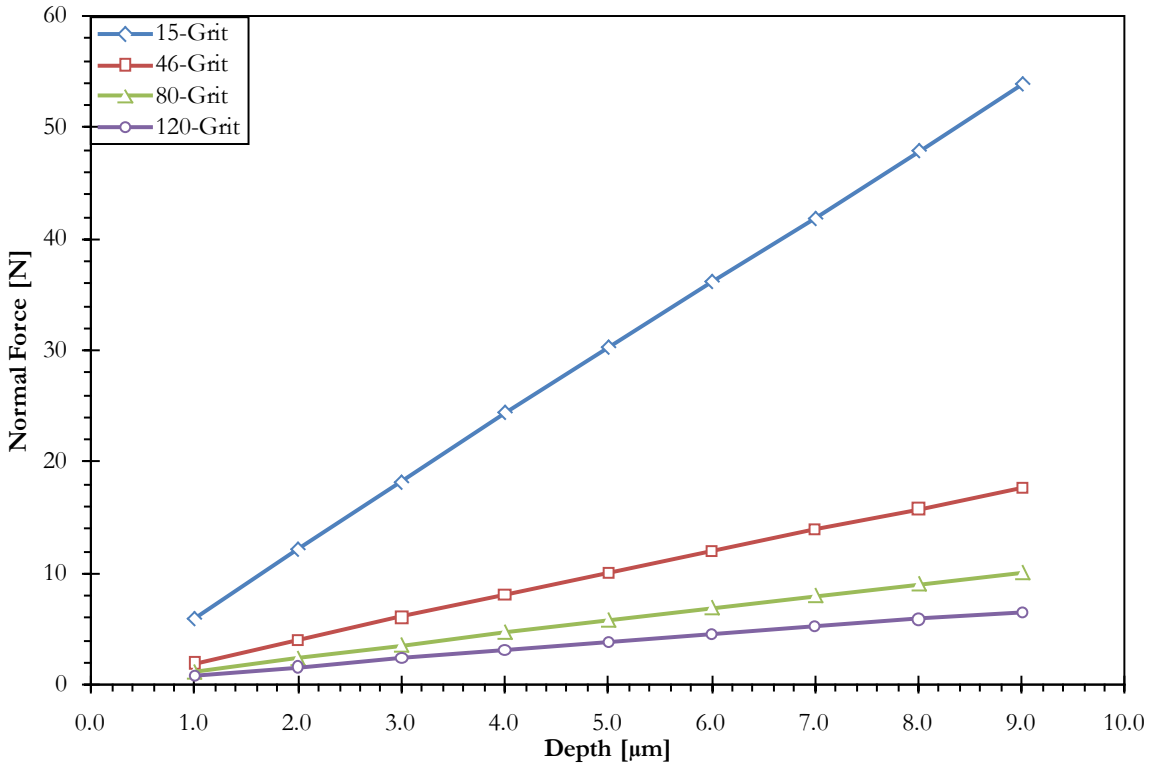

Figure 6.34 - Effect of grain size on normal forces.

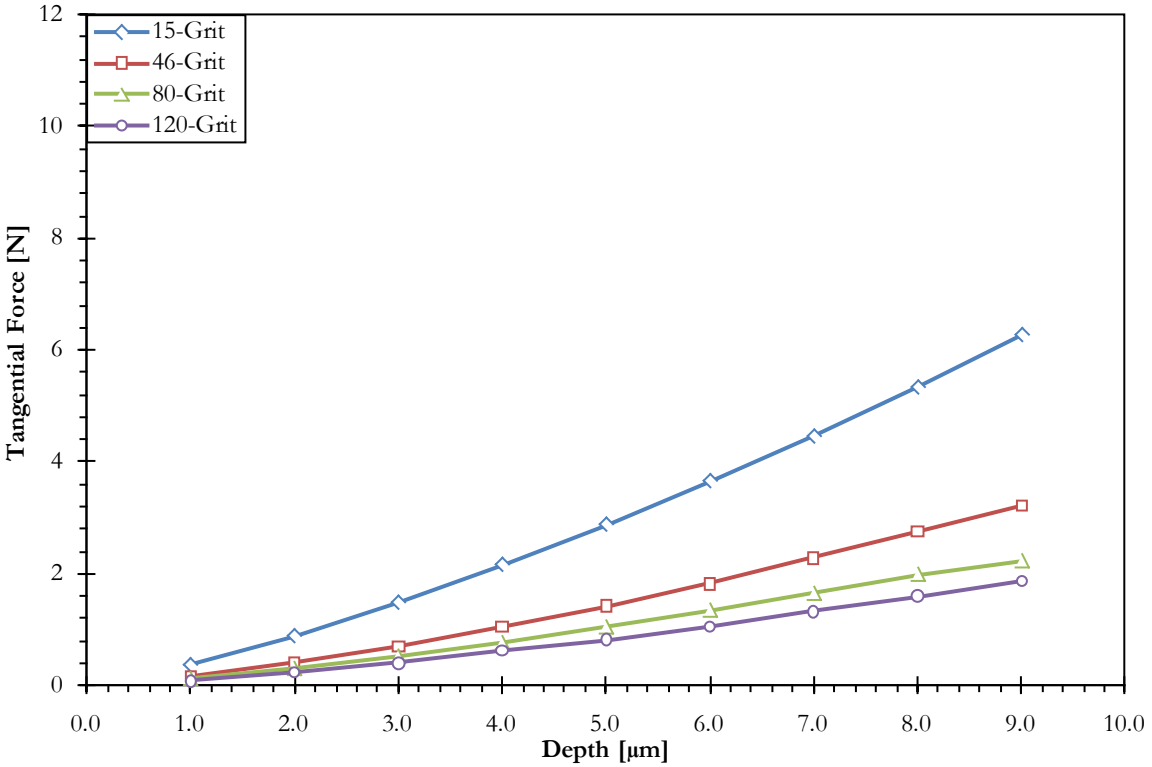

Figure 6.35 - Effect of grain size on tangential forces.

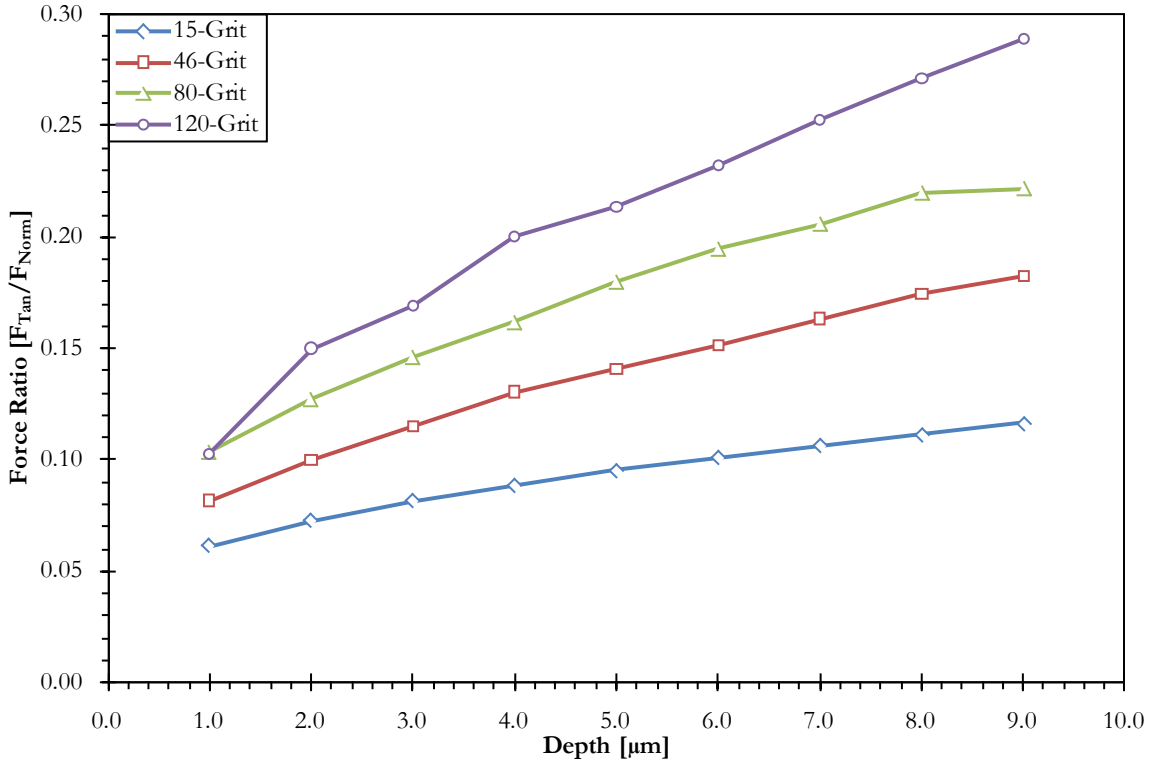

Figure 6.36 - Effect of grain size on force ratios.

This improvement in the process efficiency can be confirmed by examining Figure 6.37 which shows that the calculated specific energies decreased as the grain size was decreased. This decrease in specific energy as the grain size was decreased is important as it suggests that smaller grains should be used; however, it can be seen in the figure that the specific energies for the three more common abrasive sizes are very close to each other, which indicates diminishing returns as the grain size is decreased. The reduction in the specific energy can likely be attributed to a change in the relative rubbing, plowing, and cutting energies. The reduction in the grain size results in a reduction in the amount of rubbing between the stylus and the workpiece due to the reduced contact area.

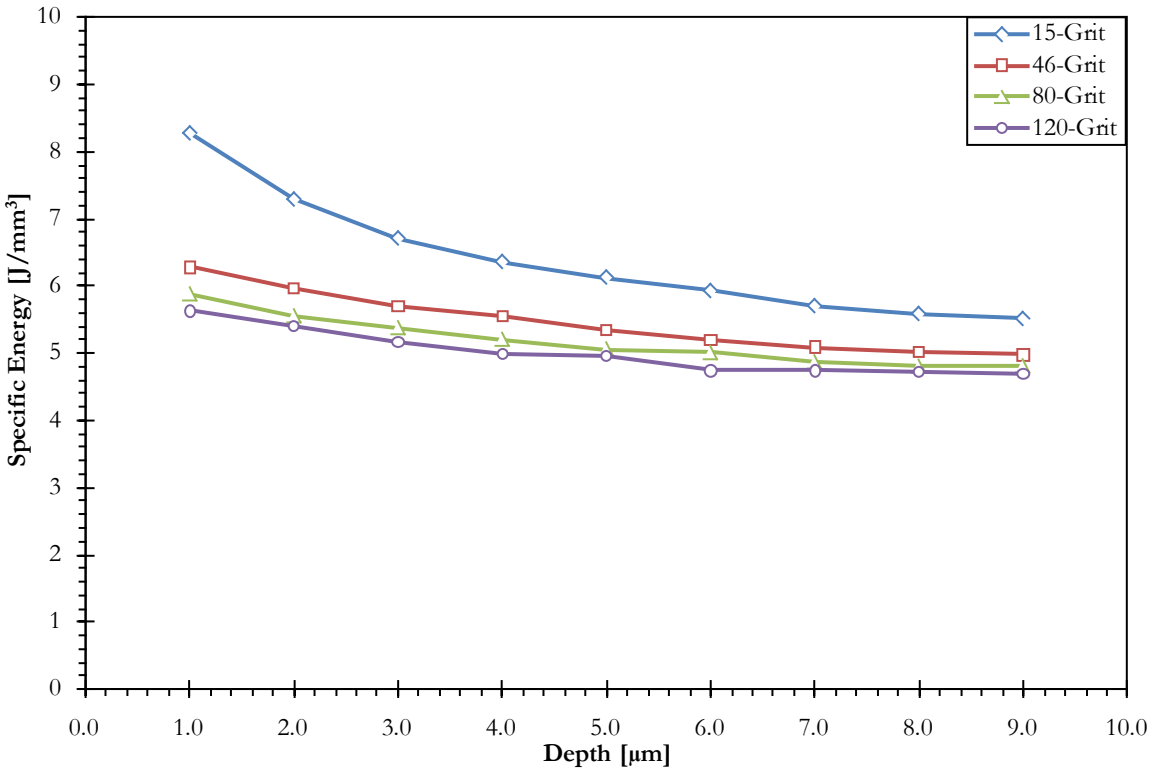

Figure 6.37 - Effect of grain size on specific energy.

The decrease in the normal force, tangential force, and specific energy as the grain size was decreased can likely be related to the change in the effective rake angle of the smaller abrasive grains, as illustrated in Figure 6.38. The figure shows that as the grain size is reduced the effective rake angle would become less negative. According to the Merchant

equation discussed in Section 3.2, a less negative rake angle would result in a larger shear plane angle and subsequently lower forces to cause material shearing.

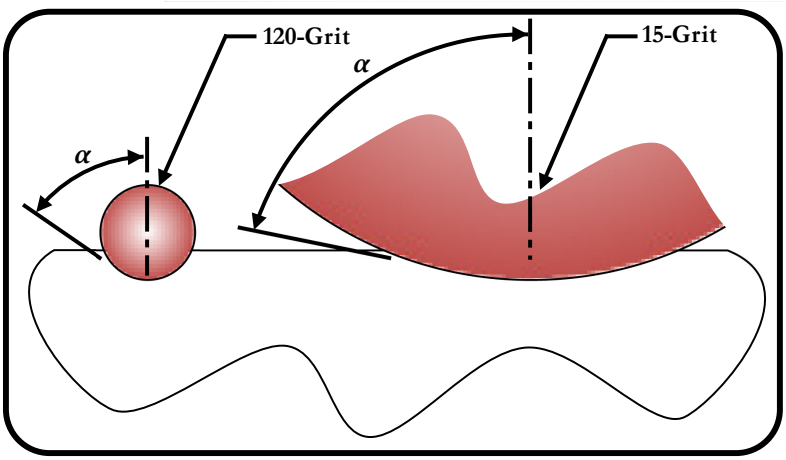

Figure 6.38 - Effect of grain size on effective rake angle.

The change in the subsurface stresses as the grain size was decreased is shown in Figure 6.39, which shows the von Mises stresses on the XY-symmetry plane for a scratching speed of 30 m/s and a depth of cut of 5 μm, where the dashed lines indicate the approximate location of the yield surface. The figure shows that the volume of stressed material and the volume of yielded material decreased as the grain size was decreased; however, the maximum stress increased slightly, from 1.28 GPa for the 15-grit abrasive grain to 1.33 GPa for the 120-grit abrasive grain. The decrease in the volume of stressed material and the increase in maximum stress can be related to the smaller contact area created by the smaller abrasive grains. Lower subsurface stresses may improve the finished quality of ground parts due to a reduction in the residual stresses. Furthermore, a reduction in the subsurface stresses may reduce the likelihood that unfavourable tensile residual stresses occur.

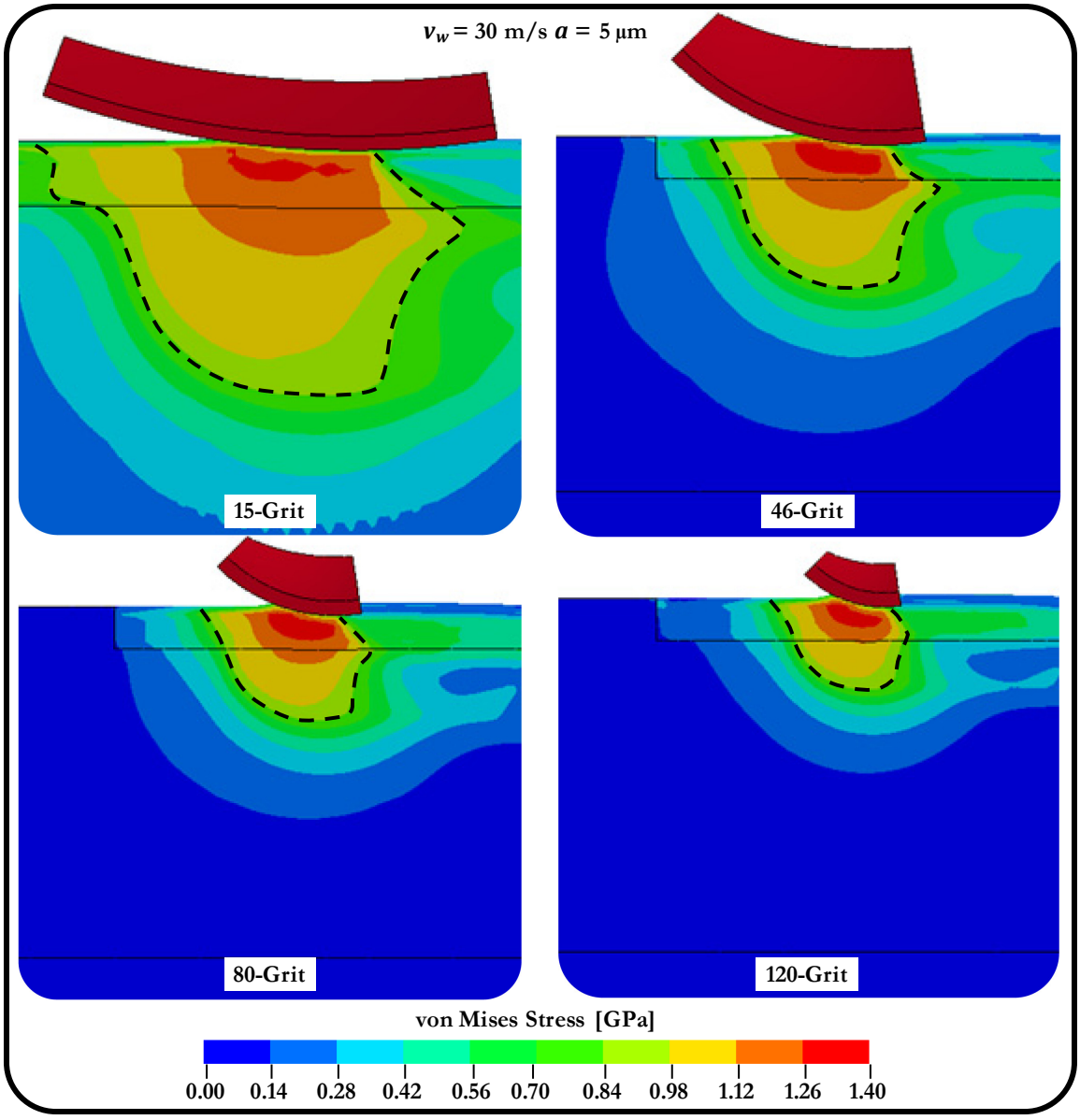

Figure 6.39 - Effect of grain size on subsurface von Mises stress.

6.4 Summary

This chapter presented the finite element scratching model, the experimental scratching data, and an in-depth analysis of the scratching process for the round-nosed stylus. The finite element scratching model was introduced based on the numerical parameters established with the indentation model and was shown to agree with the experimental data. The experimental data was used in conjunction with the finite element model to thoroughly investigate the high-speed scratching process. It was found that the normal forces increased

as the scratching speed increased due to strain-rate hardening of the workpiece and that the tangential forces decreased as the scratching speed was increased due to a reduction in the coefficient of friction between the stylus and the workpiece and a due to a change in the cutting mechanics. The scratch profiles showed that the cutting mechanics changed as the scratching speed was increased due to a reduction in the material pile-up height as the scratching speed was increased. The approximate depths of cut for the transitions from elastic, elastoplastic, and fully plastic scratching were identified and were found to increase as the scratching speed was increased. A case study showed that decreasing the grain radius resulted in decreases in the normal force, tangential force, specific energy, and volume of stressed material, and an increase in the force ratio and maximum subsurface stress. Based on the findings in this chapter it is recommended that the process parameters are chosen such that: down grinding is performed, higher cutting speeds are used, and larger maximum chip thicknesses are created. Additionally, smaller abrasive grains should be chosen provided that the uncut chip thickness remains constant as the abrasive size is decreased. These parameters will: maximize the material removal rate, minimize the specific energy, minimize the adverse affects on the surface roughness, and improve the service life of the finished part. The next chapter will discuss the results from the flat-nosed stylus scratching tests.

Chapter 7 Flat-Nosed Scratch Testing

This chapter will continue the discussion of high-speed scratch testing; however, a flat-nosed diamond stylus will be investigated to simulate the effects of a worn abrasive grain. The same experimental apparatus that was used with the round-nosed stylus was used for the flat-nosed stylus. The scratching speed was 20 m/s and the depth of cut range was 0.3 μm to 5.0 μm. The refinements that were made to the finite element model to accommodate the new stylus geometry will also be discussed.

7.1 Experimental Results

Figure 7.1 shows a representative three-dimensional scan of a portion of a workpiece that has been scratched with the flat-nosed stylus, where the heights have been scaled five times their actual height for improved visibility. As was the case with the round-nosed stylus there was sufficient space between each scratch to prevent interactions. It can also be seen in the figure that the bottom of the scratches were not flat which was a result of the taper introduced during the workpiece preparation. This effect was less pronounced with the

round-nosed stylus because of the sphere's symmetry, as represented by Figure 7.2. Note that the taper has been exaggerated for clarity. The consequence of the workpiece taper of approximately 0.28° when using the flat-nosed stylus was that the depth of cut varied along the width of the stylus and that the stylus did not become fully engaged with the workpiece until a depth of cut of approximately 1.6 μm was achieved. For simplicity, the depths reported below indicate the maximum depth of cut achieved.

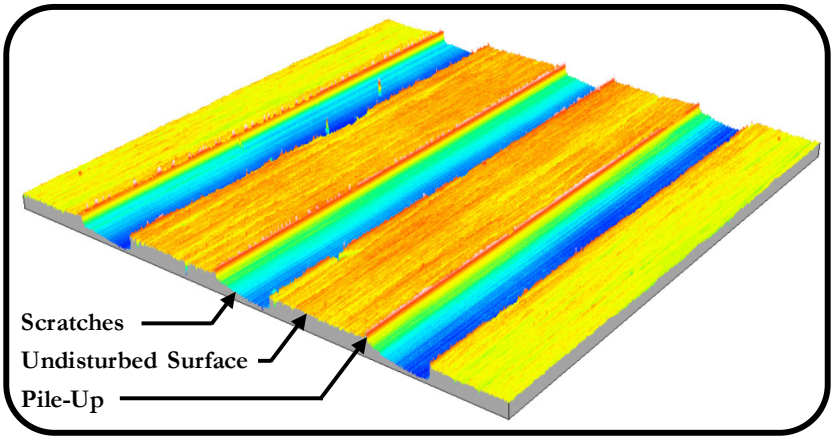

Figure 7.1 - Three-dimensional scan of scratches from flat-nosed stylus.

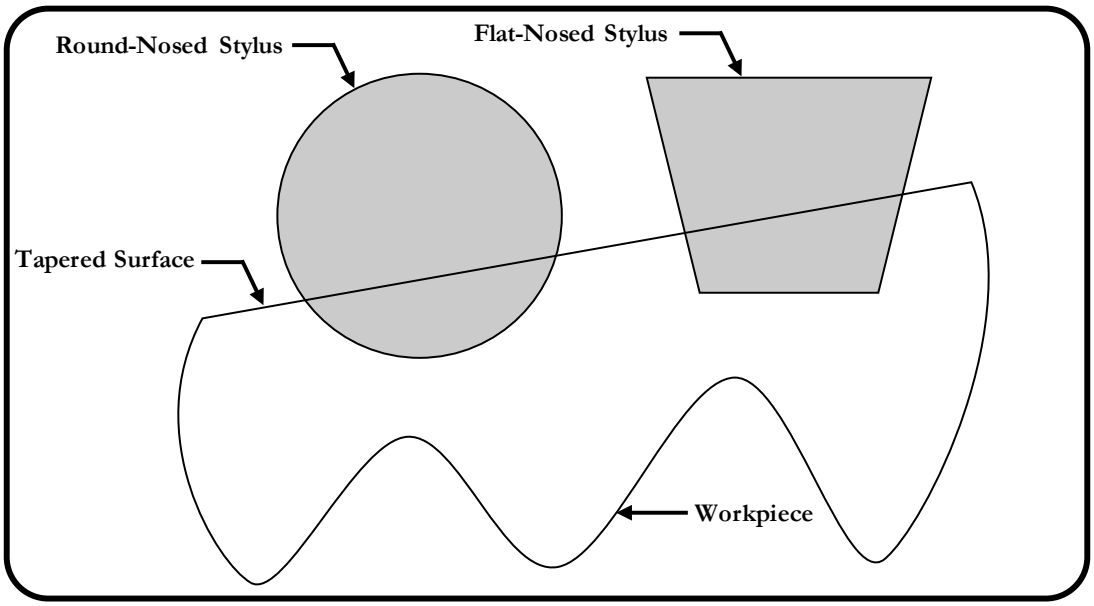

Figure 7.2 - Effect of workpiece taper on round-nosed and flat-nosed stylus.

It is apparent from Figure 7.1 that there was much less pile-up forming at the edges of the scratches with the flat-nosed stylus as compared to the round-nosed stylus. This lack of pile-

up becomes more clear when examining the scratch profiles shown in Figure 7.3. As the figure shows the piled-up material was localized to the edges of the residual groove and there was very little bulk deformation of the workpiece beyond approximately 10 μm from the edge of the residual groove, probably due to the improved cutting efficiency of the flat-nosed stylus. Figure 7.4 also shows that the average pile-up height decreased as the depth of cut was increased.

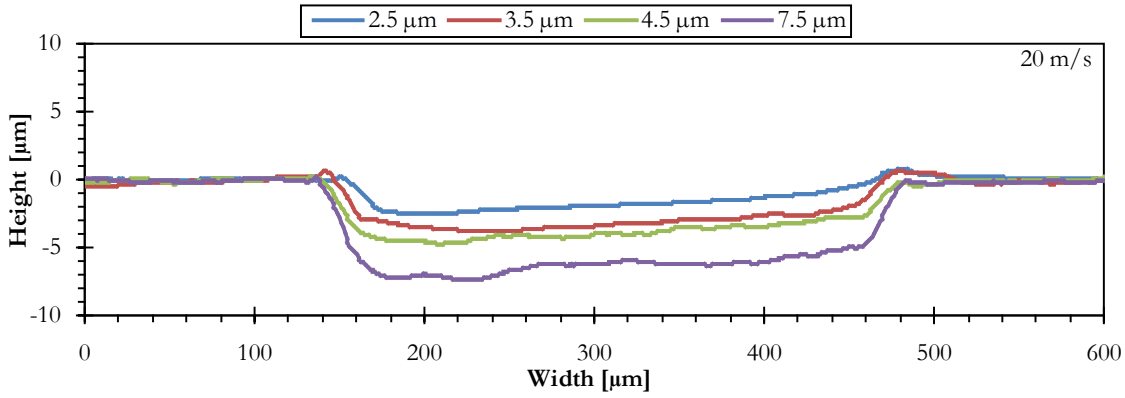

Figure 7.3 - Scratch profiles from flat-nosed stylus.

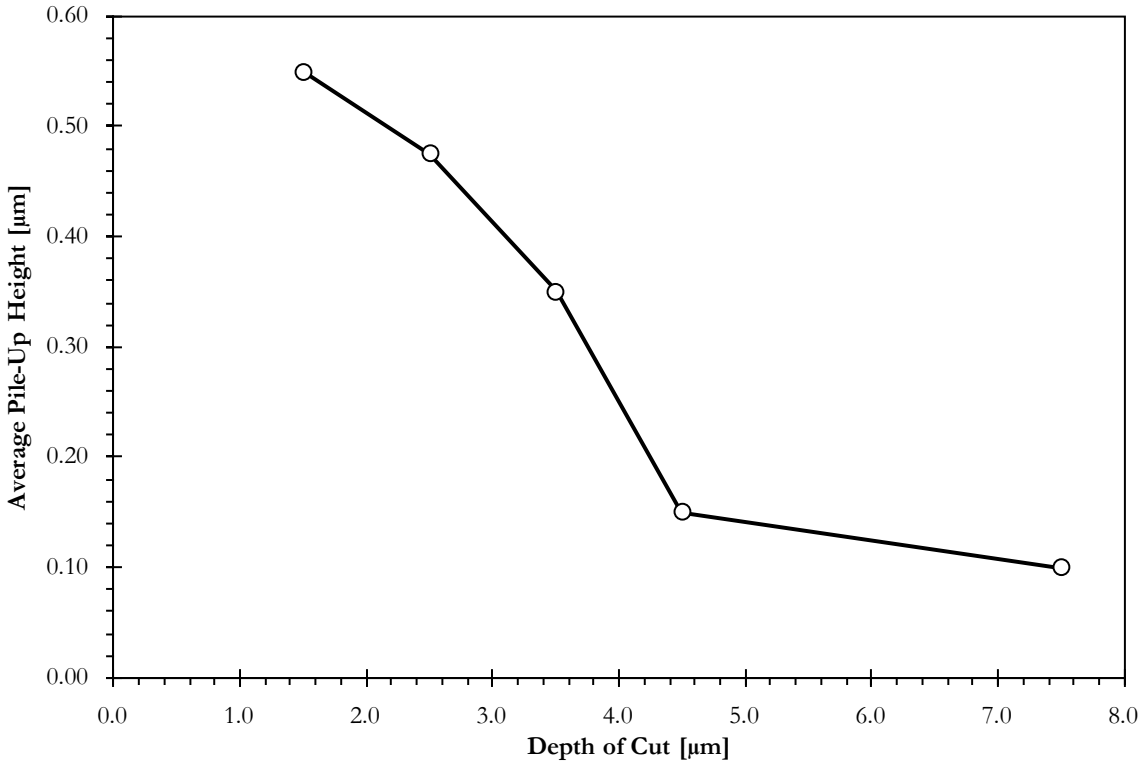

Figure 7.4 - Average pile-up height as a function of depth of cut for the flat-nosed stylus.

The experimental normal forces for the flat-nosed stylus are plotted in Figure 7.5. As can be seen in the figure the normal force increased rapidly until a depth of cut of approximately 1 μm was reached due to the rapid initial increase in tool width engagement caused by the workpiece taper and the surface texture of the workpiece. Beyond a depth of cut of 1 μm the normal force increased more slowly. This leveling of the normal force can be explained by the relatively constant contact due to the small cone angle of the stylus. The area projected in the normal direction only increases by approximately 0.17% for each micrometer increase in the depth of cut and can safely be ignored. The normal force shown in the figure increases at a rate of approximately 3%, which may be due to the additional plastic strain produced by the larger depth of cut.

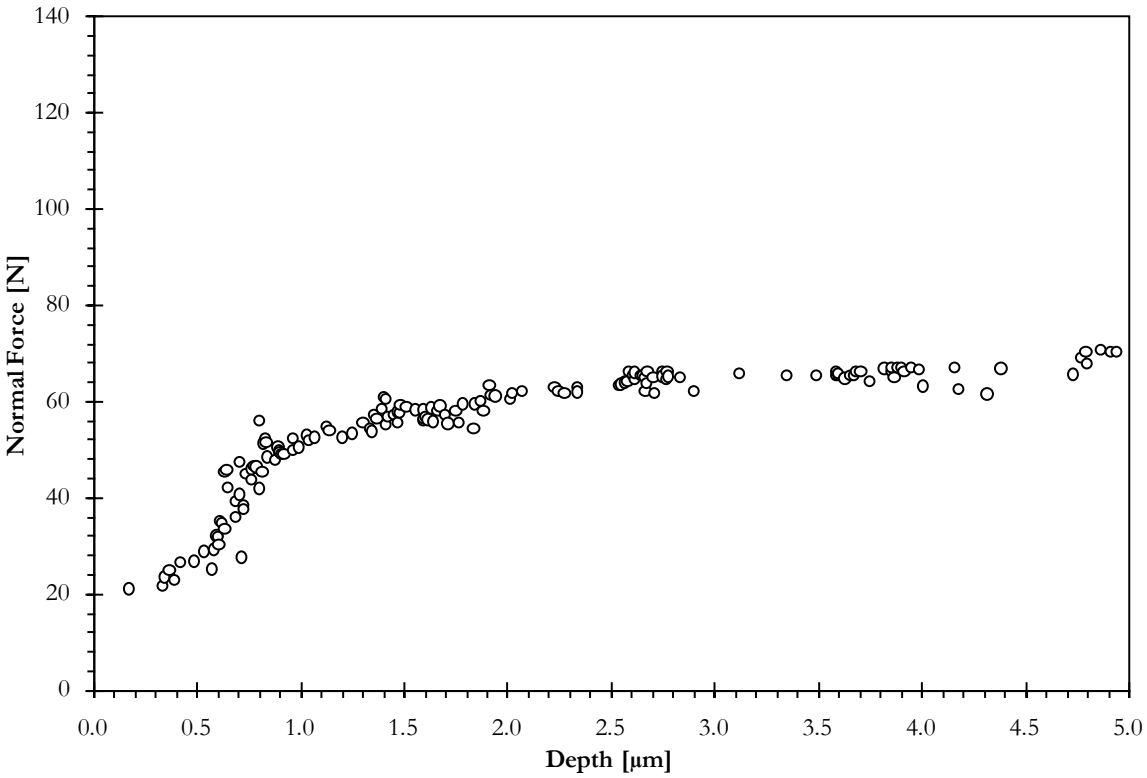

Figure 7.5 - Normal force as a function of depth of cut for flat-nosed stylus.

The normal forces were higher with the flat-nosed stylus as compared to the round-nosed stylus for a given depth of cut as shown in Table 7.1. The table provides the normal forces F_{Norm}, contact areas A_c, and contact pressures p at several depths of cut for both stylus geometries. The table shows that the forces and areas were higher but the pressures were

lower with the flat-nosed stylus. Based on the contact areas, the flat-nosed stylus would be expected to produce higher forces for a given depth of cut as it should require a larger force to push a larger object into the workpiece. The contact pressures indicate that the subsurface stresses are elastic with the flat-nosed stylus and plastic with the round-nosed stylus based on the approximate yield strength of 883 MPa. The lower pressures with the flat-nosed stylus may be indicative of the reduction in material flowing under the stylus due to the increase in the amount of cutting. Interestingly, the pressures decreased with the round-nosed stylus as the depth of cut was increased which may indicate a transition from rubbing to plowing and cutting.

Table 7.1 - Normal force comparison between two stylus geometries.

	Flat-Nosed			Round-Nosed		
Depth of Cut [µm]	F_{Norm} **[N]**	A_c **[µm²]**	p **[MPa]**	F_{Norm} **[N]**	A_c **[µm²]**	p **[MPa]**
2.0	61	82994	735	16	6384	2506
3.0	64	83268	768	22	9576	2297
4.0	66	83542	790	29	12767	2272

The experimental tangential forces for the flat-nosed stylus are plotted in Figure 7.6. The figure shows that the tangential force increased at a linear rate. The lack of the parabolic to linear transition as was seen in the round-nosed stylus data was likely due to the more pronounced cutting action of the flat-nosed stylus. It may be that rubbing and plowing were occurring at very low depths of cut and could not be detected in the experiments.

The comparison between the forces obtained with the flat-nosed and round-nosed styli is shown in Table 7.2, which shows the tangential forces F_{Tan}, the width of cut w, and the force per unit width F_{Tan}/w for the two stylus geometries. The forces were higher with the flat-nosed stylus as compared to the round-nosed stylus and this increase was likely attributable to the increase in the width of cut. The force per unit width was larger with the flat-nosed stylus because more work was being done in front of the stylus as a result of the improved cutting action.

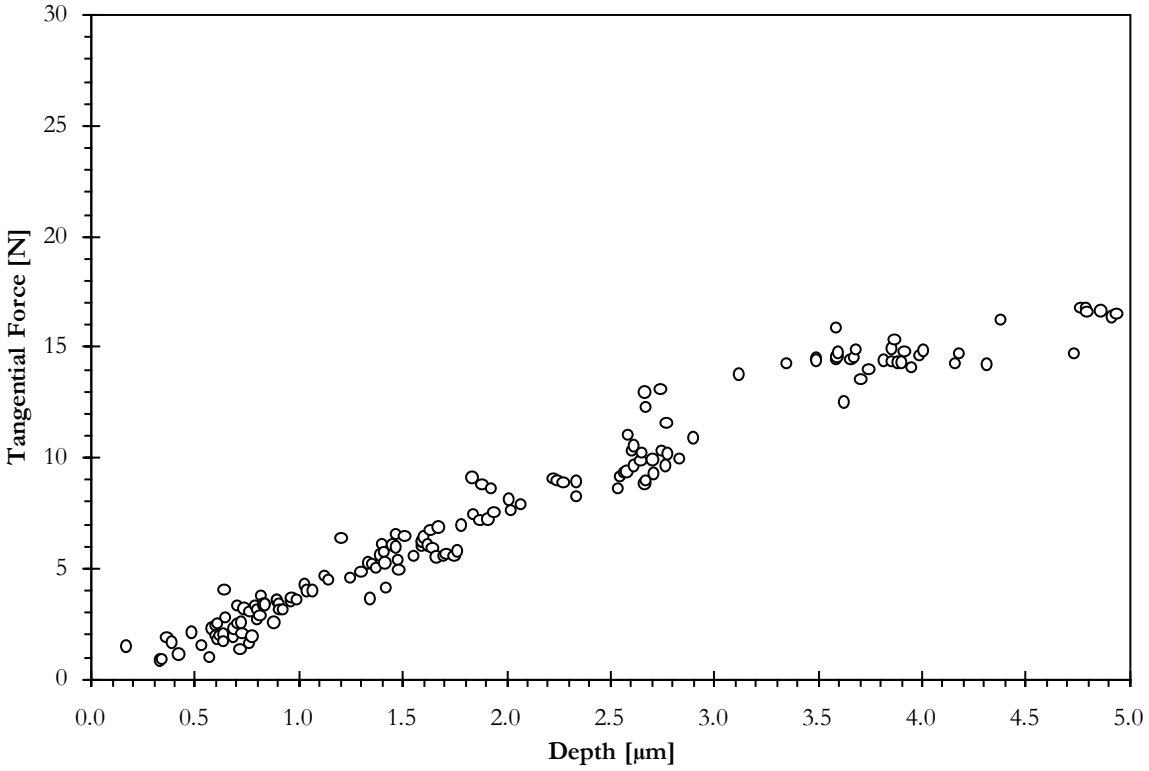

Figure 7.6 - Tangential force as a function of depth of cut for flat-nosed stylus.

Table 7.2 - Tangential force comparison between two stylus geometries.

	Flat-Nosed			Round-Nosed		
Depth of Cut [µm]	F_{Tan} **[N]**	w **[µm]**	$\frac{F_{Tan}}{w}$ **[N/µm]**	F_{Tan} **[N]**	w **[µm]**	$\frac{F_{Tan}}{w}$ **[N/µm]**
2.0	7.9	325.1	0.024	1.7	90.1	0.019
3.0	11.9	325.6	0.037	2.9	110.3	0.026
4.0	14.5	326.1	0.044	4.1	127.3	0.032

Figure 7.7 is a plot of the force ratio for the flat-nosed stylus and as the figure shows the force ratio increased linearly as the depth of cut was increased The fitted force ratio data for the round-nosed stylus is also included in the figure for reference purposes. The force ratio for the flat-nosed stylus was within the same range as was seen with the round-nosed stylus; however, it seems that the force ratio with the flat-nosed stylus continues to increase in contrast to the leveling that occurred with the round-nosed stylus. Since it was shown that the adhesion friction between the stylus and the workpiece material was unaffected by depth of cut it was not surprising that the force ratios were similar between the two stylus geometries. The force ratios were higher with the flat-nosed stylus because of the improved

cutting action, which was also demonstrated by the reduced pile-up height shown in Figure 7.3.

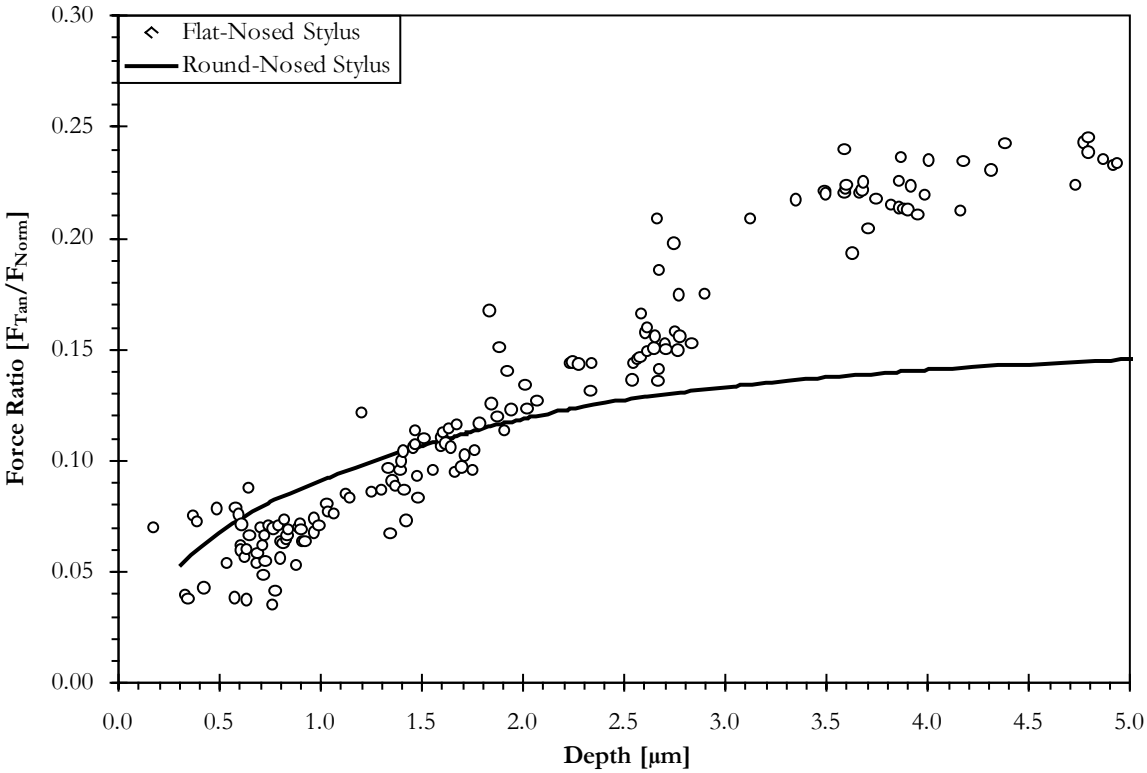

Figure 7.7 - Force ratio as a function of depth of cut for flat-nosed stylus.

The specific energy was calculated to determine the efficiency of the flat-nosed stylus in a similar manner as the round-nosed stylus. However, to determine the MRR with the flat-nosed stylus required calculating the intersection area for two cases: when the depth of cut was less than 1.6 μm and when the depth of cut was greater than 1.6 μm. The first case is illustrated in Figure 7.8 with the taper angle exaggerated for clarity, where the width of the flat nose X was 0.324 mm, the taper angle ψ was approximately 0.28°, the half-cone angle of the stylus Υ was 15°, and the depth of cut was a. The two additional angles, λ and ς, can be found from:

$$\lambda = 90° + \Upsilon \tag{7.1}$$

$$\varsigma = 180 - \psi - \lambda \tag{7.2}$$

Through trigonometric relationships, the width of cut w can be calculated from:

$$w = \frac{a \sin \lambda}{\sin \psi \, sin\varsigma} \tag{7.3}$$

which leads to the area of the triangle to be:

$$A_S = \frac{1}{2} wa \tag{7.4}$$

which reduces to:

$$A_S = \frac{1}{2} \frac{a^2 \sin \lambda}{\sin \psi \, sin\varsigma} \tag{7.5}$$

The second case, when a was greater than 1.6 μm, is illustrated in Figure 7.9, where the taper angle is exaggerated for clarity. The area is calculated as the difference between the shaded region A_s and the area to be removed:

$$A_s = \left[\frac{1}{2} \frac{a^2 \sin \lambda}{\sin \psi \, sin\varsigma}\right] - \left[\left(\frac{1}{2} \frac{a^2 \sin \lambda}{\sin \psi \, sin\varsigma}\right)\left(\frac{\sin \lambda \sin \psi \left(\frac{a}{\sin \psi} - X\right)}{\sin \gamma}\right)\right] \tag{7.6}$$

where in the second case:

$$\lambda = 90° - \Upsilon \tag{7.7}$$

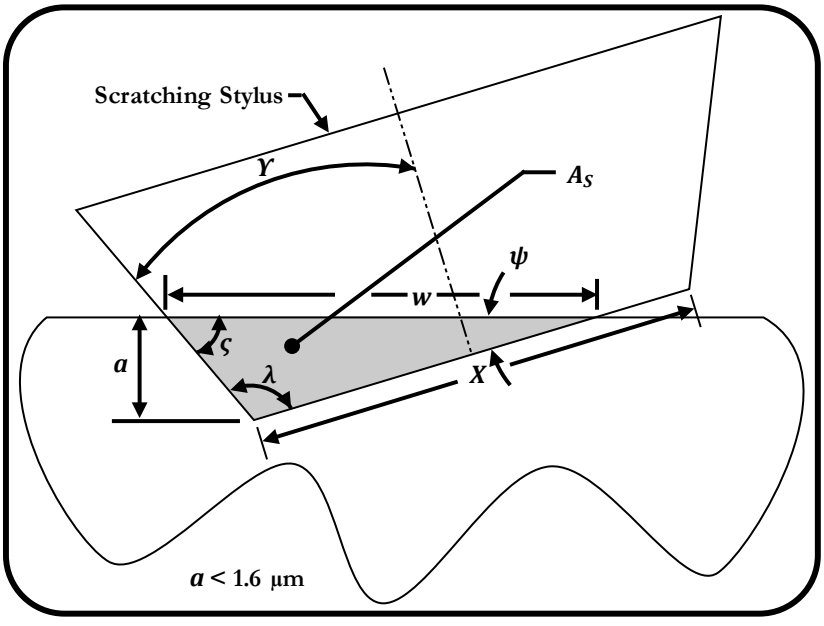

Figure 7.8 - Flat-nosed stylus-workpiece interaction area for a depth of cut less than 1.6 μm

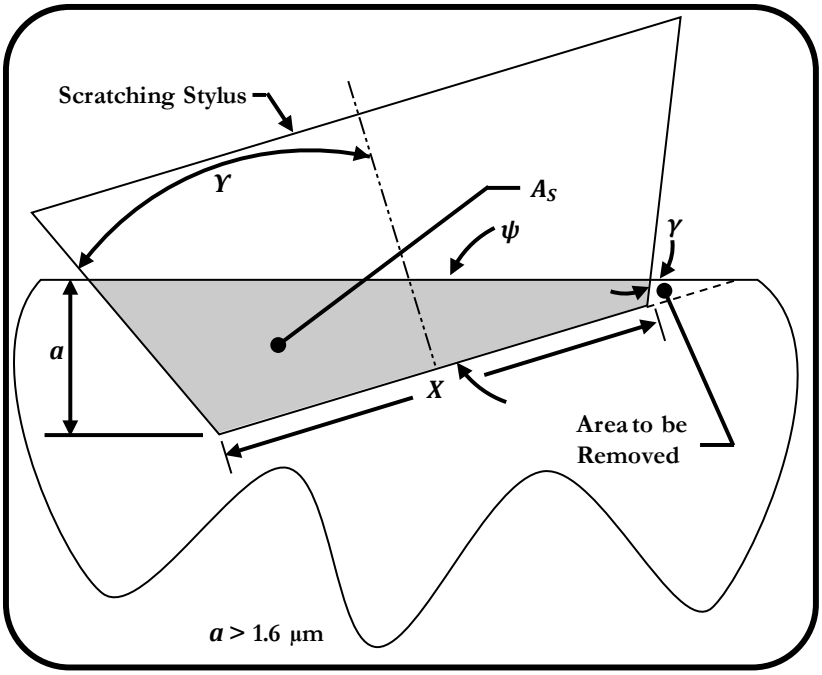

Figure 7.9 - Flat-nosed stylus-workpiece interaction area for a depth of cut greater than 1.6 μm

Figure 7.10 depicts the specific energy obtained with the flat-nosed stylus. As was the case with the round-nosed stylus, there was a noticeable size effect at low depths of cut and there appeared to be a natural minimum value that was obtained as the depth of cut was increased. The size effect seemed to be less pronounced with the flat-nosed stylus in that the specific energies decreased less rapidly as compared to the round-nosed stylus as shown in Figure 7.11. Note that fitted data based on the raw tangential forces was used in the figure to more clearly display the trends of the two data sets. The round-nosed specific energy may be more prone to the asperity contact due to the increased rubbing at low depths of cut as compared to the flat-nosed stylus. The most interesting aspect of the figure is that both stylus geometries converged to the same specific energy. The depth at which the two values become identical may indicate when cutting becomes the dominant mode of material removal for the round-nosed stylus. This data seems to indicate that there is a natural minimum to the specific energy, as reported by Malkin [2], regardless of the geometry of the abrasive grain. In the case of 4340 steel it appears to be approximately 14 J/mm^3, which is very close to the value of 13.8 J/mm^3 reported by Malkin.

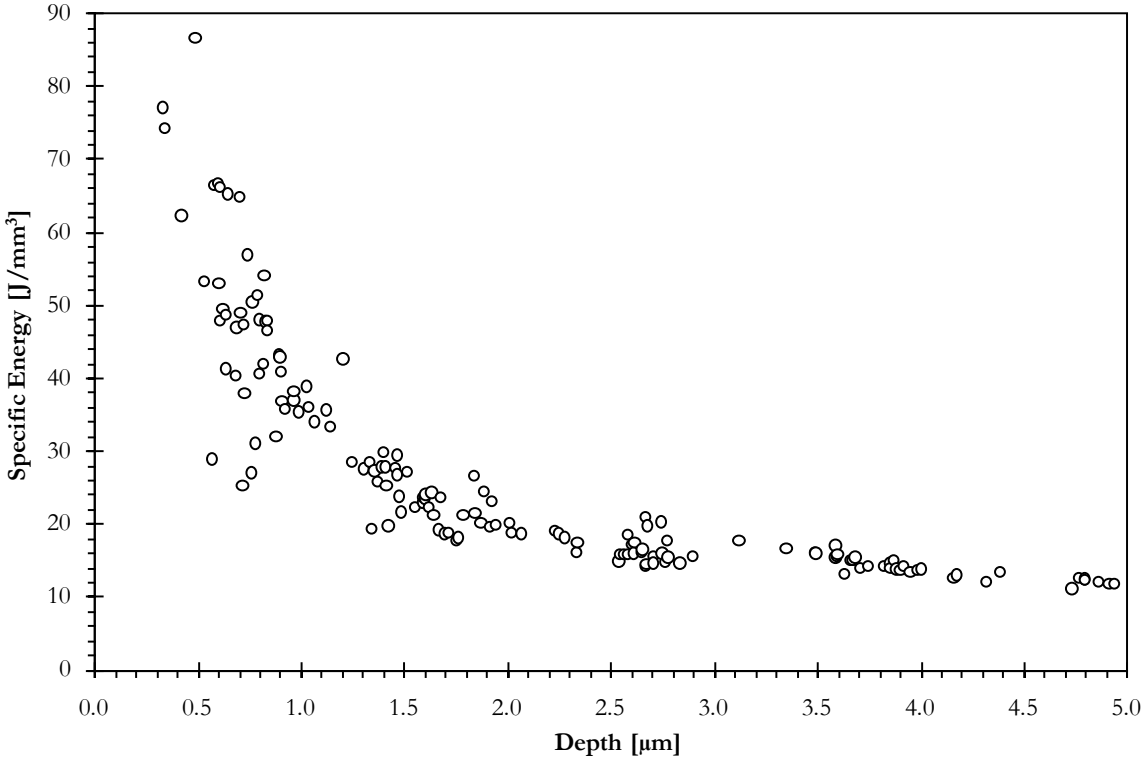

Figure 7.10 - Specific energy as a function of depth for flat-nosed stylus.

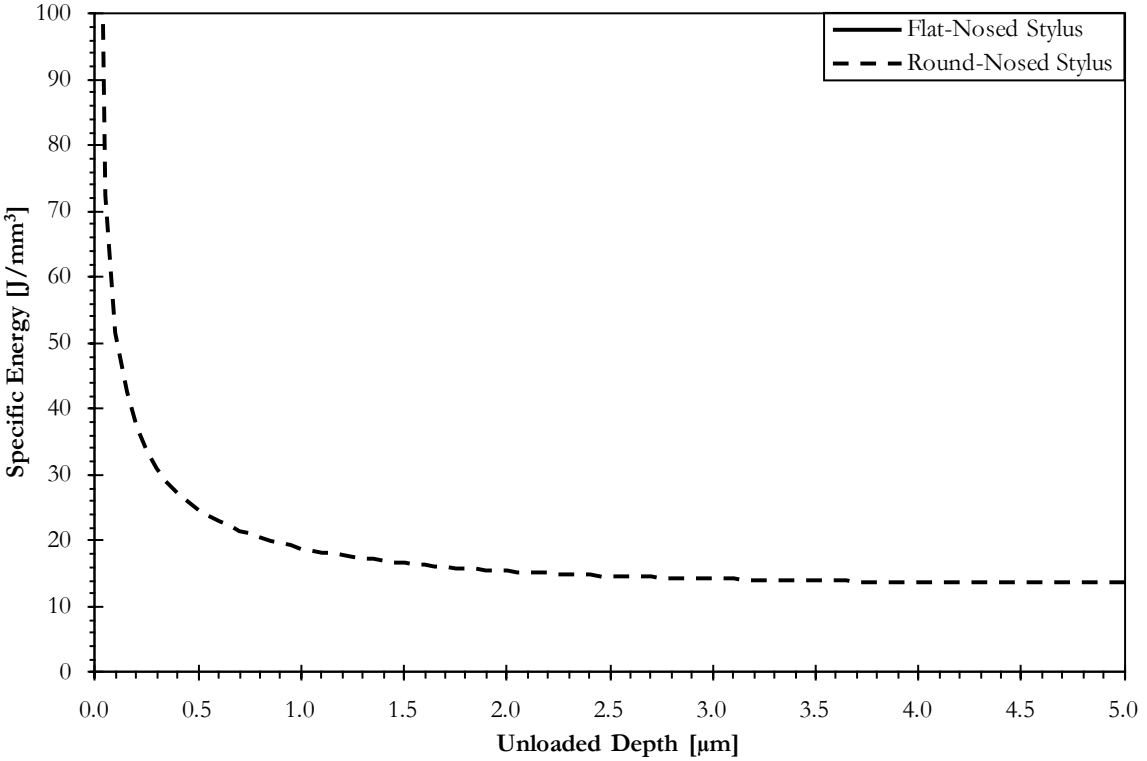

Figure 7.11 - Comparison of round-nosed and flat-nosed specific energy for 20 m/s scratching speed.

7.2 Flat-Nosed Stylus Scratching Model

The finite element model that was employed for the round-nosed stylus required several modifications so that it could be used for the flat-nosed stylus. The first modification became evident after initial testing revealed that the subsurface stresses were more localized when using the flat-nosed stylus as shown in Figure 7.12 where the von Mises stress contours are shown on the XY-symmetry plane for a depth of cut of 9 μm and a scratching speed of 30 m/s. The workpiece model shown in the figure was the same model that was used for the round-nosed stylus at the largest depths of cut. As the figure shows the stress contours were localized to the top of the workpiece. This result occurred due to the more efficient cutting action that was occurring with the flat-nosed stylus as opposed to the severe subsurface deformation that occurred with the round-nosed stylus. Therefore, the first modification was to reduce the depth of the model. The second modification was to increase the width of the high deformation zone where the cutting was occurring. This modification was necessary due to the wider contact area of the flat-nosed stylus as compared to the round-nosed stylus. The third modification was to increase the length of the workpiece and the height of the void material. A longer workpiece was required for the chip formation to achieve steady-state and a larger void space was required to capture the taller chips. The fourth, and final, modification was to switch the material plasticity model from the Johnson-Cook model to the plastic kinematic material model. This final modification was required as the Johnson-Cook model was having difficulty converging causing the simulations to terminate prematurely. It is thought that the high stress and strain gradients in three dimensions prevented the Johnson-Cook plasticity algorithm from converging. A more refined mesh may have solved the convergence issues; however, this refinement would have resulted in a very large number of elements on the order of two million or greater. This number of elements was too great to solve in a respectable amount of time, even on ACEnet. A representation of the final workpiece model for the flat-nosed stylus can seen in Figure 7.13. The figure shows that the hybrid Eulerian-Lagrangian method continued to be employed and that there was no longer any need for a Lagrangian elastoplastic definition due to the localized stress fields. Despite the reduction in the height of the workpiece model the number of nodes and elements increased by a factor of approximately 3 to 542,999 and 483,111, respectively, when compared to the large workpiece model for the round-nosed stylus. These increases in elements and nodes are accounted for

by the two fold increase in the length of the workpiece and the nine fold increase in the height of the void material of the flat-nosed workpiece model as compared to the largest round-nosed workpiece model. Symmetry along the X-axis was exploited to reduce the size of the model by one half and appropriate boundary conditions were placed on the XY-face to account for the symmetry. The bottom and outer faces of the model were constrained in all directions to prevent unwanted motion of the workpiece, which was valid as the stresses and strains at these locations were sufficiently low.

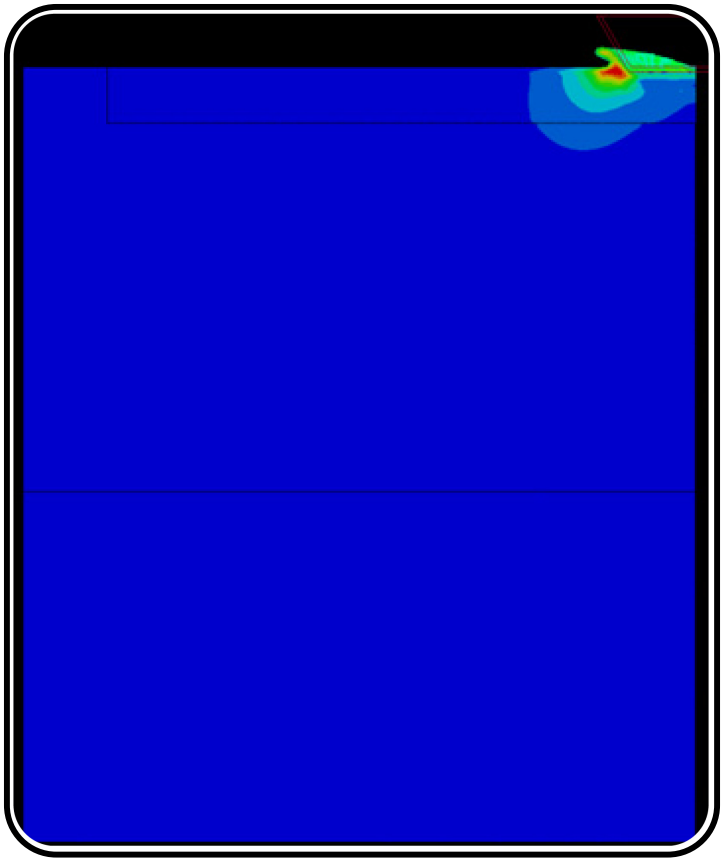

Figure 7.12 - Initial subsurface stresses for flat-nosed stylus.

Figure 7.14 shows a representative image of the finite element mesh of the flat-nosed diamond stylus. Since the stylus was assumed rigid, only one layer of elements was required.

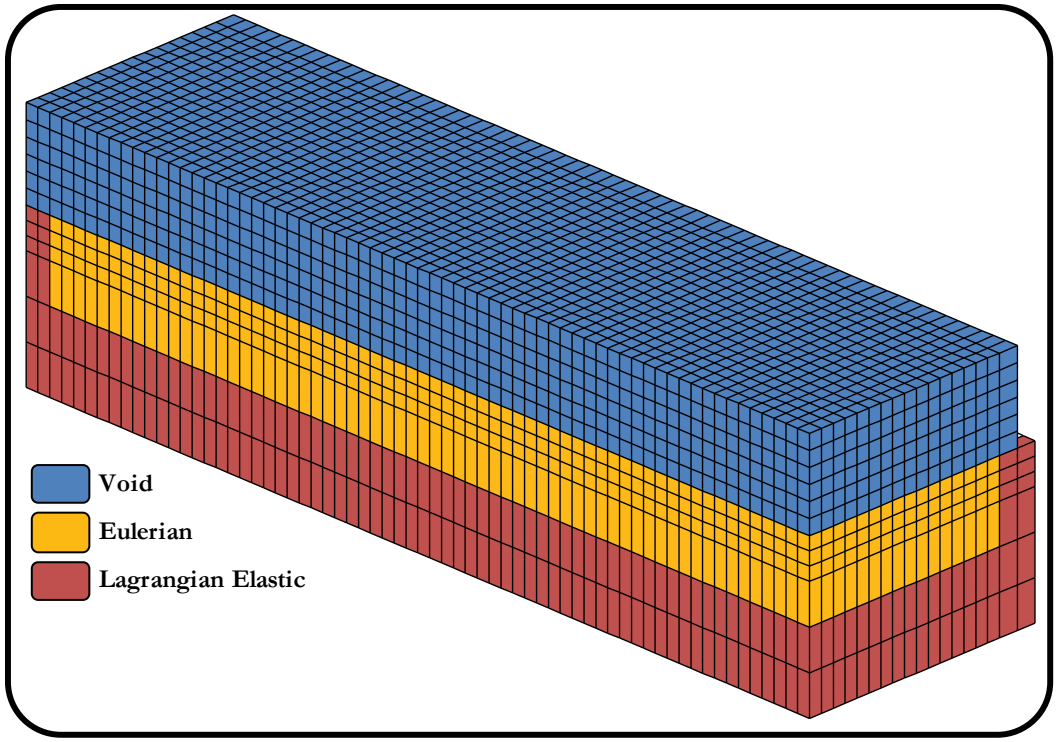

Figure 7.13 - Representative finite element workpiece mesh for the flat-nosed stylus.

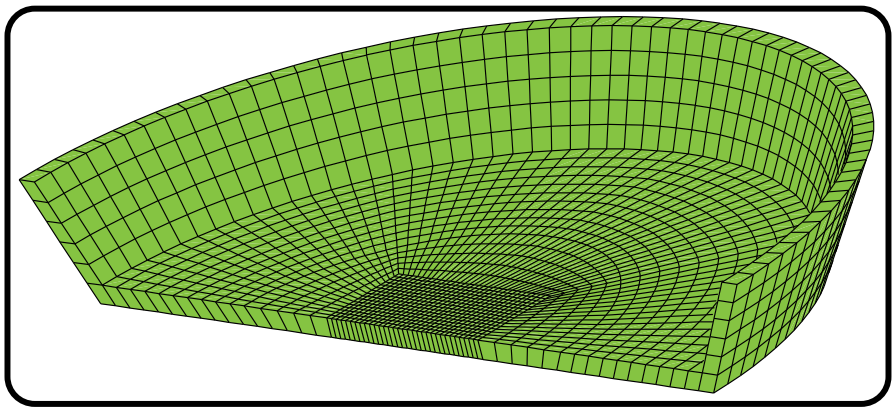

Figure 7.14 - Representative finite element mesh of the flat-nosed diamond stylus.

7.3 Finite Element Model Results

Figure 7.15 shows the comparison between the numerical normal force and experimental normal force. The agreement between the numerical and experimental normal forces for the flat-nosed stylus was not as good as for the round-nosed stylus. The average error was approximately 34.3% for the flat-nosed stylus as compared to approximately 12.6% for the round-nosed stylus. There are several reasons that the finite element model would over

predict the normal forces. Firstly, the plastic kinematic material model may not accurately predict the workpiece stresses at the moderately high strain rates of the scratching process, which were in the range of 2000 s^{-1} along the shear plane. Also, the plastic kinematic material model did not incorporate a thermal softening term; therefore, the forces in the finite element model will be higher as was shown with the round-nosed scratching model. The inclusion of softening may create a leveling of the numerical data as the depth of cut is increased due to the direct relation between the change in temperature and plastic strain in the workpiece. Secondly, the scratches created in the finite element model were perfectly flat; however, the actual measured scratches displayed a tapered surface at the base of the scratch as was shown in Figure 7.1. This experimentally observed taper would tend to create a lower average depth of cut and consequently lower forces. Finally, the stress gradients were much higher with the flat-nosed stylus; therefore, a finer mesh may be required to properly capture these gradients and the resulting forces.

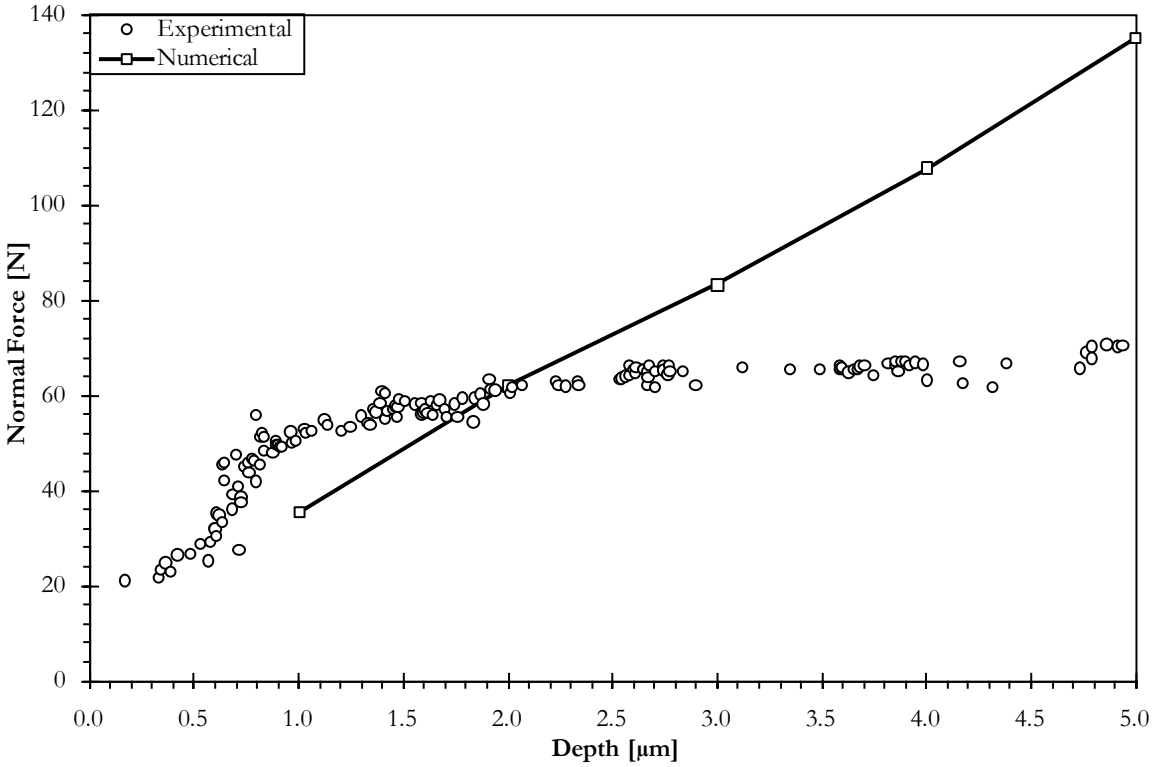

Figure 7.15 - Comparison between experimental and numerical normal forces for flat-nosed stylus.

Figure 7.16 compares the numerically determined tangential forces to the experimental tangential forces. As the figure shows the agreement is relatively good with errors in the

vicinity of 14%. It should be mentioned that the coefficient of friction was not altered to improve the numerical results. The same coefficient of friction that was determined for the round-nosed stylus was used for the flat-nosed stylus. It can be seen that the numerical forces begin to diverge from the experimental forces after a depth of cut of approximately 3 μm and this may be explained by the additional complexity introduced due to chip formation. As mentioned in Section 3.3.2, the Eulerian formulation in LS-DYNA® does not permit the formation of discontinuous chips due to the absence of fracture definitions. It is plausible that discontinuous chips were being created during the experiments as it was difficult to see the chips once the scratching had been completed. It would likely have been easier to see and collect chips if continuous chips had formed. Also, the geometry of the flat-nosed scratching stylus did not lend itself well to the creation of continuous chips since it did not present a flat face perpendicular to the direction of motion. So, in the finite element model continuous chips were being created which would increase the load against the scratching stylus and subsequently increase the tangential forces. This effect can be confirmed by analyzing Figure 7.17 (a - d) which shows the initial chip formation for a scratching speed of 20 m/s and a depth of cut of 5 μm at four distinct times. From the figure it can be seen that there was a large amount of material in front of the stylus, which was likely impeding the motion of the stylus and increased the tangential forces. If the material had been able to break away then it is expected that the forces would decrease. As the simulation progressed it became clear where cracks in the chip would form as the material flowed away from these areas to form gaps as highlighted in the figure. This thinning of the material makes sense because the material flow must maintain continuity as it flows around stylus. It is expected that these gaps are one of the modes of chip cracking that would produce discontinuous chips. The other mode of cracking was likely along the root of the chip. This form of cracking was not visible in the current finite element model, but may become visible if an obstruction to chip flow were introduced. This obstruction would simulate the bond material and other abrasives that are in close proximity in a real grinding wheel.

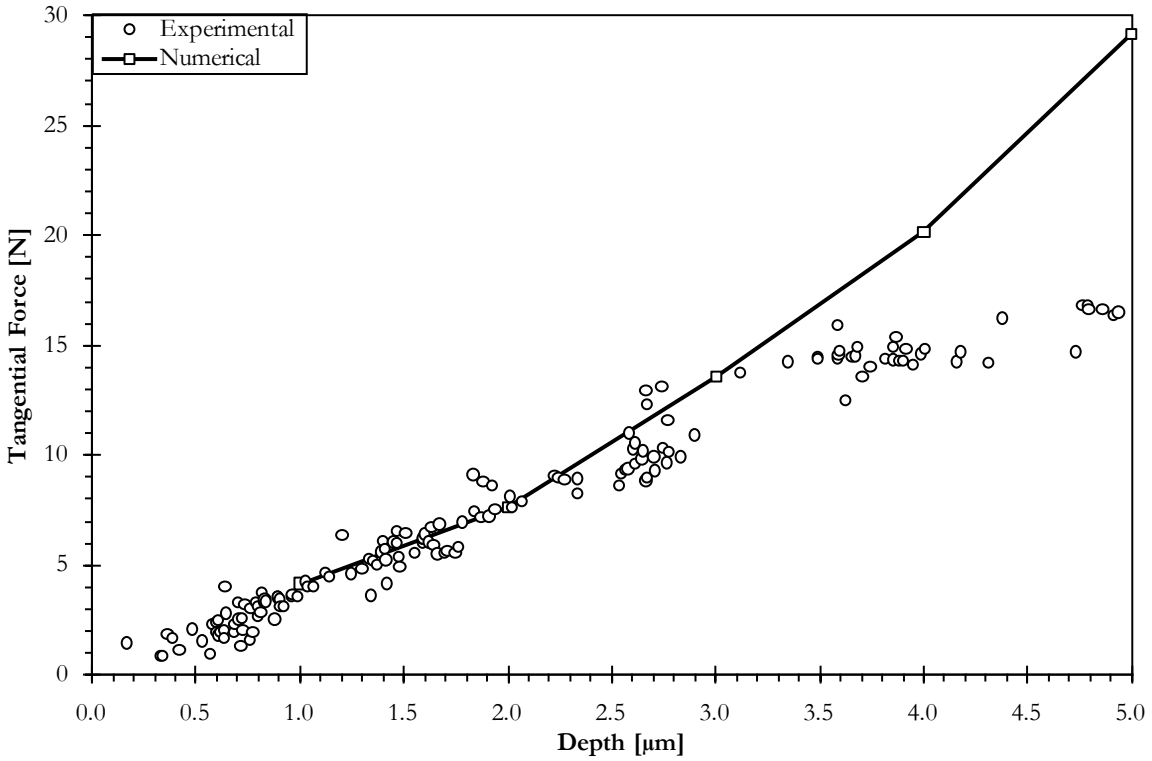

Figure 7.16 - Comparison between experimental and numerical tangential forces for flat-nosed stylus.

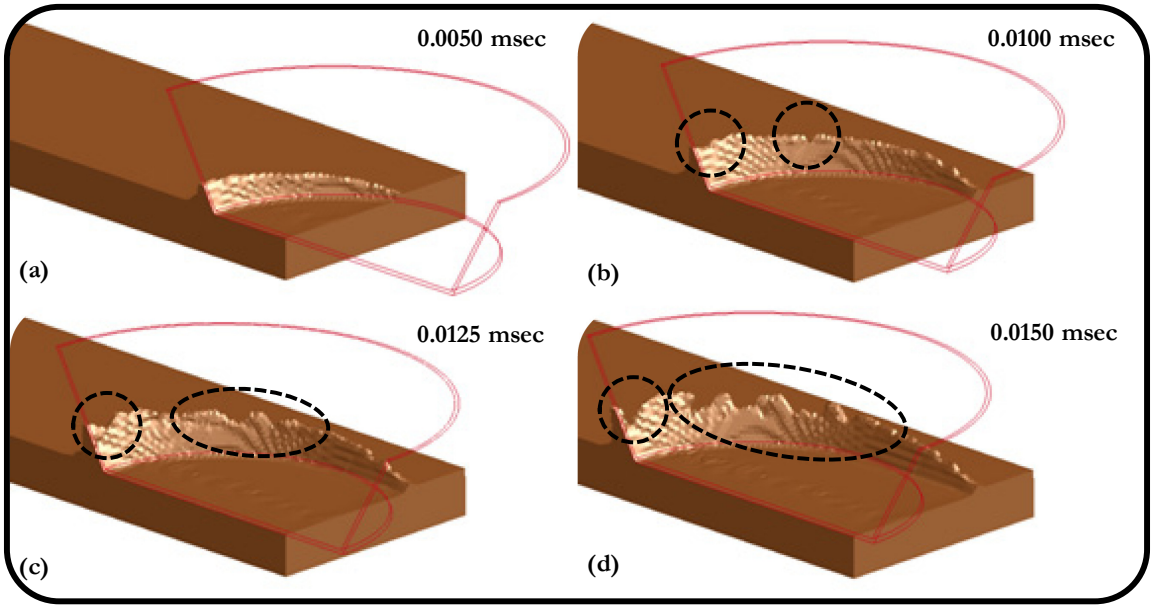

Figure 7.17 (a - d) - Initial chip formation with flat-nosed stylus.

Figure 7.18 shows the von Mises stresses for a depth of cut of 5 µm. The figure shows that the highest stresses occurred along the shear plane as expected according to metal cutting

theory. The figure also shows that the stresses under the stylus were low which indicated that there was less rubbing between the stylus and the workpiece and less material flowing under the stylus. The reduction in the subsurface stresses also highlights the importance of increasing the cutting action as the volume of stressed material was much higher when rubbing and plowing were more dominant in the round-nosed simulations.

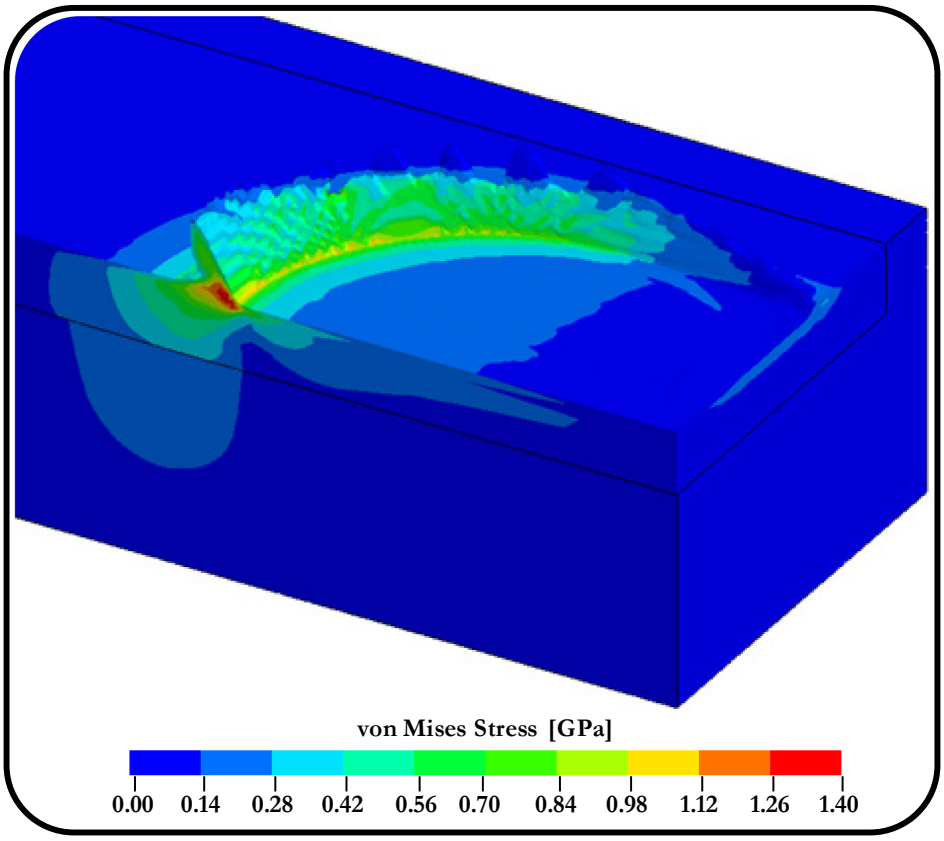

Figure 7.18 - von Mises stresses due to chip formation.

Figure 7.19 compares the subsurface von Mises stresses on the XY-symmetry plane for the flat-nosed and round-nosed stylus geometries, where the dashed lines indicate the approximate location of the yield surface. Both plots have been scaled to the same approximate linear dimensions. As the figure shows, the maximum stresses were nearly identical between the two geometries; however, the location of the maximum stress as well as the size of the stress fields were vastly different. The flat-nosed stylus produced a more localized maximum stress along the shear plane of the chip with a small stress field extending ahead of the stylus, which is indicative of the improved cutting action created by

the stylus geometry. The stresses below the flat-nosed stylus were within the elastic limit of the workpiece material, which confirms the contact pressures reported earlier in Table 7.1. The round-nosed stylus produced a much larger volume of plastic deformation both ahead and below the stylus, which is indicative of the poor cutting qualities of the round-nosed stylus. During a real grinding process it is probable that the stress fields are a combination of the two shown in the figure because the geometry of a real abrasive grain is more like a combination of the two stylus geometries.

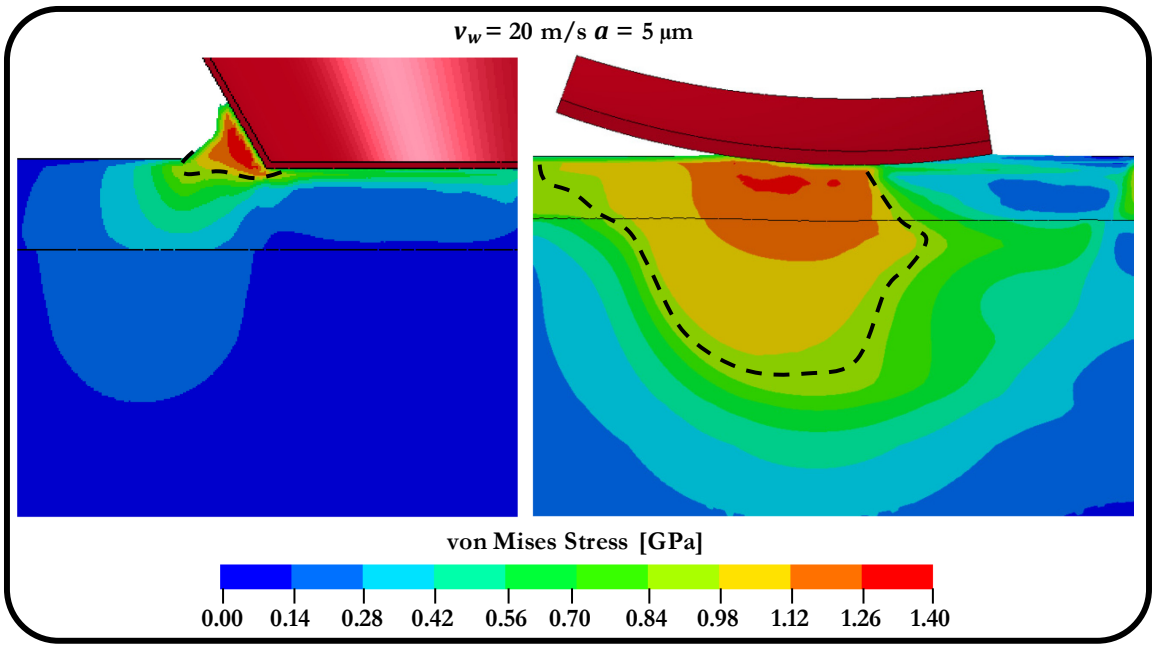

Figure 7.19 - Comparison of von Mises stresses for flat-nosed and round-nosed styli.

7.4 Summary

This chapter has presented the experimental and numerical results of the flat-nosed scratching stylus for a scratching speed of 20 m/s. The results showed that there was a significant increase in the cutting action of the scratching process with the flat-nosed stylus as compared to the round-nosed stylus, which resulted in an improved surface finish due to the reduced pile-up height. The normal force did not seem to be affected by the depth of cut beyond approximately 2 µm due to the gradual increase in contact area. The error between the experimental and numerical normal force data was higher with the flat-nosed stylus as compared to the round-nosed stylus, but was still within acceptable limits. The

correlation between the experimental and numerical tangential data was very good without having to adjust the coefficient of friction. The finite element model revealed the complex flow pattern of the workpiece material around the stylus and showed that the subsurface stress fields were much smaller and more localized to the shear band in the chip. The specific energies of the flat-nosed and round-nosed stylus geometries were compared and the results showed that the round-nosed stylus was more affected by the size effect; however, both stylus geometries attained the same minimum specific energy of approximately 14 J/mm^3.

Chapter 8 Conclusions

A grinding wheel consists of a large number of abrasive grains that interact with a workpiece at high speeds to remove material. Due to the large number and the variability of the abrasive grains it is exceptionally difficult to isolate the effects that a single grain has on the grinding operation from the whole. Therefore, the purpose of this work was to investigate the cutting mechanics of a single abrasive grain. The cutting mechanics of an abrasive grain were investigated using a combination of experimental observations and simulations using the finite element technique.

The experimental observations consisted of high-speed scratch tests using a round-nosed stylus and a flat-nosed stylus. The round-nosed stylus was used to approximate a 15-grit abrasive grain while the flat-nosed stylus was used to approximate a worn 46-grit abrasive grain. The high-speed scratch tests were performed on AISI 4340 steel samples and were designed to mimic the conditions that an abrasive grain would be subjected to during the grinding operation; namely, high scratching speeds ranging from 5 m/s to 30 m/s and small

depths of cut ranging from 0.3 μm to 7.5 μm. The scratch profiles were measured using a three-dimensional optical profilometer. This system provided the ability to measure the scratch features with a resolution of 5 nm permitting accurate scratch depths and pile-up heights.

The finite element simulations were developed in stages with each stage undergoing separate validation. The first stage consisted of indentation testing, which was chosen to simplify the problem by removing the relative motion between the stylus and workpiece. The initial indentation model was compared to well-known analytical solutions of the spherical indentation process. Once the finite element model was found to agree with the analytical solutions, it was compared to experimental data. The model was refined until acceptable agreement was obtained as compared to the experimental data. The next stage of development consisted of introducing relative motion to the model and validating it against the high-speed scratch testing data. The coefficient of friction was utilized as a tuning parameter to create the best fit to the tangential data. Once the finite element model was completely validated it was used alongside the experimental data to perform an in-depth analysis of the scratching process.

The results of the scratching process provided many insights into the abrasive-grain cutting process. The normal forces were found to increase linearly for a given depth of cut as the scratching speed was increased with the round-nosed stylus due to strain-rate hardening of the workpiece material. This result was important as it implies that machine deflections will increase as the scratching speed is increased which reduces the accuracy of the process. The normal force increased rapidly up to an approximate depth of cut of 2 μm with the flat-nosed stylus due to asperity contact and then leveled off due to the slow increase in the contact area.

The tangential forces were found to decrease with scratching speed with the round-nosed stylus due to a reduction in the coefficient of friction and a change in the cutting mechanics. The shape of the tangential data was found to be parabolic up to an approximate depth of cut of 2 μm followed by a linear trend. The coefficient of friction was found to decrease from 0.133 at a scratching speed of 5 m/s to 0.047 at a scratching speed of 30 m/s.

Additionally, it was found that the coefficient of friction did not change with the depth of cut, unlike the overall force ratio. The increase in the force ratio with an increase in the depth of cut was found to be a result of plowing friction, which did not depend on the scratching speed. The changes in the cutting mechanics were identified by analyzing the evolution of the scratch profiles as the scratching speed and depth of cut were changed. It was found that higher scratching speeds reduced the height of the piled-up material, which indicated that more material was being cut from the workpiece. The tangential force linearly increased as the depth of cut was increased with the flat-nosed stylus. The flat-nosed stylus also produced less pronounced pile-up due to the increase in the cutting action of the stylus.

The specific energy of the scratching process was found to decrease as the scratching speed and depth of cut were increased with both of the stylus geometries and was attributed to the change in the cutting mechanics from rubbing and plowing to cutting. Cutting is a more efficient process; therefore, the energy requirement reduced as the cutting action increased. The specific energy data also displayed the well-known size effect where the energies were initially very high at low depths of cut followed by a rapid decrease and convergence towards a minimal value. A comparison between the specific energies of the round-nosed and flat-nosed stylus geometries showed that the round-nosed stylus was more susceptible to the size effect and was attributed to the asperity contact between the stylus and the surface texture of the workpiece. The specific energies of both stylus geometries converged towards the same value, which may indicate the point where cutting became dominant with the round-nosed stylus.

It was found that there was no clear transition from rubbing to plowing to cutting for the round-nosed stylus. These three stages of material removal were found to coexist with different weightings depending on the process parameters. Rubbing was more dominant at higher cutting speeds and lower depths of cut while cutting was more dominant at higher depths of cut.

The elastic, elastoplastic, and fully plastic states of the workpiece were identified for the round-nosed stylus. A fully elastic state occurred at depths of cut of approximately 0.06 μm for a 5 m/s scratching speed to approximately 1.09 μm for a 30 m/s scratching speed. The

increase in the depth as the scratching speed was increased was attributed to strain-rate hardening of the workpiece. The elastoplastic state was found to occur in the parabolic region of the tangential data while the fully plastic state was found to occur in the linear region of the tangential data.

A numerical case study was performed with the round-nosed stylus scratching model to investigate the effects that a reduction in the grain size would produce. It was found that the normal force, tangential force, and specific energy decreased due to the reduction in contact area between the stylus and the workpiece. The force ratio was found to increase due to the increase in the plowing friction. The volume of stressed material decreased and the maximum subsurface stress increased due to the reduced contact area. The smaller grain sizes increased the effective rake angle which increased the amount of cutting.

Based on the results and observations of the scratching process it can be concluded that down grinding should be performed at higher cutting speeds with larger maximum uncut chip thickness and smaller abrasive grains. These parameters will reduce the specific energy requirements, improve the surface finish of the workpiece, and reduce the forces. However, the higher cutting speeds may result in increased tool wear and greater machine deflections.

8.1 Contributions

There were several important direct contributions that resulted from this work, some of which has been approved for publication in respected peer-reviewed journals:

- Development of a validated three-dimensional finite element model of single abrasive-grain cutting with chip formation
- Numerical identification of the role of strain-rate hardening and thermal softening
- Implementation of the hybrid Euler-Lagrange formulation for abrasive-grain cutting
- Development of a novel experimental apparatus for high-speed scratch testing
- Experimental identification of the change in cutting mechanics
- Identification of purely elastic rubbing limit
- Identification of elastic to elastoplastic transition

- ❖ Identification of elastoplastic to plastic transition

To the best of the author's knowledge, the finite element models developed and validated for the present work are the first three-dimensional thermo-structural models of single abrasive-grain cutting with chip formation. Previous models by other researchers lacked experimental validation and relied more on qualitative comparisons. There have been some excellent works that modeled abrasive cutting in two dimensions; however, as was shown in the present work the material flow is far more complex than a simple two-dimensional model can predict. Finally, there has been at least one work that detailed a three-dimensional experimentally-validated model; however, it lacked thermal softening in the material model definition and only concentrated on the rubbing and plowing phases of material removal. The inclusion of thermal softening was important as it permitted the study of its effects on the forces and stress distributions. Although the effect was small compared to the effect of strain-rate hardening, it was still shown to exist and may become more important with the inclusion of frictional heating.

The hybrid Euler-Lagrange implementation is unique to the present work for metal cutting. This hybrid method has only been found in-use by one other researcher in the field of ballistic impact and penetration. This implementation was vital for the present work as it permitted substantial reductions in computational time. Without this formulation, it may not have been possible to perform the large number of simulations that were required to tune, test, and refine the finite element models.

The experimental apparatus that was used for the present work was unique due to its modular nature and its ability to replicate the cutting speeds and depths of cut experienced during the grinding operation. The inclusion of the three-dimensional optical profilometer bolstered the capability of the experimental apparatus to enable detailed studies of the scratch evolution as the cutting conditions were changed. Previous works either did not include direct scratch measurements or utilized much more costly and time consuming SEM techniques.

The combined use of experimental data and finite element simulations permitted a detailed study of the scratching process. Unlike previous works, there were not any distinct changes in the cutting mechanics of the scratching process; rather, the changes occurred gradually with the three phases occurring simultaneously. It was shown that the state of stress in the workpiece transitioned from purely elastic at small depths of cut to elastoplastic and eventually fully plastic as the depth of cut was increased. It can be argued that at suitably low depths of cut pure rubbing is occurring during the fully elastic state; however, beyond the elastic limit of the workpiece rubbing, plowing, and cutting are all occurring.

8.2 Recommendations for Future Work

There are several avenues that could be explored to continue the work presented in this thesis. The experimental apparatus could be altered such that single-point turning was performed on a cylindrical workpiece. This altered experimental apparatus would only be possible based on recent improvements to the current optical measurement system. Single-point turning would allow long continuous scratches to be produced, possibly eliminating the difficulties imposed by the natural frequencies of the force dynamometer. These long scratches may permit higher cutting speeds to be investigated. The cutting effectiveness of different grain geometries could be explored experimentally and numerically, which may provide insight into the optimal grain geometry and size. The cutting mechanics of multiple grains could be studied to determine how the forces change as multiple grains are engaged in the workpiece. Features that were left out of the finite element model could be added as newer versions of LS-DYNA® are released; specifically, a fracture or damage model to study discontinuous chips and frictional heating to create a more complete thermo-structural model.

References

1. U.S. Department of Commerce. (2004) *Manufacturing in America. A Comprehensive Strategy to Address the Challenges to U.S. Manufacturers.* Washington, D.C..

2. Malkin, S. (1989) *Grinding Technology. Theory and Applications of Machining with Abrasives.* Dearborn: Society of Manufacturing Engineers.

3. World Bank. (2009) *Total GDP 2008.* World Development Indicators Database..

4. American National Standards Institute. (1977) *Markings for Identifying Grinding Wheels and Other Bonded Abrasives.* New York.

5. Lachance, S. (2003) *Development of an Automated System to Evaluate the Surface Condition of Grinding Wheels, Master's Thesis.* Department of Mechanical Engineering, Dalhousie University, Halifax Nova Scotia, Canada.

6. Marshall, E.R., and Shaw, M.C. (1952) *Forces in Dry Surface Grinding.* Transaction of the ASME. 74:51 - 58.

7. Hahn, R.S. (1962) *On the Nature of the Grinding Process.* Proceedings of the 3rd International Machine Tool Design & Research Conference; Manchester. 129 - 154.

8. Marinescu, I.D., Tonshoff, H.K., and Inasaki, I. (2000) *Handbook of Ceramic Grinding and Polishing.* New York: William Andrew Publishing.

9. Subramanian, K., Ramanath, S., and Tricard, M. (1997) *Mechanisms of Material Removal in the Precision Production Grinding of Ceramics.* ASME Journal of Manufacturing Science and Engineering. 199:509 - 519.

10. Zhao, H.H., Cai, C.Q., and Gao, X.J. (2006) *Model Establishment of Chip-Formation due to Shock Under Ultra-High Speed Grinding.* Key Engineering Materils. 304 - 305:246 - 250.

11. Backer, W.R., Marshall, E.R., and Shaw, M.C. (1952) *Size Effect in Metal Cutting.* Transactions of the ASME. 74:61 - 71.

12. Groover, M.P. (2002) *Fundamentals of Modern Manufacturing. 2nd ed.*: John Wiley & Sons.

13. Doman, D.A. (2008) *Rubbing & Plowing Phases in Single Grain Grinding, Doctoral Thesis.* Department of Mechanical Engineering, Dalhousie University, Halifax Nova Scotia, Canada.

14. Merchant, M.E. (1944) *Basic Mechanics of the Metal Cutting Process.* ASME Journal of Applied Mechanics. 11:168 - 175.

15. Malkin, S. (1979) *Negative Rake Cutting to Simulate Chip Formation in Grinding.* Annals of CIRP. 28:209 - 212.

16. Ostrovskii, V.I. (1985) *Model of Chip Formation in Grinding.* Sverkhtverdye Materialy. 7:30 - 35.

17. Moufki, A., Devillez, A., Dudzinski, D., and Molinari, A. (2004) *Thermomechanical Modeling of Oblique Cutting and Experimental Validation.* International Journal of Machine Tools and Manufacture. 44:971 - 989.

18. Molinari, A., and Moufki, A. (2005) *A New Thermomechanical Model of Cutting Applied to Turning Operations. Part I. Theory.* International Journal of Machine Tools and Manufacture. 45:166 - 180.

19. Strenkowski, J.S., Albert, J., and Shih Jong-Cherng, L. (2002) *An Analytical Finite Element Model for Predicting Three-Dimensional Tool Forces and Chip Flow.* International Journal of Machine Tools and Manufacture. 42:723 - 731.

20. Usui, E., Hirota, M., and Masuko, A. (1978) *Analytical Prediction of Three Dimensional Cutting Processes: Part I. Basic Cutting Model and Energy Approach.* ASME Journal of Engineering for Industry. 100:222 - 228.

21. Bao, W.Y., and Tansel, I.N. (2000) *Modeling Micro-End-Milling Operations. Part I: Analytical Cutting Force Model.* International Journal of Machine Tools and Manufacture. 40:2155 - 2173.

22. Kang, I.S., Kin, J.S., Kim, J.H., Kang, M.C., and Seo, Y.W. (2007) *A Mechanistic Model of Cutting Force in the Micro End Milling Process.* Journal of Materials Processing Technology. 187 - 188:250 - 255.

23. Zaman, M.T., Senthil Kumar, A., Rahman, M., and Sreeram, S. (2006) *A Three-Dimensional Analytical Cutting Force Model for Micro End Milling Operation.* International Journal of Machine Tools and Manufacture. 46:353 - 366.

24. Son, S.M., Lim, H.S., and Ahn, J.H. (2005) *Effects of the Friction Coefficient on the Minimum Cutting Thickness in Micro-Cutting.* International Journal of Machine Tools and Manufacture. 45:529 - 535.

25. Newby, S., Venkatachalam, S., and Liang, S.Y. (2007) *Empirical Analysis of Cutting Force Constants in Micro-End-Milling Operations.* Journal of Materials Processing Technology. 192 - 193:41 - 47.

26. Moufki, A., and Molinari, A. (2005) *A New Thermomechanical Model of Cutting Applied to Turning Operations. Part II. Parametric Study.* International Journal of Machine Tools and Manufacture. 45:181 - 193.

27. Usui, E., and Hirota, A. (1978) *Analytical Prediction of Three Dimensional Cutting Process: Part 2. Chip Formation and Cutting Force with Conventional Single-Point Tool.* ASME Journal of Engineering for Industry. 100:229 - 235.

28. Mackerle, J. (1999) *Finite-Element Analysis and Simulation of Machining. A Bibliography (1976 - 1996).* Journal of Materials Processing Technology. 86:17 - 44.

29. Mackerle, J. (2003) *Finite Element Analysis and Simulation of Machining. An Addendum. A Bibliography (1996 - 2002).* International Journal of Machine Tools and Manufacture. 43:103 - 114.

30. Vaz Jr, M., Owen, D.R.J., Kalhori, V., and Lundblad, M. (2007) *Modelling and Simulation of Machining Processes.* Archives of Computational Methods in Engineering. 14:173 - 204.

31. Kalhori, V. (2001) *Modelling and Simulation on Mechanical Cutting, Doctoral Thesis.* Department of Mechanical Engineering, Lulea University of Technology, Lulea, Sweden.

32. Borouchaki, H., Laug, P., Cherouat, A., and Saanouni, K. (2005) *Adaptive Remeshing in Large Plastic Strain with Damage.* International Journal for Numerical Methods in Engineering. 63:1 - 36.

33. Marusich, T.D., and Ortiz, M. (1995) *Modelling and Simulation of High-Speed Machining.* International Journal of Numerical Methods for Engineering. 38:3675 - 3694.

34. Klocke, F., Raedt, H.W., and Hoppe, S. (2001) *2D-FEM Simulation of the Orthogonal High Speed Cutting Process.* Machining Science and Technology. 5:323 - 340.

35. Mamalis, A.G., Branis, A.S., and Manolakos, D.E. (2002) *Modelling of Precision Hard Turning Using Implicit Finite Element Methods.* Journal of Materials Processing Technology. 123:464 - 475.

36. Grzesik, W., Bartoszuk, M., and Nieslony, P. (2005) *Finite Element Modeling of Temperature Distribution in the Cutting Zone in Turning Processes with Differently Coated Tools.* Journal of Material Processing Technology. 164 - 165:1204 - 1211.

37. Shet, C., and Deng, X. (2000) *Finite Element Analysis of the Orthogonal Metal Cutting Process.* Journal of Materials Processing Technology. 105:95 - 109.

38. Shi, G., Deng, X., and Shet, C. (2002) *A Finite Element Study of the Effects of Friction in Orthogonal Metal Cutting.* Finite Element Analysis and Design. 38:863 - 883.

39. Liu, C.R., and Guo, Y.B. (2000) *Finite Element Analysis of the Effect of Sequential Cuts and Tool-Chip Friction on Residual Stresses in a Machined Layer.* International Journal of Mechanical Sciences. 42:1069 - 1086.

40. Baker, M., Rosler, J., and Siemers, C. (2002) *Finite Element Simulation of Segmented Chip Formation of Ti6Al4V.* ASME Journal of Manufacturing Science and Engineering. 124:485 - 488.

41. Guo, Y.B., and Yen, D.W. (2004) *A FEM Study on Mechanisms of Discontinuous Chip Formation in Hard Machining.* Journal of Materials Processing Technology. 155 - 156:1350 - 1356.

42. Lai, X., Li, H., Li, C., Lin, Z., and Ni, J. (2008) *Modelling and Analysis of Micro Scale Milling Considering Size Effect, Micro Cutter Edge Radius and Minimum Chip Thickness.* International Journal of Machine Tools and Manufacture. 48:1 - 14.

43. Subbiah, S., and Melkote, S.N. (2007) *Evidence of Ductile Tearing Ahead of the Cutting Tool and Modeling the Energy Consumed in Material Separation in Micro-Cutting.* ASME Journal of Engineering Materials and Technology. 129:321 - 331.

44. Liu, K., and Melkote, S.N. (2006) *Material Strengthening Mechanisms and their Contribution to Size Effect in Micro-Cutting.* ASME Journal of Manufacturing Science and Engineering. 128:730 - 738.

45. Ohbuchi, Y., and Obikawa, T. (2003) *Finite Element Modeling of Chip Formation in the Domain of Negative Rake Angle Cutting.* ASME Journal of Engineering Materials and Technology. 125:324 - 332.

46. Doman, D.A., Bauer, R., and Warkentin, A. (2009) *Experimentally Validated Finite Element Model of the Rubbing and Ploughing Phases in Scratch Tests.* Proceedings of the Institution of Mechanical Engineers Part B: Journal of Engineering Manufacture. 223:1519 - 1527.

47. Benson, D.J., and Okazawa, S. (2004) *Contact in Multi-Material Eulerian Finite Element Formulation.* Computer Methods in Applied Mechanics and Engineering. 193:4277 - 4298.

48. Raczy, A., Altenhof, W.J., and Alpas, A.T. (2004) *An Eulerian Finite Element Model of the Metal Cutting Process.* 8th International LS-DYNA® Users Conference; Michigan.

49. Joyot, P., Rakotomalala, R., Pantale, O., Touratier, M., and Hakem, N. (1998) *A Numerical Simulation of Steady State Metal Cutting.* Proceedings of the Institution of Mechanical Engineers, Part C: Journal of Mechanical Engineering Science. 212:331 - 341.

50. Miguelez, H., Zaera, R., Rusinek, A., Moufki, A., and Molinari, A. (2006) *Numerical Modeling of Orthogonal Cutting. Influence of Cutting Conditions and Separation Criterion.* Journal de Physique IV. 134:417 - 422.

51. Ozel, T., and Zeren, E. (2005) *Finite Element Modeling of Stresses Induced by High Speed Machining with Round Edge Cutting Tools.* 2005 ASME International Mechanical Engineering Congress and Exposition; Orlando.

52. Barge, M., Hamdi, H., Rech, J., and Bergheau, J.M. (2005) *Numerical Modelling of Orthogonal Cutting: Influence of Numerical Parameters.* Journal of Materials Processing Technology. 164-165:1148 - 1153.

53. Movahhedy, M.R., Gadala, M.S., and Altintas, Y. (2000) *Simulation of Chip Formation in Orthogonal Metal Cutting Process. An ALE Finite Element Approach.* Machining Science and Technology. 4:15 - 42.

54. Pantale, O., Rakotomalala, R., Touratier, M., and Hakem, N. (1996) *A Three-Dimensional Numerical Model of Orthogonal and Oblique Metal Cutting Processes.* ASME Engineering Systems Design and Analysis. 3:199 - 206.

55. Olovsson, L., Nilsson, L., and Simonsson, K. (1999) *An ALE Formulation for the Solution of Two-Dimensional Metal Cutting Problems.* Computers and Structures. 72:497 - 507.

56. Limido, J., Espinosa, C., Salaun, M., and Lacome, J.L. (2007) *SPH Method Applied to High Speed Cutting Modelling.* International Journal of Mechanical Sciences. 49:898 - 908.

57. Espinosa, C., Lacome, J.L., Limido, J., Salaun, M., Mabru, C., and Chieragatti, R. (2008) *Modeling High Speed Machining with the SPH Method.* 10th International LS-DYNA® Users Conference; Detroit. 12-9 - 12-20.

58. Akarca, S.S., Song, X., Altenhof, W.J., and Alpas, A.T. (2008) *Deformation Behavious of Aluminum During Machining: Modelling by Eulerian and Smoothed-Particle Hydrodynamics Methods.* Proceedings of the Institution of Mechanical Engineers, Part L: Journal of Materials: Design and Applications. 222:209 - 221.

59. Benson, D.J. (1992) *Computational Methods in Lagrangian and Eulerian Hydrocodes.* Computer Methods in Applied Mechanics and Engineering. 99:235 - 394.

60. Liu, K., and Melkote, S.N. (2007) *Finite Element Analysis of the Influence of Tool Edge Radius on Size Effect in Orthogonal Micro-Cutting Process.* International Journal of Mechanical Sciences. 49:650 - 660.

61. Li, H., Lai, X., Li, C., Feng, J., and Ni, J. (2008) *Modelling and Experimental Analysis of the Effects of Tool Wear, Minimum Chip Thickness and Micro Tool Geometry on the Surface Roughness in Micro-End-Milling.* Journal of Micromechanics and Microengineering. 18:1 - 12.

62. Ohbuchi, Y., and Obikawa, T. (2005) *Adiabatic Shear in Chip Formation with Negative Rake Angle.* International Journal of Mechanical Sciences. 47:1377 - 1392.

63. Ohbuchi, Y., and Obikawa, T. (2006) *Surface Generation Model in Grinding with Effect of Grain Shape and Cutting Speed.* JSME International Journal - Series C. 49:114 - 120.

64. Greer, A.D. (2006) *Numerical Modeling for the Prediction of Primary Blast Injury to the Lung, Master's Thesis.* Department of Mechanical Engineering, University of Waterloo, Ontario, Canada.

65. Sharma, A.C., Sewak, B., and Singh, M. (2008) *Simulation of Impact and Penetration with Hydrocodes.* Proceedings of the 2008 Spring Simulation Multiconference; Ottawa. 729 - 736.

66. Huertas-Ortecho, C.A. (2006) *Robust Bird-Strike Modeling Using LS-DYNA®, Master's Thesis.* Department of Mechanical Engineering, University of Puerto Rico, Mayaguez Campus.

67. Boffi, D., and Gastaldi, L. (2004) *Stability and Geometric Conservation Laws for ALE Formulations.* Computer Methods in Applied Mechanics and Engineering. 193:4717 - 4739.

68. Gadala, M.S., Movahhedy, M.R., and Wang, J. (2002) *On the Mesh Motion for ALE Modeling of Metal Forming Processes.* Finite Element Analysis and Design. 28:435 - 459.

69. Kuhl, E., Askes, H., and Steinmann, P. (2004) *An ALE Formulation Based on Spatial and Material Settings of Continuum Mechanics. Part 1: Generic Hyperelastic Formulation.* Computer Methods in Applied Mechanics and Engineering. 193:4207 - 4222.

70. Askes, H., Kuhl, E., and Steinmann, P. (2004) *An ALE Formulation Based on Spatial and Material Settings of Continuum Mechanics. Part 2: Classification and Applications.* Computer Methods in Applied Mechanics and Engineering. 193:4223 - 4245.

71. Pantale, O., Bacaria, J.L., Dalverny, O., Rakotomalala, R., and Caperaa, S. (2004) *2D and 3D Numerical Models of Metal Cutting with Damage Effects.* Computer Methods in Applied Mechanics and Engineering. 193:4383 - 4399.

72. Movahhedy, M., Gadala, M.S., and Altintas, Y. (2000) *Simulation of the Orthogonal Metal Cutting Process Using an Arbitrary Lagrangian-Eulerian Finite Element Method.* Journal of Materials Processing Technology. 103:267 - 275.

73. Movahhedy, M.R., Altintas, Y., and Gadala, M.S. (2002) *Numerical Analysis of Metal Cutting with Chamfered and Blunt Tools.* ASME Journal of Manufacturing Science and Engineering. 124:178 - 188.

74. Lucy, L.B. (1977) *A Numerical Approach to the Testing of the Fission Hypothesis.* The Astronomical Journal. 82:1013 - 1024.

75. Cleary, P.W., Prakash, M., and Ha, J. (2006) *Novel Applications of Smooth Particle Hydrodynamics (SPH) in Metal Forming.* Journal of Materials Processing Technology. 177:41 - 48.

76. Buyuk, M., Kan, C.D.S., and Bedewi, N.E. (20064) *Moving Beyond the Finite Elements. A Comparison Between the Finite Element Methods and Meshless Methods for a Ballistic Impact Simulation.* 8th International LS-DYNA® Users Conference; Detroit. 81 - 96.

77. Schwer, L. (2006) *Lagrange Erosion, MM-ALE & SPH. A Comparative Case Study of Aluminum Plate Perforation.* Blast & Penetration LS-DYNA® Training Class; Windsor.

78. Schwer, L. (2004) *Preliminary Assessment of non-Lagrangian Methods for Penetration Simulation.* 8th International LS-DYNA® Users Conference; Detroit. 8-1 - 8-12.

79. Hallquist, J.O. (2007) *LS-DYNA® Users Manual.* Livermore: LSTC.

80. Automations Creations, Inc. MatWeb. [Online].; 2009 [cited 2009 November 4.

81. Johnson, G.R., and Cook, W.H. (1983) *A Constitutive Model and Data for Metals Subjected to Large Strains, High Strain Rates and Temperatures.* 7th International Symposium on Ballistics; The Hague. 541 - 547.

82. Johnson, G.R., and Cook, W.H. (1985) *Fracture Characteristics of Three Metals Subjected to Various Strains, Strain Rates, Temperatures and Pressures.* Engineering Fracture Mechanics. 21(1):31 - 48.

83. Kurtaran, H., Buyuk, M., and Eskandarian, A. (2003) *Ballistic Impact Simulation of GT Model Vehicle Door Using Finite Element Method.* Theoretical and Applied Fracture Mechanics. 40:113 - 121.

84. Holmquist, T.J., Templeton, D.W., and Bishnoi, K.D. (2001) *Constitutive Modeling of Aluminum Nitride for Large Strain, High-Strain Rate, and Pressure Applications.* International Journal of Impact Engineering. 25:211 - 231.

85. Mason, C., and Worswick, M.J. (2001) *Adiabatic Shear in Annealed and Shock-Hardened Iron and in Quenched and Tempered 4340 Steel.* International Journal of Fracture. 111:29 - 51.

86. Banerjee, B. (2007) *The Mechanical Threshold Stress Model for Various Tempers of AISI 4340 Steel.* International Journal of Solids and Structures. 44:834 - 859.

87. Schwer, L. (2007) *Optional Strain-Rate Forms for the Johnson-Cook Constitutive Model and the Role of the Parameter Epsilon_0.* 6th European LS-DYNA® Users Conference; Gothenburg.

88. Hallquist, J.O. (2006) *LS-DYNA® Theoretical Manual.* Livermore: LSTC.

89. Cowper, G.R., and Symonds, P.S. (1958) *Strain Hardening and Strain Rate Effects in the Impact Loading of Cantilever Beams.* Brown University, Applied Mathematics.

90. Aquelet, N., Souli, M., and Olovsson, L. (2005) *Euler-Lagrange Coupling with Damping Effects: Application to Slamming Problems.* Computer Methods in Applied Mechanics and Engineering. 195:110 - 132.

91. Benson, D.J. (2008) *Momentum Advection on Unstructured Staggered Quadrilateral Meshes.* International Journal for Numerical Methods in Engineering. 75:1549 - 1580.

92. Johnson, K.L. (1985) *Contact Mechanics.* United Kingdom: Cambridge University Press.

93. Tabor, D. (1951) *The Hardness of Metals.* United Kingdom: Oxford University Press.

94. Tirupataiah, H.K., and Sundararajan, G. (1987) *A Comprehensive Analysis of the Static Indentation Process.* Materials Science and Engineering. 91:169 - 180.

95. Mackerle, J. (2004) *Finite Element Modelling and Simulation of Indentation Testing. A Bibliography (1990 - 2002).* Engineering Computations. 21:23 - 52.

96. Kucharski, S., and Mroz, Z. (2001) *Identification of Hardening Parameters of Metals from Spherical Indentation Tests.* ASME Journal of Engineering Materials and Technology. 123:245 - 250.

97. Kucharski, S., and Mroz, Z. (2001) *Identification of Plastic Hardening Parameters of Metals from Spherical Indentation Tests.* Materials Science and Engineering A. 318:65 - 76.

98. Kucharski, S., and Mroz, Z. (2007) *Identification of Yield Stress and Plastic Hardening Parameters from a Spherical Indentation Test.* International Journal of Mechanical Sciences. 49:1238 - 1250.

99. Nayebi, A., El Abdi, R., Bartier, O., and Mauvoisin, G. (2002) *New Procedure to Determine Steel Mechanical Parameters from the Spherical Indentation Technique.* Mechanics of Materials. 34:243 - 254.

100. Hyungyil, L., Lee, J.H.J., and Pharr, G.M. (2005) *A Numerical Approach to Spherical Indentation Techniques for Material Property Evaluation.* Journal of the Mechanics and Physics of Solids. 53:2037 - 2069.

101. Chudoba, T., Schwarzer, N., and Richter, F. (1999) *New Possibilities of Mechanical Surface Characterization with Spherical Indenters by Comparison of Experimental and Theoretical Results.* Thin Solid Films. 355 - 356:284 - 289.

102. Vanimisetti, S.K., and Narasimhan, R. (2006) *A Numerical Analysis of Spherical Indentation Response of Thin Hard Films on Soft Substrates.* International Journal of Solids and Structures. 43:6180 - 6193.

103. Rodriguez, J., and Garrido Maneiro, M.A. (2007) *A Procedure to Prevent Pile-Up Effects on the Analysis of Spherical Indentation Data in Elastic-Plastic Materials.* Mechanics of Materials. 39:987 - 997.

104. Taljat, B., and Pharr, G.M. (2004) *Development of Pile-Up During Spherical Indentation of Elastic-Plastic Solids.* International Journal of Solids and Structures. 41:3891 - 3904.

105. Hertz, H. (1882) *Uber die Beruhrung Fester Elastiche Korper (On the Contact of Elastic Solids).* J. Rein und Angewandte Mathematik. 92:156 - 171.

106. Biwa, S., and Storakers, B. (1995) *An Analysis of Fully Plastic Brinell Indentation.* Journal of Mechanics and Physics of Solids. 43:1303 - 1333.

107. Lu, Y.C., Kurapati, S.N.V.R.K., and Yang, F. (2008) *Finite Element Analysis of Deep Indentation by a Spherical Indenter.* Journal of Material Science. 43:6331 - 6336.

108. Shainer, G., and Kher, S. (2008) *Optimizing LS-DYNA® Productivity in Cluster Environments.* 10th International LS-DYNA® Users Conference; Dearborn.

109. Makino, M. (2008) *The Performance of 10-Million Element Car Model by MPP Version of LS-DYNA® on Fujitsu PRIMEPOWER.* 10th International LS-DYNA® Users Conference; Dearborn.

110. Doman, D.A., Bauer, R., and Warkentin, A. (2008) *Optical Microscopy-Aided Indentation Tests.* ASME Journal of Engineering Materials and Technology. 130:0110081.

111. National Instruments. NI Vision. 2007.

112. Mackerle, J. (2005) *Coatings and Surface Modification Technologies. A Finite Element Bibliography (1995 - 2005).* Modelling and Simulation in Materials Science and Engineering. 13:935 - 979.

113. Li, J., and Beres, W. (2007) *Scratch Test for Coating/Substrate Systems - A Literature Review.* Canadian Metallurgical Quarterly. 46:155 - 174.

114. Wang, H., Subhash, G., and Chandra, A. (2001) *Characteristics of Single-Grit Rotating Scratch with a Conical Tool on Pure Titanium.* Wear. 249:566 - 581.

115. Cai, G.Q., Feng, B.F., Jin, T., and Gong, Y.D. (2002) *Study of the Friction Coefficient in Grinding.* Journal of Materials Processing Technology. 129:25 - 29.

116. Guo, C., Krishnan, N., and Malkin, S. (1993) *Matching Forces and Powers in Creep-Feed Grinding.* Society of Manufacturing Engineers 5th International Conference; Cincinati. 1 - 10.

117. Zorev, N.N. (1963) *Interrelationship Between Shear Processes Occurring Along Tool Face and on Shear Plane in Metal Cutting.* Proceedings of the International Production Engineering Research Conference; New York. 42 - 49.

118. Molinari, A., Estrin, Y., and Mercier, S. (1999) *Dependence of the Coefficient of Friction on the Sliding Conditions in the High Velocity Range.* ASME Journal of Tribology. 121:35 - 41.

119. Philippon, S., Sutter, G., and Molinari, A. (2004) *An Experimental Study of Friction at High Sliding Velocities.* Wear. 257:777 - 784.

120. Yurkov, A.L., Skvortsov, V.N., Buyanovsky, I.A., and Matvievsky, R.M. (1997) *Sliding Friction of Diamond on Steel, Sapphire, Alumina and Fused Silica With and Without Lubricants.* Journal of Materials Science Letters. 16:1370 - 1374.

121. Subhash, G., and Zhang, W. (2002) *Investigation of the Overall Friction Coefficient in Single-Pass Scratch Test.* Wear. 252:123 - 134.

122. Marinescu, I.D., Rowe, W.B., Dimitrov, B., and Inasaki, I. (2004) *Tribology of Abrasive Machining Processes.* New York: William Andrew Publishing.

123. Bull, S.J. (1991) *Failure Modes in Scratch Adhesion Testing.* Surface and Coating Technology. 50:25 - 32.

124. Burnett, P.J., and Rickerby, D.S. (1987) *The Relationship Between Hardness and Scratch Adhesion.* Thin Solid Films. 154:403 - 416.